Amjad Al Taleb

PhD. Thesis 2017

Surface Structure and Dynamics of Epitaxial

Studied by Helium Atom Scattering

UNIVERSIDAD AUTONOMA
DE MADRID

Surface Structure and Dynamics of Epitaxial Graphene on Metals

Studied by Helium Atom Scattering

Disertación presentada para la obtención del título de
Doctor en Ciencias Físicas
Departamento de Física de la Materia Condensada
Universidad Autónoma de Madrid

Amjad Al Taleb
supervised by
Daniel Farías Tejerina

Madrid 2017

To the memory of
Ghaith and Sausan

Preface

Seeing is believing, and even if one believes, a picture is worth a thousand words. That's why the most omnipotent being in human mythology needed there to be light in order to start working. This need to see has fueled the human quest towards developing various kinds of microscopes in use today.

Recent years have witnessed an accelerating interest in the development of a neutral helium atom microscope as a continuation of the natural path of the evolution of the microscope which started with the optical microscope and recently witnessed the commercialization of the He ion microscope. The development of He microscope builds on top of advances in the fields of He atom scattering and X-ray microscopy. The production and detection of He beams is basically the same for both spectroscopic and microscopic applications. Advances in X-ray microscopy have inspired similar approaches for focusing He beams.

The major problem in realizing the neutral He microscope lies in the focusing element. Helium cannot pass through materials to be focused like light and cannot be manipulated with electric or magnetic fields to be focused like electrons and ions. Therefore one of the most promising options is to focus a He beam by reflection from a concave surface. The reflecting surface needs to be chemically stable and atomically flat. This is where Graphene is of interest. Since its isolation, graphene has drawn the attention of the scientific community due to its unique electronic and mechanical properties. A chemically inert and highly stable material, it can be used to protect other materials from corrosion and oxidation.

This work investigates the surface structure and lattice dynamics of graphene grown on three different surfaces: Cu(111), Ni(111) and Ir(111) using the technique of He atom scattering. Cu(111) is the most interesting material for commercial applications, the weak graphene-Cu interaction makes the transfer of CVD graphene easier to accomplish than with other materials and the abundance of copper in the earth crust makes the production cheaper than with other catalysts. Ni(111) is characterized by the strong graphene-Ni interaction and the low lattice mismatch which results in a (1×1) layer of epitaxial graphene. Nickel is a very reactive material, however it can be easily passivated with graphene. Ni(111) and Cu(111) are interesting for the application of a focusing mirror as they provide flat surfaces. Furthermore, these metals are not brittle, they can be made into thin crystals (100 µm) and bent with relatively

much ease in comparison with other materials. The last surface investigated in this work is graphene on Ir(111), this could be considered the least interesting as a focusing surface since the scattered He beam exhibits intense diffraction modes in the vicinity of the specularly reflected beam. However, its complex surface structure and dynamics provide a plethora of information that help in understanding the He-graphene interaction.

This thesis is divided into two parts: Methods and Results. The first part comprises two chapters: Chapter 1 provides a background of the recent advances in He microscopy, a review of the structure and dynamics of graphene grown on metallic surfaces and finally an introduction to the theory of He atom scattering. Chapter 2 provides a description of the experimental aspects of He atom scattering and the apparatus used in this work.

When I started composing the second part of this manuscript I could not follow the advice of the King of Hearts on how to tell a story, namely, "to start and the beginning and go on till I reach the end then stop" as it does not provide a comparative narrative. Therefore, the results of this work are grouped by objective instead of being divided by subject. Chapter 3 is dedicated for measurements that involve only elastic scattering from the three surfaces. Other observations like thermal expansion are also included. Chapter 4 covers inelastic processes: it starts with Debye-Waller measurements then follows with surface phonon measurements. Chapter 5 is somewhat different from the previous two as it addresses angle and energy resolved Ne scattering from clean Ni(111) surface followed by Ne scattering from Gr/Ni(111) and Gr/Ir(111). Finally, Chapter 6 is a concise summary of the main conclusions of this work.

Acknowledge

We refugees live on the edge, not the cutting edge which people race to, but the dull one that brings nothing but frustration and agony. The work of this thesis has been interrupted for more than a year as I found myself in the limbo of IDs and Permits. It was mainly the support and backing from my thesis supervisor Daniel Farías that helped me get through these troublesome times and continue the work of this thesis. I am very grateful to him, not just for the support he has provided and the amount of bureaucracy he had to go through for my sake, but also because he helped me learn in the lab from my mistakes; advising without interfering, he guided me throughout a tough and long journey towards becoming the scientist I am today.

The work for this thesis started when Rodolfo Miranda received me in his office and granted me the chance to work in his group for my master's degree, then to sponsor me for the first two years of my PhD work. In that meeting at his office he took a chance on me; I would not be working in Spain now if it were not for that chance.

I have benefited in several occasions from discussions with J. R. Manson who had a unique way in explaining various concepts so that even a student with no background on the subject can visualize the physical phenomenon he is explaining with great clarity. My deepest gratitude goes to Nikolaï Mikuszeit who introduced me to the world of Mathematica in a course he volunteered to give to students in the lab. I will be forever indebted to Marina Minniti who provided help and authority in times of doubt. The presence of Jesús Álvarez in the lab has been a great inspiration and motivation for a new interest that I started developing recently with electronics. I am grateful to him for going out of his way every time I had a question to provide the best and clearest answer for me. My gratitude to Gloria Anemone who carried out several measurements on my behalf and helped in writing the papers we have published in the course of the last few year. I also acknowledge the help of Paolo Perna and Davide Maccariello with whom I worked on bringing ERASMO to a working status.

Agradezco mucho la ayuda brindada por los equipos técnicos del departamento; Andrés Buendía, José Luis Romera, Juan Manuel Benayas, Santiago Marquez, José María Pérez y José María Castilla. La gran experiencia y paciencia de todos ellos ha sido crucial para mantener y desarrollar las máquinas utilizadas en esta tesis. Entre ellos agradezco especialmente a Andrés, Santiago y José Pérez porque no solo hicieron el trabajo necesario, sino que me

enseñaron los trucos que tenían bajo las mangas para realizar trabajos complicados. Gracias a ellos me he motivado para aprender a usar AutoCAD y Solid Works y hacer planos técnicos. Existe mucha burocracia en el trabajo en una institución pública. Este trabajo podía haber sido mucho más difícil si no fuera por la profesionalidad de Elsa Fuentes y Luisa Carpallo; especialmente, porque yo no hablaba español durante los primeros años de mi trabajo de tesis. Les agradezco mucho toda la ayuda que me han proporcionado.

The long years that have passed since I started my PhD research have been the most volatile in my life, and it would have been impossible to succeed if it were not for the benevolence and love of many people I came to know along these years. Bisher and Ahmad have been the greatest help that I needed when I was a stranger in a strange land struggling to stand on my feet. Mazhar Toutounjee with whom I worked in my last year in Syria has left a deep impression on my thinking that I only came to realize several years after starting my new life in Spain. Cecilia, Fabiola and Viviana have been friends and critics helping me to become a better person. Totó a companion with whom I could laugh at the absurdities of life. Finalmente, Ana! Ha sido mi pareja y mi familia. No sé qué haría sin ella.

Motivation

Recent developments of neutral He microscope show that currently used focusing methods, namely, Fresnel plate zone diffraction and pin-hole aperturing have intrinsic limitations like chromatic aberration and low intensity. Focusing by reflection from a concave mirror is limited only by technical factors like the quality and stability of the surface of the concave mirror.

The objective of this work is to study graphene-passivated metal surfaces and find the best surface that offers high intensity and small width of the specularly reflected beam on one hand and stability, especially under ambient conditions, on the other hand.

Graphene on metals is an interesting subject of study on its own. Since it is expected to play an important role in thermal management of new electronic devices, it is important to understand its lattice dynamics and how it is affected by the interaction with metallic substrates.

Abstract

This work is a comparative study of the surface structure and lattice dynamics of Gr/Cu(111), Gr/Ni(111) and Gr/Ir(111) surfaces using He atom scattering. The dispersion of the flexural mode (ZA) has been measured for graphene on several metallic substrates for the first time with high resolution at low energies (< 10 meV). The results of this thesis show the inadequacy of the conventional Debye-Waller model in describing atom-surface scattering on layered materials like graphene on metals. Ne scattering in classical regime was used to investigate multi-phonon scattering at the onset of quantum decoherence. Theoretical calculations using a classical model that describe the experimental results of Ne scattering from Ni(111) are presented. We show that Gr/Ni(111) is a promising option to be used as a He focusing mirror as it provides high intensity and quality of the specularly reflected beam.

Resumen

En esta tesis se ha realizado un estudio comparativo de la estructura y dinámica de grafeno (Gr) crecido en Cu(111), Ir(111) y Ni(111) mediante la técnica de Helium Atom Scattering. En particular, se ha medido por primera vez la dispersión del modo de fonones ZA ("flexural mode") de Gr en varias superficies a muy bajas energías (debajo de 10 meV). Se muestran además las limitaciones del modelo convencional de Debye-Waller al describir la dispersión de He en superficies de materiales laminados, como Gr/metales. Este estudio se ha complementado con medidas empleando haces de Ne en el régimen clásico, con el que se ha investigado la dispersión de muchos fonones que marcan el inicio de la decoherencia cuántica. Se muestra que Gr/Ni(111) es una opción prometedora para ser utilizada como espejo de enfoque en el microscopio de He, ya que proporciona a la vez muy alta intensidad y calidad del haz especularmente reflejado.

Contents

Part I

Methods

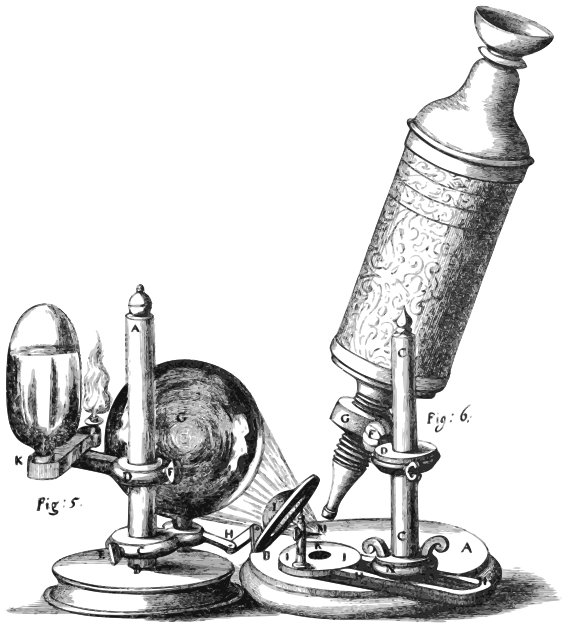

©Robert Hooke's microscope

The first part of the thesis comprises two chapters. Chapter 1 provides a fundamental background. It starts with a short review of the recent advances in He microscopy, which is the main motivation behind this work, followed by a review of the published literature on graphene structure and lattice dynamics and how they are affected by interaction with metals, which is the subject of the current work. The last section in this chapter provides a theoretical background of He-atom scattering which is the experimental technique used in this measurements presented in this thesis. Chapter 2 provides the experimental details of the apparatus used in this work.

Chapter 1

Background and Theory

This chapter starts with a section that reviews the milestones and recent advances that shaped state-of-the-art neutral-atom He microscope. The second chapter is a review of graphene's structure and lattice dynamics with focus on CVD graphene on metals and the final section is an introduction to Helium Atom Scattering (HAS).

1.1 Matter-Wave Microscopy

Understanding the duality of wave and matter opened the door for many advances in the field of microscopy in the 20^{th} century. Light has been manipulated for centuries in different applications, including microscopy, before understanding its nature. However, other microscopic techniques were developed only out of a deep understanding of the nature of matter and its interactions.

The optical microscope was born in the early 1600s and soon it became an indispensable investigation tool thanks to van Leeuwenhoek, who perfected lensmaking for his textile trade, and to Robert Hook who was a brilliant painter as well as a great scientist. The optical microscope was condemned by Abbe's limit of diffraction to a resolution of a few micrometers. This has resulted in several workarounds for improving the optical resolution, like using light with decreasing wavelengths as in using 405 nm in Blue-ray discs instead the DVD's 650 nm or the invention of the X-ray microscope that yields a resolution of few tens of nanometers. Several optical techniques managed to stretch Abbe's limit, and finally a *super-resolved fluorescence microscopy* was developed over the

last few decades to use visible light with spatial resolution close to 250 nm. This work was awarded the Nobel Prize in chemistry in 2014.

The electron microscope was invented by Knoll and Ruska in 1932. State of the art electron microscopes have reached mind-boggling levels of development. With a sub-Ångstrom spatial resolution it is capable of identifying not just the position of single atoms, but also in many cases different types of atoms. The ability of combining it with electron energy loss spectroscopy (EELS) makes it a versatile technique that provides a wide spectrum of valuable information at high speeds. Bonding configurations, spin state and stoichiometry, among others, can now be spatially resolved. And now electron microscopy faces new limits, not posed by technology, but rather by quantum mechanics and the nature of electron-atom interaction [1]. Using electron microscopy with nonconducting samples requires coating the material with a thin layer of gold to avoid charging the surface, and the increase of spatial resolution which requires decreasing the electron wavelength comes at the price of increasing the energy and thus the potential for sample damage.

Helium ion microscopy (HIM) is a technique that combines nanofabrication with characterization on a nanoscale. The beam is created using a gas field ion source with a sharp emitter that concentrates a very high electric field on its tip where the He ionization happens, then optical parts focus and accelerate the ions towards the sample with a virtual source size < 250 nm and an energy of 30 keV with < 1 eV spread. The use of electrons for charge neutralization enables HIM to obtain high resolution images of insulating and biological samples without coating. High focal depth can be obtained. However, with such a high energy, HIM is penetrative and can easily damage the studied sample [2].

Light, electrons and He-ions are probes used in wave-matter microscopy, they have basically the same instrumental concept of a beam of wave-matter focused towards a sample to either reflect from it or pass through it towards a detector. Scanning probe microscopy (SPM) uses a different concept entirely and will not be discussed in this manuscript.

In the presence of such powerful techniques, is there need for a new one? Whereas the above techniques cover a wide range of resolutions and applications, they all employ relatively high energies; photosensitive samples for example will be destroyed by optical methods, electron microscope works on conductive materials only, and HIM is a destructive technique by design.

HAS has been a valuable surface science technique for decades. With very

low incident beam energies (10 to 100 meV), light mass and short wavelengths it provides a nonpenetrative, nondestructive and exclusively-surface sensitive technique. And since He is a neutral particle with no internal structure, it can be used even in the presence of external electric or magnetic fields which makes it suitable for studying the surface structure of magnetic materials or the effect of applying electric/magnetic fields on the surface structure without any interference with the probing beam [3, 4, 5, 6]. A He microscope can be used to obtain not only topological information; it can also give chemical and structural information thanks to differences in Debye-Waller factor between different materials and structures [7].

1.1.1 Recent Advances in Helium Microscopy

The possibility of a He microscope was clear since the first measurements that demonstrated the wave nature of molecular beams. However, focusing a beam of neutral atoms with no spin to manipulate is not easy, and thus, what makes He favorable for certain applications is exactly what makes it hard to use in microscopy.

A microscope, in general, works by focusing the incident beam or amplifying the reflected or transmitted beam, the latter does not seem feasible for neutral He microscopy. Focusing the incident beam can be achieved by reflection from a concave mirror, diffraction on or through a grating, and finally by trimming via a pin-hole (aperturing). All three methods have their advantages, limitations and technical complications discussed later in details. First we start with a brief chronological list of the advances along the road toward realizing the He microscope.

- *1911* Louis Dunoyer demonstrated that atoms flow in a straight line in vacuum [8].
- *1930* I. Estermann and O. Stern [9] performed the first molecular beam diffraction measurements from a crystalline surface (H_2 and He on LiF and NaCl) and developed the theory behind it verifying the "matter wave" nature to molecular beams. Three years later, they both became refugees in the USA.
- *1951* A. Kantrowitz and J. Grey [10] proposed using miniature nozzle followed by a skimmer in the production of high intensity molecular

beams which was created and tested by G. Kistiakowsky and W. Slichter [11] who reported an effective monochromatization of velocities and an increase of 20 times in intensity.

- *1988* D. Keith et al. [12] reported the first measurement of transmission diffraction of Na atoms using a grating that was developed for X-ray spectroscopy.

- *1989* J. Berkhout et al. [13] showed the possibility of focusing an atomic beam by quantum reflection. They used a concave spherical mirror to focus a $\varnothing 18$ mm beam of cold ($T < 0.5$ K) H atoms down to $\varnothing 0.5$ mm. The mirror was coated with a film of super-fluid helium to obtain 80% reflectivity at normal incidence thanks to the extremely weak H-He interaction.

- *1991* O. Carnal et al. [14] used a Fresnel zone plate to focus a beam of metastable helium atoms from 210 µm (the diameter of the plate) to a width of 18 µm. However, the intensity of the focused beam was extremely low since only the first-order focus was usable in the focusing measurement.

- *1992* R. Doak [4] showed the possibility of focusing a molecular beam using a bent crystal mirror formed from epitaxial gold overlayer deposited on mica substrate. The FWHM of the reflected beam was reduced from 0.4° to 0.12°. The focusing effect was limited by the quality of the gold layer. Doak lamented the experimental complexity imposed by the need of maintaining a clean mirror surface for long times.

- *1997* B. Holst and W. Alison [15] focused a He beam to a spot size of 210 µm by reflection from an electrostatically-bent (111) surface of a H-passivated 50 µm-thick silicon crystal. The solid angle of the unfocused beam is reduced by a factor of about 100. The mirror reflectivity remained constant over several months in 10^{-6} mbar.

- *1997* J. Braun et al. [16] developed micrometer-sized nozzles and skimmers made from drawn glass tubes for the production of demagnified supersonic He atom beams.

- *1999* R. Doak et al. [17] used a Fresnel zone plate of diameter $\varnothing 100$ µm along with state-of-the-art microskimmers which improved the spatial

resolution and He flux and thus obtained a focused beam density several orders of magnitude larger than that in the work of Carnal at al. [14]. The measured diameter of the focused beam 2-25 µm depending on the skimmer diameter.

- *2008* B. Holst and coworkers [18] showed the first images of with a neutral helium microscopy using Fresnel focusing in transmission mode with a resolution ~ 2 µm. The imaged sample was a hexagonal copper grating with a period of 36 µm and a rod thickness of 8 µm.

- *2008* D. Farías and coworkers [19] reported an improvement on the reflectivity of the mirror surface used in Ref. [15] from <1% to 20% using certain thicknesses of Pb thin films.

- *2009* W. Schöllkopf and coworkers [20] demonstrated 1D focusing of a thermal helium atom beam down to 1.8 µm by quantum reflection from a cylindrical concave quartz mirror at near-grazing incidence where surface defects and proposed using two concave elliptical mirrors in a Kirkpatrick–Baez arrangement for 2D focusing.

- *2010* K. Fladischer et al. [21] focused a He beam down to a 26.8 µm × 31.4 µm almost-circular spot, using the same reflecting surface as in Ref. [15] with a modified electrostatic bending setup. The have also benefited from the micrometer-sized nozzles and skimmers [16].

- *2010* E. Sutter et al. [22] found that graphene can grow uniformly on polycrystalline Ru thin films on patterned fused silica and it remains stable in ambient gases.

- *2011* D. Farías and coworkers [23] measured a high reflectivity (20%) for He scattered from epitaxial graphene on Ru(0001).

- *2011* P. Witham and E. Sanchez [24] proposed a simple design of a He microscope by removing the skimmer and reducing the source-sample-detector distances. They reported images in reflection mode with a resolution of 1.5 µm.

- *2011* D. Farías and coworkers measured a high reflectivity of He (23%) for graphene-terminated Ru(0001) thin films grown epitaxially on c-axis sapphire.

- *2012* B. Holst and coworkers [25] achieved submicron focusing using a Fresnel zone plate.

- *2012* P. Witham and E. Sanchez [26] produced images with a 350 nm spatial resolution with a few modifications to their minimalist design.

- *2012* W. Allison and coworkers [27] designed a compact model of scanning He microscope (SHeM) with off-the-shelf parts reducing the cost and improving the maintainability of the microscope.

- *2016* W. Allison and coworkers [28] presented SHeM micrographs demonstrating image contrast arising from a range of mechanisms including chemical contrast observed from a series of metal–semiconductor interfaces.

1.1.2 Challenges and Prospects of He Microscopy

So far, the advances in He microscopy revolved around improving the focusing element. Three methods have been investigated, reflection, diffraction and apertuering.

Bent-crystal mirrors offer both achromatic focusing and a large numerical aperture. However, precise bending a crystal surface on atomic-length scales remains problematic, and maintaining the mirror surface atomically clean for long periods is difficult. W. Schöllkopf and coworkers showed that by using quantum reflection the complication of preparing and maintaining microscopically flat surfaces can be avoided because quantum reflection takes place tens of nanometers away from the surface and is hardly affected by its roughness [29]. While quantum reflection promises high reflectivity and is more forgiving on the side of preparing the surface, it requires 2-step process, where in each step the beam is focused in one dimension. As a result the alignment of lenses is more complicated but not impossible; a two-step scattering measurement was performed in 1930 by Estermann, Frisch and Stern and in 1981 by Mason and Williams [30]. In our group we have recently found that graphene-passivated Ni(111) gives a high reflectivity of He (20%) similar to Ru(0001), we also found that graphene reduces the surface roughness of the Ni(111) surface. In theory, reflection from a concave surface is limited only by technical issues like surface quality and bending uniformity. Graphene is useful in not only passi-

vating the surface but also in improving its quality by reducing the roughness of step edges on the surface.

Recently, B. Holst and coworkers started investigating focusing of a He beam with a photon-sieve structure [31] since the first-order focus of a Fresnel plate is limited theoretically to 30-50 nm due to the fabrication method whereas, a photo-sieve promises higher resolution and is easier to fabricate. In a recent work, C. Brand et al. [32] fabricated transmission diffraction gratings made of single-layer and bilayer graphene to reduce undesirable effects of the beam interaction with the grating walls. This method can be useful in fabricating Fresnel zone plates with improved precision. Fresnel zone plates can suffer chromatic aberration which sets an intrinsic limit to the focusing resolution, and since it uses only one diffracted mode it suffers from a low efficiency. T. Kaltenbacher [33] recently suggested combining the Fresnel zone plate with a pinhole in analogy with the linear monochromator set-up in X-ray microscopy.

The recent work of W. Allison and coworkers is directed towards the commercial application of He microscopy where delicate and photosensitive materials are out-of-reach of optical and electronic microscopes when there is no need for a resolution lower than one micrometer. Trimming the beam by passing it through an aperture reduces its size effectively. Aperturing is limited by the size of the pinhole, however, decreasing the pinhole size causes a huge decrease of intensity which complicates the microscope's design even more. Since He has the highest ionization energy among the elements and a very low ionization probability, special detectors were developed for this approach.

1.2 Graphene

This introductory section will be dedicated to a review of the most relevant properties of graphene. Firstly, the structure, elastic and thermal properties of free-standing graphene will be presented, then the modifications to lattice dynamics of graphene by contact with a metal substrate are discussed.

1.2.1 Structure and Lattice Dynamics of Graphene

Graphene (Gr) is a monolayer of sp^2 hybridized carbon atoms arranged in a honeycomb network with the nearest neighbor distance of 1.42 Å [34]. The honeycomb structure is a 2D-hexagonal lattice with a unit cell containing two

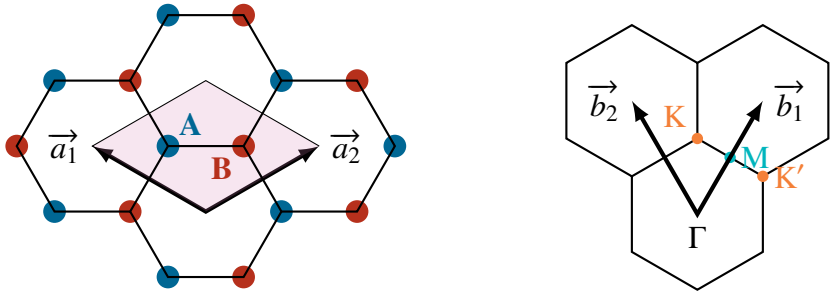

Figure 1.1: Left: Lattice structure of graphene in real-space, showing the inequivalent carbon atoms A and B and lattice vectors. Right: Reciprocal-space unit cell of graphene showing the hexagonal surface Brillouin zone, reciprocal lattice vectors and high-symmetry points.

inequivalent carbon atoms and a lattice constant $a = 2.463\,\text{Å}$ (measured for graphite by X-ray diffraction [35]).

The sp^2 orbitals (s, p_x, p_y) form the strong interlayer σ covalent carbon bonds, the p_z orbitals from neighboring atoms overlap resulting in delocalized π bands with a linear dispersion that give graphene its unique electronic properties.

With two atoms in the unit cell, Gr has six phonon branches, three are acoustic (A) and three are optic (O). These phonon branches are classified according to their polarization; out-of-plane (Z) modes where the atomic displacement vector is along the axis normal to the Gr surface and in-plane modes where the displacement is confined in the Gr layer. The in-plane phonon modes are, in turn, classified as longitudinal (L) or transverse (T) according their polarization relative to the direction of the carbon bonds. Longitudinal mode refer to vibrations parallel to the C–C bonds, which is equivalent to the $\overline{\Gamma\text{M}}$ direction, and the transverse mode polarization is perpendicular to the carbon bonds and thus it is polarized along the $\overline{\Gamma\text{K}}$ direction [36, 37]. This notation is summarized in Table 1.1.

Due to the large difference between intralayer and interlayer forces of C atoms, the physical properties of graphene are very anisotropic. On one hand this makes studying graphene phonons a good approximation for understanding the phonons of graphite, on the other hand this requires the consideration of distant interatomic interactions in the basal plane (up to 16^{th} nearest-neighbor [38]) to get good results from *ab initio* calculations. This anisotropy also

Table 1.1: Phonon modes in graphene single layer.

Label	Character	Polarization	Bending
ZA ZO	Acoustic Optical	Sagittal Vertical (SV)	out–of–plane
TA TO	Acoustic Optical	Shear Horizontal (SH)	in–plane
LA LO	Acoustic Optical	Longitudinal (L)	in–plane

explains why in-plane phonon modes have higher frequencies compared to out-of-plane modes [39]. The same line of thinking can explain why the strong interaction with a substrate which modifies the π-band softens graphene phonons [40, 41].

Fig. 1.2 shows the phonon dispersion curves in graphite measured by HREELS [42, 43], X-ray scattering [35] and neutron scattering [44]), compared to DFT calculations from Refs. [45, 46]. In general, very good agreement is found with this and other calculations, although some discrepancies appear with the phonon frequencies predicted at the $\overline{\Gamma}$, $\overline{\mathrm{K}}$ or $\overline{\mathrm{M}}$ points of the Brillouin zone [46, 47]. These calculations show the overall similarity of the graphite phonon spectrum with the six phonon branches of Gr. The only significant difference appears at low energies, near the $\overline{\Gamma}$ point, where the weak interlayer interactions in graphite lead to a splitting of the ZA mode. The value of ZA at $\overline{\Gamma}$ provides a way to quantify the strength of the Gr–substrate interaction.

Raman spectroscopy is the most widely used technique in characterizing the vibrational modes of Gr thanks to the high energy of its phonons (200 meV) [48]. The most prominent features in Raman spectra are the G and G' bands (see Fig. 1.3), the spectra also can include the disorder-induced D band at a frequency half that of the G' band [36]. The G band is a first-order Raman scattering process which belongs to the doubly degenerate (TO/LO) phonon mode at the Brillouin zone center $\overline{\Gamma}$. G' and D bands, on the other hand, originate from a second-order process near the $\overline{\mathrm{K}}$ point, involving two TO phonons or one TO phonon and one defect, respectively. The frequency of

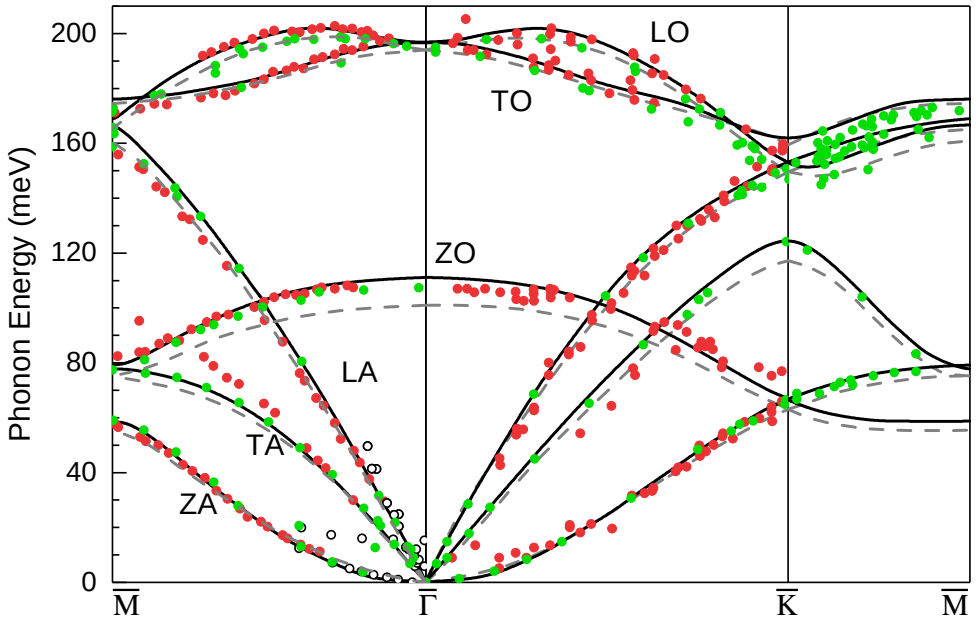

Figure 1.2: Phonon dispersion of graphite from HREELS (red dots, [42, 43]), X-ray scattering (green dots, [35]) and neutron scattering (open circles, [44]). DFT calculations are shown by gray dashed lines ([45]) and solid lines ([46]).

D and G' changes as a function of laser energy because they originate from a double-resonance Raman process.

In double-resonance Raman process, the wave-vectors q of the involved phonons couple to the electronic states with wave-vectors k, such that $q \simeq 2k$. The G' band is generated when an electron-hole pair is excited near the $\overline{\mathrm{K}}$ point by absorbing a photon, the electron then scatters inelastically by a TO phonon to the vicinity of $\overline{\mathrm{K}'}$ point then scatters back to its previous state near the $\overline{\mathrm{K}}$ point by a second TO phonon and finally recombines with a hole and emits a photon. It can happen that instead of two scattering processes of the electron, the hole along with the electron, each can scatter from one TO phonon and the recombination can take place near the $\overline{\mathrm{K}'}$ point. This mechanism is used to explain the high intensity of G' band. The energy of the excited electron-hole pair depends on the energy of the absorbed photon and a continuous range of energies is available due to the linear dispersion of the electronic bands. Therefore, the emitted photon energy changes with the energy of the laser [36].

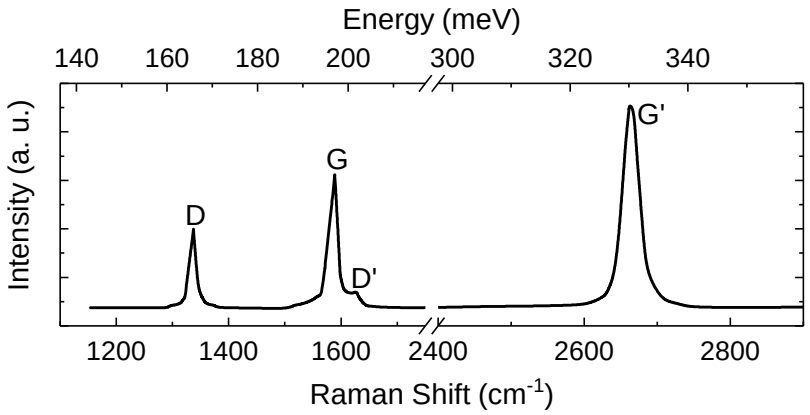

Figure 1.3: Raman spectrum of a graphene edge, showing the main Raman features, the D, G and G' bands taken with a laser excitation energy of 2.41 eV. Adapted with permission from [36] ©(2009) Elsevier.

The *D* band is basically the same as G', however, one of the inelastic scattering processes is replaced by an elastic scattering from a defect. Therefore, the presence of a *D* band in the Raman spectra is an indication of the presence of defects in the graphene layer. The width of the G' band can be used to indicate the presence of multiple layers of graphene, since the latter results in a splitting of the electronic and phonon bands and thus the double-resonance process can include many combinations of the different branches of the electronic bands which results in different frequencies of the emitted photons and thus a broadening of the G' band. The D' band is another double-resonance process involving the LO mode at the $\overline{\mathrm{K}}$ point and a defect [36].

The Raman signal is suppressed in systems with a strong Gr-metal interaction, like Gr/Ru(0001) and Gr/Ni(111) due to strong hybridization of the carbon π bands with the orbitals from the substrate atoms. The hybridization changes the Fermi level of the system and reduces the electron-phonon coupling, when the change is large enough (relative to the *G* band phonon energy) the Kohn anomalies are suppressed and the resonance condition for Raman scattering is lost [36, 49]. In general, the presence of a Raman signal is an indication that graphene is only weakly physisorbed and not chemisorbed on the metallic substrate.

Phonon energy will be presented in meV throughout this manuscript, it can be converted to other commonly used units as follows [50]: wavenumber

(cm^{-1}) = 0.124 meV, frequency (THz) = 4.13 meV and angular frequency (10^{13} rad/s) = 6.55 meV.

Electron-phonon coupling and Kohn anomalies

The coupling of phonons with the electronic excitation spectrum of a solid may lead to the appearance of phonon anomalies. This mechanism is one of the key signatures of electron-phonon coupling and corresponds to the breakdown of the adiabatic separation of ionic and electronic degrees of freedom. In general, atomic vibrations are partially screened by electronic states. In a metal this screening can change rapidly for vibrations associated with certain $\mathbf{q}$ points of the Brillouin zone, which is determined by the shape of the Fermi surface. The consequent softening of some phonon modes, called Kohn anomaly [51], has been reported for a variety of systems [52].

Note that in particular, this means that it is not possible to derive the phonon branches at $\overline{\Gamma}$ and $\overline{\mathrm{K}}$ of Gr by using a force constant approach. Kohn anomalies may occur only for wave vectors $\mathbf{q}$ such that there are two electronic states $\mathbf{k}_1$ and $\mathbf{k}_2 = \mathbf{k}_1 + \mathbf{q}$ on the Fermi surface [51]. The Fermi surface of pristine Gr consists of two equivalent points at $\overline{\mathrm{K}}$ and $\overline{\mathrm{K}'}$ which reflect the tips of the Dirac cones. Since $\overline{\mathrm{K}'} = 2\overline{\mathrm{K}}$, these are connected by the vector $\overline{\mathrm{K}}$. Thus, Kohn anomalies are expected at $\overline{\Gamma}$ and $\overline{\mathrm{K}}$ [53]. In graphite, two Kohn anomalies are present in the phonon dispersion of the highest optical phonon at $\overline{\Gamma}$ (LO/TO mode) and at $\overline{\mathrm{K}}$ (TO mode) [35, 53].

Heat transport and acoustic phonons

Thermal conductivity in metal composes electronic and lattice dynamics while in semiconductors and insulators electronic contribution is limited whereas phonons are the main thermal energy carriers. Since Gr is a semimetal with no gap and a zero electronic density of state in the Fermi surface at 0 K, it is natural to expect that its thermal properties are mainly a product of its lattice dynamics [54]. The specifics of the phonon dispersion and relative contributions of different phonon polarization are important for gaining a complete understanding of thermal properties of Gr and other 2D materials [55].

The thermal conductivity of bulk graphite is $\sim 2000\,\mathrm{W\,m^{-1}\,K^{-1}}$ at room temperature. The corresponding value for free–standing Gr is known to be much larger, reaching 4000–5000 $\mathrm{W\,m^{-1}\,K^{-1}}$ at 300 K. The main carriers are

acoustic phonons with a mean free path around 240 to 750 nm [56, 57].

The thermal conductivity in Gr is size-dependent. It is also sensitive to the density of defects and to their type. Furthermore, it was found that increasing the contribution of ^{13}C in CVD graphene causes a significant decrease in thermal conductivity [58]. Gr/substrate interface has a decreased thermal conductivity as in Gr/SiO_2 ($600\,W\,m^{-1}\,K^{-1}$) and 2 to 4-layer Gr (2800 to $1300\,W\,m^{-1}\,K^{-1}$). Interpretations include suppression of ZA mode, cross-plane coupling of low-frequency phonons and the enhancement of interface phonon scattering. On the other hand, interaction with a substrate can affect phonon scattering and increase thermal conductivity as was observed for encapsulated few layer graphene and boron nanoribbons. The thermal conductivity in Gr increases with decreasing temperature due to the reduction of Umklapp scattering and reaches a peak below 200 K [56, 57, 59].

However, the relative contributions of the different acoustic phonon modes to the thermal conductivity of Gr is still an open question. Recent reviews on the subject are still debating it from the theoretical side. D. Nika and A. Balandin [57] argue that ZA mode is the main heat carrier only for low temperatures $T < T_{lim}$, while LA and TA phonons dominate for $T > T_{lim}$. The value of T_{lim} (100-150 K) depends on the size and whether graphene is suspended or supported on a substrate. The contribution of the in-plane phonons to thermal conductivity also increases with increasing length of the Gr ribbon since the large intrinsic mean free path of LA and TA modes makes them more sensitive to edge scattering while ZA modes are predominantly affected by substrate scattering. The contribution from ZA is neglected due to its large Grüneisen parameter and its small group velocity compared to in-plane modes. Furthermore, a deviation from the quadratic dispersion of ZA branch (as in supported graphene) results in lower values of group velocities, and thus, could slightly decrease the relative contribution from ZA phonons to thermal conductivity [57]. On the other hand, a review by X. Xu et al. [56] indicated to the theoretical studies that found a larger contribution of ZA mode which, compared to in-plane phonons, has larger relaxation time (10-40 ps at 300 K), specific heat and partial density of states at small wavevectors [56].

It is clear that more work is needed in order to understand the relative contributions of the ZA, LA and TA modes to the thermal conductivity of supported Gr. From the experimental side, it could be very helpful to get more acoustic phonons measurements for Gr grown on different substrates.

Mechanical Properties

Graphene is the "strongest material ever measured" with a 2D Young's modulus of $Y_{2D} = 340\,\mathrm{N\,m^{-1}}$ [60]. The high in–plane stiffness of graphene is a direct result of its hexagonal lattice and the carbon–carbon bonds. The increase in the coupling strength between graphene and its substrate will enhance the thermal conductivity, because the coupling of the flexural mode to the substrate Rayleigh waves results in a hybridized mode with linear spectrum and higher group velocity than the original flexural mode in graphene [54]. The frequency of the flexural mode is proportional to the square root of the Young's modulus [54]. Besides the in-plane elastic properties, graphene is highly flexible due to its monoatomic thinness. These characteristics make graphene a versatile material for coating surfaces.

1.2.2 CVD Graphene on Metals

The Gr-metal interface might be a result of chemisorption like with Ni and Ru, where the electronic structure results from hybridization of the Gr π and metal d orbitals, or weak adsorption as in the case of Cu, Ag and Pt, where the characteristic electronic structure of Gr remains almost intact. Due to the large difference between intralayer and interlayer forces witnessed by C atoms, the physical properties of Gr are very anisotropic. This allows to describe the changes to the phonon dispersion in Gr/metal systems in terms of changes in the in-plane or the out-of-plane bonds.

Preparation and structure

Generally speaking, Gr-metal interfaces can be classified considering two main aspects: i) lattice mismatch, and ii) strength of the Gr-metal interaction. On Ni(111) and Co(0001) the mismatch between the lattice constants of Gr and the substrate is less than 2%, which allows Gr to form (1×1) structures by slightly stretching or quenching the C–C bonds. In contrast, Gr on, e.g., Ir(111), Pt(111), Rh(111) and Ru(0001) exhibits a lattice mismatch of $\sim 10\%$, which leads to the formation of moiré superlattices. Usually, it is possible to find growth conditions such that Gr forms one domain, which is aligned with the main symmetry direction of the metal substrate. This is the case for Gr on Ru, Rh, Re and Ir. However, for most growth conditions on weakly interacting metals, such as Cu and Pt, different rotational domains are observed

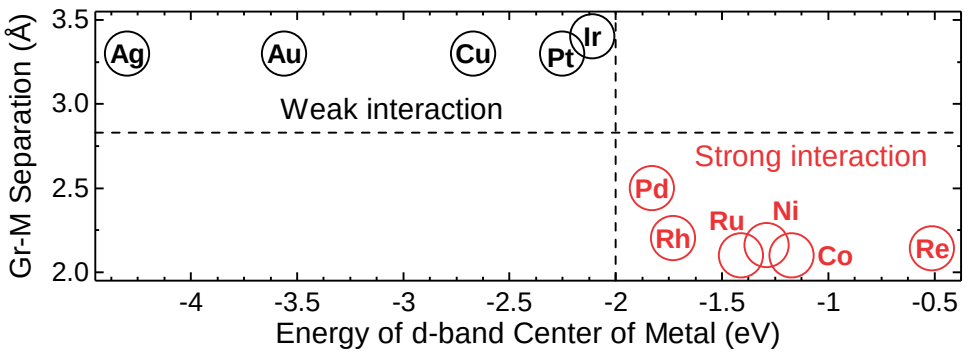

Figure 1.4: Correlation of Gr-metal separation with the energy of the d–band center of the transition metal. A transition from “weak" to “strong" interaction occurs at a d–band center position ~ 2 eV below the Fermi-level. Adapted from [63].

[40, 61]. The moiré superstructure is often used as a template for the growth of two-dimensional molecular networks [62].

From the view point of the interaction, Gr-metal interfaces can be divided into strongly and weakly interacting systems [41, 61]. One measure of the interaction strength is the Gr–metal separation. Fig. 1.4 shows a plot of the Gr-substrate distance as a function of the binding energy of the d–band center relative to Fermi energy for different metals There are essentially two groups in which the separation can be categorized: a value close to 2.1 Å for strongly interacting metals, and a separation of 3.3 Å for weakly interacting metals, which is close to the c-axis spacing in graphite. Figure 1.4 also shows that the transition from strongly to weakly interacting transition metals occurs at a d–band center binding energy of ~ 2 eV [61].

Table 1.2 shows some relevant characteristics of the metallic substrates that are commonly used for CVD Gr growth. The preparation temperature in low pressure conditions decreases with increasing C solubility in the substrate.

Surface phonons of graphene on Metals

Since Gr/metal systems can be categorized according to whether the Gr-metal interaction is weak or strong, we will discuss the general trends observed in the phonon dispersion curves wholesale for each category. Fig. 1.5 shows the phonons for different systems of Gr/metal in the $\overline{\Gamma M}$ high-symmetry direction from published literature. Strong-interaction systems are plotted on left panel

Table 1.2: Summary of relevant information of metallic substrate commonly used in CVD Gr preparation: Period of the transition d-metal, surface lattice constant of the substrate a, the energy of the d-band center of d-shell transition metal surfaces E_d, the graphene-metal separation d_{GM}, carbon solubilities (atom%) at 1000 °C Sol_C [63, 64], the preparation temperatures taken from several sources:

Metal	Period	a (Å)	E_d (eV)	d_{GM} (Å)	Sol_C	T_{CVD} (K)
Ni(111)	3d	2.47	-1.29	2.1	2.03	750
Ru(0001)	4d	2.71	-1.41*	2.1	1.56	1150
Ir(111)	5d	2.71	-2.11	3.4	1.35	1400
Pt(111)	5d	2.77	-2.25	3.3	1.76	1150
Cu(111)	3d	2.56	-2.67	3.3	0.04	1273**

* value of the lowest distance along the corrugated system

** High pressure CVD

and weak-interaction systems are plotted on the right one, for comparison DFT calculations for free standing graphene are also shown.

For strong Gr-metal interaction systems, the most pronounced feature is the hybridization of the ZA mode with the Rayleigh wave (RW) of the substrate [75]. This leads to the appearance of the substrates RW in the phonon spectra, as observed for Gr grown on the (111) surfaces of TiC, TaC and HfC [66, 65], Gr/Ni(111) [this work] and Gr/Ru(0001) [71]. These results explain the surprisingly high reflectivity for He atoms reported for Gr/Ru(0001) (20%) [23, 76] and Gr/Ni(111) (20%) [this work]. The removal of the (quasi-)parabolic dispersion of the ZA mode in Gr and its replacement with the linearly dispersed RW of the substrate shows that it is just a consequence of a strong C-metal interaction. Coupling to the substrate leads to splitting of the ZA mode, i.e. it does not go to zero for $Q_{\parallel} \rightarrow 0$. The energy ω_{ZA} at the $\overline{\Gamma}$ point is a direct measure of the Gr-substrate bond strength. Large values correspond to strongly interacting systems: 39 meV has been reported for Gr/ZrC(111) [67], 34 meV for both TaC(111) and HfC(111) [66, 65], 20 meV for Gr/Ni(111) [this work] and 16 meV for Gr/Ru(0001) [71]. On the other hand, lower values are observed for weak Gr-metal interactions; $\omega_{\mathrm{ZA}} \sim 6$ meV has been measured for both Gr/Ir(111) [74] and Gr/Cu(111) [this work]. Surprisingly,

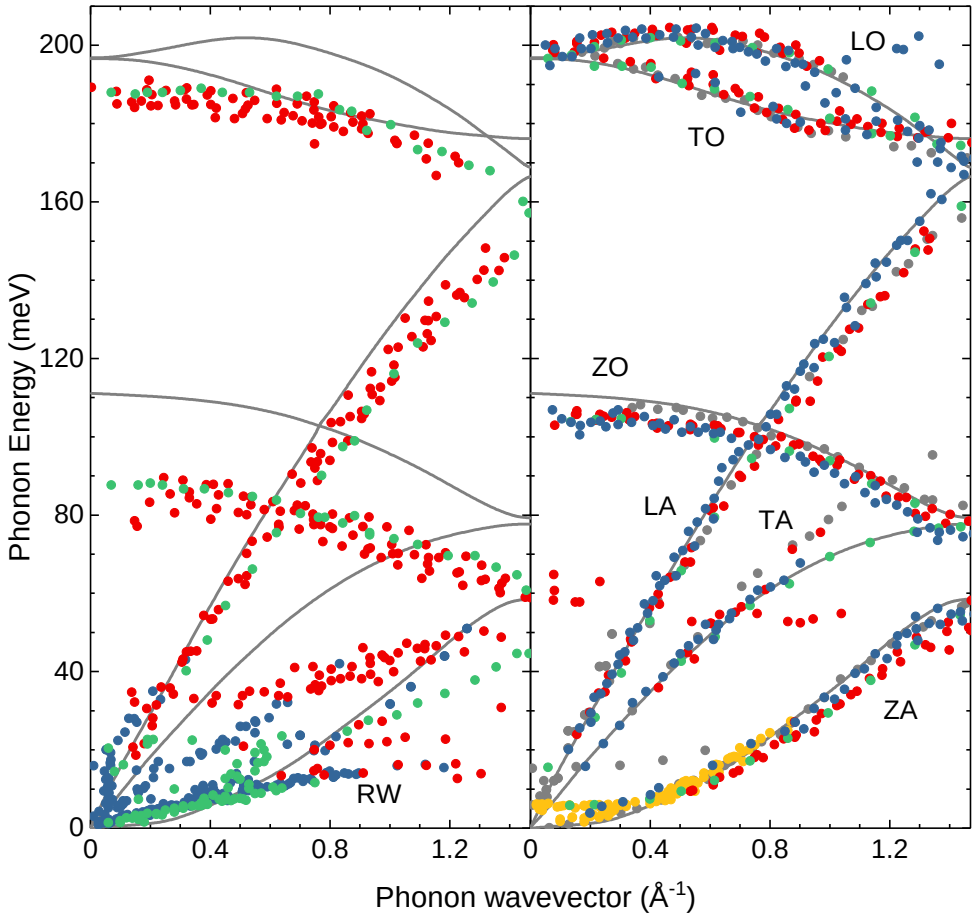

Figure 1.5: Experimentally determined surface phonons of Gr/M (M is metal or metal carbide) in the $\overline{\Gamma M}$ direction (colored circles) with DFT calculations for free standing graphene (lines) from [46]. Left: Gr on strongly interacting substrates: (111) surface of TaC, TiC, HfC, ZrC and NbC [65, 66, 67, 68](red), Ni(111) [69, 70](green) and Ru(0001) [71]. Right: Gr on weakly interacting substrates: (001) surface of TaC, ZrC and NbC [66, 67, 68](red), graphite(0001) [44, 42](gray), Pt(111) [68, 72](blue), Cu(111) [73](orange) and Ir(111) [74](green).

these energies are much lower than the ones reported for graphite: 12.5 meV has been reported using X-ray scattering [35], and 15.3 meV using neutron scattering [44]. Further work is needed to clarify this issue.

Concerning the optical branches, the most relevant feature observed for

systems with a strong Gr-metal interaction is a pronounced softening of the LO, TO and ZO modes throughout the entire surface Brillouin zone. Softening of the ZO mode at the $\overline{\Gamma}$ point amounts 20 meV for Gr/Ni(111) [69, 77], 35 meV for Gr/Ru(0001) [78] and ca. 25 meV for Gr on TaC(111), TiC(111) and HfC(111) [66, 65]. In addition, for Gr/Ni(111) there is a splitting of the ZA and ZO modes of 16 meV and 13 meV at $\overline{\mathrm{M}}$ and $\overline{\mathrm{K}}$, respectively. These values are reproduced by calculations, although they are overestimated [49].

Since in both ZA and ZO modes carbon atoms vibrate vertically, they are expected to be most affected in cases of strong Gr-substrate interaction. This is confirmed by data reported for Gr/Ni(111) [69, 70, 77] and Gr/Ru(0001) [71, 78], which show that ZA and ZO modes deviate considerably from the ones of graphite. The softening of the ZO bond is a consequence of the strong interaction, i.e. hybridization of the metal d-band with Gr π-bands, a interpretation suggested by Oshima et al. [69, 79, 80] and confirmed later by DFT calculations [49]. In the LA and LO modes, in contrast, carbon atoms vibrate parallel to the surface and the influence of the Gr-substrate interaction is much smaller. Therefore, a signature for the existence of a graphite-like overlayer is provided by the observation of these two modes, especially from the LA mode, which has a characteristic large dispersion. This is nicely illustrated by several examples discussed above for both strongly and weakly interacting Gr-metal systems. The strength of this interaction leaves its mark on the two Kohn anomalies present in graphite at $\overline{\Gamma}$ (LO mode) and $\overline{\mathrm{K}}$ (TO mode) [53, 45]. The two anomalies are clearly observed in Gr/Ir(111) [74] and Gr/Pt(111) [72], and the LO anomaly can be restored in Gr/Ni(111) after intercalation of Cu, Ag or Au [77, 81, 82].

1.3 Helium Atom Scattering

Helium atom scattering is the only experimental technique used in the work of this thesis. This section provides a theoretical background of processes involved in He scattering from surfaces.

1.3.1 He-Surface Interaction

A He atom impinging on a surface will sense the attractive van der Waals potential which is proportional to z^3, where z is the atom distance from the

surface. At a certain distance from the surface, the attractive potential will overlap with a repulsive one (Pauli exclusion) and the total interaction potential will rise steeply. This repulsive part is a result of atom-atom interaction and thus it is modulated by the atomic corrugation of the surface. As a result, the He-surface interaction potential $V(z, \mathbf{R})$ is a function of the position on the surface $\mathbf{R}$ as well as the distance of the He atom from the surface [5].

The impinging He atom can approach a certain site on a surface as long as its kinetic energy is larger than the repulsive potential at this site, typically 2-3 Å. This distance, named the classical turning point, varies with $\mathbf{R}$. For example, a He atom impinging on top of a surface atom will be repelled farther from the surface than a He atom impinging on a bridge site [5]. However, this picture of gas-surface interaction is too simplistic as measurements using other noble gases scattering revealed that anticorrugation effects can give a different picture of the surface depending on the probe gas [83, 84, 85, 86].

HAS is a very useful surface-characterization technique due to its inertness, simple internal structure, light mass and low employed energies. These properties make it a nondestructive probe especially suitable for studying insulating and delicate samples that can be easily damaged by other techniques. HAS is exclusively-surface sensitive. It is also not affected by the presence of electric or magnetic fields which makes it suitable for monitoring thin-film growth. These characteristics simplify the kinematics of the scattering event.

He atoms are scattered either elastically or inelastically from surfaces. Elastic scattering includes diffraction which gives information on the surface structure (atomic periodicity and corrugation) and selective adsorption resonances where the motion of He atoms is confined parallel to the surface with a z-motion energy equal to one of the eigenvalues of the potential, this phenomenon can relate information on the He-surface potential [87]. Elastic scattering can also be in the form of a diffuse background where information on the amount and nature of the surface defects can be obtained [88]. Inelastic scattering can be either via a single interaction with a surface vibrational mode or via multiphonon scattering, also known as Debye-Waller factor, which appears as a broad feature in TOF spectra that can affect the resolution of phonon measurements.

Finally, HAS is extremely sensitive to dilute adsorbates, this allows an accurate determination of minute amounts of surface impurities (down to 0.001 ML) [89]. Due to this sensitivity, He can be inelastically scattered by the vibrational motion of adsorbates or surface defects, this results in the broadening

of all features in diffraction and TOF spectra.

1.3.2 Structural Information from HAS

A periodically corrugated surface provides a two-dimensional grating from which a He beam scatters in constructive and destructive interference that results in a diffraction pattern determined by the surface structure and the beam wavevector. The periodicity of a surface is described by the position vector $\mathbf{R}_{pq} = p\mathbf{a}_1 + q\mathbf{a}_2$, where p and q are integers and $\mathbf{a}_i$ are the primitive lattice vectors. The reciprocal lattice vector is described by the vector $\mathbf{G}_{pq} = p\mathbf{b}_1 + q\mathbf{b}_2$, where p and q are integers and $\mathbf{b}_i$ are the reciprocal lattice vectors. The relation between the real and reciprocal lattice vectors is given by

$$\mathbf{b}_i = 2\pi \frac{\mathbf{a}_j \times \hat{z}}{\mathbf{a}_i (\mathbf{a}_j \times \hat{z})} \quad \text{and} \quad \mathbf{b}_j = 2\pi \frac{\mathbf{a}_i \times \hat{z}}{\mathbf{a}_j (\mathbf{a}_i \times \hat{z})}, \tag{1.1}$$

where $\hat{z}$ is the unit vector normal to the surface. A standard notation, used in most HAS literature, describes vectors by their components parallel and perpendicular to the surface, for example a vector $\mathbf{m}$ has the components $\mathbf{M}$ and m_z parallel and perpendicular to the surface, respectively which can be written as $\mathbf{m} = (\mathbf{M}, m_z)$. This notation will be used in this manuscript.

A beam of atoms with an initial energy E_i and a mass m will have a wavevector $\mathbf{k}_i = (\mathbf{K}_i, k_{iz})$ whose norm is given by the its de Broglie wavelength

$$|\mathbf{k}_i| = \frac{2\pi}{\lambda} = \frac{\sqrt{2mE_i}}{\hbar}. \tag{1.2}$$

In elastic scattering experiments where energy and momentum are conserved $E_i = E_f$ and $\mathbf{k}_i = \mathbf{k}_f$, a beam that impinges on a surface will scatter with a wavevector $\mathbf{k}_f = (\mathbf{K}_f, k_{fz})$ defined by the Bragg condition which relates the incoming and outgoing wavevectors to the reciprocal lattice vector

$$\Delta\mathbf{K} = \mathbf{K}_f - \mathbf{K}_i = \mathbf{G}_{pq}. \tag{1.3}$$

In a fixed source-detector angle apparatus where $\theta_i + \theta_f = \Theta_{SD}$ the sample is preferably oriented so that one high-symmetry direction of the surface lattice is contained in the sagittal plane. A diffraction spectrum is obtained by rotating the sample around an axis perpendicular to a plane defined by the incoming beam $\mathbf{k}_i$ and the normal to the sample surface $\mathbf{z}$, see Fig. 1.6. The specular

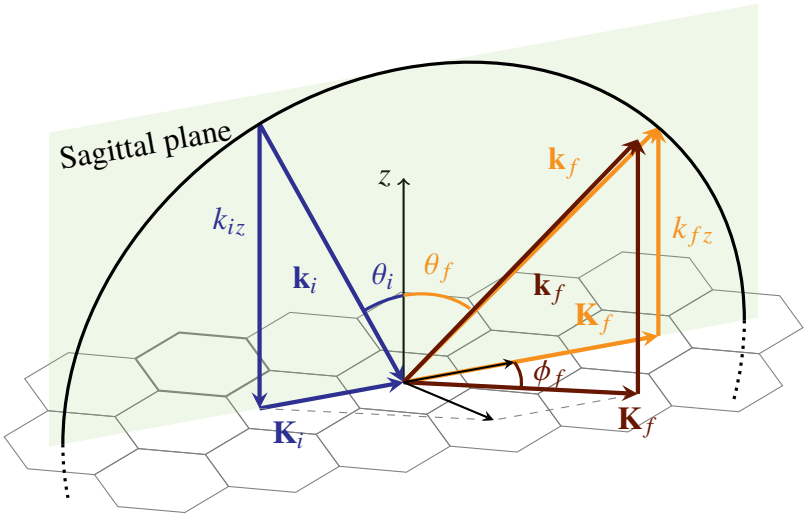

Figure 1.6: A scheme of kinematics of diffraction showing the reciprocal lattice structure of a hexagonal surface with reciprocal lattice vectors (black), the incident wavevector (blue) and two diffracted wavevector in-plane (orange) and out-of-plane (dark red).

position corresponds to the angular position where the incident and final angles are equivalent ($\theta_i = \theta_f = \Theta_{SD}/2$). This is the position where the (0,0) diffraction peak (which represents specular reflection) is detected. And thus, the Bragg condition in Eq.(1.3) can be reduced for a fixed Θ_{SD} apparatus to one-dimensional problem as

$$\Delta K = k_i(\sin\theta_f - \sin\theta_i) = G_{pq}, \tag{1.4}$$

here the surface is rotated so that the angle between $\mathbf{K}_i$ and $\mathbf{G}_{pq}$ is zero. Thus, a diffraction spectrum obtained in this geometry is a measure of scattered intensity as a function of the change in the incident angle relative to specular position $\Delta\theta_i = \Theta_{SD}/2 - \theta_i$. And the diffraction peaks will appear at angles $\pm\Delta\theta_i$ given by the relation

$$\sin\Delta\theta_{i,pq} = \frac{\lambda\, G_{pq}}{4\pi\cos\left(\Theta_{SD}/2\right)}. \tag{1.5}$$

A more general approach to the scattering problem is more convenient for a fixed θ_i setup. In such setup the detector is mounted on a two-axis goniometer

and scans a part of a sphere centered approximately at the sample position. When no geometrical restrictions are assumed on the incident beam, namely, the azimuthal angle between the incident beam and any of the real space lattice vector is not zero; a more general formula of Bragg condition gives the outgoing polar (in-plane) $\theta_{f,pq}$ and azimuthal (out-of-plane) $\phi_{f,pq}$ diffraction angles as [90]

$$\begin{aligned}\sin\phi_{f,pq} =& \lambda\left[-\frac{p}{a_1}(\sin\phi_i + \cos\phi_i\cot\beta) + \frac{q}{a_2}\frac{\cos\phi_i}{\sin\beta}\right];\\ \sin\theta_{f,pq} =& \frac{1}{\cos\phi_{f,pq}}\left[\sin\theta_i + \lambda\frac{p}{a_1}(\cos\phi_i - \sin\phi_i\cot\beta) + \lambda\frac{q}{a_2}\frac{\sin\phi_i}{\sin\beta}\right],\end{aligned} \tag{1.6}$$

where β is the angle between the real-space lattice vectors, θ_i is the angle of incidence, and ϕ_i is the angle between $\mathbf{K}_i$ and $\mathbf{a}_1$.

Angle resolved resonances

There are two types of resonances that can be resolved in a diffraction measurement, i.e. without energy analysis of the scattered molecular beam. The first is related to the atom–surface potential and can be detected when E_i is comparable to the potential depth. This phenomenon is called selective adsorption resonance and is elastic in nature. The second which is inelastic in nature appears when a molecule with an internal structure and a defined vibrotational state (v_i, J_i) scatters from the surface in a different vibrotational state (v_i, J_i). This phenomenon is called rotationally inelastic diffraction since it generates well defined peaks in the diffraction spectra. Although the physics of these two phenomena is very different, their kinematics is simple and somewhat similar. That is why they are discussed in together this section.

Selective adsorption resonances (SAR) Solving the Bragg condition in Eq.(1.5 and 1.6) gives the values of the diffraction angles. The result should be a real number and this is the case for small values of reciprocal wavevector indices p and q. These are called open diffraction channels. Increasing the values of the reciprocal wavevector indices will eventually give an imaginary solution to the Bragg condition, these are called closed diffraction channels. This results from the geometry of the diffraction kinematics where open channels satisfy the condition $k_{fz}^2 > 0$.

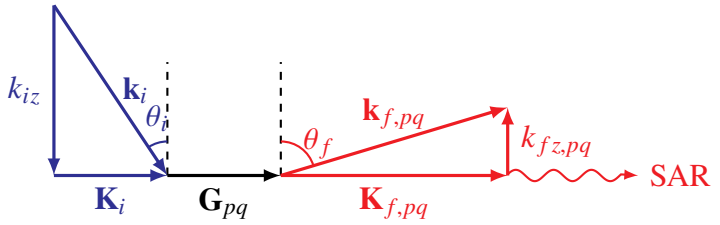

Figure 1.7: A scheme of kinematics of selective adsorption resonances.

However, due to the presence of a potential well, a particle that would normally scatter back from the surface with $k^2_{fz,pq} > 0$ might be trapped on the surface when the energy associated to the z motion fulfills

$$\frac{\hbar\, k^2_{fz,pq}}{2\, m} = \epsilon_n, \tag{1.7}$$

where m is the molecule mass and ϵ_n is an eigenvalue of the molecular–surface potential well.

From this picture one can see that SAR is more favorable when $E_{i\perp}$ is comparable to D. The kinematic condition for resonance into a bound state with binding energy $\epsilon_n < 0$ can be easily derived from the conservation of energy and parallel momentum

$$\epsilon_n = \frac{\hbar^2}{2m}\left[|\mathbf{k}_i|^2 - \left|\mathbf{K} + \mathbf{G}_{pq}\right|^2\right]. \tag{1.8}$$

SARs are useful for obtaining information on the atom-surface interaction potential. This can be done by measuring the intensity of a diffracted beam (typically the specular one) as a function of either (1) the angle of incidence or (2) the azimuthal angle or (3) the incident beam energy, while keeping the other two parameters constant. SAR features appear as sudden minima (or maxima) in an otherwise smooth profile of intensity. From an experimental point of view, (1) is the easiest to perform and it is thus the most employed method. SARs are not observed in the scattering from low-corrugation surfaces (like the close-packed metal surfaces) due to the weakness of diffractive coupling [5]. The motion of the bound particles is not restricted in the surface plane, they can keep moving depending on their $\mathbf{K}_{f,pq}$ until they desorbed either by an elastic transition into some allowed diffraction channel, or by inelastic scattering from the lattice or surface defects.

Rotationally inelastic diffraction (RID) This phenomenon does not affect noble gases since they do not have internal degrees of freedom. It involves other molecules like H_2 and D_2. And since only thermal energy beams are used in our laboratory, the molecules will be in the ground vibrational states. RIDs, as the name suggests give rise to extra peaks in the diffraction spectra like the spectra in Fig. 1.8.

When a molecule impinges on a surface it can either scatter elastically or, under certain incident conditions, energy exchange can take place between internal degrees of freedom of the molecule. The energy difference can be either gained or dissipated into the surface. The undergoing kinematics of this process are simple, where the Bragg condition is applied in combination with an energy conservation condition

$$E_i = E_f - \Delta E_{rot}, \tag{1.9}$$

where ΔE_{rot} is the energy gap between the molecule's rotational levels. Finding the positions of the diffraction peaks is simply done by calculating E_f from the above formula and using the corresponding wavelength in Eq.(1.6).

For example, the rotational energies of the $j = 0 \rightleftharpoons 2$ and $j = 1 \rightleftharpoons 3$ transitions of D_2 are 22.2 meV and 36.88 meV, respectively [91]. Fig. 1.8

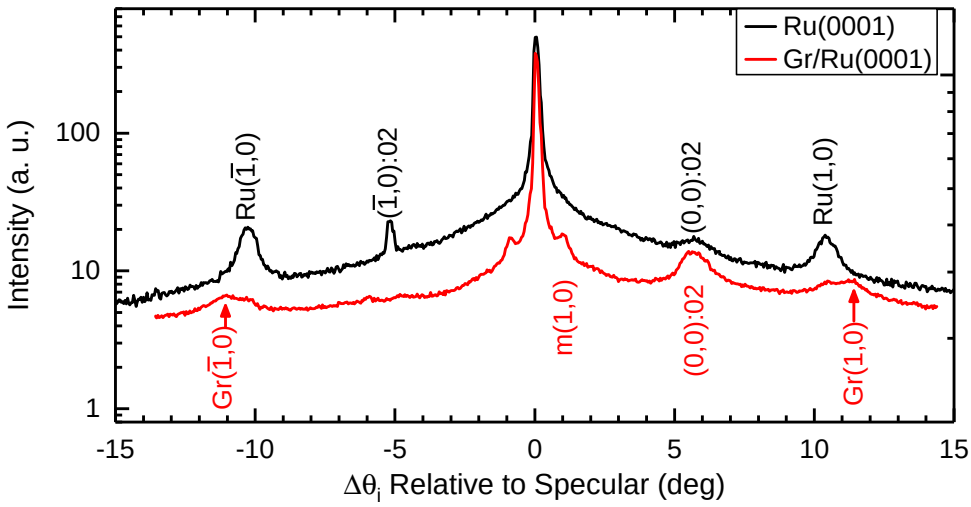

Figure 1.8: Angular diffraction of D_2 with $E_i = 87$ meV from Ru(0001) (black) and Gr/Ru(0001) (red) with $T_S = 430$ and 130 K, respectively.

shows an example of diffraction spectra of D_2 from Ru(0001) (black) and Gr/Ru(0001) (red). Typical elastic diffraction peaks appear at $|\Delta\theta_i| \sim 10°$ for the first order diffraction peaks (Ru(1,0) and Gr(1,0)) and at $|\Delta\theta_i| \sim 1°$ for the moiré superstructure on Gr/Ru(0001) (m(1,0)), these peaks are similar to the ones observed in He diffraction spectra from these surfaces [71]. Additional diffraction peaks appear on the Ru(0001) curve at $\Delta\theta_i \sim -5.2°$ and $5.7°$ which are a result of the $(\bar{1}, 0)$ and (0,0) RIDs from the $0 \rightarrow 2$ transition, a shorter notation (0,0):02 is more convenient. The diffraction spectrum from Gr/Ru(0001) shows an intense RID peak at $\Delta\theta_i \sim 5.6°$ associated with the (0,0):02, two other RID peaks with low intensities can be seen at $\Delta\theta_i \sim -5°$ and $-6.1°$ which are associated with the $(\bar{1}, 0)$:02 peaks of the periodicities of graphene and Ru(0001), respectively.

1.3.3 Surface Lattice Dynamics from iHAS

The coupling of motion of the atoms in a solid gives rise to its phonon modes. A flat surface breaks the 3D-translational symmetry of the solid, which gives rise to surface localized modes whose vibrational amplitudes decay rapidly away from the surface. The projection of the bulk modes onto the surface forms a continuum (bulk bands) since the component of their wave vector parallel to the surface are arbitrary [92]. When surface modes appear in the continuum occupied by bulk bands they are called resonances, otherwise, they are pure surface modes. The resonances which are bulk phonons with large amplitudes at the surfaces may or may not couple (hybridize) with the bulk modes. Depending on the mode polarizations, when surface resonances have the same polarization as the equivalent bulk modes they hybridize and their displacement field does not decay to zero far inside the crystal, but when they have an orthogonal polarization to the bulk modes they remain localized at the surface [3, 93].

Experimental determination of surface phonons

The production of an intense monochromatic helium beam with a relative velocity resolution of 1% has been achieved by J. P. Toennies and coworkers in 1981 by the introduction of a new mode of operation of nozzle beam sources and the use of a carefully designed system of differential pumping to increase the sensitivity of the detector. The He beam is chopped into pulses of controlled

widths where the energy spread is 1.5% to 5% depending on the initial energy and pulse width [94, 95].

The measurements are done in a fixed-geometry setup where the detector is fixed and the sample is rotated, this allows for exciting phonons even beyond the first surface Brillouin zone (SBZ), depending on the incident energy of the helium beam. The scattered beam is time-resolved by a multichannel analyzer connected to a detector consisting of an electron bombardment ionizer followed by a mass spectrometer to separate probe ions from the residual gas background. The collected spectra are then transformed into energy-exchange spectra.

Inelastic helium atom scattering (iHAS) is accompanied with an excitation or an annihilation of elementary excitations on the surface, which could be phonons, molecular vibrations of adsorbates, electronic transitions or plasmons, and thus the probing particle scatters off the surface with an energy $E_f = E_i \pm E_q$ where E_q is the energy of the elementary excitation.

In the usual experiment, an energy exchange spectrum is measured for a fixed $|k_i|$ and θ_i, explicitly speaking: the energy of the beam and its angle on incidence are kept fixed, and a time-of-flight (TOF) spectrum $I(t)$ is collected often for several hours (increasing signal-to-noise ratio). A complete set of TOF spectra includes different measurements for different beam energies and angles of incidence. A straightforward conversion gives TOF spectra as $I(\Delta E)$ then energy and momentum conservation laws give $\Delta K(\Delta E)$ for each single event featured in the TOF spectrum. In order to compare the experimental results with the theoretical dispersion curves the crystal is usually lined up so that $\Delta\mathbf{K}$ is parallel to one of the high symmetry directions of the reciprocal lattice of the surface.

Before addressing the dynamics of iHAS, it might be useful to highlight the main aspects of another experimental technique used more often in surface phonon measurements: high resolution energy loss electron spectroscopy (HREELS). The electron beam source in the last generation of HREELS Spectrometers is composed of a two-step monochromator resulting in a resolution of 0.5 meV and a significant increase of intensity in the high resolution range, the incident energy can be increased up to 250 eV. Probing the phonons along the SBZ is achieved by rotating the detector while keeping the sample at a fixed θ_i or by changing the incident energy E_i. The detector is composed of a single-stage energy analyzer and a channel electron multiplier detector (channeltron) where the scattered beam is directly energy resolved.

Electrons can lose energy on a surface via dipole scattering which is used

for studying the vibrational modes of adsorbed molecules. Low momentum transfer is associated with this event and thus, the scattered beam suffers only small deflections from the specular direction. The relevant energy loss for phonon measurements is the impact scattering regime where electrons with higher incident energies penetrate the surface to undergo short-range interactions with the atomic potential in the close vicinities of ion cores. They collide with the ions of the first few layers on the substrate and scatter off after exchanging energy and momentum with the surface lattice vibrations, impact-scattered events are easier to resolve as they appear in off-specular directions. Due to the relatively large cross section of electron inelastic scattering, the mean free path of electrons in the relevant energy range is of the order of 1 nm and all elastically backscattered electrons thus stem from the first few monolayers of the crystal [50, 92].

Time-of-flight measurement

Energy analysis of the scattered molecular beam is achieved experimentally by a TOF measurement. The first step is creating monochromatic pulses of the probe gas which can be achieved using a pulsed nozzle or by mechanically chopping the beam into pulses using a rotating disc that contains at least one slit with a determined width. The mechanical chopper is the most used approach in iHAS due to its durability.

Fig. 1.9 shows a scheme of the TOF measurement. The incident beam with kinetic energy E_0 is chopped into short pulses before reaching the sample which is aligned in certain θ_i and ϕ_i angles. The scattered atoms will leave the surface either with the same incident energy and thus the same speed, or gain (lose) energy from the surface and thus travel at higher (lower) speeds and arrive to the detector earlier (later) than the elastically scattered part of the pulse.

Experimentally, TOF spectra are a measure of reflected intensity as a function of arrival time which has to be converted into energy to be useful. This conversion can be obtained from the relation between flight times and the traveled distances and using the kinetic energy relation $E = \frac{1}{2}mv^2$. A detailed analysis is presented in Chapter 2.

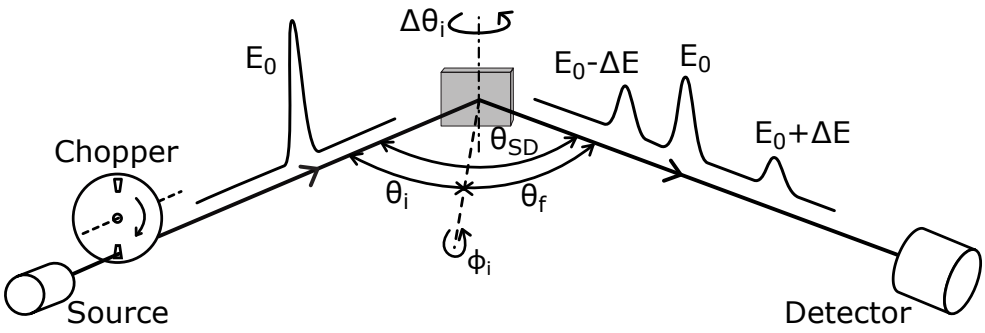

Figure 1.9: Scheme of a TOF measurement.

iHAS Dynamics

Gaining or losing energy upon scattering corresponds to phonon annihilation or creation, respectively. Conservation laws now include the energy and momentum of the created/annihilated phonon

$$\Delta\mathbf{K} = \mathbf{G} + \mathbf{Q} \quad \text{and} \quad \Delta E = \pm\hbar\omega(Q), \tag{1.10}$$

where $\mathbf{Q}$ is the phonon momentum parallel to the surface. The signs + and - refer to the phonon annihilation and creation processes, respectively. Combination of the conservation laws results in a general kinematical condition for inelastic atom-surface scattering called the scan curve [96]

$$\frac{\hbar\omega(\mathbf{Q})}{E_i} = \frac{(\sin\theta_i - \Delta K/k_i)^2}{\sin^2\theta_f} - 1\,. \tag{1.11}$$

Fig. 1.10 shows a schematic representation of a Rayleigh wave (RW) phonon mode in an extended surface Brillouin zone diagram of an arbitrary lattice, typical scan curves of He-scattering in a fixed source–detector angle setup ($\Theta_{SD} = 105.4°$) are plotted using two incident beam energies $E_i =$ 15 and 25 meV and several angles $\Delta\theta_i = -30$ to 30° relative to the specular position whose scan curves pass from the axes origin. Horizontal lines indicate the incident energy of the He beam and demonstrate the energy cutoff for phonon creation which is only possible for $|\Delta E| < E_i$.

When a scan curve crosses a phonon mode dispersion curve it means that the incident conditions allow for detecting a single phonon scattering event in the measurement and thus a peak in the corresponding TOF spectrum. When a

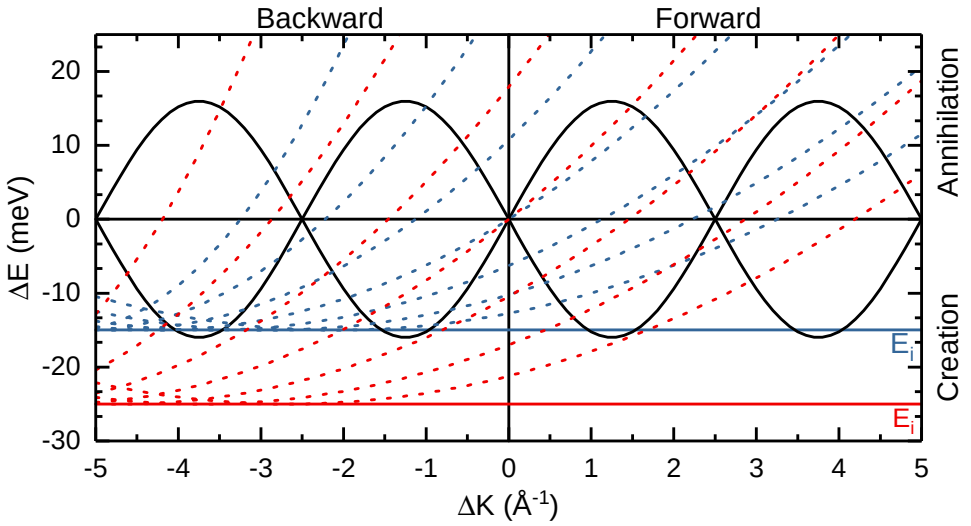

Figure 1.10: Schematic representation of a RW phonon in an extended zone diagram (solid black). Dashed lines are typical scan curves for a fixed source-detector angle setup ($\Theta_{SD} = 105.4°$) of He scattering with $E_i = 15$ and 25 meV (blue and red, respectively).

scan curve crosses a phonon mode dispersion curve in a perpendicular manner it results in a sharp peak in the TOF spectrum while a scan curve that is tangent to the phonon dispersion curve will result in a wide (smeared) peak. Fig. 1.10 shows that it is kinematically possible to observe both phonon creation and annihilation in forward and backward scattering in a single TOF spectrum, although not necessarily in the same Brillouin zone.

Fig. 1.11 shows a set of TOF spectra of He scattering from the surface of graphene/Cu(111)/Al_2O_3 using two incident beam energies indicated on their corresponding panels. Left panel shows the converted TOF spectra where intensity is plotted as a function of energy exchange. Right panels show the raw TOF spectra, notice from the arrival time values how the beam with lower incident energy arrives later to the detector and the inelastic peaks are farther apart and thus easier to resolve. This shows that decreasing the incident beam energy improves the measurement resolution but increasing the incident energy is required to avoid energy cutoff.

The aforementioned smearing which results from a scan curve being tangent to a phonon dispersion curve is called kinematic focusing (KF) [97]. It results

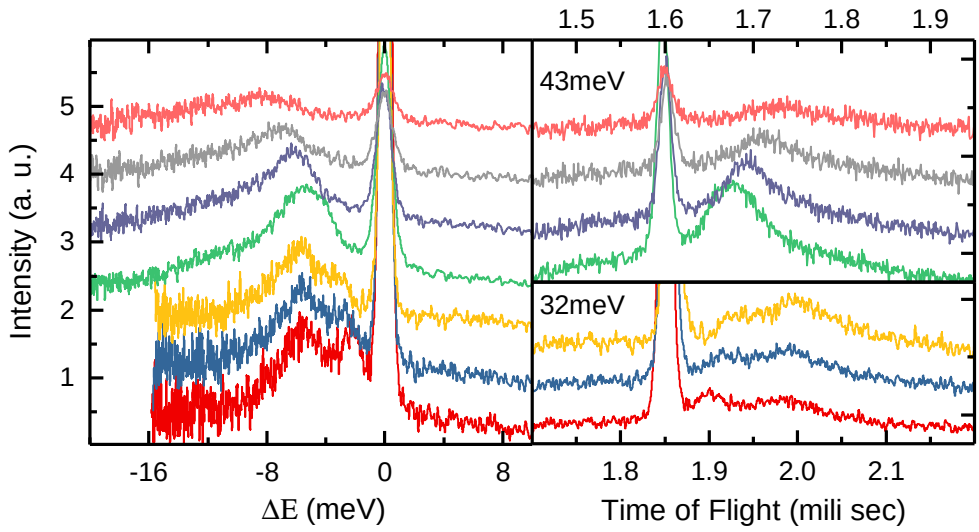

Figure 1.11: Right: TOF spectra of He scattered from Gr/Cu(111)/Al_2O_3 for two different incident energies (43 meV and 32 meV). The corresponding inelastic scattering intensity as a function of energy loss is shown on the left panel. Surface temperature is 120 K.

in enhanced inelastic scattering that affects the atoms in SAR status. This effect is manifested as a sharp small peak at the corresponding angular position in the diffraction spectra. The kinematic condition for the KF can be obtained by introducing the energy and momentum of the involved phonon in the SAR condition in Eq.(1.8) to get

$$\epsilon_n = \frac{\hbar^2}{2m}|\mathbf{k}_i|^2 \pm \hbar\omega_{KF}(\mathbf{Q}_{KF}) - \frac{\hbar^2}{2m}\left|\mathbf{K} + \mathbf{G}_{pq} + \mathbf{Q}_{KF}\right|^2, \tag{1.12}$$

here $\hbar\omega(\mathbf{Q}_{KF})$ is the phonon energy corresponding the KF condition and $\mathbf{Q}_{KF}$ is its momentum.

Quantum sonar effect

The inelastic scattering probability $P(k_i, k_f)$ for one-phonon creation processes is proportional to the Debye-Waller factor $P(k_i, k_f) \propto e^{-2W(\mathbf{p})}$; where $2W(\mathbf{p}) = \left\langle(\mathbf{p}.\mathbf{u})^2\right\rangle/\hbar^2$, $\mathbf{p}$ and $\mathbf{u}$ are the phonon's momentum and displacement, respectively [98]. This explains why multiphonon scattering probability increases with increasing surface temperatures. Analyzing the He-phonon forces

at a metal surface where the He-metal potential and the surface lattice dynamics were treated equally shows that the surface electrons experience forces by the He-atom which are transferred to the ions by electron-phonon coupling. The indirect He-phonon interaction can be interpreted as the Coulomb electron-phonon force integrated on the region of the variation of the metal density induced by the He atom [99]. Recently, the inelastic scattering probability of He-atom by a single-phonon creation process was found to be proportional to the electron-phonon coupling strength $\lambda_{Q\nu}$ (mass correction factor) for that specific phonon (mode-λ) [100]. This factor correlates with the Kohn anomalies observed in dispersion curves of phonons measured by HAS. Therefore; to a good approximation the HAS amplitudes for individual phonons are proportional to the respective electron-phonon coupling constants $\lambda_{Q\nu}$. The range of the electron-phonon interaction determines how deep a sub-surface atomic displacement can be detected by HAS. This is especially the case for small Q where the out-of-plane mode of sub-surface layers can be easily measured by HAS through the "quantum sonar effect" [100].

Selection rules

The polarizations of the surface phonons are customarily referred to using the sagittal plane, which is defined by the incident wave vector $\mathbf{k}_i$ and the surface normal $\hat{z}$, experiments are typically conducted in the **sagittal scattering** regime where the final scattered wave vector $\mathbf{k}_f$ lies in the sagittal plane. Surface modes are thus classified into three types: transverse (T), longitudinal (L) and shear horizontal (SH). The polarization vector of SH is normal to the sagittal plane whereas L and T modes form a coherent mixture of both polarizations that lie within the sagittal plane; with the name indicating the largest relative amplitude. When the sagittal plane along a high symmetry direction coincides with a mirror plane of the surface structure SH is odd relative to it while T and L are even, and thus the coupling of atoms to the SH mode becomes forbidden [3].

This is because the wavefunctions of the initial and final states of the projectile are even to the mirror plane reflection. However, the odd modes become visible along the same direction if the mirror plane of the sample is tilted with respect to the scattering plane [101, 102]. Misalignment from the high symmetry directions as well as the existence of domains with random orientations will render selection rules inactive. The violation of selection rules

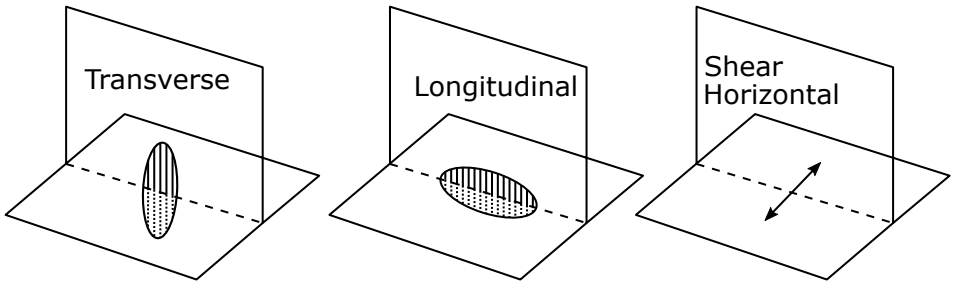

Figure 1.12: Scheme of scattering geometry showing the surface and sagittal plane, and the polarizations of three phonon modes: transverse, longitudinal and shear horizontal. With permission from [3]. ©(1991) Springer.

also occurs due to lowered crystalline quality which breaks the translational symmetry and thus can be interpreted as a signal of the disorder in the sample [38]. Finally, the interaction of an overlayer with a substrate also can break or reduce the symmetry as in a Gr layer on a metallic substrate and thus reduce or even remove all selection rules [101].

Umklapp scattering This effect is a form of phonon-phonon scattering involving the exchange of surface reciprocal lattice vectors **G**. Here a phonon is created by scattering with a wavevector extending beyond the first Brillouin zone of the surface, this can result in a backward scattering phonon upon zone folding. For large phonon wavevectors the intensity of Umklapp processes increases and this scattering mechanism starts to dominate [103].

He atoms carry enough momentum to allow for Umklapp scattering processes, this can be exploited to measure shear horizontal phonons near the zone boundary which can be accessible in sagittal plane scattering when the momentum transfer extends beyond the Brillouin zone boundary [3]. A surface with a small surface Brillouin zone, like a moiré superstructure which has a lattice constant ~ 25 Å, provides favorable conditions for Umklapp scattering.

Debye-Waller effect

The Debye-Waller factor is used in to describe the attenuation of diffracted intensities caused by the thermal motion of the crystal atoms. The principal observable effect of the thermal vibrations of surface atoms is the attenuation

of the coherent diffraction intensities without a change of the peak shape. The Debye-Waller factor relates the intensity $I(T_S)$ of a diffraction peak from a surface at temperature T_S to the intensity I_0 from the lattice at rest by

$$\ln[I(T_S)/I_0] = -2W(T_S) = -\frac{24m(E_i \cos^2\theta_i + D)T_S}{Mk_B\Theta_D^2} \tag{1.13}$$

where m and M are the atomic masses of the projectile and surface, respectively, E_i and θ_i are the incident energy and angle of the beam, k_B is the Boltzmann constant, T_S is the surface temperature, D is the well-depth of the projectile-surface potential and Θ_D is the surface Debye temperature. This equation indicates that the strength of the diffraction intensities should be highest for low incidence energy and surface temperatures and for grazing incidence angles. On the other hand, increasing surface temperature and beam energy will reduce diffraction peak intensities to levels where elastic scattering is no longer observed and the scattering process can be described using classical models.

The Debye-waller model was originally developed for X-ray and neutron scattering with the assumptions that the interaction in the scattering event is both weak and short in duration. This is not the case in HAS, however, the Debye-Waller factor in Eq.(1.13) has been successfully used in describing many experiments rather well [5].

A recently-published quantum theory showed that the Debye-Waller exponent is directly proportional to the electron-phonon coupling constant λ [104]. This opens the possibility of directly extracting the electron-phonon coupling strength in quasi-2D conducting systems from the dependence of HAS intensities on the surface temperature or the incident beam energy.

Classical smooth surface model (SSM)

Chapter 5 of this work addresses classical scattering of Ne from Ni(111) where the classical smooth surface model (SSM) is used to describe the results. In the classical SSM the transition rate $w(\mathbf{p}_f, \mathbf{p}_i)$ for scattering of a projectile atom with incident momentum $\mathbf{p}_i = (\mathbf{P}_i, p_{iz})$ into a state of final momentum $\mathbf{p}_f = (\mathbf{P}_f, p_{fz})$ is given by [105, 106, 107]:

$$\omega(\mathbf{p}_f, \mathbf{p}_i) \propto \frac{1}{(4\pi k_B T_S \Delta E_0)^{3/2}} |\tau_{fi}|^2 \exp\left\{-\frac{(E_f - E_i + \Delta E_0)^2 + 2v_R^2\mathbf{P}^2}{4\pi k_B T \Delta E_0}\right\}, \tag{1.14}$$

where E_i and E_f are the initial and final energies of the projectile, $\mathbf{P}$ is the component of the momentum transfer parallel to the surface, $\Delta E_0 = (\mathbf{p}_f - \mathbf{p}_i)^2/2M$ is the classical recoil energy with M the effective mass of the surface, T_S is the surface temperature, the Boltzmann constant is denoted by k_B and v_R is a weighted average of phonon speeds parallel to the surface [105, 106]. The matrix element τ_{fi} is the transition matrix of the interaction potential taken with respect to the initial and final states of the projectile atom. It is approximated by the value obtained for a rigid repulsive hard wall potential where it is proportional to the product of the initial and final momenta perpendicular to the surface, $\tau_{fi} \propto p_{fz} p_{iz}$.

Equation (1.14) has successfully described scattering spectra for several systems such as heavy rare gas scattering from molten metals [108] or other clean metal substrate targets [109, 110]. In order to compare the transition rate of Eq.(1.14) with experiment it must be converted into a differential reflection coefficient. The differential reflection coefficient is obtained by multiplying $w(\mathbf{p}_f, \mathbf{p}_i)$ by a Jacobian which is proportional to the magnitude of the final momentum p_f and dividing by the incident atomic flux which is proportional to p_{iz}.

Chapter 2

Experimental

This chapter provides a general description of the He scattering apparatus where the production and propagation of supersonic atom beams. Details of the two HAS apparatus used in this work are presented. Afterwards, a discussion of the experimental considerations in HAS measurements is presented. And finally, a few modifications and additions made during this work to the experimental setup are listed. Further information on the subjects of this chapter can be found in Refs. [3, 4, 8, 89, 90, 111, 112].

2.1 Production and Detection of Helium Beams

The procedure to produce a He beam is basically by creating a leak of pressurized gas into a vacuum chamber; under the right conditions the He beam can travel hundreds of kilometers. Free jet sources have been developed during the last century as has been mentioned in Section 1.1.1. The translational energy of a gas in equilibrium using the Maxwell–Boltzmann distribution is given by $E_{tr} = \frac{1}{2} m v^2 = \frac{3}{2} R T$, where R is the ideal gas constant, T is the equilibrium temperature, m and v are the mass and average velocity of the gas atoms. The mean free path of an atom of such gas is $\lambda = k_B T/(\sqrt{2}\pi P \sigma 2)$, where P is the pressure in (Pa), σ is the atomic diameter in (m) and k_B is the Boltzmann constant [8, 112].

2.1.1 Free Jet Sources

Free jet molecular beam is a neutral beam of atoms extracted from an underexpanded part of a supersonic continuum, expanding from a high-pressure (P_0) gas source into a low-pressure (P_b) ambient background. The following is a brief summary of book chapter by D. R. Miller in Atomic and Molecular Beam Methods [111].

The expanding beam, out of the nozzle, is comprised of two parts: The core known as the zone of silence and the outer layer known as the compression waves, a skimmer placed at the end of the zone of silence serves to extract the centerline beam. The gas starts from a reservoir at the stagnation state (P_0, T_0) with a negligibly small velocity, it accelerates through the nozzle due to the imposed pressure difference ($P_0 - P_b$). The flaw may reach sonic speeds (Mach 1) at the source exit provided $P_0/P_b > G = ((\gamma + 1)/2)^{\gamma/(\gamma-1)}$, which is less than 2.1 for all gases. If the pressure ratio is less than the critical value, then the flow will exit subsonically with pressure nearly equal to P_b without any further expansion. γ is the heat capacity ratio $\hat{C}_P/\hat{C}_V$ which is related to the degrees of freedom of the gas molecule by $\gamma = 1 + 2/f$. The total number of degrees of freedom of a molecule is $f = 3N$ with N being the number of atoms in the molecule. These degrees of freedom divided into translational, rotational and vibrational depending on the molecule's symmetry. Every molecule has a defined number of degrees of freedom: 3 translational, rotations are 3 (or 2 for linear molecules), vibrations are $3N - 6$ (or $3N - 5$ for linear molecules). Vibrational motion of molecules contributions to the heat capacity is negligible at thermal energies. $\gamma = 5/3$ for monoatomic gases like He. In reality γ deviates from the values derived from symmetry but can be determined precisely by experiment.

In supersonic flow, unlike subsonic flow, the flow velocity (M) increases as the area of the flow increases, so as the gas starts expanding from the source exit its Mach number becomes much larger than 1. Furthermore, a supersonic flow cannot "sense" downstream boundary conditions, this is a crucial feature caused by the fact that information propagates at the speed of sound whereas the gas flows faster than that ($M >> 1$). The gas starts expanding isentropically with a continuously increasing M, in order to compensate for its overexpansion it creates a system of shock waves which is composed of a barrel shock at the sides and the Mach disk shock normal to the centerline. The Mach disk location x_M is given by $(x_M/d) = 0.67(P_0/P_b)^{1/2}$, where d is the nozzle diameter. The

width of the Mach disk is estimated to be of the order $0.5x_M(\pm 25\%)$, but the correct value depends on γ and P_0/P_b. For example, a beam created using a gas reservoir of 4 bar, which flows into a vacuum chamber of 4×10^{-5} mbar through a 10 µm nozzle results in $x_M = 9.5$ mm.

By considering the expanding gas to be ideal with no viscous and heat conduction effects, which are good approximations for high-speed flow, the stagnation enthalpy per unit mass is given by $H_0 = H + v^2/2$. As the gas expands and cools that enthalpy decreases and the mean velocity increases. For ideal gases, $dH = \hat{C}_P dT$, this gives

$$v^2 = 2(H_0 - H) = 2\int_T^{T_0} \hat{C}_P dT. \tag{2.1}$$

If $\hat{C}_P$ is constant over the range of interest of beam temperatures then $v = \sqrt{2\hat{C}_P(T_0 - T)}$. For an ideal gas $\hat{C}_P = (\gamma/(\gamma - 1))R/m$, where R is the ideal gas constant and m is the molecular mass. If the gas is cooled substantially in the expansion $T << T_0$ we obtain a maximum or terminal velocity:

$$v_\infty = \sqrt{\frac{2R}{m}\frac{\gamma}{\gamma - 1}T_0}, \tag{2.2}$$

the mean velocity approaches v_∞ quickly after exiting the source. From this equation the kinetic energy of noble gas beams becomes

$$E = \frac{1}{2}mv^2 = R\frac{\gamma}{\gamma - 1}T. \tag{2.3}$$

Thus, for an ideal gas $R = 0.086$ meV and $\gamma = 5/3$ at $T = 300$ K the beam energy is $E = 64.635$ meV. The energy resolution of a beam is proportional to T/v^2.

Using a mix of gases requires the usage of the average heat capacity $\bar{C}_P = \Sigma X_i C_{Pi} = \Sigma X_i \gamma_i/(\gamma_i - 1)R$ and the molar average molecular weight $\bar{m} = \Sigma X_i m_i$, where X_i is the mole fraction. From this we get that the mean velocity is proportional to the reciprocal of the molar weight. Hence, we can accelerate a heavy species by diluting it in a light gas or decelerate a light species by diluting it in heavy gas. The flow rate of an ideal gas through a nozzle in supersonic expansion is given by:

$$f^{\cdot} = P_0 A\left[\frac{\gamma m}{RT_0}\left(\frac{2}{\gamma + 1}\right)^{(\gamma+1)/(\gamma-1)}\right]^{1/2} \tag{2.4}$$

in $\mathrm{kg\,s^{-1}}$, where $A = \pi d^2/4$ is the area of the nozzle exit, thus, the flow rate using 80 bar through a 10 µm is 2.4×10^{-5} sccm.

2.1.2 Helium Detectors

In principle, every method suitable for measuring low pressures in a vacuum chamber can be used to detect molecular beams if the sensitivity is increased sufficiently, because the measured intensity is usually of the same level as the background gas in the chamber.

Helium is the element with the highest ionization energy ~ 25 eV and a very low ionization probability. Thus, high intensity and high voltage ionization currents are needed in the detection of scattered He beam since the density of a scattered beam is comparable to the density of background gases. The most commonly used type is a cross-beam quadruple detector where the ionization zone is optimized to provide better sensitivity. Electron multipliers with high dynamic range are required because of the difference in peak intensities in one diffraction measurement can be seven orders of magnitude.

2.1.3 Helium Scattering Machines

Two HAS machines were used in this work. The first, nicknamed ERASMO, is a high-resolution time-of-flight machine with a fixed source-detector angle. The design of this apparatus provides high intensity and high energy resolution, both are requirement for TOF measurements. The second scattering apparatus enables the determination of absolute diffraction intensities by measuring the incident and scattered beams using the same movable detector and thus, the normalization to detector sensitivity is not needed [113]. The movable detector also allows for out-of-plane measurements of diffraction peaks. Throughout this manuscript this apparatus will be referred to by its acronyms TEAMS which stand for *thermal energy atomic and molecular scattering*. Both machines are located in the Surface Science Laboratory in Universidad Autónoma de Madrid (LASUAM).

Fixed angle setup: ERASMO

The apparatus used for this work was first designed by E. Hulpke and built by H. J. Ernst for conducting high resolution measurements of surface phonons,

and modified later by J. Ludecke, W. Steinholg and B. Flach as part of their PhD work. The system was built in Max Planck Institut für Strömungsforschung in Göttingen (Germany). It was then donated by J. P. Toennies and moved to LASUAM by D. Farías in 2004. Installation and calibration were performed by D. Barredo during his PhD work [114]. Fig. 2.1 shows a top-view diagram of ERASMO. The main chambers are the source, target, and detector chamber.

The source is composed of three partially connected sections each one of them is equipped with an independent pumping system. The first section, where the beam is produced from the nozzle, is connected to an 8000 l/s diffusion pump and a roots pump with a capacity of 500 m^3/h. This high capacity pumping allows the usage of high stagnation pressure which reduces the velocity spread of the beam. The background pressure in this part of the source chamber is usually 10^{-4} mbar using 80(30) bar stagnation pressure and a nozzle with diameter $\varnothing$10(20)µm. The nozzle can be cooled down using a closed-cycle He cooling system; the lowest practical temperature that can reached is $\sim$ 85 K (E_{He} = 18.5 meV). The nozzle temperature is controlled using an independent PID controller from *Lake Shore* connected to a Pt100 sensor and a heater (two resistances in series) with a total power of 20 W. We do not use a temperature higher than 400 K because the Pt100 sensor is soldered to the connector cables using lead. The PID controller used to be the managed by the computer software with a stability of 0.1 K with some occasional instabilities; the independent PID controller is more stable with a precision of 0.01 K, it provides a faster response and a smaller overshoot.

The beam leaves the nozzle part through a $\varnothing$0.6 mm skimmer from *Beam Dynamics* to the second section where the *chopper* is installed. This skimmer was installed recently, it is 2.54 cm in length, which is almost 1 cm smaller than to original skimmer, thus some modifications had to be made in the chamber to bring the nozzle closer to the skimmer. The second section of the source is connected to a 3000 l/s diffusion pump which is necessary for the TOF measurements as most of the propagating beam is blocked by the chopper. This pumping system keeps a pressure of 10^{-6} mbar during the measurements. The beam leaves this section through a $\varnothing$1.2 mm diaphragm to a differential pumping stage before entering the main chamber. This stage is useful for reducing the background pressure in the target chamber, in addition, movable diaphragms can be introduces at this stage when more collimation of the beam is needed. The diaphragms are $\varnothing$1.1 and 0.5 mm holes mounted on a movable flag inside the differential pumping stage.

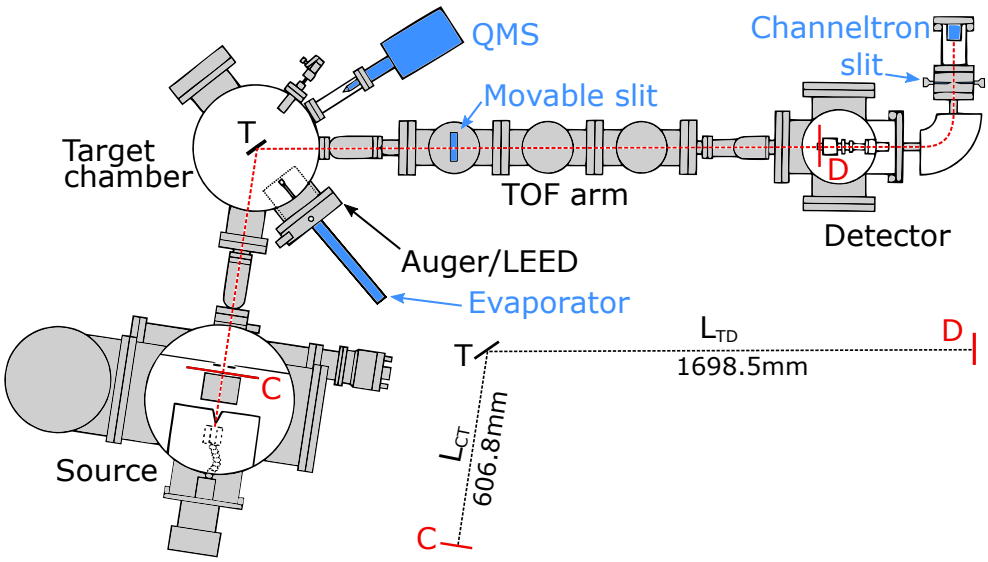

Figure 2.1: Top-view scheme of ERASMO. Red dashed line is the beam trajectory from production to detection. The inset shows the distances involved in TOF measurements: chopper (C) to target (T) to detector (D). Recreated from [114]. Some modifications made during this work are highlighted in blue.

The chopper, indicated by a red "C" in Fig. 2.1, is a ⌀200 mm disc attached to a motor capable of rotating at 500 Hz. The chopper has two triangular windows used in creating short pulses of the beam as seen in Fig. 1.9. This setup can provide pulses of a width 12 µs at a frequency of 1000 Hz. Creating shorter pulses with one chopper is impossible due to the intrinsic energy spread of the beam. All TOF measurements in this work were conducted using pulses at a frequency 800 Hz; the pulse width was changed between 12 and 25 µs to obtain the highest intensity when the energy spread of the beam is too large.

Finally, the beam enters the target chamber to impinge on the surface of the sample. The calibrated chopper-sample distance is $L_{CT} = 606.8$ mm. The pressure in the main chamber is in the low range of 10^{-10} mbar, it increases to 2×10^{-8} mbar in the presence of the He beam. A large turbo pump with a capacity of 520 L/s is used on this chamber. After scattering from the sample surface, the beam travels a distance of $L_{TD} = 1.6985$ m through the TOF arm before reaching the detector. The TOF arm is composed of three small chambers separated by (3 × 5 mm) slits, each chamber is equipped with a turbo

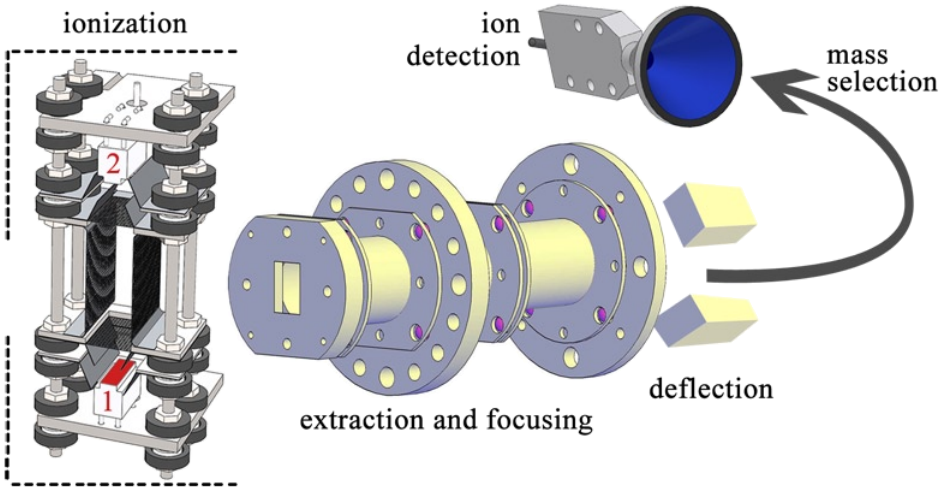

Figure 2.2: Conceptual representation of He detector in TEAMS. Individual section are rotated arbitrarily for better view.

pump, the exhaust of these pumps passes through one diffusion pump to reduce to backflow of light molecules in the turbo pumps.

The detector is located in a separate chamber which is equipped with a molecular turbo pump followed by a diffusion pump. It comprises an ionization and extraction part, followed by acceleration and focusing parts then a mass selection permanent magnet (250 mT) and finally a secondary electron multiplier or most recently a channeltron.

Fig. 2.2 shows a conceptual representation of the detector. The filaments, indicated by (1) and (2), are rectangular dispenser cathodes made of a barium impregnated porous tungsten which is heated by a tungsten filament passing through it. The active surface of the filament is 10 mm long in the direction of the beam propagation and 3 mm wide (colored red). While this helps in increasing the sensitivity, since the probability of ionizing an atom of the beam increases with the time spent in the ionization zone, it also means that atoms with lower energies have higher probability in being detected. Furthermore, the registered flight time of an atom depends on the location along the ionization zone it was ionized, this will smear out the features in the TOF spectra, and thus the length of the ionization zone is limited by the resolution requirements of phonon measurements.

Rotary detector setup: TEAMS

This apparatus was donated by the Freie Universität Berlin and installed by Pablo Nieto for his PhD thesis [115]. The apparatus is composed of two parts, source and scattering chambers separated by a UHV valve; Fig. 2.3 shows a schematic diagram.

The source chamber is three-staged differentially pumped with one diffusion pump in each of the first two stages (5000 l/sec each) and a turbomolecular pump (350 l/sec) in the third stage. Molecular beams are generated by supersonic expansion through a $\varnothing 10\,\mu m$ Pt nozzle (N) where the stagnation pressure is typically 50 bars and the background pressure below 10^{-3} mbar. The nozzle can be cooled down to 100 K using liquid nitrogen and heated up to 800 K using a filament, the temperature is controlled using a PID controller. The expanded beam is extracted via a skimmer of $\varnothing 0.5$ mm (S). A rotatable disk with different aperture diameters (0.2-4 mm) provides further collimation in the last stage of the source chamber.

Before accessing the main chamber, the beam is modulated by a mechanical chopper rotating at 50 Hz and coupled to a lock-in amplifier to increase the signal-to-noise ratio of the detected beam. This is important because the detector is located in the same chamber with the sample and the background

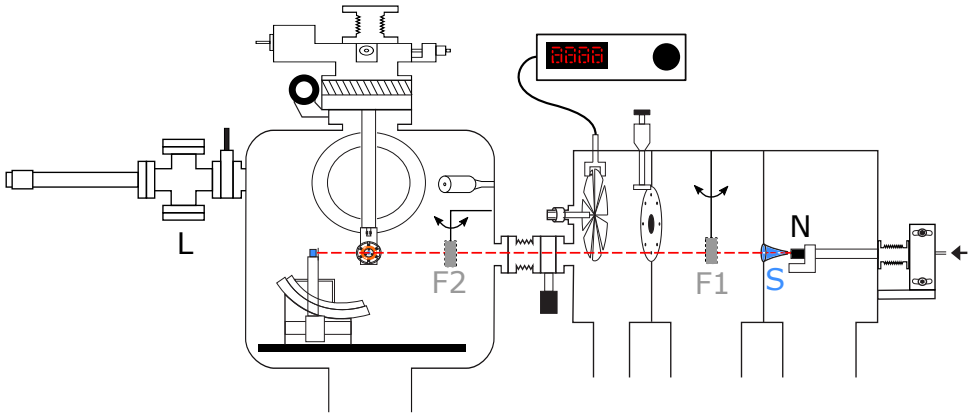

Figure 2.3: Schematic presentation of TEAMS. Red dashed line is the beam trajectory from the nozzle (N), through the skimmer (S) to the sample (orange) and the detector which is mounted on the goniometer. F1, F2 are flags, L is the load-lock chamber. From [115].

increases significantly in the presence of the molecular beams.

The sample is mounted on a manipulator with 5 degrees of freedom, allowing the adjustment of spatial, azimuthal and polar positions of the sample. The sample temperature can be varied between 100 and 1700 K. The detector is a crossbeam quadrupole mass spectrometer (Mod. Balzers QMG 511) mounted on a two-axis goniometer inside the scattering chamber. The detector can rotate 200° in the scattering plane and ±15° in the perpendicular direction in steps of 0.02°. The scattered beam is collimated by a ⌀1 mm diaphragm mounted on the detector at 55 mm from the sample providing an angular resolution of 1.04° in the diffraction spectra. The machine is equipped with two flags to be used in sticking measurements by King and Wells method.

2.2 HAS Measurements

In textbooks, experiment always agrees with theory, in the laboratory it seldom does. Section 1.3 provided an introduction to the kinematics and dynamics of HAS. This section provides an insight on the experimental limitations in HAS measurements.

2.2.1 Angular Resolution Considerations

A mathematical solution of HAS kinematics gives a spectrum with diffraction peaks of zero widths, but the measured diffraction peaks have a finite width that results from three factors: the beam quality, the surface quality and the instrumental resolution.

The instrumental resolution is controlled by the geometrical design of the scattering apparatus. Collimating the incident and scattered beams and increasing the source-surface and surface-detector distances improves the angular resolution [116, 117]. Fig. 2.4 represents the dimensions that control the instrumental resolution which is given by

$$(\Delta_\theta \theta_f)^2 \simeq \left(\frac{\cos\theta_i}{\cos\theta_f}\frac{\delta_S}{D_S}\right)^2 + \left(\frac{\cos\theta_i}{\cos\theta_f}\frac{\delta_a}{D_a}\right)^2 + \left(\frac{\cos\theta_f}{\cos\theta_i}\frac{\delta_a}{D_a}\frac{D_S}{D_d}\right)^2 + \left(\frac{\delta_d}{D_d}\right)^2 \quad (2.5)$$

where δ_S, δ_a, δ_d are the widths of the skimmer, collimating diaphragm and detector apertures, and D_i are distances indicated in Fig. 2.4. In TEAMS,

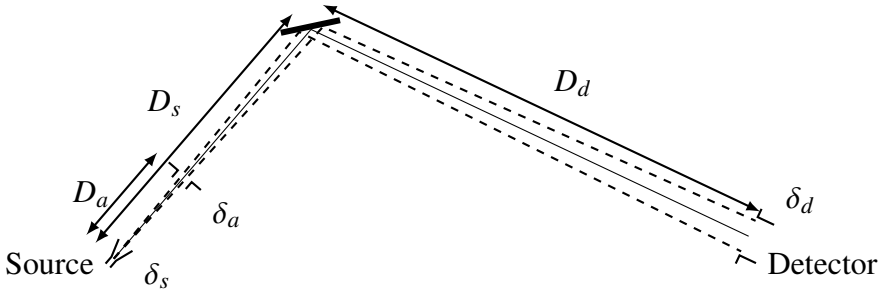

Figure 2.4: Scheme of instrumental broadening in diffraction measurements.

the first two terms have negligible contributions compared to the last two. In ERASMO, on the other hand, the first term can be ignored and the second term is the most important in the angular resolution. The instrumental resolution of TEAMS is 1.3° when a ⌀0.4 mm diaphragm is used, on the other hand, the angular resolution of ERASMO is 0.13°.

The broadening due beam quality stems from the Bragg law, it is given by

$$\Delta_E \theta_f \simeq \frac{\left|\sin\theta_i - \sin\theta_f\right| \sqrt{\frac{\overline{(\Delta E_i)^2}}{E_i^2}}}{\cos\theta_f}, \tag{2.6}$$

where $\overline{(\Delta E_i)^2}$ is the mean-square energy spread in the beam. Clearly the beam quality affects only the diffraction peaks as it disappears for the specular peak where $\theta_i = \theta_f$.

The broadening due to surface quality is derived from a relation that relates the intensity of the specularly reflected beam to the average domain size, also known as *coherence length* l_c [117]

$$I \sim l_c \left(\frac{\sin \frac{1}{2} l_c \Delta K}{\frac{1}{2} l_c \Delta K} \right)^2. \tag{2.7}$$

The angular broadening is equivalent the FWHM of the specular peak. The half-height of the reflected intensity occurs when $1/2 l_c \Delta K = 1.391$ and thus we get

$$\Delta_{lc} \theta_f = \frac{5.564}{l_c \, k_i \cos\theta_i}. \tag{2.8}$$

The value of $\Delta_{lc}\theta_f$ decreases with increasing values of l_c, i.e. with improving quality of the surface, and finally it becomes negligible in comparison with $\Delta_\theta\theta_f$. This limit is called the instrumental *transfer width* and defines the largest value of a lateral domain size that can be resolved with the measuring instrument. Eq.(2.8) can be used to estimate the average domain size of a surface as

$$l_c = \frac{2.782}{\Delta_{lc}\theta_f \, k_i \cos\theta_i}. \tag{2.9}$$

The total angular broadening in diffraction spectra is given by

$$\Delta\theta_f^2 = \Delta_\theta\theta_f^2 + \Delta_E\theta_f^2 + \Delta_{lc}\theta_f^2. \tag{2.10}$$

From the above discussion it is clear that angular resolution can be improved by beam collimation, but this will decrease the intensity of the beam relative to the background in the detector region. A good example of this is was observed in Ar diffraction from Ru(0001) where diffraction peaks appear when the beam collimation is increased while the total intensity is decreased [86].

Decreasing the beam energy spread can be achieved by increasing the stagnation pressure and decreasing the nozzle temperature; both are limited with cluster creation which can clog the nozzle. Increasing the nozzle diameter d also decreases the energy spread but this will increase the gas output as d^2 and thus waste more He and increase the background pressure which might overload the pumps. In fact, beam collimation improves the angular resolution not only due to geometrical reasons; it also functions as energy selection mechanism as it limits the velocity spread in the direction perpendicular to the beam propagation.

Further improvements are obtained by increasing the volume of the ionization zone in the detector and the distances between skimmer, collimating diaphragms, sample and detector. This is mainly limited by the cost and technical feasibility if only diffraction measurements are considered. Further limitations arise for TOF measurements.

2.2.2 Time-of-Flight Measurement

Energy spread of a molecular beam increases with distance traveled by the beam. Thus, resolving inelastic features in TOF spectra improves for longer TOF arms. This is, however, limited by the intrinsic energy spread of the beam as the widths of these features will increase with traveled distance and they

will start overlapping. To complicate the matter, the scattered intensities in phonon measurements are very low which requires a substantial increase in detector sensitivity and dwell times. This is solved by increasing the length of the ionization region, as shown in Fig. 2.2, which in turn causes another problem as the registered flight time of the detected atom will depend on where along the ionization region it was ionized. This effect can be decreased when the TOF arm length is chosen to be sufficiently long relative to the length of the ionization region. A compromise between all these factors has to be achieved for deciding the length of the TOF arm.

Decreasing the effect of intrinsic energy spread can be obtained by decreasing the chopper-surface distance. The only limitations here are technical, since the mechanical beam chopping increases the background in the chopper chamber, it is necessary to have a differential pumping stage that separates the chopper and the target chambers. Furthermore, since the energy broadening start at the nozzle, decreasing the total nozzle-target distance is what really affects the quality of the pulse. This explains why the source chamber is ERASMO is much smaller than that in TEAMS, since the angular resolution is more important in the latter.

Pulses created by the mechanical chopper have a width controlled by the width of the slit on the chopper disc and its rotation frequency. The mechanical chopper in ERASMO has two triangular slits and can rotate at 500 Hz (see Fig. 1.9). The position of the chopper can be changed so that the beam can be chopped at the wider base of the slit or at the narrow region near the triangle's head and thus, using low beam energies, a pulse width of 10 µs can be obtained, which is equivalent to $\Delta E_i = 0.5$ meV. Further improvement is limited with the TOF arm length, which is related to the beam energy, and thus, at higher beam energies the smallest possible pulse width increases and it becomes more convenient to increase the chopping width in the chopper to increase the beam intensity.

While decreasing the beam energy improves the pulse quality and thus the TOF resolution, the scan curves in Fig. 1.10 showed how incident atoms with low energies cannot excite high-energy phonons. In fact, the coupling of the motion of impinging atoms with lattice vibrations is limited in a more complicated way for both phonon creation and annihilation events. This is known as the energy and momentum cutoffs which can be understood in a classical picture in analogy to the uncertainty principle. The atom-phonon coupling is limited by the atom's size and the interaction time. The atomic

size poses a lower limit on spatial resolution, or the area of interaction on the surface, in the reciprocal space this means an upper limit of the interaction over the surface Brillouin zone. This is the momentum cutoff. The interaction time limits the shortest visible event, or in the frequency domain, the highest frequency or energy visible in the interaction. This is the energy cutoff. From this one can see the benefits of using He atoms, they are the smallest and fastest among noble gases at thermal energies. This is also why it is necessary to increase the He energy if phonons with high-frequency or large wavevectors are being investigated.

Kinematic focusing was mentioned in Sec. 1.3.3. It happens when a scan curve is tangent to a phonon dispersion curve. This results in a smearing of single-phonon feature in TOF spectra. Furthermore, the energy spread of the incident beam will increase this smearing; the scan curves plotted in Fig. 1.10 did not include the energy spread of the incident beam, which (when included) would show that even for a perpendicular crossing of dispersion and scan curves there is an unavoidable width of the single-phonon feature in TOF spectra. The only way to decrease this width is to improve the energy spread in the beam, at least in the direction parallel to the surface.

TOF analysis

The analysis of TOF spectra, itself, has its effects on the resolution of measured phonon energies. The time of flight of the elastically t_e and inelastically t_i scattered particles from the chopper to the detector are measured; the distances L_{CT} (chopper-target) and L_{TD} (target-detector) are known, and thus, the incident energy of the particles E_i and final energies of inelastically scattered particles E_f are given by

$$\begin{aligned} E_i &= \frac{1}{2}m\left(\frac{L_{CT}}{t_{CT}}\right)^2 = \frac{1}{2}m\left(\frac{L_{CD}}{t^e_{CT}}\right)^2, \\ E_f &= \frac{1}{2}m\left(\frac{L_{TD}}{t^i_{TD}}\right)^2, \end{aligned} \tag{2.11}$$

where $L_{CD} = L_{CT} + L_{TD}$, m is the mass of the probe atom, and the indices C, T, and D represent the chopper, target, and detector, respectively.

From these two equations the energy transfer ΔE that takes place in the

interaction of He atoms with surface phonons is given by

$$\Delta E = \frac{m}{2}\left[\left(\frac{L_{TD}}{t^i_{CD} + t^e_{CD}\left(\frac{L_{TD}}{L_{CD}} - 1\right)}\right)^2 - \left(\frac{L_{CD}}{t^e_{CD}}\right)^2\right]. \tag{2.12}$$

The transformation of TOF spectra to an energy transfer scale affects spectra shapes due to including the Jacobian in this transformation i.e. the peak intensities will be given by

$$f_E(E) = f_t(t(E))\frac{dt(E)}{dE}. \tag{2.13}$$

Due to the length of the ionization region the probability of ionizing a gas atom increases with the time the projectile spends in passing through the detector, and this time is inversely proportional to the speed or momentum of the projectile. The importance of this effect increases for lower projectile speeds and for increasing energy exchange when scattering from the surface because the detector correction changes the shape of the peak which can result in a shift in the peak's position as well as its intensity. Therefore, a *detector correction factor* has to be added to the Jacobian in Eq.(2.13) and the total conversion function of the measured intensity in TOF spectra denoted by $I_t(t_{TD})$ to the intensities in the energy domain, denoted by $I_{\Delta E}(\Delta E)$ are given by [118]:

$$\begin{aligned} I_{\Delta E}(\Delta E) &= \frac{t^e_{TD}}{t^i_{TD}}\, I_t(t^i_{SD})\left|\frac{dt}{dE}\right|_{t_{SD}} \\ &= \frac{t^e_{TD}}{t^i_{TD}}\, I_t(t^i_{SD})\frac{(t^i_{TD})^3}{m(L_{TD})^2}; \\ &= I_t(t^i_{SD})\frac{t^e_{TD}}{mv_f^2}; \end{aligned} \tag{2.14}$$

The factor t^e_{TD}/t^i_{TD} is the detector correction. The detector correction does not have an appreciable effect on the widths of the peaks but rather it affects their intensities and maximum positions. Thus it is important in the analysis of the multi-phonon background in TOF spectra as shown in Fig. 2.5.

Since the Jacobian is a non-linear transformation, it strongly affects the heights and widths of the phonon peaks; however, it conserves the total peak

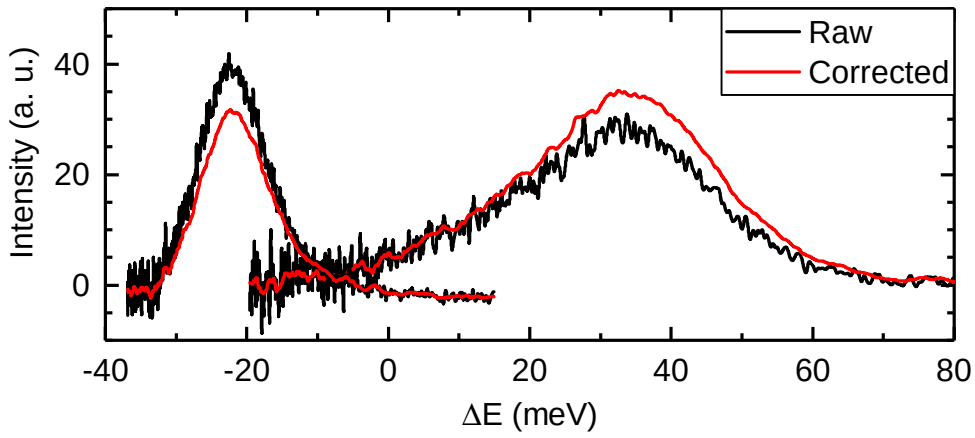

Figure 2.5: Effect of applying detector correction to intensity conversion Jacobian Eq.(2.14). Two TOF spectra of Ne (66 meV) scattering from Ni(111) (420 K) presenting gain and loss scenarios with (red) and without (black) including detector correction factor.

intensities. The phonon annihilation peaks become broader and lower, while the phonon creation peaks become narrower and higher, thus the error in phonon energy in the annihilation side is increased. Unfortunately, the noise in the extreme creation regions is strongly amplified.

2.3 Changes to the Measurement Setup

Detailed descriptions of the experimental apparatuses ERASMO and TEAMS can be found in the PhD dissertations of D. Barredo and P. Nieto [114, 115]. However, a few changes have been made in the course of this work, they are listed below.

Using a channeltron in the detector

We are now using a channeltron from *Dr. Sjuts* instead of an electron multiplier from *Hamamatsu*, the channeltron provides a higher dynamic range and a lower dark count rate. Fig. 2.6 shows a comparison of diffraction spectra from Gr/Ir(111) under the same experimental conditions using the old SEM and the new channeltron. More peaks can be resolved with the latter.

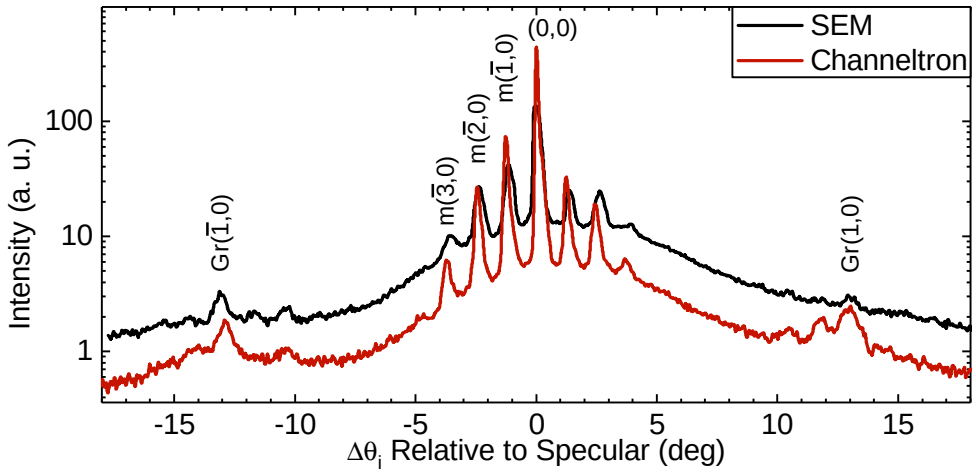

Figure 2.6: Improved quality of detected beam when switching to a channeltron. Data from Gr/Ir(111) using He beam $E_i = 66$ meV, $T_S = 120$ K.

Using a commercial QMS for diffraction measurements

The homemade detector used in ERASMO is prone to failure due to aging. Fixing the detector in a few cases took several month and thus it was crucial to implement another detector even if it had lower intensity. For this purpose we connected the commercial quadrupole mass spectrometer (QMS) *Pfeiffer Prisma* which was up till now used for a different purpose (see Fig. 2.1). This detector is very slow for TOF measurements and its sensitivity is very low compared to the homemade detector, however, it is convenient for diffraction and Debye-Waller measurements. The modification made to the scattering chamber is that the QMS was pulled out from the scattering chamber using a straight tube extension of 35 cm, and was separated from the scattering chamber using circular ⌀1 mm diaphragm. The extension tube is also connected to separate turbo pump.

Figure 2.7 shows diffraction spectra of He scattering from Ni(111) (red) and He and Ne scattering from Gr/Ni(111) (black and blue, respectively). Diffraction peaks from Gr/Ni(111) are visible in these spectra, while diffraction peaks from Ni(111) are not visible because of the low corrugation of this surface. The source–detector angle in this setup is $\Theta_{SD} = 131.15°$. These diffraction spectra exhibit a very sharp specular peak, FWHM is 0.17, 0.2 and

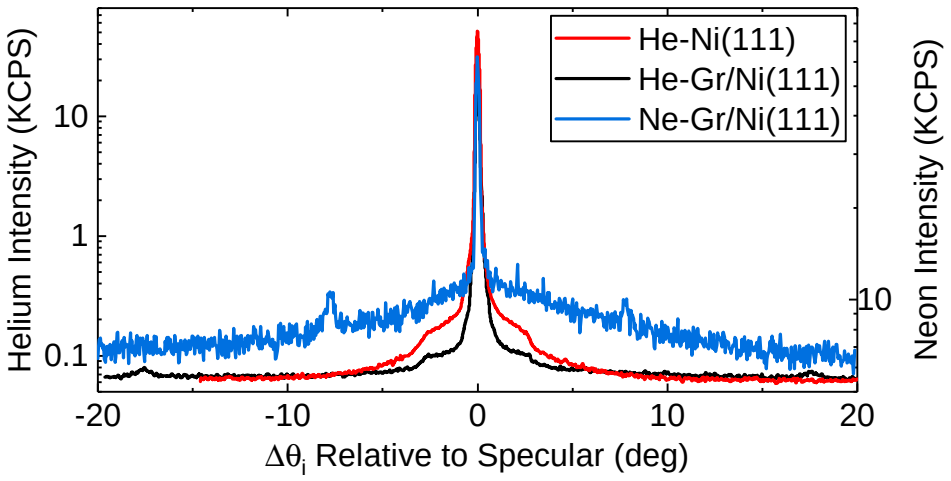

Figure 2.7: Angular diffraction of He and Ne scattering from Ni(111) and Gr/Ni(111) using a commercial detector.

0.25° of the He-Gr/Ni(111), He-Ni(111) and Ne-Gr/Ni(111), respectively.

Measuring different masses with the homemade detector

The homemade detector in ERASMO is impressively sensitive to small amounts of the studied gas to due to the large area of its ionization zone. Although this detector was designed for the detection of He, it can be easily modified to measure other masses by changing the magnitude of the magnetic field used in mass selection. This was done for the first time during the work of this thesis. Chapter 5 shows results of diffraction and TOF measurements with Ne beams carried out using this detector.

Figure 2.8 shows diffraction spectra of H_2 scattered from Gr/Ni(111) using two incident beam energies indicated on the panel. RIDs are identified on spectra as calculated using Eq.(1.9). Using H_2 in measurements is problematic since its intensity in the scattered beam is much lower than that in the residual background. The inset shows smoothed TOF spectra collected using E_i = 100 meV at two angles where RIDs were observed as indicated by arrows of the same color.

The yellow spectrum was measured at the (0,0) peak after a transition of rotational states $j = 0 \rightleftharpoons 2$. The measured energy of transition was −42.75 meV.

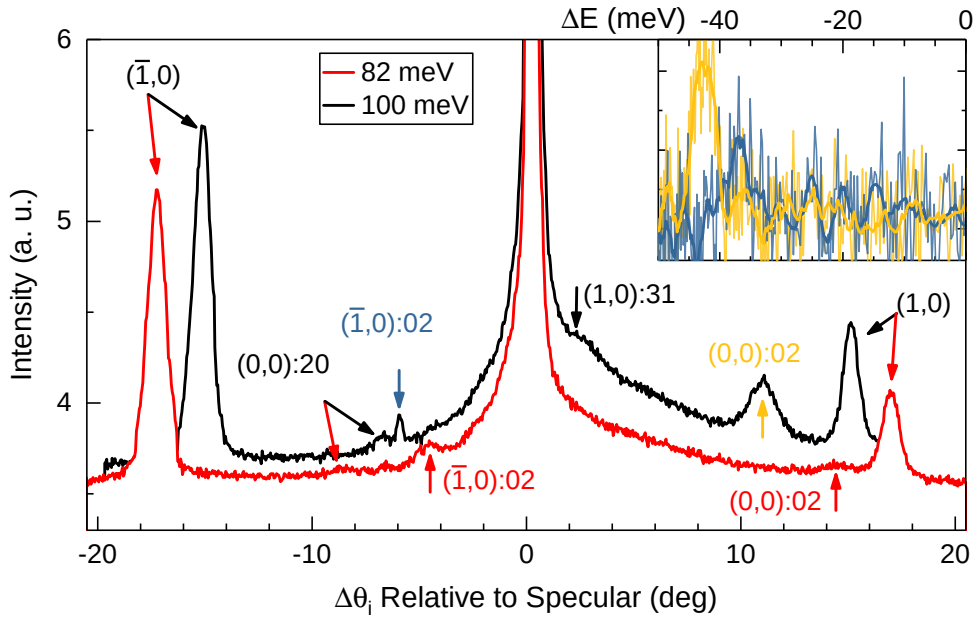

Figure 2.8: Angular diffraction of H_2 scattering from Gr/Ni(111) using two different E_i values. RID peak names are indicated. The inset shows two TOF spectra collected using $E_i = 100$ meV at angles indicated with arrows of the same color.

The blue spectrum at $(\bar{1}, 0)$ of the $j = 0 \rightleftharpoons 2$ transition shows a maximum at -37.2 meV and the peak position is shifted $-0.4°$ from the calculated position. Although a TOF spectrum (not shown) measured at this peak position $(\bar{1}, 0) : 02$ using 82 meV gave a correct energy transition -42.19 meV. These measurements are useful indication that the old calibration of the apparatus parameters does not need new adjustments.

New LabVIEW Software

Almost halfway in the work of this thesis, the computer used in measurement control and data acquisition crashed, as a result a new LabVIEW software had to be built since the older version was built using LabVIEW 7.0 which is not supported anymore and did not run on new PCs with MS Windows 7 or later. This was an opportunity to build a modern measurement program that utilizes new features in LabVIEW 14.0, several bugs and limitations of the older version were solved and new features were added, like new modules to automate the

measurements and to perform diffuse-elastic diffraction measurements where each point in a diffraction spectrum is a TOF measurement and the time window is limited to the diffuse-elastic peak width. Sample heating is also automated and a new angular encoder to read the polar angle of the sample has been installed and connected via an arduino interface to the PC. This encoder has a rotational resolution of 0.018°.

Part II

Results

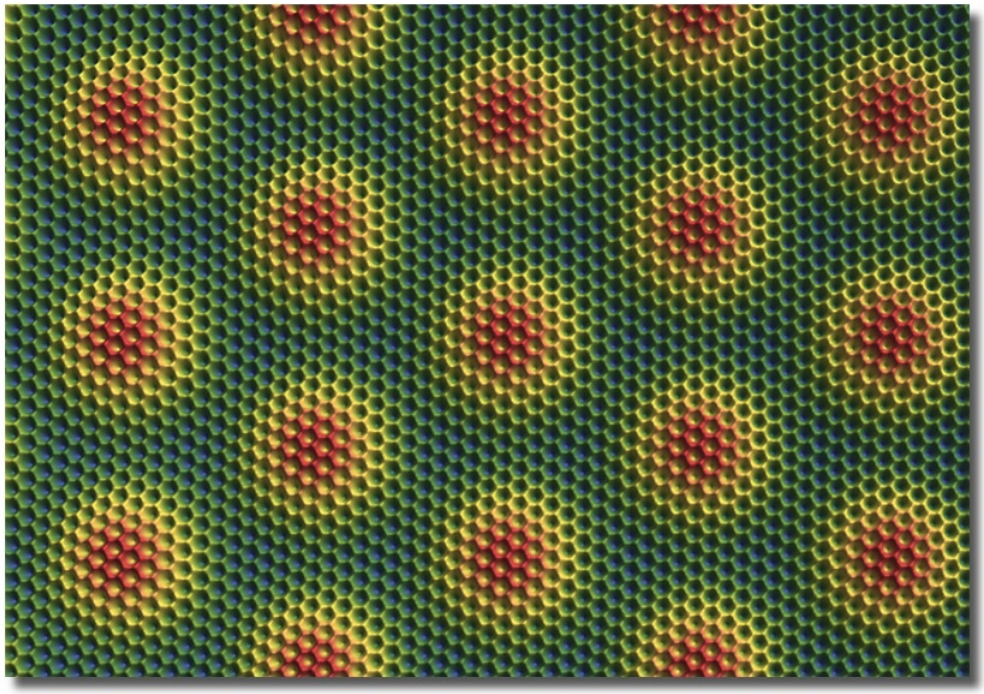

The experimental results of this study are divided on three chapters. The first chapter (Chapter 3) presents elastic HAS measurements with analysis of the surface structures of Gr/Cu(111), Gr/Ni(111) and Gr/Ir(111). Inelastic scattering is discussed in the following chapter (Chapter 4) first a comparative analysis of the Debye-Waller factor of the studied surfaces is presented then surface acoustic-phonon measurements are discussed for each surface. Chapter 5 addresses angle and energy resolved Ne scattering measurements from Ni(111) followed by diffraction from Gr/Ni(111) and Gr/Ir(111). Finally, Chapter 6 is a summary of the conclusions of the previous chapters.

Chapter 3

Surface Structure from Elastic Scattering

The main objective of this work is to study different Graphene passivated surfaces and how they affect the scattered He beam. The following chapters will address the structure of three surfaces, namely Gr/Cu(111), Gr/Ni(111) and Gr/Ir(111). The first two are model cases for weak and strong interaction, respectively, of graphene with its metallic substrate with small or no lattice mismatch, allowing graphene growth without an additional superstructure. It would be useful to contrast the two systems to get an insight on how the bond strength will affect the scattered He beam.

Gr/Ir(111), on the other hand, is of special interest since it can be compared with Gr/Ru(0001), which was characterized by D. Maccariello in his PhD thesis [119]. These two surfaces exhibit a moiré superstructure due to a large lattice mismatch between Gr and the substrates. However, the nature of Gr-interaction with Ru(0001) and Ir(111) is different, the former is an example of strong interaction and the latter is an example of weak interaction. Comparing Gr/Ir(111) with Gr/Cu(111) would show how two systems with weak interaction might be different due to a lattice mismatch.

A systematic comparison of these surfaces can be useful in understanding different aspects of the Gr-metal interface. The first section will describe diffraction measurements of He from Gr/Cu(111) surface which is the closest example we can find to free standing Gr. The second section will be a similar analysis of the Gr/Ni(111) surface. And in the final section, He diffraction measurements from Gr/Ir(111) are presented, it is a return to weak interaction

where the moiré superstructure is the main difference from Gr/Cu(111).

3.1 Gr/Cu(111)

Graphene grown by chemical vapor deposition (CVD) has triggered interest for its promising industrial scalability due to the weak interaction that allows roll-to-roll transfer. However, producing mm- to cm-size samples in industrially useful amounts remains a challenge. Graphene grown by chemical vapor deposition (CVD) on copper foils is a potential solution, especially with the relatively low cost of the growth catalyst [120, 121, 122].

We have tested several samples of Gr on a copper foil from Graphenea. The samples were of very good quality when analyzed by the manufacturer using Raman spectroscopy. However, when investigated using HAS in our laboratory they did not produce any detectable He reflectivity. We tried then Gr/Cu(111) samples that were prepared using a new CVD graphene method developed by H. Yu in the group of A. Wodtke at the Max Planck Institute for Biophysical Chemistry in Göttingen. The development in this method is actually in the preparation of the copper catalyst which resulted in exclusively (111) orientation, discussed below in details. Graphene grown on this catalyst was characterized by H. K. Yu et al [123]. Domains as large as 100 µm were obtained when characterized with polarized optical microscopy, this is 2 orders of magnitude larger than that obtained from a normal copper foil. The charge carrier mobility of peeled-off graphene was found to be as high as 29 000 $cm^2\ V^{-1}\ s^{-1}$ in comparison to 1500 to 10 000 $cm^2\ V^{-1}\ s^{-1}$ for reference graphene. These features were interpreted as a result of a higher degree of order and reduced impurity doping in graphene prepared using the new method. This sample is nicknamed *super G* and it will be referred to by this name in the rest of the text to distinguish it from Gr/Cu(111)/Al_2O_3 which was also prepared by the Wodtke group and is characterized in the following sections together with *super G*.

3.1.1 Preparation: High Pressure CVD

Samples used in this study were prepared in Göttingen and then transported by courier to Madrid for HAS experiments. As a result the samples were exposed to air for several days (up to one week) before being introduced in

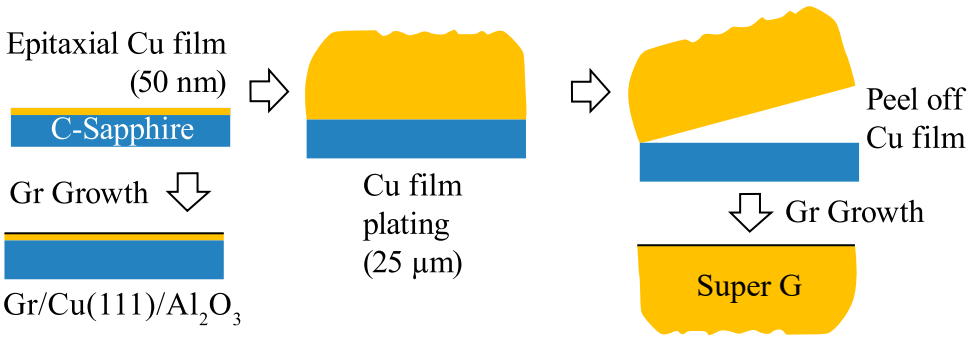

Figure 3.1: Scheme of the preparation of the two Gr/Cu(111) surfaces. Adapted with permission from [123]. ©(2014) American Chemical Society.

the UHV chamber. In the following section, a comparative study is presented of two graphene surfaces made by CVD on two differently prepared Cu films as shown in Fig. 3.1. In the first one, an epitaxial Cu(111) film (500 nm) was grown on C-plane sapphire using electron beam evaporation method (0.3 nm/sec) followed by Gr growth to get Gr/Cu(111)/Al_2O_3. The second, *super G*, was obtained by additional Cu electroplating then it was peeled-off from the sapphire substrate, as reported in Ref. [123].

The graphene growth process was different for the two Cu samples used here. The same growth procedure reported in Ref. [123] was used for the *super G* sample used in this work. However, the temperature should be lower than 1000 °C to make a flat graphene on epitaxial Cu(111)/Al_2O_3 samples. Otherwise, due to Cu evaporation and migration, the surface morphology of the Cu film was found to be too rough for HAS. Cu migration and evaporation can be reduced at 850 °C, but this leads to reduction of carbon solubility as well, resulting in small size of graphene. As a result, a compromise was found by preparing the graphene at 850 °C by CVD and doing additional C_2H_4 annealing in UHV to get a high HAS signal. This process is explained below in details.

A typical growth process of Gr/Cu(111)/Al_2O_3 is as follows: First, the pressure in the growth chamber is pumped down to 3 Torr using a mechanical pump; second, a 40 sccm flow of hydrogen gas is introduced into the chamber at 950 mTorr; third, the sample was heated to 850 °C over 50 min; fourth, 6 sccm flow of methane gas with 20 sccm hydrogen is introduced into the chamber for

3 min with a total pressure of 460 mTorr for graphene synthesis; after growth, the furnace was cooled down rapidly to room temperature under a 20 sccm flow of hydrogen.

Samples were then shipped from Göttingen to Madrid and mounted in the scattering chamber for He diffraction after exposure to ambient conditions for several days. Several samples were used in this study. The as-mounted samples presented a very low He-specular reflectivity, which could be improved after degassing the sample by heating to 540 K, presumably due to desorption of contaminants adsorbed on the surface (Dark brown curve in Fig. 3.2). Further heating to 650 K led to a strong decrease of the specular signal to 26% of its initial value (red curve in the inset in Fig. 3.2). This means that the surface quality deteriorates when heating above 650 K. Recently it has been reported that Cu_2O is formed at the Gr/Cu(111) interface during transportation under ambient conditions and that it disappears when heating above ca. 650 K [124]. This is consistent with our observation of a pressure increase when heating the sample to 650 K, which might be due to oxygen desorption. The significant decrease of He specular signal indicates that the density of defects on the graphene layer has increased through the heating process. The most likely interpretation is that disappearance of the Cu_2O layer induces etching of the graphene layer.

This degradation of the surface quality can be avoided by a healing process where the sample is heated in the presence of a pressure of C_2H_4 until the oxygen is completely desorbed. Fig. 3.2 shows several angular distributions of He atoms scattered from Gr/Cu(111)/Al_2O_3. Little or no HAS signal was observed from the as-mounted samples (not shown). However after degassing the sample by a brief heating to 540 K, the dark brown curve is obtained. Subsequent heating to 800 K with 2×10^{-7} mbar of C_2H_4 led to further improvement in HAS (brown). Further heating cycles to 860 K in the absence of C_2H_4 led to additional improvement of the surface quality (light brown curve). The increased specular intensity is accompanied by the appearance of the first order (10) and ($\bar{1}$0) diffraction peaks. The position of these peaks allows us to derive the lattice constant, $a = (2.44 \pm 0.02)$ Å, which agrees well with the value 2.46 Å, the periodicity of a single carbon layer in graphite [125, 126].

These observations show through the increase of specular reflectivity and the appearance of graphene diffraction peaks that the heating cycles improve the long-range order and through the increased specular intensity reduce the defect density resulting from, for example adsorbates or domain boundaries.

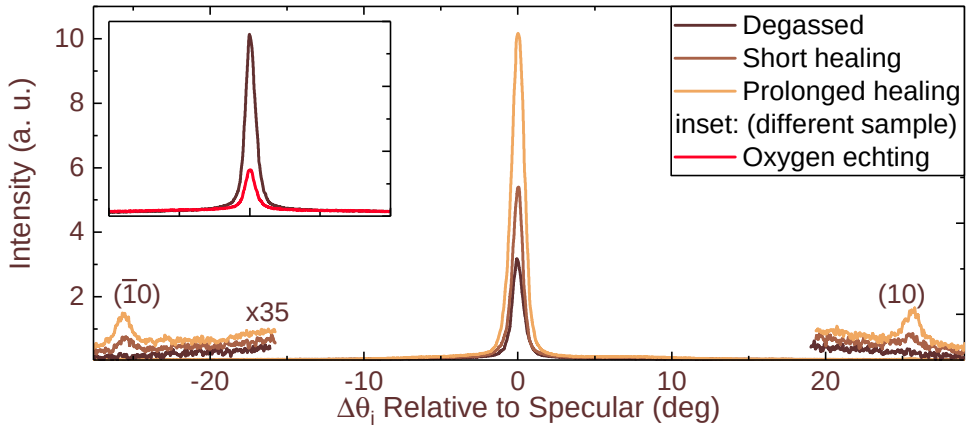

Figure 3.2: Graphene healing process monitored by He diffraction. (Dark brown) soft degasification of the surface (540 K), (brown) first healing cycle with C_2H_4 (800 K at 2×10^{-7} mbar), (light brown) after several healing cycles at 860 K. Inset: (different sample) Dark brown is the same as before, red shows degradation after oxygen desorption (650 K).

The short healing step (Fig. 3.2) can be a result of compensating the etched-away carbon atoms during oxygen desorption by carbon atoms from C_2H_4. The prolonged healing process, on the other hand, might be due to reordering of the copper substrate since graphene is expected to be stable at this temperature.

This healing process was needed only for Gr/Cu(111)/Al_2O_3 surface. Heating the *super G* in UHV to 650 K was not accompanied by an increase in pressure as has been the case for Gr/Cu(111)/Al_2O_3 and did not decrease the intensity of the reflected He beam. Furthermore, prolonged heating with or without C_2H_4 did not have an effect on the measured diffraction patterns. Thus, an as-mounted *super G* needed only one flash to 700 K to completely remove all adsorbates on the surface to obtain maximum reflectivity from the surface. This proves the effect that graphene has in protecting metallic surfaces from oxidation, although this protection is disrupted by the presence of defects in the graphene layer.

The higher thermal stability of the several µm thick copper catalyst in *super G* compared to the thin (100 nm) copper film used in the epitaxial Cu/Al_2O_3 is a key factor in the quality of the graphene layer.

3.1.2 Structure: A Comparison of Two Preparation Methods

We investigated the crystallinity of the Gr/Cu(111)/Al_2O_3 sample by recording He-diffraction angular distributions for different azimuthal orientations - Fig. 3.3 (left). Angular distributions were measured for different azimuthal rotations, the inset at the right side of the panel is a diagram of the reciprocal lattice with lines indicating by color the azimuthal orientation of the sample for each curve. The dark brown curve (denoted 0°R) shows HAS diffraction when the sample is oriented to the $[\bar{2}11]$ symmetry direction of the Cu(111) substrate, as determined independently by LEED (left inset). Here, we observe the strongest diffraction signals, denoted (10) and $(\bar{1}0)$. As before, the diffraction features yield a lattice constant that unambiguously belongs to graphene. The brown curve was obtained for a sample azimuthally rotated by 30°. It exhibits weaker but still clear diffraction peaks that belong to graphene domains rotated 30° (denoted as 30°R). For all azimuthal orientations recorded between these two main symmetry directions the angular distributions were similar to the light brown curve, where only traces of diffraction peaks are seen. The LEED image in the inset of Fig. 3.3 shows a similar diffraction pattern where intense point correspond to the 0°R domain, less intense points correspond to the 30°R domain and low intensity ring at the same diffraction position is visible. These results show that two rotational domains are present for Gr/Cu(111)/Al_2O_3, whereas only a single rotational domain is present for *super G* as seen be HAS and LEED. *super G* also exhibits a much narrower specular scattering peak.

These observations give simple and valuable information about the orientation domains in this sample over a 1 mm^2 area. Specifically, it shows the Gr/Cu(111)/Al_2O_3 sample is dominated by two orientation domains - 0°R and 30°R - which are themselves oriented with respect to the Cu(111) substrate - that is, for the 0°R domain the $[11\bar{2}0]$ symmetry direction of the graphene layer is parallel to the $[\bar{2}11]$ direction of the Cu(111) lattice, or, the $\overline{\Gamma M}$ high symmetry direction of both lattices are aligned. The relative abundance of these two domains can also be determined (~85% 0°R and ~15% 30°R) since the intensity of the first order diffraction peaks is proportional to the domain's population in the 1 mm^2 area probed by the He beam.

Diffraction measurements of He from *super G*, as in the right panel in Fig. 3.3, show basically two differences from Gr/Cu(111)/Al_2O_3. Firstly, He diffraction peaks were observed only for azimuthal orientation along the $\overline{\Gamma M}$

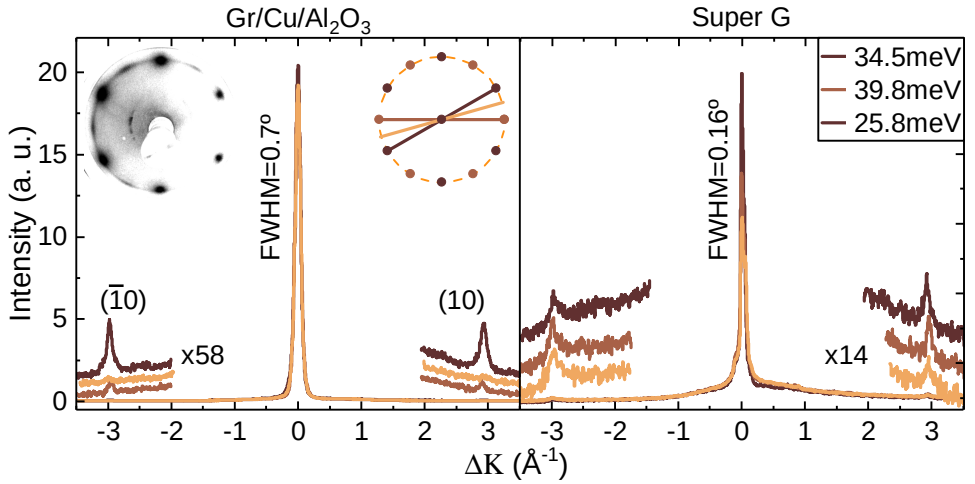

Figure 3.3: Comparison of He atom scattering from two Gr/Cu(111) samples. (LEFT) Gr/Cu(111)/Al_2O_3: Diffraction is seen mainly for two azimuthal orientations (brown and dark brown). Between these azimuthal angles diffraction is undetectable (light brown). E_i = 21.5 meV. The corresponding directions on the reciprocal lattice are schematically shown in the right inset and a LEED image of this sample is shown in the left inset. (RIGHT) *super G*: Diffraction is observed for a single azimuthal orientation, diffraction spectra using different beam energies are shown, energies indicated in legend. Specular peak width for each sample is indicated.

symmetry direction of the epitaxial Cu(111) foil (as determined by LEED), which means that 0°R graphene rotational domains are produced exclusively by this CVD technique. Secondly, the width of the specular peak in diffraction spectra from *super G* is much smaller than in those from Gr/Cu(111)/Al_2O_3.

The angular width of the specular peak is related directly to the average domain size in the surface area probed by the He beam also known as the *coherence length* [117]. A Gaussian fit to the specular peaks in Fig. 3.3 gives FWHM = 0.16° for *super G* and FWHM = 0.7° for Gr/Cu(111)/Al_2O_3. Using Eq.(2.8) we obtain a lateral domain size l_c = 390 and 89 Å, respectively. This gives approximately a domain size of 1500 nm^2 and 80 nm^2, respectively.

It is worth mentioning that recent studies on the effect of defects on the tensile strength of graphene have shown that rotational domains with large-angle boundaries are stronger and more favorable in graphene growth compared to low-angle boundaries as they allow a better accommodation of the heptagon-

pentagon defects reducing the stress on the C-C bonds in the grain-boundaries [127]. This can explain why 30°R rotational domains are more abundant than other orientations.

3.1.3 Surface Thermal Expansion

HAS provides a method for investigating the interactions of graphene with the copper substrate by measuring the thermal expansion of the surface. Fig. 3.4 (left) shows angular diffraction spectra of He from Gr/Cu(111)/Al_2O_3 at different sample temperatures from 100 to 500 K.

The sample temperature was stabilized for each measurement within ±2 K. The diffraction peaks of graphene were detected only up to 500 K, due to the strong attenuation caused by the Debye-Waller effect. The dependence of the diffraction angles on the lattice constant given by Bragg condition yields that a change in the lattice constant from 2.440 Å to 2.445 Å should produce a change in the diffraction angle from 24.80° to 24.75°, which should be clearly detectable with our setup. The derived graphene lattice constants are plotted in Fig. 3.4 (right) over this temperature range, together with the calculated temperature dependent lattice constant of Cu(111) [128]. Within experimental

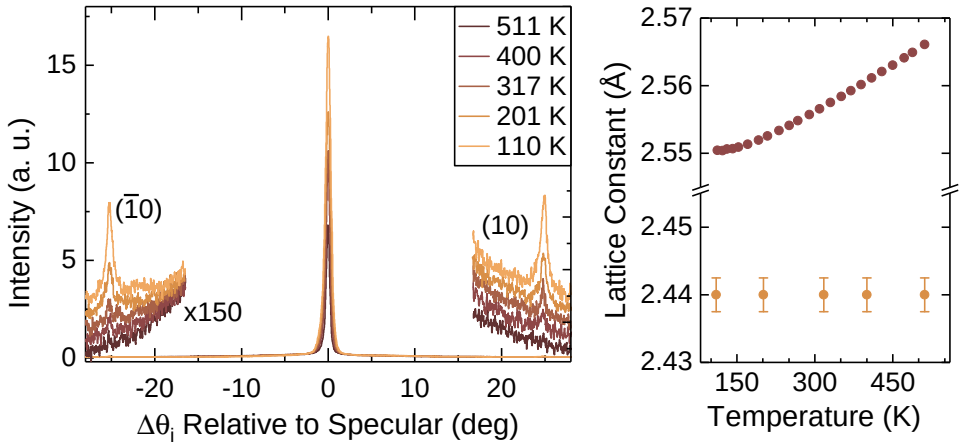

Figure 3.4: (a) Temperature dependence of diffraction from Gr/Cu(111)/Al_2O_3 (E_i = 18 meV). The graphene lattice constant derived from this data is plotted in panel (b) together with the expected variation of the Cu lattice constant in the same temperature range.

error (0.005 Å), the derived graphene lattice constants are temperature independent, a result that is in quantitative agreement with calculations for free standing graphene [129]. The observation of a temperature independent graphene lattice constant in contact with a thermally expanding copper substrate is an evidence of the weak interactions between copper and graphene.

3.2 Gr/Ni(111)

Gr/Ni(111) is an especially interesting system due to the strong Gr-Ni interaction and the small lattice mismatch between Gr and Ni(111). These two factors result in an epitaxial (1×1) graphene layer with a single well-defined rotational orientation. Although, using elevated preparation temperatures can result in multiple rotations [130]. The strong interaction of Gr with Ni results in opening a band gap in the electronic structure and modifies the phonon dispersion which suppresses the graphene Raman signal [63].

3.2.1 Preparation: Low Temperature CVD

The Ni(111) simple crystal used in this study is a disk with a diameter of 8 mm and a thickness of 2 mm. The crystal was mounted on a sample holder which can be heated by electronic bombardment or cooled to 100 K using liquid nitrogen. Sample temperature was measured with a K-type thermocouple spot welded to the sample edge.

Clean Ni(111) surface is prepared in UHV by repeated cycles of ion sputtering (1.5 KeV $P_{Ar} \simeq 1 \times 10^{-5}$ mbar) and flash-annealing at ca 1400 K. Graphene is prepared after the final annealing, where the sample is cooled down to 750 K and maintained there during exposure to C_2H_4 at a pressure $P_{C_2H_4} = 5 \times 10^{-7}$ mbar for 20 minutes. The inertness of the Gr/Ni(111) surface was checked by monitoring the specular He–intensity while exposing the sample to oxygen. Furthermore, graphene-passivated samples exhibited a constant He–reflectivity, even one week in UHV after sample preparation. Fig. 3.5 shows a comparison of He reflectivity of Ni(111) (blue) and Gr/Ni(111) (black) after introducing water at a pressure 4×10^{-7} mbar whit the samples at room temperature. Due to its high scattering cross-section from defects on the surface, the He intensity drops quickly from water adsorbed on the Ni(111) surface, while it remains constant for Gr/Ni(111).

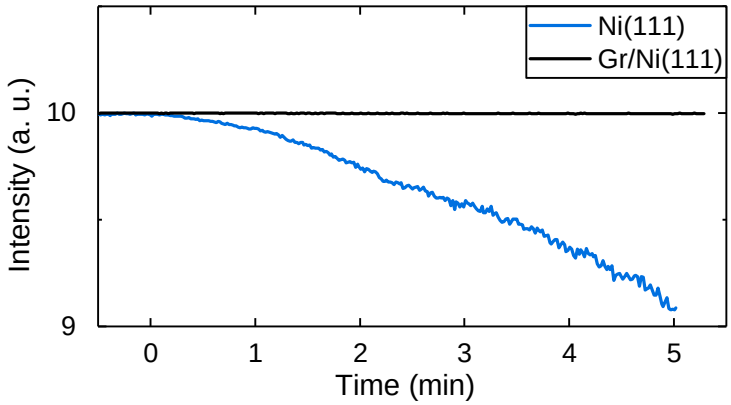

Figure 3.5: Effect of water exposure (4×10^{-7} mbar) on He reflectivity from Ni(111) (blue) and Gr/Ni(111) (black) with samples at room temperature.

3.2.2 Structure: Epitaxial Graphene

Figure 3.6 shows a comparison of He Angular Distributions from clean Ni(111) and Gr/Ni(111) samples, measured at the same incident beam energy E_i = 66 meV along the $\overline{\Gamma M}$ direction. Sharp diffraction peaks and high specular intensity are indications of the existence of a well-ordered Ni(111) surface and the excellent quality of the graphene monolayer. First order ($\bar{1}0$) and (10) diffraction peaks are clearly visible for both surfaces; their appearance at the same angular position for both systems confirms the formation of a (1×1) graphene layer. These peaks are one order of magnitude more intense in the case of Gr/Ni(111), indicating a higher surface corrugation. The relative-to-specular intensity of the first order diffraction peaks I_{01}/I_{00} is 1.4% for Gr/Ni(111) and 0.02% for bare Ni(111). Fitting these values using eikonal approximation gives the corrugation values 0.07 Å and 0.009 Å for Gr/Ni(111) and Ni(111), respectively. These corrugations agree well with the recently published 0.06 Å and 0.005 Å for Gr/Ni(111) and Ni(111), respectively [131]. The measured surface corrugation by HAS follows a surface of constant total electron density at the classical turning point of the He atoms [5] which, in turn, is a function of the He kinetic energy [132]. In other words, He atoms with higher energies can take a closer look at the surface where the charge density is more corrugated. The degree to which such an effect can take place depends on the stiffness of the repulsive part of the He-surface potential. A very stiff potential (hard wall) will repel the He atoms with different energies

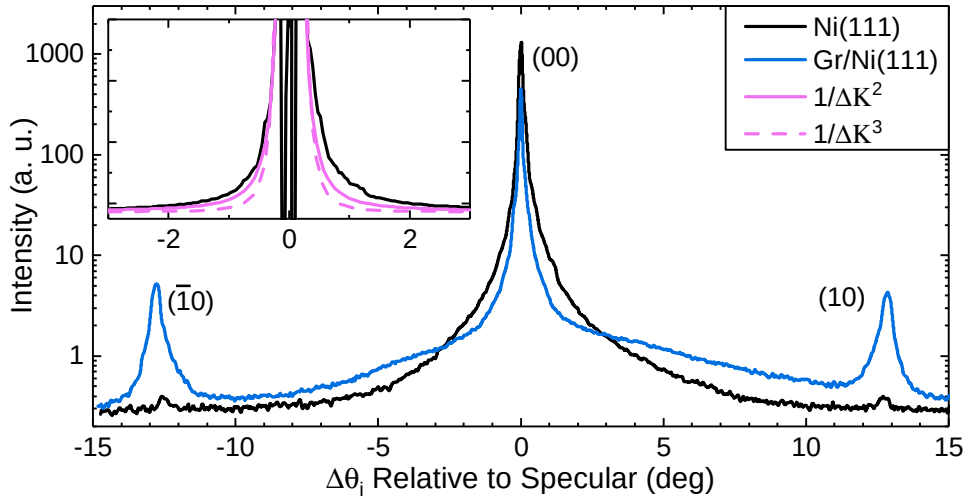

Figure 3.6: Angular distribution of He scattering from Ni(111) (black) and Gr/Ni(111) (blue) along the $\overline{\Gamma M}$ direction. The inset shows the residual of a Gaussian fit of the Ni(111) spectrum (black) compared with two form factors $1/\Delta K^2$ and $1/\Delta K^3$ (solid and dashed magenta, respectively). $E_i = 66\,\text{meV}, T_S = 100\,\text{K}$.

at the same distance from the surface, while for a soft potential a He atom with high energy can approach the surface closer than an atom with low energy. This can explain the slightly smaller corrugation values obtained using a He beam with energy 8 meV in Ref. [131] compared to our data using 66 meV.

The angular position of the diffraction peaks corresponds to a lattice constant $a = (2.48 \pm 0.02)$ Å for Gr/Ni(111). This means that graphene is stretched by ca. 1.6% compared to the value (2.44 ± 0.02) Å obtained also by HAS for Gr/Cu(111) [73] and by 0.8% compared to the periodicity of a single carbon layer in graphite measured by X-ray diffraction 2.46 Å [125, 35]. The specular reflectivity of Gr/Ni(111) compared to the intensity of the directly measured incident He-beam is $I/I_0 = 20\%$ at $T_S = 100\,\text{K}$, $E_i = 28\,\text{meV}$ and $\theta_i = 60°$, whereas, at the same conditions, the bare Ni(111) reflectivity is 40%.

A quite remarkable result from the comparison of the spectra in Fig. 3.6 is the observation of a sharper specular peak for the graphene-covered substrate. By performing Gaussian fits to the specular peaks, we obtained peak widths FWHM = 0.13° for Ni(111) and FWHM = 0.08° for Gr/Ni(111). The latter is actually below to the angular resolution of the instrument, since the diffraction pattern is obtained while rotating the sample in steps of 0.04°. This low angular

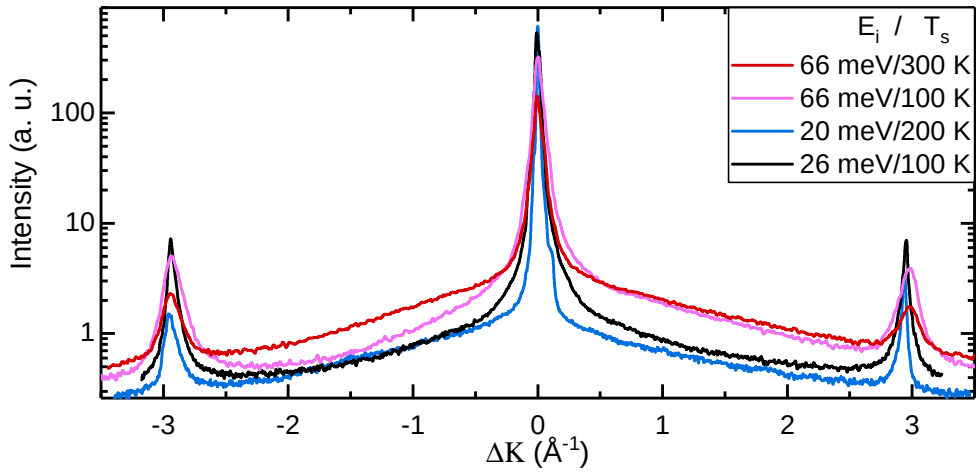

Figure 3.7: Angular distributions of He scattering from Gr/Ni(111) for different beam energies and surface temperatures.

width of the specular peak is a result of the extremely high surface quality of the sample where the graphene sheet softens the step edges of the substrate. The reduced FWHM value obtained for Gr/Ni(111) can be further understood by investigating the different shapes of the background measured from the two samples. The form of the background is determined by inelastic single- and multi-phonon scattering as well as diffuse elastic scattering by defects on the surface. If the diffuse elastic contribution is due to point defects we would expect to see a decay consistent with a $1/\Delta K^3$ envelope, as opposed to a $1/\Delta K^2$ envelope expected for step edges normal to the sagittal scattering plane [88].

The inset in Fig. 3.6 shows the residual of a Gaussian fit of Ni(111) specular peak (in black) and two form factors (in magenta), solid and dashed curves corresponding to $1/\Delta K^2$ and $1/\Delta K^3$, respectively. The $1/\Delta K^2$ curve gives a better fit of the fit residual, indicating the importance of scattering from step edges in the broadening of the specular peak. On the other hand, the background of Gr/Ni(111) does not fit any of these forms but rather has a shifted Gaussian shape, which is well explained by inelastic multi-phonon scattering. To better illustrate this effect, we compare in Fig. 3.7 different angular diffraction spectra from Gr/Ni(111) measured at different experimental conditions (E_i and T_S). When helium atoms with a high incident energy ("hot particles") hit a "cold surface" as in the magenta spectrum, they lose energy on average and thus the background is higher on the energy loss side which is the

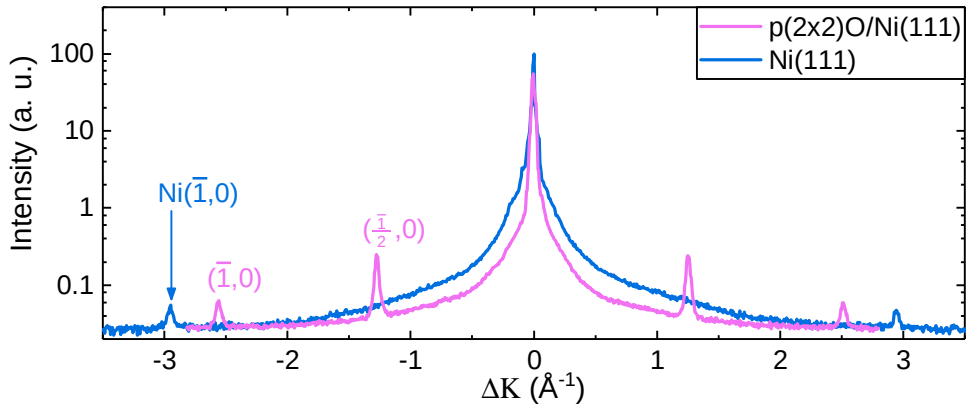

Figure 3.8: He diffraction spectra from (120 K) Ni(111) and p(2 × 2)O/Ni(111) with E_i = 34 and 22 meV, respectively, show that relaxation of Ni(111) surface due to oxidation.

phonon creation direction ($\Delta K = k_i(\sin(\theta_f) - \sin(\theta_i)) > 0$). Contrarily, when cold particles hit a hot surface (blue spectrum) they gain energy on average and the background is shifted to $\Delta K < 0$. Otherwise, cold particles hitting a cold surface and hot particles hitting a hot surface (black and red spectra) lose and gain energy with similar probabilities and the background is more symmetric relative to the specular peak [133, 98]. This also can be noticed in the small asymmetry of the background of the clean Ni(111) spectrum shown in Fig. 3.6.

In conclusion, the graphene layer on Ni(111) reduces elastic scattering from step edges, while the lower surface mass results in increasing the inelastic scattering through the Debye-Waller factor.

Earlier studies using high-energy He^+-ion scattering [134] reported a 0.15 Å expansion of the first layer of Ni(111) due to oxidation. Later, near-edge X-ray-absorption studies confirmed this value [135] while LEED measurements obtained a much lower value (< 0.07 Å) [136, 137]. HAS measurements (Fig. 3.8) point to a larger value of the Ni(111) surface expansion. The diffraction peak of the Ni(111) spectrum (blue) at 2.915 $Å^{-1}$ corresponds to a periodicity 2.49 Å as expected for Ni(111) surface. Two diffraction peaks are detected in the p(2 × 2)O/Ni(111) spectrum (magenta) at 1.28 $Å^{-1}$ and 2.56 $Å^{-1}$. These are the 1^{st} and 2^{nd} order diffraction peaks from a periodicity 5.68 Å, which is an expansion of 0.35 Å (14%) over the original Ni(111) surface

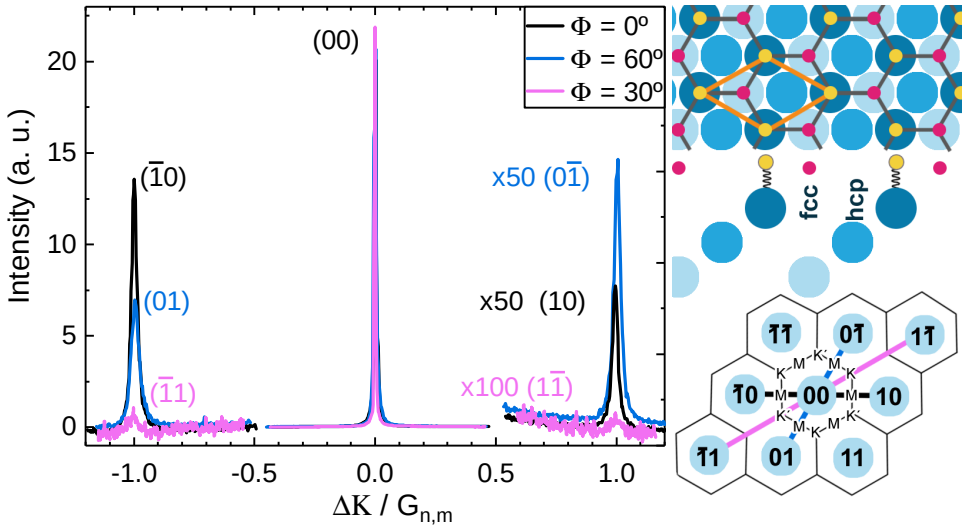

Figure 3.9: (Left) Angular diffraction from Gr/Ni(111) with three different azimuthal angles indicated in the legend. (right) Top and side view of real and reciprocal lattice structure of Gr/Ni(111). Red and yellow circles correspond to the inequivalent carbon atoms of the two sublattices. The equal unit cell of Gr and Ni(111) is lined in orange. The reciprocal lattice of the surface is shown on the right with lattice notations. Colored lines indicate the direction of the diffraction spectra. Black and blue spectra are taken along $\overline{\Gamma M}$ direction by rotating the sample 60° and magenta is along $\overline{\Gamma K}$ direction. Parts of the spectra showing the diffraction peaks are amplified 50 times for $\overline{\Gamma M}$ spectra and 100 times for $\overline{\Gamma K}$ spectrum.

periodicity. The intensities of the peaks also indicate a small corrugation, this might be a result of low coverage, as earlier reports indicated a coverage of $\frac{1}{4}$ layer for p(2 × 2)O/Ni(111) [134]. The faster decay of the background on p(2 × 2)O/Ni(111) compared to Ni(111) indicates the importance of point defects, like oxygen vacancies, rather than edge defects.

Graphene grows on Ni(111) epitaxially creating a (1 × 1) structure [138]. According to several experimental and theoretical works [63], the preferred arrangement of the graphene layer is when one C atom sits on top of a Ni atom, and a second C atom occupies a three-fold fcc hollow site. These two inequivalent C atoms have a different distance from the 1^{st} Ni-layer Δd = 0.05 Å [138]. DFT calculations for the Gr-Ni(111) bonding showed that there is an electron transfer of ~ 0.14 electrons per unit cell from Ni(111) to graphene and that only the C atoms located directly above surface Ni atoms accumulate

electrons [139]. This indicates that the two C atoms in the graphene unit cell are not only topologically inequivalent, they also have different electronic densities in their vicinities.

Although the fcc(111) surface and graphene both have six–fold symmetry, the different positioning and interaction of the C atoms with the Ni atoms results in a triangular rather than hexagonal surface and the overall symmetry is reduced from C_6 to C_3 [140]. However, in principle it is not clear if this small asymmetry could be detected by HAS, as the He atoms are scattered by the surface electrons where their density is of the order of 10^{-4} a.u. about 3 Å far from the topmost ion cores [5].

Fig. 3.9 shows diffraction measurements from Gr/Ni(111) with different azimuthal orientations of the sample. Azimuthal orientation of the sample for each diffraction spectrum is indicated by lines of the same color in the inset which shows a scheme of the lattice in reciprocal space, names of the diffraction points are indicated. Three lines corresponding to two nonequivalent $\overline{\Gamma M}$ directions (black and blue) and one $\overline{\Gamma K}$ direction. The different intensities observed for the first order diffraction peaks in each spectrum prove that, even at the low densities sampled by He atoms, the Gr/Ni(111) surface exhibits a three–fold symmetry. This asymmetry in the measurements is not a result of bad azimuthal alignment of the Ni(111) crystal, as could sometime be the case. In fact, for each spectrum shown in Fig. 3.9 the azimuthal orientation has been adjusted to maximize the diffraction peak with the lowest intensity even though this resulted in lowering the intensity of the other diffraction peak. Finally, the second order diffraction peaks $(\bar{1}1)$ and $(1\bar{1})$ are detected in the magenta spectrum in Fig. 3.9 measured along $\overline{\Gamma K}$, this confirms the larger corrugation of Gr/Ni(111) as compared to clean Ni(111) as well as the good quality of its long range crystalline order.

In conclusion: one cannot just dismiss the asymmetry of diffraction peaks as a result of incorrect azimuthal adjustment. In the case of Gr/Ni(111) this asymmetry is real and reveals the existence of 3-fold surface symmetry (instead of 6-fold), this symmetry is important in modeling the surface in close-coupling calculations for example.

3.2.3 Thermal Expansion: Substrate Effect

Figure 3.10 shows diffraction spectra of He from Gr/Ni(111) with beam energy 21.5 meV and increasing surface temperatures from 150 to 650 K. The chang-

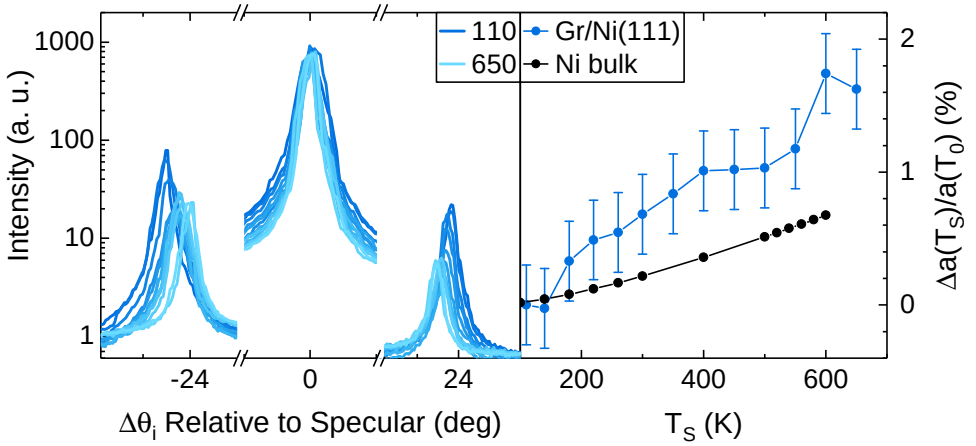

Figure 3.10: Thermal expansion of Gr/Ni(111). (left) Diffraction spectra and (right) measured change in surface periodicity of Gr/Ni(111) compared to bulk nickel [141]

ing position of the diffraction peaks indicate a change in surface periodicity. The intensities of diffraction peaks of the Ni(111) surface are too low and disappear quickly with sample heating as expected from Debye-Waller model, thus it was not possible to compare with HAS measurements from this surface, other experimental measurements or theoretical calculations of the expansion of Ni(111) surface were not available, therefore, we compared our data to bulk nickel from [141].

Our measurements of the thermal expansion of Gr/Cu(111) showed no surface expansion in this range of temperatures (see Fig. 3.4). We can assume from the data in Fig. 3.10 that the graphene layer expands with the expansion of the Ni(111) surface, as expected from the strong Gr-Ni interaction.

3.2.4 Structure Modification by Point Defects

Graphene is expected to play important diverse roles in modern electronics, among which it will be useful in protecting metal surfaces from oxidation and corrosion [63, 142, 143, 144]. However, several studies have shown that defects are reactive sites in the graphene layer [61, 145, 146]. Defects also affect the mechanical properties of graphene such as its stiffness and thermal and electrical conductivity [54, 56, 127, 147, 148]. Controlled defect creation in graphene can be achieved by Ar^+ sputtering [147, 149]. Recent theoretical

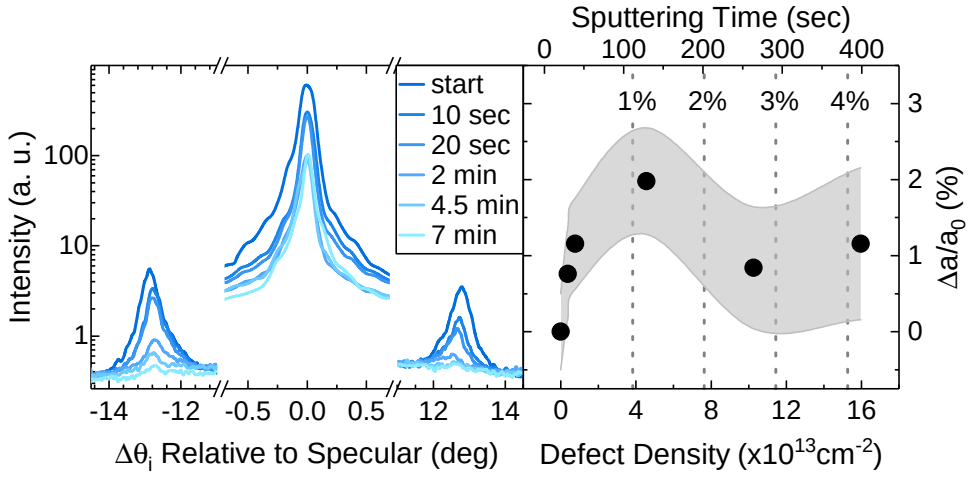

Figure 3.11: (left) Angular diffractions of He scattered from Gr/Ni(111) surface as prepared (start) and after consequent cycles of Ar^+ sputtering and annealing at 600 K. (right) Change in lattice constant as a result of defect creation (black dots), gray area envelopes the estimated error in reading the position of the diffraction peaks. Dotted gray lines indicate the density of defects as a percentage of one Gr monolayer.

studies have shown that increasing defect concentration in graphene causes the graphene layer to expand which caused a free standing layer to create out-of-plane wrinkles [148] or buckle due to compressive lateral stress [150]. No studies were made on supported or epitaxial graphene and experimental evidence of this effect is not available.

We have introduced defects on the Gr/Ni(111) surface by several (consequent) cycles of Ar^+ sputtering ($P_{Ar} = 9 \times 10^{-6}$ mbar, $E = 120$ eV) and annealing for 2 minutes at 600 K. Fig.3.11 shows diffraction measurements of Gr/Ni(111) before and after introducing point defects in the graphene layer, total sputtering times are indicated in the legend. As expected, the intensity of the specular and diffraction peaks decreased dramatically (by almost 80%) after 7 minutes of sputtering and the diffraction peaks became undetectable.

The density of defects can be estimated according to Ref. [147] from the current of Ar^+ which yields the rate of ionic bombardment on the total surface of sample and holder. The total surface of Ni(111) sample and its holder is ($4 \times 3 - 0.5 = 11.5\,cm^2$), and sputtering current was 7×10^{-7} A. This gives an ion flux $3.8 \times 10^{11}\ s^{-1}\,cm^{-2}$. The density of atoms in a Gr surface

(3.82×10^{15} cm^{-2}) can be derived from the lattice constant which also gives a $\rho_{2D} = 7.6 \times 10^{-8}$ g cm^{-2}. Assuming that each argon ion removes one carbon atom upon impact, the density of defects can be related directly to the sputtering time.

The width of the specular peak is not affected by point defects since it is mainly affected by the average domain size which did not change with point defects. What is surprising in the angular diffraction measurements in the left panel of Fig. 3.11 is the inward drift in the position of the diffraction peaks which corresponds an increase in the surface lattice constant as shown in the right panel. We can clearly see that a defect concentration of only 4×10^{13} cm^{-1} (1% ML) causes the graphene layer to expand by 1%. This can be understood as a relaxation of the graphene layer where the defects allow it to better accommodate the lattice of Ni(111).

3.3 Gr/Ir(111)

Graphene lattice is incommensurate with that of Ir(111) due to the large lattice constant difference: 2.45 and 2.715 Å, respectively. Therefore, a moiré superstructure appears on the surface with a periodicity of 25.2 Å and a corrugation of $\sim$ 0.3 Å as measured by STM [151, 152]. The electronic π-band of Gr remains almost intact, it shows a small gap at the Dirac point (<200 meV). Furthermore, the Dirac crossing is shifted 100 meV above the Fermi level, which means that Gr/Ir(111) is slightly p-doped by the substrate [153]. An ARPES study on rotational domains of Gr/Ir(111) showed that 30°R domains are physisorbed while 0°R are chemisorbed on the Ir(111) substrate, as a result, 0°R domains do not give a Raman signal which in contrast can be detected from 30°R domains [154].

3.3.1 Preparation: Need for High Temperature

The Ir(111) single crystal used in the study is a disk with a diameter of 10 mm and a thickness of 2 mm. Clean Ir(111) surface was prepared in UHV by repeated cycles of ion sputtering (1.5 keV, $P_{Ar} \simeq 1 \times 10^{-5}$ mbar) and flash-annealing at ca. 1600 K until sharp diffraction peaks were observed by LEED and HAS (see Fig. 3.12). The azimuthal alignment of the sample has been optimized using a p(2 × 2)O/Ir(111) layer prepared by exposing the surface to

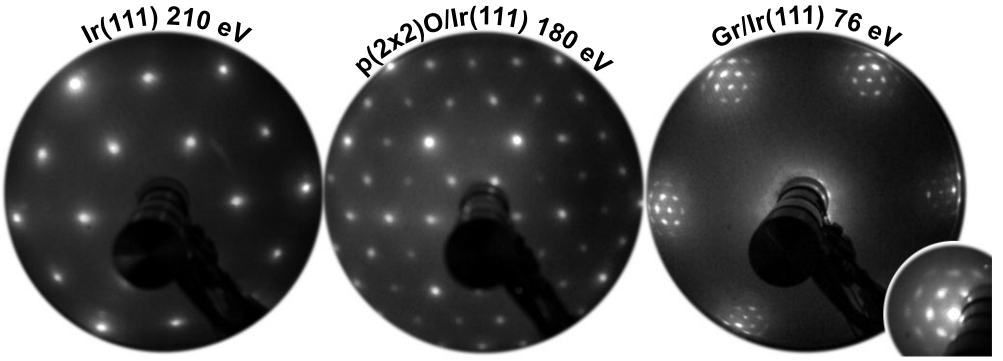

Figure 3.12: LEED diffraction patterns from Ir(111) (left), p(2×2)O/Ir(111) (middle) and Gr/Ir(111) (right). Different electron beam energies used are indicated, the inset in the bottom-right angle is a close up to the (0,0) peak and its surrounding satellites.

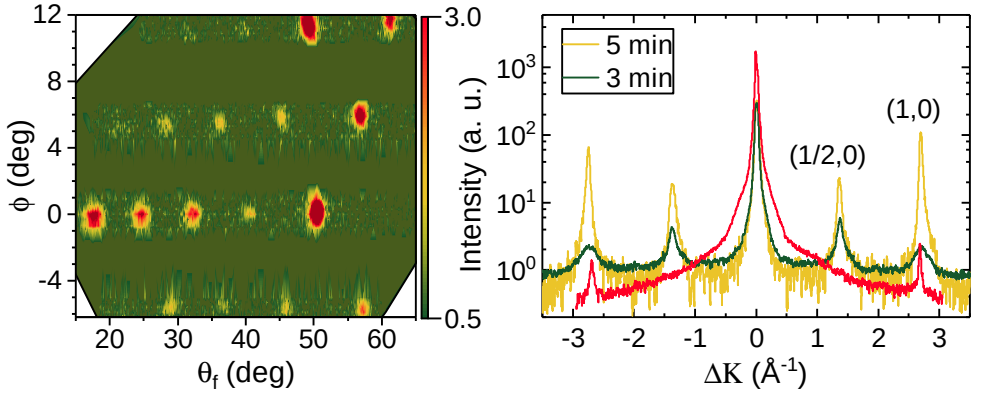

Figure 3.13: (Left) In-plane and out-of-plane diffraction of He at $E_i = 66\,\text{meV}$ and $\theta_i = 50°$ from p(2×2)O/Ir(111) measured using TEAMS. (Right) In-plane diffraction of He (using ERASMO) at $E_i = 20.5\,\text{meV}$ from two p(2 × 2)O/Ir(111) surfaces prepared by annealing in O_2 for different times indicated in the legend.

2×10^{-7} mbar of oxygen and heating it to 1100 K for 5 minutes [155]. Surface oxide is useful in adjusting the azimuthal orientation of a surface since it gives intense helium diffraction peaks due to its high corrugation.

The left panel in Fig. 3.13 shows a 2D diffraction pattern of He scattering from p(2 × 2)O/Ir(111) surface with $\theta_i = 50°$ and $E_i = 66\,\text{meV}$. A classical rainbow behavior can be seen from the intensities of the diffraction peaks due

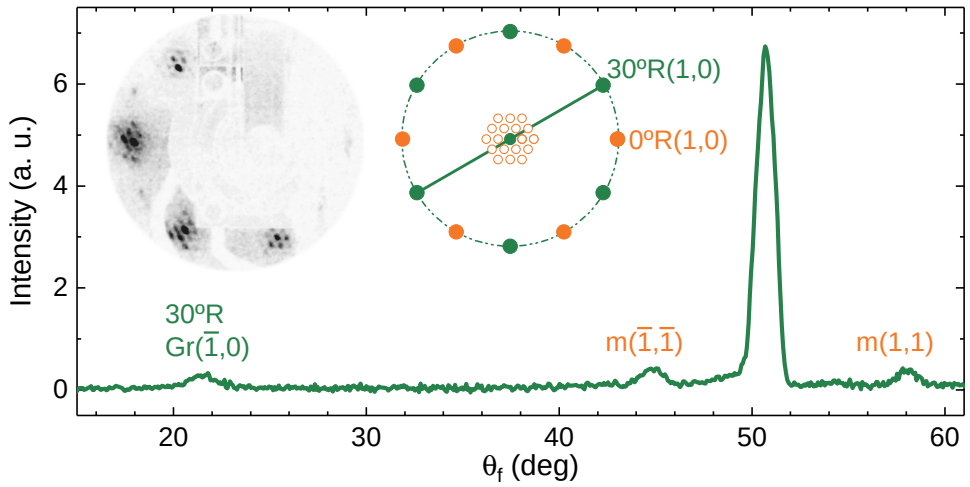

Figure 3.14: LEED and angular diffraction of He from Gr/Ir(111) with multiple rotational domains 0°R (orange) and 30°R (green). $E_i = 28\,\text{meV}$ and $\theta_i = 50.5°$. Names of diffraction peaks are indicated. Scan direction is indicated by the green line in the inset which shows a scheme of the reciprocal space of Gr/Ir(111) with multiple rotational domains.

to the high corrugation of the surface. The diffraction pattern is composed of 37 horizontal scan lines with steps of $\Delta\phi_f = 0.3°$. No scans were made with ϕ_f values where diffraction peaks are not expected.

Fig. 3.13 (right) shows a comparison of diffraction spectra from two surfaces of p(2 × 2)O/Ir(111) prepared at the same conditions of temperature and pressure but for different times of preparation (green and yellow), and a diffraction spectrum from clean Ir(111) (red). The position of the first order diffraction peak of Ir(111) coincides with the second peak of p(2×2)O/Ir(111). This confirms the (2 × 2) structure and therefore the peak in p(2 × 2)O/Ir(111) spectra are named as indicated in the figure ($\frac{1}{2}$,0) and (1,0). The preparation of p(2 × 2)O/Ir(111) requires annealing in O_2 for 5 minutes as discussed before, this gives the observed rainbow in the left panel and the yellow spectrum in Fig. 3.13 (right). Using lower exposure times results in a less corrugated surface and the ($\frac{1}{2}$,0) diffraction peak has higher intensity compared to the (1,0) peak.

The graphene overlayer is prepared by annealing the Ir(111) to 1650 K then exposing it to C_2H_4 at 4×10^{-7} mbar for 5 minutes. Inspecting the surface with LEED showed no traces of rotational domains, which has been

the case when the sample was prepared at 1500 K for example as can be seen in Fig. 3.14. A 30°R domain appears also if the sample cooling was slow. This rotational domain gives a diffraction peak corresponding to the lattice constant of graphene $a = (2.45 \pm 0.02)$ Å indicated Gr$(\bar{1}, 0)$ in Fig. 3.14. The scan direction of this measurement corresponds to the $\overline{\Gamma M}$ direction of the 30°R Gr/Ir(111) and the $\overline{\Gamma K}$ direction of the 0°R Gr/Ir(111) and the moiré superstructure as indicated by the green line in the inset in Fig. 3.14 which represents the reciprocal space of this surface as also has been confirmed by LEED. The visible diffraction peaks near the specular peak correspond to the second order diffraction peaks of moiré. Note that no moiré superstructure appears for the 30°R Gr domain.

3.3.2 Structure: Moiré Superstructure

The ability to measure the intensity of the He beam before and after scattering from a surface using the same detector allows us to obtain the absolute value without the need to worry about the detection probability of the projectile or changes in the efficiency of the detector. Ir(111) reflectivity is determined by this type of measurement $I/I_0 = 31.5\%$ when surface temperature $T_S = 80$ K, beam energy $E_i = 65$ meV and angle of incidence $\theta_i = 37.5°$, where I_0 is the intensity of the direct beam. This high reflectivity is mainly an effect of the high effective mass of the surface atoms. At the same beam energy the reflectivity of Gr/Ir(111) $I/I_0 = 7(18)\%$ when $\theta_i = 53(67)°$, following the Debye-Waller model (i.e. $I \propto I_0 \exp(-\cos^2 \theta_i)$).

Figure 3.15 shows a comparison between the angular distributions of He scattering from Ir(111) (red) and Gr/Ir(111) (green) taken with similar beam energies, 21.3 meV and 17.7 meV, respectively. Plotting the data in ΔK instead of $\Delta\theta_i$ permits us to compare the diffraction patterns directly. The angular position of the Ir(1,0) peak matches that of an intense diffraction peak in the Gr/Ir(111) curve. Thus, in the rest of this manuscript this peak in the Gr/Ir(111) diffraction spectra will be referred to as Ir(1,0).

The diffraction pattern of He scattering from Gr/Ir(111) exhibits several peaks as a result of the moiré structure. It is helpful to compare it with the diffraction pattern of He scattering from Gr/Ru(0001) [71] (black curve in inset in Fig. 3.15) since these surfaces share many aspects. The reciprocal lattice vector of a moiré pattern $\mathbf{k}_{moiré}$ of Gr on a metal is given by the difference between the reciprocal lattice vectors $\mathbf{k}_{Gr}$ and $\mathbf{k}_{Mt}$ of Gr and the metal surface,

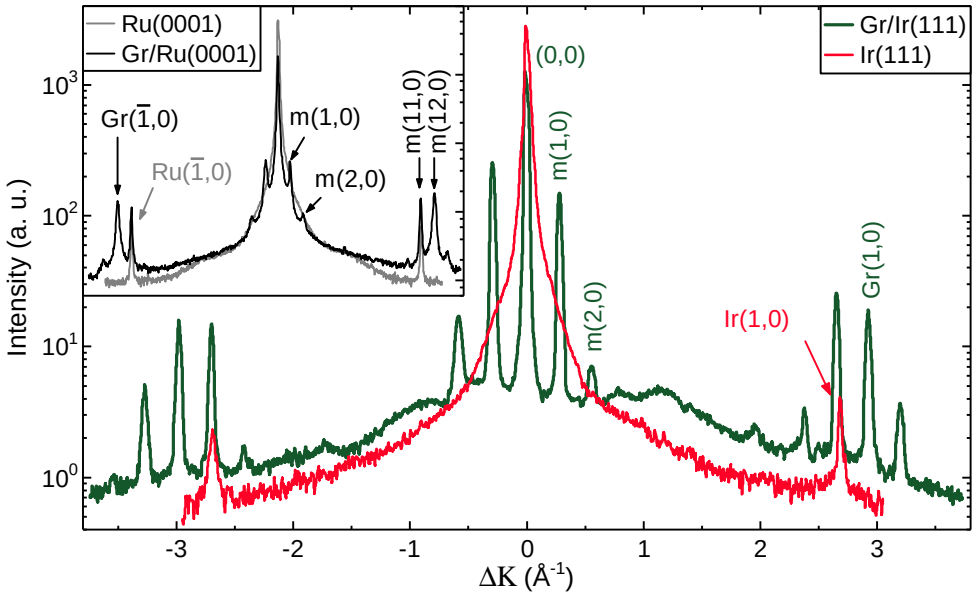

Figure 3.15: Angular distribution of He scattering from Gr/Ir(111) (dark green) and bare Ir(111) (red). E_i = 17.7 and 21.3 meV, respectively. Names of significant diffraction peaks are indicated. Inset: Diffraction from Gr/Ru(0001) (black) and Ru(0001) (gray) [71].

respectively

$$\mathbf{k}_{moiré} = \mathbf{k}_{Gr} - \mathbf{k}_{Mt}. \tag{3.1}$$

This means that the angular position of the first order diffraction peak of moiré m(1,0) is equal to the difference between the angular positions of Gr(1,0) and Ir(1,0) (or Ru(1,0)), and this is true for the diffraction spectra in Fig. 3.15. Additionally, for commensurate Gr/Ru(0001) certain high order diffraction peaks of moiré will match in position the first diffraction peaks of Gr and Ru(0001). As can be seen in the inset in Fig. 3.15 where the angular positions of m(11,0) and m(12,0) peaks match the positions of Ru(1,0) and Gr(1,0), respectively. This means that 11(12) ruthenium (graphene) lattices are contained in 1 moiré lattice, and thus every 12 Gr lattices fit on 11 Ru lattices.

This simple relation of the diffraction peak does not apply to the incommensurate Gr/Ir(111). The angular position of m(1,0) is equivalent to the difference in angular positions of Gr(1,0) and Ir(1,0). However, no higher order of moiré diffraction peaks matches in position the first order diffraction peaks of either

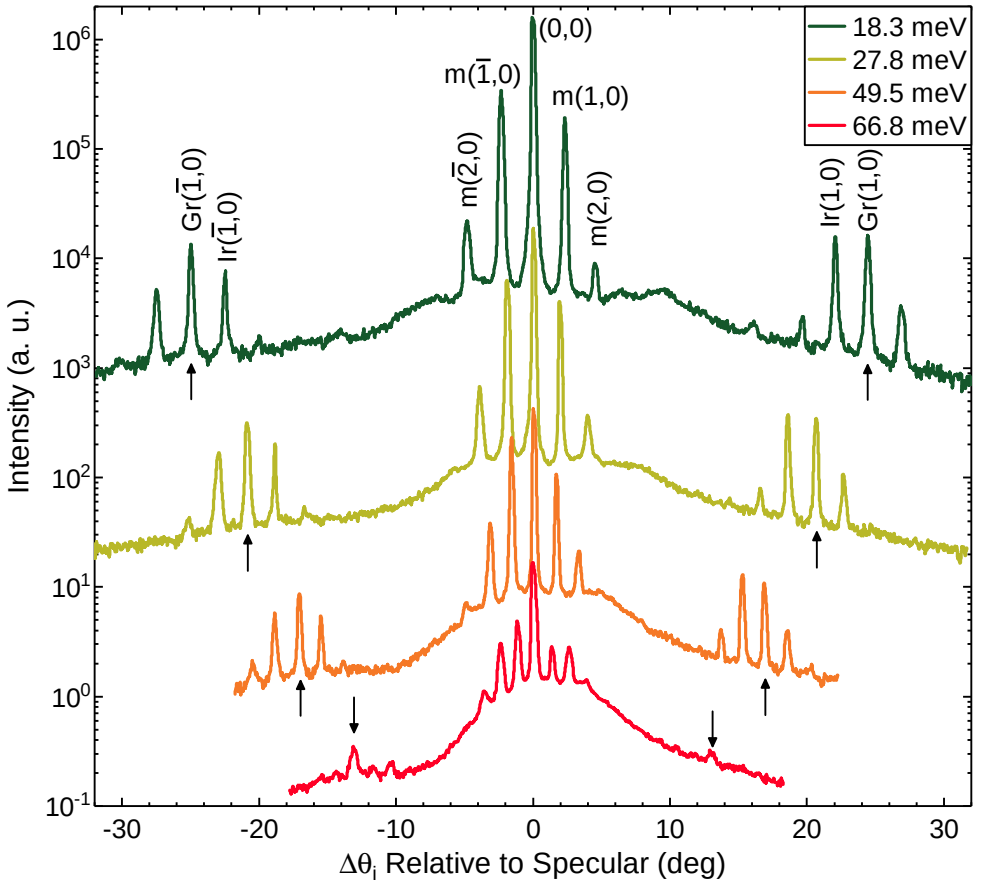

Figure 3.16: Angular distributions of He beam at different incident energies indicated in the legend scattered from a Gr/Ir(111) surface. The arrows indicate the Gr(1,0) peaks.

Gr or Ir. It was not clear from the He diffraction from Gr/Ru(0001) whether the moiré satellites around Gr(1,0) are high order diffraction peaks (10, 11, 12 and 13) that originate from the specular peak (0,0) (as in classical rainbow) or if they originate from Gr(1,0) and thus a different notation should be used. He diffraction from the incommensurate Gr/Ir(111) shows clearly that these satellites originate from Gr(1,0).

Decreasing the He beam energy increases the angular resolution of the diffraction measurement as it increases the separation of the diffraction peaks and reduces the inelastic scattering that appears as a broad Gaussian back-

ground. Spectra in Fig. 3.16 were taken with beam energies from 66.8 to 18.3 meV. Black arrows follow the drift of the Gr(1,0) peak which corresponds to a lattice constant $a_{Gr} = (2.45 \pm 0.01)$ Å, in very good agreement with STM and LEED measurements [152]. Ir(1,0) peak gives a periodicity $a_{Ir} = (2.708 \pm 0.006)$ Å and from m(1,0) peak the moiré periodicity is $a_m = (25.89 \pm 0.31)$ Å. Using Eq.(3.1) we obtain a moiré periodicity (26.04 ± 1.50) Å, in very good agreement with previous work [152].

The intensities of the moiré diffraction peaks in Fig. 3.16 are higher in backward scattering ($\Delta K < 0$) than in forward scattering, while the opposite is true for Gr(1,0) and its satellites. Ir(1,0) in the red spectrum with 66.8 meV was not detected for $\Delta\theta_i > 0$ due to the increase of inelastic background in energy loss direction relative to the energy gain direction as has been explained earlier in Section 3.2.2. Mapping the in-plane and out-of-plane moiré diffraction peaks as seen in Fig. 3.17 yields a 3-fold symmetry rather than the expected 6-fold from the hexagonal structure of the moiré ripples, the same 3-fold symmetry was reported by LEED [156].

The angular diffraction pattern in Fig. 3.17 was measured using TEAMS with fixed θ_i and a rotary detector. The sample was rotated so that the $\overline{\Gamma K}$ symmetry direction of the graphene lattice is parallel to the sagittal plane. The map is created from horizontal scan lines, where each line was obtained by moving the detector to the vertical position where diffraction peaks are expected to appear. Thus each map in Fig. 3.17 is composed of 1 in-plane and 6 out-of-plane scan lines. Beam energy was $E_i = 25.4$ meV for both maps taken at $\theta_i = 46°$ (left) and 56° (right).

White circles in Fig. 3.17 are calculated positions of the diffraction peaks according to Eq.(1.6), error bars which are contained inside the circles indicate the error in angular position due to the forward and backward movement of the detector. Calculated values of ϕ_f agree with the measurement within 0.2°, the measured values of θ_f show quantitative and qualitative divergence from the calculated values. According to Eq.(1.6), the values of θ_f increase with increasing ϕ_f, so the white circles in Fig. 3.17 follow an arc curved to the right, however, the measured values of θ_f follow an arc curved to the left. The kinematics of diffraction in Eq.(1.6) were developed for flat surfaces. The effect of a wavy surface like Gr/Ir(111) on the kinematics of HAS might explain this observation.

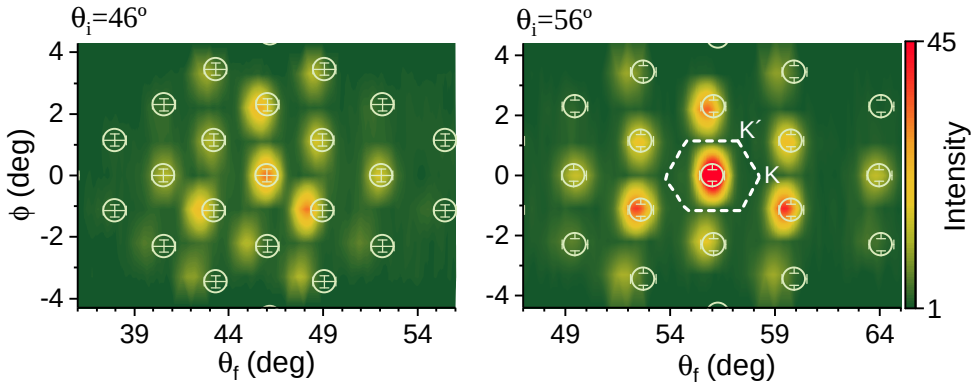

Figure 3.17: In- and out-of-plane diffraction pattern of He beam at $E_i = 25.4$ meV scattered from Gr/Ir(111). $\overline{\Gamma K}$ is parallel the sagittal plane. Dashed hexagon is a rough drawing of the first Brillioun zone of the moiré superstructure. White empty circles are calculated positions of the moiré diffraction peaks.

Surface Corrugation

The intensities of diffraction peaks yield information on the corrugation of the surface, due to the presence of the moiré superstructure in Gr/Ir(111) we can obtain the values of two different corrugations, the first is on the atomic level of the carbon atoms in the graphene layer and the second is of the larger periodicity of the moiré ripples. Fig 3.18 shows a comparison between the diffraction patterns of scattered He from Gr/Ir(111) and Gr/Ru(0001). The golden curves are the measured data while green and red curves are multi-peak Gaussian fits. To facilitate the description of the figure, we use the names m(1,0) and m(2,0) for the first and second order diffraction peaks of the moiré periodicity, Gr(1,0) is the diffraction peak corresponding to the graphene periodicity and Mt(1,0) is the diffraction peak corresponding to the metal's periodicity. Panel (c) is a histogram of the intensities of these peaks normalized to the intensity of the specular peak in each diffraction spectrum. The Gr diffraction peaks have almost the same intensity in both surfaces, this means that the atomic corrugation of the graphene layer is similar on both surfaces.

The corrugation of the moiré pattern on Gr/Ru(0001) was investigated using several techniques. HAS with close-coupling calculations gave a value of 0.15 Å, while STM measurements gave a value varying from 1.1 to 0.5 Å depending on the tunneling bias. Analysis of XRD data gave a value of 0.85 Å

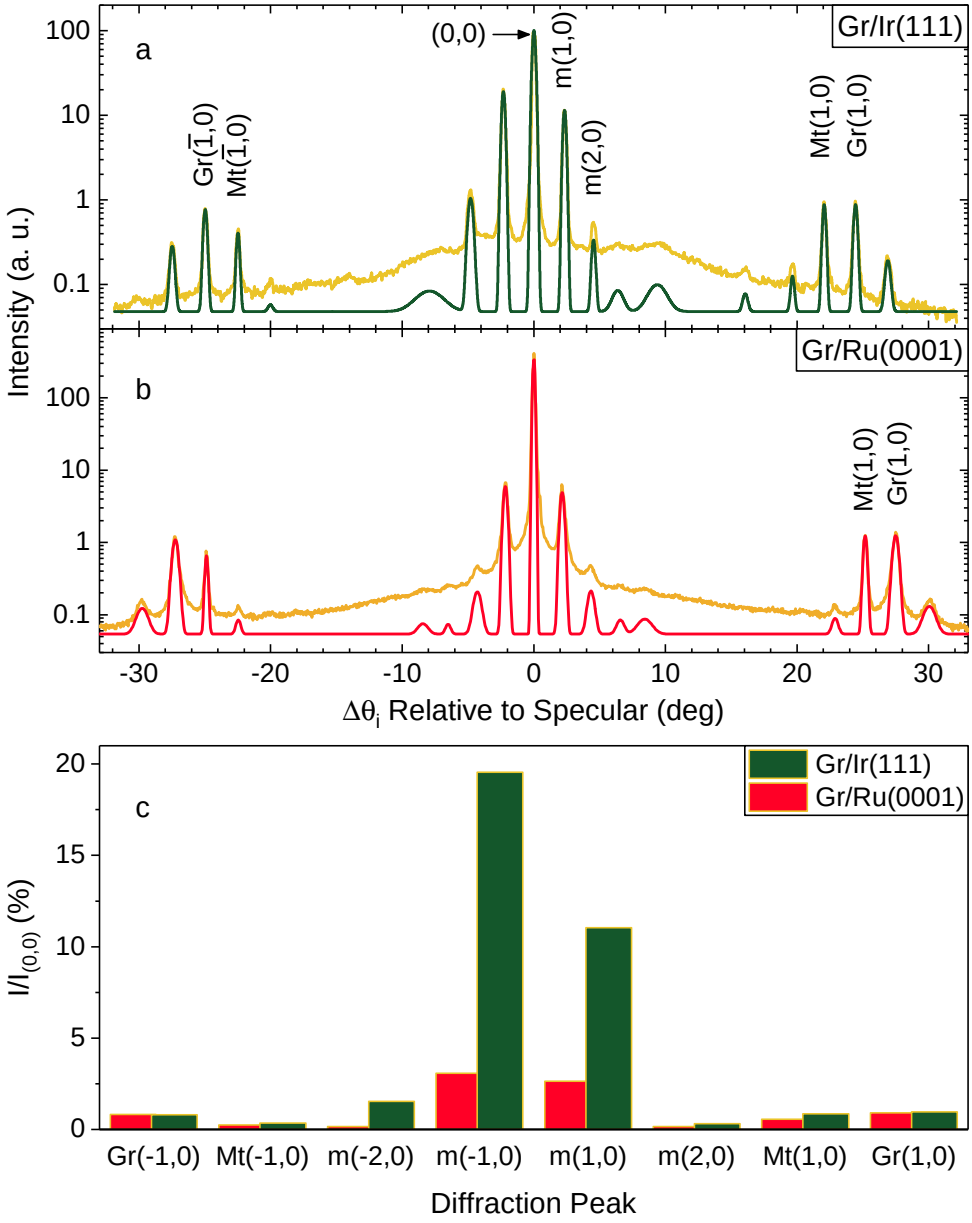

Figure 3.18: (a and b) Angular distribution of He scattering from Gr/Ir(111) and Gr/Ru(0001) with E_i = 18.3 and 15.5 meV, respectively. Golden spectra are measured data, green and red are multi-peak Gaussian fits. (c) Intensities of selected diffraction peaks normalized to the intensity of the specular peak for each spectrum.

Table 3.1: Normalized intensities and widths (in deg) of diffraction peaks of Gr/Ir(111) and Gr/Ru(0001) from spectra in Fig. 3.18. (Specular peak widths are 0.2 and 0.28°, respectively).

Peak	$I/I_{(0,0)}$ (%)		$W - W_{(0,0)}$ (deg)	
Name	Gr/Ru	Gr/Ir	Gr/Ru	Gr/Ir
Gr($\bar{1}$, 0)	0.81	0.80	0.10	0.03
Mt($\bar{1}$, 0)	0.24	0.35	0.05	0.00
m($\bar{1}$, 0)	3.07	19.56	0.07	0.01
m(1,0)	2.64	11.05	0.07	-0.01
Mt(1,0)	0.56	0.86	0.06	0.01
Gr(1,0)	0.91	0.96	0.10	0.05

[157]. While the corrugation of moiré pattern in Gr/Ir(111) is $\sim$ 0.3 Å as measured by STM [151, 152]. Clearly STM measurements indicate that the moiré pattern corrugation of Gr/Ru(0001) is at least twice as large as that of Gr/Ir(111). HAS measurements give the opposite result; the intensities of the moiré peaks in Fig. 3.18 indicate that Gr/Ir(111) has a much larger corrugations. Close-coupling calculations require a long time to be done, they have not been used in this thesis, however, judging from experience we can estimate that the calculations would give a value of the corrugation of the moiré superstructure in Gr/Ir(111) similar to that measured by STM. The reason why HAS measurements on Gr/Ru(0001) gave such a low value require more investigation, we present a hypothesis based on Debye-Waller and phonon measurements in Section 4.4.

Finally, we note how the widths of Gr peaks is significantly different between the two Gr/metal systems (see Table 3.1). The widths of the specular peaks are 0.2° and 0.28° for Gr/Ru(0001) and Gr/Ir(111), respectively, which means that the average lateral domain size is larger in the former. On the other hand, the widths of Gr peaks are 0.44° and 0.33°, respectively. DFT calculations indicated the presence of two regions characterizing the structure of Gr/Ru(0001) [71] where the C-C bonds are stretched in order to adjust as much as possible to ruthenium periodicity in the strongly interacting region while they are not distorted in the highest regions. We do not observe this

effect in Gr/Ir(111) and the widths of the diffraction peaks are mainly limited by the domain size.

3.3.3 Surface Thermal Expansion: Complications of Moiré Superstructure

Increasing the temperature of Gr/Ir(111) results in an abrupt change of peak positions as shown in Fig. 3.19, where only the first order diffraction peaks are indicated, namely m($\bar{1}$,0), Gr($\bar{1}$,0) and Ir($\bar{1}$,0). The derived changes in periodicities are plotted on the right panel as a relative change $\Delta a/a$. The data is separated in two groups, full upward triangles and solid lines are from $(\bar{1}, 0)$ peaks whereas half-full downward-pointing triangles and dashed lines are from the (1,0) peaks. The solid gray line is from the thermal expansion of iridium [158].

The periodicities obtained using $(\bar{1}, 0)$ peaks are straightforward to understand, the surface lattice of Gr/Ir(111) expands with increasing surface temperature on a rate slightly higher than that of bulk Ir, the corresponding moiré periodicity decreases as expected from Eq.(3.1) (red symbols in Fig. 3.19). This result agrees with an XPS study which showed that the overlayer in Gr/Ir(111) expands with its substrate [159]. LEED measurements showed that moiré periodicity remains constant between 300 and 600 K then decreases monotonically [156], which agrees qualitatively with the results presented in Fig. 3.19.

The periodicities obtained using only Gr$(\bar{1}, 0)$ and Ir$(\bar{1}, 0)$ diffraction peaks (orange and green upward-pointing triangles) show a monotonic increase, slightly higher than that of bulk iridium [158]. On the other hand, it can be seen that the position of the Gr(1,0) and Ir(1,0) peaks moves slightly outward (expansion) then jumps inward (contraction). The right panel shows that after this jump at 200 K the periodicity remains practically constant. Since the angular positions of these peaks are very far from the specular position, they can be very sensitive to the azimuthal orientation of the sample. And the behavior of these peaks *appears* to be a result of azimuthal rotation more than lateral expansion. To clarify, it is not the sample that appears to have rotated, but rather a phase change on the surface might have caused the graphene layer to rotate and accommodate the new misfit of lattice constant between Gr and Ir(111) by twisting the graphene layer. HAS measurement on Gr/Ru(0001) [119] showed an evidence of a phase shift with increasing surface temperature,

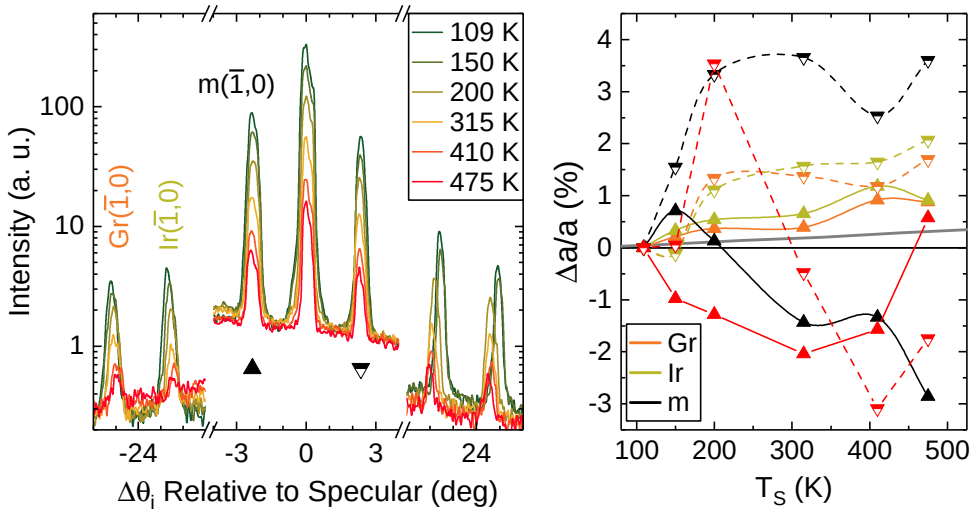

Figure 3.19: (Left) Thermal expansion of the surface of Gr/Ir(111), spectra taken with E_i = 17.5 meV He beam. Peak names are indicated, triangles below the spectra indicate the symbols used in the right panel where relative changes in periodicity are plotted, full upward triangles and solid lines are from $(\bar{1}, 0)$ peaks and half-full downward-pointing triangles and dashed lines from the (1,0) peaks, orange for Gr, green for Ir, black for moiré and red for calculated moiré lattice using Eq.(3.1). Solid gray line presents the expansion of iridium [158].

where the intensities of the peaks denoted Gr(1,0) and Ru(1,0) where monitored while increasing the surface temperature and a sudden change in the intensity of Ru(1,0) was detected at 320 K.

When comparing the periodicity change measured by the position of the m(1,0) peak (black) with that of the calculated periodicity (red) using Eq.(3.1) and the measured periodicities from Gr and Ir peaks we see that the relative periodicity change is similar in measurement and calculation at 200 K while it is completely different for the rest of surface temperatures. This might be the fingerprint of a retarded response of the moiré superstructure to the change in lattice misfit of Gr and Ir(111). Earlier LEED measurements reported a hysteresis effect in the moiré lattice constant during the heating-cooling cycle and explained the phenomenon by a strain relief mechanism where wrinkles are created in the graphene layer upon cooling to reduce its compressive strain [156, 160].

If the moiré structure were merely a result of overlap of two different peri-

odicities, the measured periodicity of the moiré superstructure is expected to follow Eq.(3.1). Since this is not the case, we conclude that the moiré structure is formed during graphene growth and does not change after decreasing the surface temperature. It is worth mentioning that earlier HAS and STM measurements [161] reported that the moiré periodicity of Gr/Ru(0001) remains the same even after the intercalation of 0.7 ML of Cu, whereas, the moiré periodicity according to Eq.(3.1) should have increased to ~ 60 Å. These observations are evidence that the periodicity of the moiré superstructure is affected by the lattice periodicities of Gr and its substrate at the growth temperature, therefore, strain will inevitably build-up on the surface as a result of cooling down. In fact, earlier reports revealed a preexisting strain in graphene due to cooling down from the growth temperature [162]. Heating the sample causes changes to the built-in strain in the graphene layer and certain temperatures will result in a combination of strain and misfit that allow the graphene layer to create sudden -instead of smooth- phase shifts. The strain builds up when the sample is cooled down after preparation, a relief mechanism by wrinkle formation has been reported earlier for Gr/Ir(111) [156], here we showed that the breaking of surface rotational-symmetry can give more insight into this mechanism.

3.3.4 Selective Adsorption Resonances

Measuring the intensity of the specularly reflected He beam from Gr/Ir(111) as a function of θ_i results in observing SARs thanks to the high atomic corrugation of the graphene layer and the small lattice constant of the graphene unit cell. Using a He beam with small E_i allows for the value of $\mathbf{K}_i$ to be comparable to the reciprocal lattice vector of graphene $\mathbf{G}$ which is a favorable condition for SARs. This also allows for the values of $E_{i\perp}$ to be close to the eigenvalues of the He-surface interaction potential so that the resonances can take place.

Fig. 3.20 shows two measurements of the intensity of specular peak of He reflected from Gr/Ir(111) as a function of θ_i using two different beam energies 22.2 and 18.5 meV. The azimuthal orientation of the sample in these measurements was rotated so that the $\overline{\Gamma\mathrm{M}}$ direction of the surface lattice of graphene is in the sagittal plane. The measurements were conducted by first moving the detector to a certain θ_f then optimizing the position of the sample (x, y, z and θ_i) to get the maximum reflected intensity. Each data point represents the measured intensity by the detector. The calibration of the polar angle was done using the position of the detector in the direct path of the

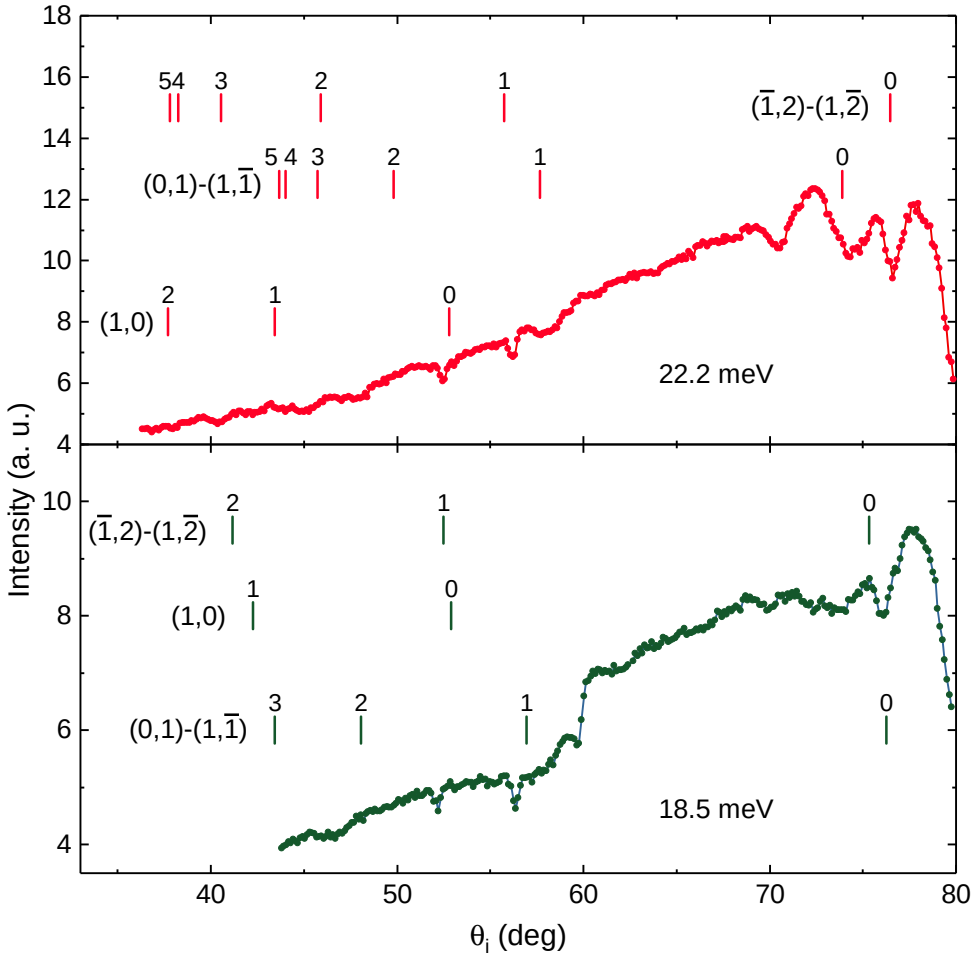

Figure 3.20: Specular intensity of HAS from Gr/Ir(111). The sample is oriented so that the $\overline{\Gamma M}$ direction of the graphene unit cell is parallel to the sagittal plane. Two different beam energies were used. Vertical bars indicate angular positions of SARs using Eq.(1.8). Notations of involved reciprocal lattice vectors and indices of eigenvalues of He-Gr/Ir(111) potential are indicated.

incident beam which equals 180°. The intensity increases with θ_i as expected from the Debye-Waller model. This increase of the intensity is interrupted by sudden minima as a result of SARs.

Angular positions of SARs can be obtained using Eq.(1.8) which relates the

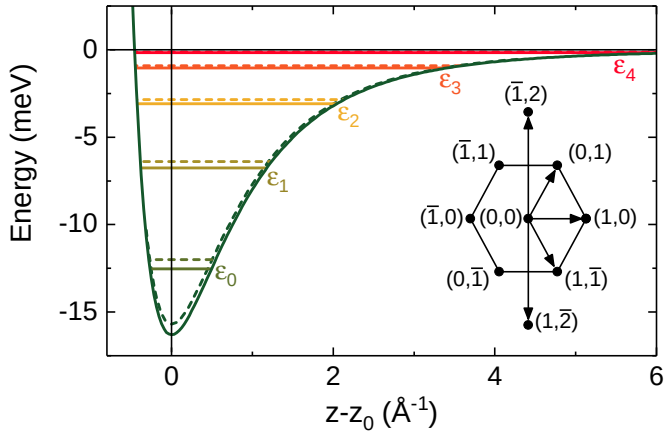

Figure 3.21: Three parameter potential of He-Gr/Ir(111) interaction and its eigenvalues as a function of He distance from surface (z) where z_0 is corresponds to the minimum of the potential with $\lambda = 1.413\,\text{Å}^{-1}$, $p = 5.3$ and $D = 16.3\,\text{meV}$. Dashed lines are the same except for $D = 15.7\,\text{meV}$ as used for graphite in Ref. [163]. Inset shows the reciprocal lattice of graphene with arrows indicating the vectors involved in observed SAR processes in Fig. 3.20.

eigenvalues of the He-surface interaction potential to the incident and scattered wavevectors and the vectors of the reciprocal lattice of the surface. The eigenvalues of the interaction potential were found by eyeballing the angular positions that satisfy Eq.(1.8) with the minima observed in Fig. 3.20 and thus we obtained the positions indicated by the vertical lines. The labels indicate the involved reciprocal lattice vectors in the SAR process and the index of the eigenvalue of the interaction potential. The inset in Fig. 3.21 shows the reciprocal lattice of graphene and the lattice vectors that were found to produce observable SAR features.

The potential used in this analysis was the one proposed by Boato et al. [163] as they showed that neither a Morse potential nor a 3-9 potential could accurately describe the experimental vibrational spectrum of He-graphite, whereas better results are obtained using the three-parameter model potential given by [164]

$$V_p(z) = D\left[\left(1+\frac{\lambda z}{p}\right)^{-2p} - 2\left(1+\frac{\lambda z}{p}\right)\right]^{-p}, \tag{3.2}$$

where D is the depth of the potential well, λ is a positive range parameter that affects the width of the interaction potential, p is a continuous parameter in the range $-1 \leq 1/p \leq 1$ that affects the range of the attractive part of the potential, z is the distance from the surface. The eigenvalues are given by

$$\epsilon_n = -D\left[1 - \frac{n + 1/2 + [\delta(p)/A]}{AS(p)}\right]^{S(p)}, \tag{3.3}$$

where h is the Plank constant, m is the mass of the gas atom, $A = \sqrt{2mD}/2h\lambda$, $\delta(p) = (1 + 1/p)/32p$ and $S(p) = \left[\frac{1}{2} - (1/4p)(3 + 1/p)\right]^{-1}$. Boato et al. [163] obtained the values $\lambda = 1.413\,\text{Å}^{-1}$, $p = 5.3$ and $D = 15.7\,\text{meV}$ from the experimental SAR measurements of HAS from graphite. Our experimental data in Fig. 3.20 for Gr/Ir(111) are better fitted using $D = 15.7\,\text{meV}$ with the same values of the other two parameters. Fig. 3.21 shows a comparison between the potential used in this work (solid lines) and the one in Ref. [163] for graphite (dashed lines). The energy levels obtained from our fit are $\epsilon_0 = -12.53$, $\epsilon_1 = -6.77$, $\epsilon_2 = -3.08$, $\epsilon_3 = -1.04$, $\epsilon_4 = -0.17\,\text{meV}$. For comparison, $\epsilon_0 = -11.98\,\text{meV}$ was measured for He-graphite interaction potential. Fitting our data using a Morse potential gives the following energy levels $\epsilon_0 = -12.52$, $\epsilon_1 = -7.14$, $\epsilon_2 = -3.26$, $\epsilon_3 = -0.88$, $\epsilon_4 = -0.005\,\text{meV}$. The eigenvalues of the 3-parameter model fit our experimental data rather well using the parameters mentioned above. However, some features in the spectra shown in Fig. 3.20 cannot be explained by this fit. The reason can be an interference from the reciprocal lattice vectors of the moiré unit cell which can be added to the reciprocal lattice vectors of the graphene unit cell in multiple combinations. This can make the fit very complicated. Fig. 3.20 shows that only three sets of the reciprocal lattice vectors of graphene are effectively involved in SAR processes.

Chapter 4

Inelastic Scattering of He from Gr Covered Metal Surfaces

This chapter presents two aspects of inelastic scattering: thermal attenuation of the intensity of diffraction peaks and phonon measurements. Basically, the interaction of a He beam with the surface phonons is the reason behind the thermal attenuation, the latter is treated using the Debye-Waller model, and the phonon dispersion curves are obtained from time-of-flight measurements using iHAS dynamics discussed on Section 1.3.3.

4.1 Debye-Waller Factor

There are two main aspects to consider when looking for a good surface to focus He atoms: The intensity and width of the reflected beam. The latter is affected by the quality (roughness) and stability of the reflecting surface and the former is mainly affected by the effective atomic mass of the surface. The attenuation of reflected beam intensity with increasing surface temperature is a useful analysis tool for investigating the impact of the surface material on the focused beam as it allows to obtain information of the effective mass of the surface atoms. By measuring the intensity of the specularly reflected beam at different surface temperatures the value of the Debye-Waller factor can be obtained. Debye-Waller factor depends also on the beam energy and angle of incidence.

Fig. 4.1 shows examples of these measurements performed in the two

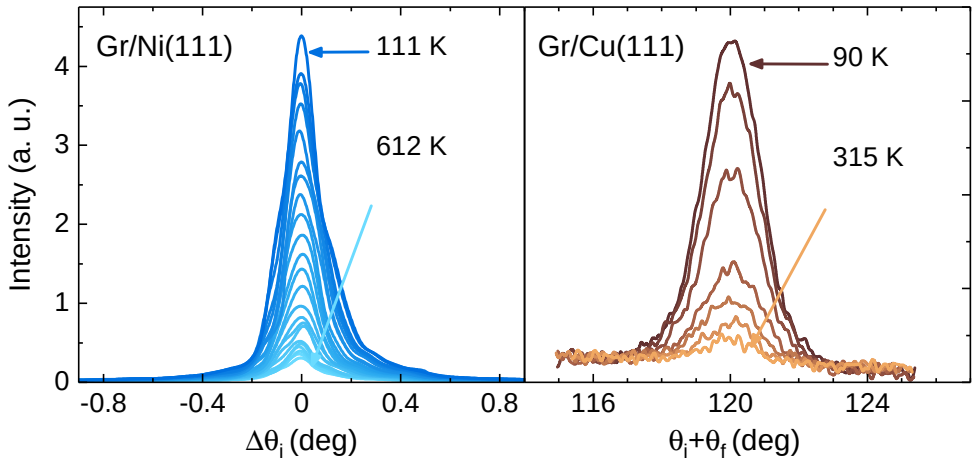

Figure 4.1: Attenuation of the specular peak intensity as a function of surface temperature for Gr/Ni(111) (left) and Gr/Cu(111) (right), measured in the two HAS machines available in our laboratory (ERASMO and TEAMS, respectively). Highest and lowest temperatures accessible for Debye-Waller measurements are indicated.

scattering machines in our laboratory. Gr/Ni(111) (left) was measured using ERASMO (the TOF machine) with beam energy $E_i = 36.6$ meV, and although θ_i is changed during the measurement it can be considered 52.7° since the angle change is small. Gr/Cu(111) (right) was measured using TEAMS (the rotary detector setup) with $E_i = 28$ meV and $\theta_i = 60°$.

The advantage of using TEAMS is that we can obtain the absolute value of reflectivity. Since the same detector is used to measure the incident and the scattered beams there is no need for any normalization. On the other hand, ERASMO (the fixed angle setup) provides better signal-to-noise ratio because the detector is separated from the scattering chamber by the long TOF arm. While the set of diaphragms between the sample and detector results in the high angular resolution of the machine, they are also responsible for the high sensitivity to changes in sample alignment.

Fig. 4.2.a shows examples of the effect of misalignment. The vertical axis in this figure represents the value of the reflected intensity at a certain surface temperature normalized to the reflected intensity at the lowest surface temperature in each measurement set. The data plotted in blue circles was obtained from a set of measurements where the surface temperature was stabilized and the sample position was aligned before each measurement. The data plotted in

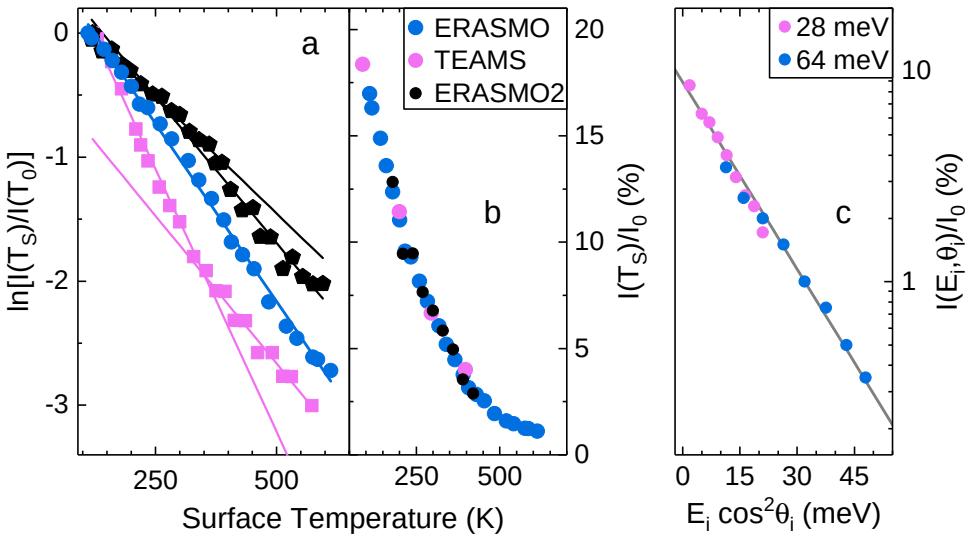

Figure 4.2: (a) Effect of changes of sample position on the precision of measuring thermal attenuation of He scattering from Gr/Ni(111) in ERASMO scattering machine. Blue data shows a set of measurements with careful alignment of the sample position for each individual measurement. Magenta and black are measurement without careful alignment while heating and cooling the sample, respectively. Solid lines are linear fits all (black) or parts (red and blue) of the data sets. (b) Thermal attenuation measurements ran in three different experimental setups (see text). (c) Debye-Waller attenuation for different E_i and θ_i and fixed $T_S = 120\,\mathrm{K}$

magenta squares and black pentagons are examples of bad alignment during the measurements which results in a change in the slopes of the curves.

Magenta squares were taken while heating the sample, the intensity starts decreasing rapidly with increasing T_S, however, adjusting the azimuth at 350 K reveals a different decrease rate, the solid lines are fits of parts of the curve before and after the position adjustment. Black pentagons where taken while cooling down the sample, in this case the intensity starts to increase with decreasing surface temperature at the expected rate, however, this rate starts to decrease gradually since the sample position is not adjusted. This can be seen from the different slopes of the linear fits of the first and second halves of the data set. This however, does not mean that the measurement will yield a high error when conducted carefully. We ran the measurements of Debye-Waller attenuation for Gr/Ni(111) in two other experimental setups, plotted in Fig.

4.2.b. Blue circles are the same as the blue data panel (a). Magenta circles were measured using TEAMS machine at the same incident beam conditions. Black circles were measured using the second detector in ERASMO which is separated by only one diaphragm from the target chamber, where $\theta_i = 65.6°$ and $E_i = 64$ meV. These measurements allow us to obtain a statistical error of 3% in the value of Debye-Waller factor argument after normalizing to experimental conditions, a remarkably low value.

Another method of validating the Debye-Waller model is to measure the intensity of the diffraction peaks at different beam energies and angles of incidence $I(E_i, \theta_i)$ while keeping the surface temperature fixed. Fig. 4.2.c shows an example of this test on Gr/Ni(111) using TEAMS machine. The data was measured at surface temperature $T_S = 120$ K while changing θ_i from 30 to 75° and using two beam energies 28 and 64 meV. The plotted data was normalized to the intensity of the incident beam I_0 for each energy. The two data sets exhibit similar slopes, indicating that He-scattering from Gr/Ni(111) obeys normal energy and angle scaling, as expected from a low-corrugated surface.

In general, the form of $W(T)$ given by Eq.(1.13) does not agree well with experiment in both the momentum and the temperature dependence [5]. A full description of the thermal attenuation for real systems can be achieved only from a detailed investigation of multiphonon exchange. For the convenience of the reader the argument of Debye-Waller factor which expresses the decay rate of the specular peak in He diffraction spectra as a function of several parameters is repeated here

$$2W(T_S) = \frac{24m(E_i \cos^2 \theta_i + D)T_S}{M_S k_B \Theta_D^2}. \tag{4.1}$$

These parameters are either a property of the studied surface, namely, the depth of the He-surface potential D, the effective atomic mass of the surface M_S and the surface Debye temperature Θ_D; or related experimental conditions, which are the mass of the projectile atom m, the beam energy E_i and angle of incidence θ_i. These two types of parameters cannot be separated directly because of the summation $E_i \cos^2 \theta_i + D$ in the numerator. Although we do not have clear information on the exact values of D for each of the studied surfaces, it will not be a bad approximation to assume that D has the same value for all graphene covered surfaces in our analysis of Debye-Waller factor, especially

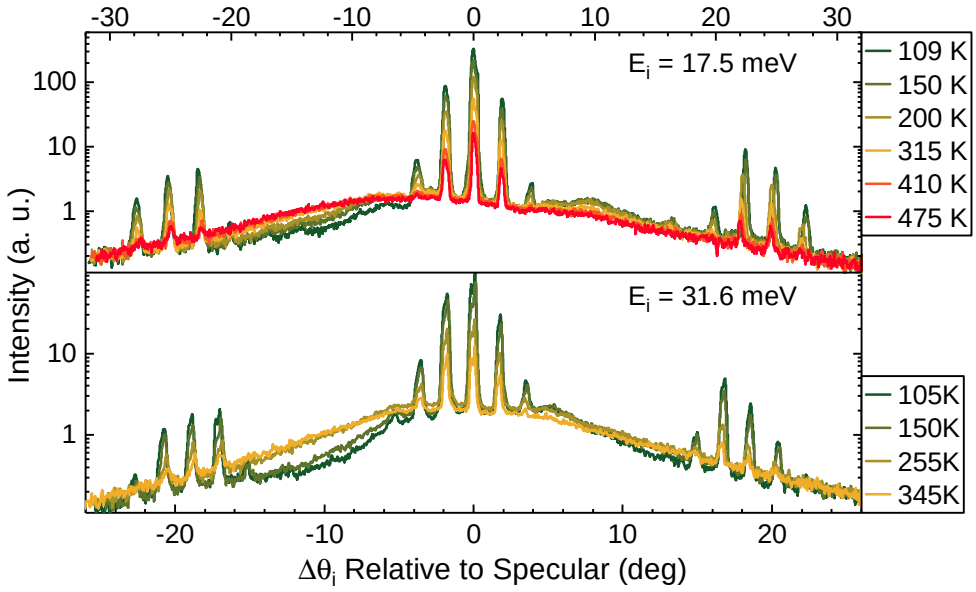

Figure 4.3: Evolution of He diffraction spectra from Gr/Ir(111) with surface temperature at two different beam energies.

since the effect of small changes in this value is lessened by the summation with $E_i \cos^2 \theta_i$.

The drop in the intensities of diffraction peaks with increasing surface temperature is accompanied with an increase in the inelastic background in the diffraction spectra. The Debye temperature term in Eq.(4.1) indicates the relation between the decrease of elastic scattering and the excitation of phonons. This is manifested in the evolution of diffraction spectra presented in Fig. 4.3. Two beam energies were used and the surface temperature was increased until the diffraction spectra disappeared under the inelastic background. A similar behavior was shown earlier for Gr/Ni(111) in Fig.3.7. The shape of the background is a Gaussian peak. The position of the background maximum shifts to negative $\Delta\theta_i$ with increasing surface temperature since more phonons are excited at the surface and the probability of the helium atom gaining energy from the surface increases.

Analysis of the intensities of the diffraction peaks of Gr/Ir(111) in Fig. 4.3 is plotted in panels (a) and (b) in Fig.4.4. The data is plotted as the intensity of the diffraction peak at different temperatures $I_{pq}(T_S)$ normalized to its intensity

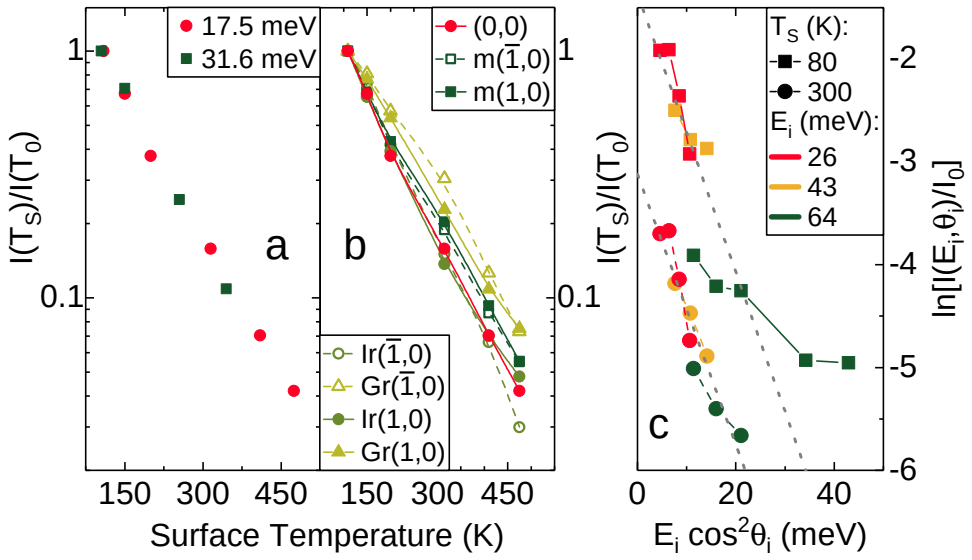

Figure 4.4: Testing Debye-Waller model with Gr/Ir(111). (a) Thermal attenuation of the specular peak for two different E_i. (b) Thermal attenuation of different diffraction peaks at $E_i = 17.5$ meV. (c) He specular intensity dependence on E_i and θ_i using two different surface temperatures and three beam energies.

at the lowest surface temperature in the measured set of spectra $I_{pq}(T_0)$, where p and q are the indices of the diffraction peak. Panel (a) shows the thermal attenuation of the specular peak using different beam energies 17.5 (red circles) and 31.6 meV (green squares). The slopes of these curves are 9.4×10^{-3} and 8.6×10^{-3}, respectively. The difference between these slopes is smaller than what is expected from the Debye-Waller model due to the difference in E_i. However, the standard error of the measured slopes is 9%, which is acceptable.

Fig. 4.4.b shows the thermal attenuation of the three first order diffraction peaks in the angular diffraction spectra of Gr/Ir(111) with $E_i = 17.5$ meV, using the peak names as in Sec. 3.3. Red circles indicate the specular peak, squares indicate the moiré first order diffraction peaks which appear at $\Delta\theta_i = \pm 2.3°$, triangles and circles indicate the Ir and Gr peaks which appear at $\Delta\theta_i = \pm 22.5°$ and $\pm 25°$, respectively. (1,0) and ($\bar{1}$,0) peaks are distinguished by solid symbols and lines for the former, and empty symbols with dashed lines for the latter. The diffraction spectra for this data were measured using ERASMO, which means θ_i is different for each peak. The Debye-Waller model predicts that the

decay rates of the (1,0) and ($\bar{1}$,0) peaks are 34% higher or 26% lower than the decay rate of the specular peak, respectively. However, this does not agree with the measured curves.

The Debye-Waller factor in Eq.(4.1) was derived by assuming that the momentum transfer parallel to the surface is zero [5]; this is a valid approximation for the specular peak and the diffraction peaks in its vicinity like the moiré diffraction peaks. The estimated difference in the decay rate of the moiré peaks compared to that of the specular peak is 3% which is lower than the statistical error in the measurement. Thus we can say that the diffraction peaks close to the specular obey the Debye-Waller model while the peaks far from the specular do not.

Finally, Fig.4.4.c shows the specular intensity dependence on the energy of the incident beam normal to the surface (similar to Fig. 4.2.c for Gr/Ni(111)). The data for Gr/Ir(111) was measured using two different surface temperatures 80 K (squares) and 300 K (circles). Three different beam energies were used, plotted in different colors, in combination with several angles of incidence. In general, the reflected intensities from the 80 K surface are higher than those of the 300 K surface as expected from Debye-Waller model. However, unlike the Gr/Ni(111) data (shown earlier) the data for Gr/Ir(111) does not follow the same slope for a certain surface temperature, contrary to what is expected from the Debye-Waller model. The slopes of the data sets decrease with increasing E_i and the normal energy scaling of the specular peak does not hold for Gr/Ir(111). The explanation can be the presence of two periodicities on the surface or because the in-plane forces have an important role and thus the assumption of zero momentum transfer parallel to the surface is not valid for this surface.

A common practice in the literature is to derive a value of the surface Debye temperature Θ_D from the thermal attenuation measurements using the Debye-Waller model. As discussed earlier, besides the experimental parameters, there are three parameters in Eq.(4.1) related to the studied surface: the depth of the He-surface potential D, the effective atomic mass of the surface M_S and the surface Debye temperature Θ_D. The common practice is to obtain the value of D from different measurements, like the selective adsorption resonances which give a very precise value of D, and substitute M_S with the value of the mass of one atom of the surface then obtain Θ_D from Eq.(4.1). This practice has been used successfully in obtaining the Debye temperature for single crystal surfaces.

However, determination of the effective atomic mass M_{eff} of the surface and its Debye temperature Θ_D is still a matter of debate in molecular scattering from surfaces [109]. For instance, an increased effective mass was used to fit Ar and N_2 scattering data from the Ru(0001) surface, whereas this effect was not observed in other metal surfaces. This was interpreted as due to the different layer stacking (fcc or hcp) of the metallic surfaces investigated, whereby the mass increase in the case of Ru(0001) is caused by Ru atoms in layers beneath the surface [165]. Furthermore, M_{eff} can be equal to the mass of several atoms of the surface because a He atom with thermal energy can interact with several atoms from the surface at a single collision event. This depends on the strength of atomic bonds in the surface plane, for example, M_{eff} of HOPG was considered equal to 6 carbon atoms in HAS measurements because of the strong C-C bond [166].

Additionally, the surface Debye temperature obtained by HAS involves only the out-of-plane acoustic phonon modes, since the optical phonons contribution is assumed to be zero in the Debye model and the momentum exchange is more efficient with atomic displacements normal to the surface [55, 133].

These observations indicate that the "common practice" discussed earlier should be approached with caution when dealing with layered materials since the in-plane atomic bonds can differ substantially from the out-of-plane ones. Shichibe et al. [167] performed thermal attenuation using several noble-gases and several graphene-covered surfaces. They showed, by comparing the measurements with the classical smooth surface model (Sec. 1.3.3), that Debye-Waller attenuation measurements can be used as a probe of the graphene-substrate interaction and found that an increased M_{eff} is sensed by the scattered atoms from Gr/Ru(0001) compared to clean Ru(0001), 230 and 281 amu, respectively. This increase of M_{eff} for Gr/Ru(0001) has been earlier used in explaining the softening of the RW branch of Gr/Ru(0001), known as the mass loading effect [71].

If we assume a mass loading effect in Gr/Ni(111), similar to that observed in Gr/Ru(0001), which is reasonable due to the similarly strong graphene-metal interaction in both systems [61], then M_{eff} is equal to 6 carbon atoms and 1 nickel atom, i.e. 130.7 amu (and 173 amu for Gr/Ru(0001)). Using these values of the effective masses of Gr/Ni(111) and Gr/Ru(0001) gives the similar values of Debye-temperature for these surfaces, 208 and 275 K, respectively. It is worth mentioning that D. Jackson has calculated $\Theta_{D\perp} = 230$ K for Ni(111) surface [168], and E. Ferrari et al. [169] have measured $\Theta_D = (295 \pm 10)$ K

for the topmost layer of Ru(0001).

On the other hand, the values of Θ_D derived by using $M_{eff} = 1$ carbon atom would give the impression that the out-of-plane lattice vibrations of Gr/Ru(0001) are of a completely different nature from those of Gr/Ni(111). This is not the case, however, as proved by the phonon dispersion measurements presented later in this chapter. The approach of including the atomic mass of the substrate cannot be applied to Gr/Cu(111) and Gr/Ir(111) as it gives unrealistically small values of Θ_D. Similarly, Shichibe et al. found that HOPG and Gr/Pt(111) have the same value of M_{eff}.

Therefore, it will be safer when comparing Debye-Waller attenuation measurements in this work to use the multiplication of $M_S\Theta_D^2$ when analyzing the data. The difference in the Debye-Waller factor $2W(T)$ can thus be explained as a difference in the effective mass of the surface which appears in the Debye-Waller factor multiplied to Θ_D. A smaller effective mass allows for a more efficient momentum and energy transfer from the impinging atoms to the surface leading to stronger attenuation with T_S, which means a smaller Debye-Waller factor.

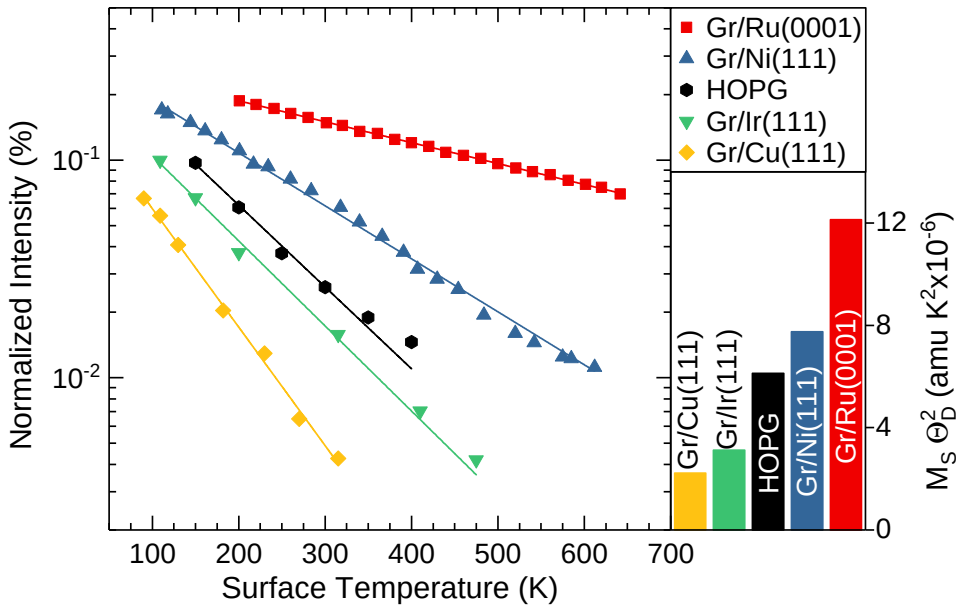

Figure 4.5: Comparison of Debye-Waller factor for different graphitic surfaces. Solid lines are fits according to Eq.(1.13). The inset shows the value of $M_S\Theta_D^2$ in (amu K^2).

Figure 4.5 shows a summary of the Debye-Waller measurements from this work. For completeness, data for Gr/Ru(0001) [23] and HOPG [166] are included. The inset demonstrates how graphene on Cu(111) and Ir(111) have significantly lower $M_S\Theta_D^2$ values when compared to graphene on Ni(111) and Ru(0001). Surprisingly, the $M_S\Theta_D^2$ value of HOPG is relatively high. In the paragraphs below we show how the Debye-Waller factor of Ni(111) and Gr/Ni(111) are very similar, the value can be found in Table 4.1.

Figure 4.6 shows the thermal attenuation behavior of the specular intensity for the scattering of He and Ne from Gr/Ni(111) (black and magenta curves, respectively) and for He scattering from bare Ni(111) (blue). The measurements were performed using the commercial quadrupole mass spectrometer where $\theta_i = 65.6°$. The data is plotted on the left panel in a conventional presentation as $\ln\left[I(T_S)/I(T_0)\right]$ as a function of surface temperature (T_S). This normalization was done with respect to the measured intensity at the lowest temperature (T_0) for each set of measurements. The data is plotted in the right panel after normalization to the atomic mass of the projectile atom m, so

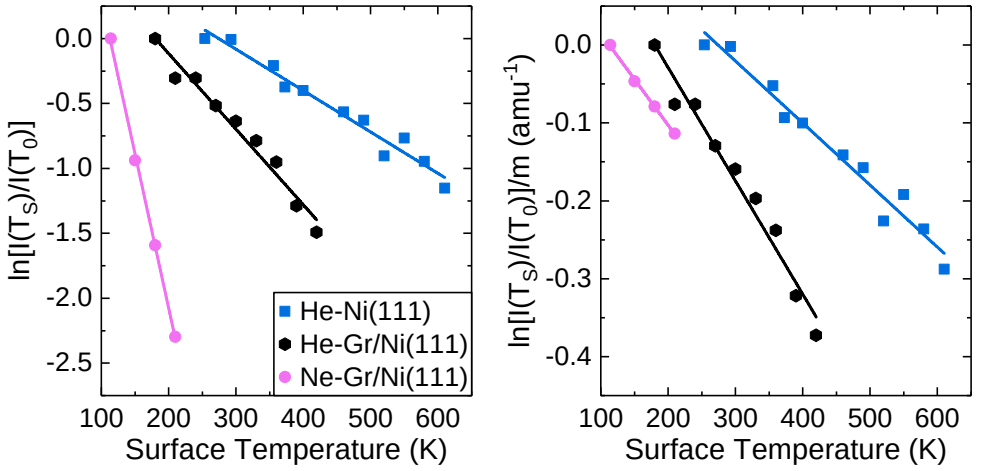

Figure 4.6: Left: Thermal attenuation of the intensity of specularly scattered He (black hexagons) and Ne (magenta circles) from Gr/Ni(111) compared to He from Ni(111) (blue squares). Left: The intensities $I(T_S)$ are normalized to the intensity at the lowest surface temperature $I(T_0)$ of each set. Right: The vertical axis represents the mass normalized Debye-Waller factor exponent where m is the projectile atom mass in amu. Lines are exponential fits. The incident beam energy is 66 meV.

Table 4.1: Temperature gradient of the Debye-Waller exponent with and without normalization to the projectile mass for bare and Gr-covered Ni(111) surfaces. The Debye-Waller argument $2W/T_S$ is in K^{-1} and the normalized argument $2W/mT_S$ is in $K^{-1}amu^{-1}$.

	Ni(111)	Gr/Ni(111)	
	He	He	Ne
$2W(T)/T_S$	0.32×10^{-2}	0.58×10^{-2}	2.38×10^{-2}
$2W(T)/mT_S$	0.80×10^{-3}	1.24×10^{-3}	1.18×10^{-3}

Eq.(1.13) becomes

$$\frac{\ln\left[I(T_S)/I_0\right]}{m} = \frac{-2W(T_S)}{m} = -\frac{24(E_i\cos^2\theta_i + D)T_S}{Mk_B\Theta_D^2}. \tag{4.2}$$

The results of fitting the data in Fig. 4.6 to Eqs. (1.13 and 4.2) are summarized in Table 4.1. The Debye-Waller factor for Ne scattering from Gr/Ni(111) is more than 4 times larger than that of He scattering. This value is acceptable within the Debye-Waller model for this change in the projectile mass. Therefore, within the experimental error, essentially the same mass-normalized Debye-Waller factor is obtained for both He and Ne atoms scattered from Gr/Ni(111). On the other hand, the Debye-Waller factor of He scattering from clean Ni(111) and Gr/Ni(111) is quite similar, especially considering that these are completely different surfaces. However, this similarity is expected because graphene binds tightly to Ni(111), and this tight binding is evidenced by the fact that the dispersion curves of the low-energy phonons from the two surfaces are quite similar, as shown in the next section.

It should also be mentioned that for very heavy atomic projectiles at low energies there is evidence that, due to longer collision times, the mass dependence of $2W$ becomes proportional to $m^{1/2}$ instead of m [170, 171, 172, 173, 174]. Although the normalized $2W$ data shown in Fig. 4.6 and Table 4.1 imply that such behavior does not apply to the lighter–mass Ne at the relatively large energy of 66 meV. The same m scaling was found by Lapujoulade et al. on Cu(100) [117].

4.2 Phonons of Supported Graphene: Gr/Cu(111)

Measurements of thermal expansion and thermal specular attenuation give semi-quantitative information about graphene's interactions with its substrate. HAS experiments also reveal acoustic phonons directly from angle resolved TOF data. As we will show, this is a valuable probe of graphene/substrate interactions - for example it provides a contact point with first principles theory. In addition, obtaining acoustic phonons by HAS also has the potential to provide critical information on thermal properties of graphene samples as acoustic phonons strongly influence the room temperature thermal conductivity of graphene [175].

Several series of TOF spectra have been taken under different incident conditions, in order to get the phonon dispersion curves. A representative series of TOF spectra measured using a Gr/Cu(111)/Al_2O_3 sample with two beam energies is shown in Fig. 4.7.(b); the ones labeled 2 to 3 were collected using beam energy 32 meV and the rest using 43 meV. The spectra were converted from flight time scale to energy exchange scale using Eq.(2.12), taking the diffuse elastic peak to set the zero energy transfer. The sharpness of the diffuse elastic peak (FWHM = 0.66 meV at E_i = 32 meV) denotes the low energy spread of the He beam. The beam energy and surface temperature were varied to find the optimum resolution of the inelastic peaks. For peaks corresponding to low energy and momentum transfer (which correspond to inelastic peaks appearing close to the specular peak) we used low beam energy and surface temperature. Best resolution for inelastic peaks appearing at higher energy and momentum transfer was obtained keeping the beam and surface at room temperature.

The dispersion curves of different surface acoustic phonon modes can be obtained from the angle dependence of the position of the inelastic features in the TOF spectra in energy exchange scale, then the momentum exchange value is obtained using the corresponding scan curve given by Eq.(1.11). Panel (a) in Fig. 4.7 shows the resulting data points from this process; each TOF spectrum gives one or two data points depending on the scattering conditions. Dark and light circles were measured from Gr/Cu(111)/Al_2O_3 and *super G*, respectively. Dashed lines are scan curves mirrored to the first quadrant, black and gray dashed lines correspond to TOF spectra labeled 2 and 4.5 in panel (b), respectively. Two phonon modes appear for small values of phonon wavevector; they appear to cross at ~ 0.35 Å^{-1} then one linear mode is present

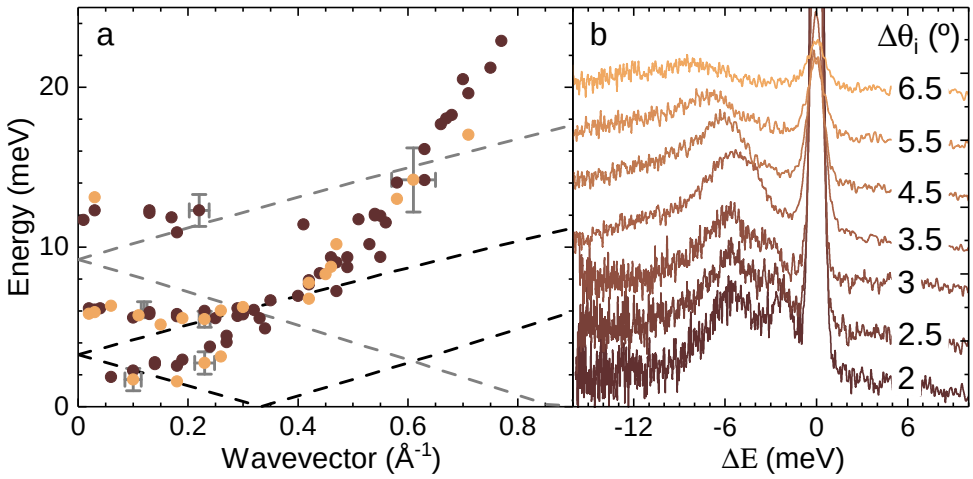

Figure 4.7: (a) Experimentally derived surface phonons for Gr/Cu(111) measured along the $\overline{\Gamma M}$ direction, dark and light points were measured using Gr/Cu(111)/Al_2O_3 and *super G* samples, respectively. Scan curves corresponding to TOF spectra from panel (b) labeled 2 and 4.5 are shown in dashed black and gray lines, respectively. (b) TOF spectra using Gr/Cu(111)/Al_2O_3 taken with beam energies 32 (2 to 3) and 43 meV (3.5 to 6.5).

for large wavevectors. This principal phonon mode can be identified as the ZA (flexural) mode of graphene.

Figure 4.8 shows the phonon dispersion curves of the two Gr/Cu(111) surfaces used in this study (closed circles) measured along the $\overline{\Gamma M}$ and $\overline{\Gamma K}$ directions compared to surface phonons of Cu(111) measured by HAS [176] (open circles) and phonon dispersion curves for Gr/Cu(111) calculated from first principles (gray curves) [177]. The thick curve is a fit of the flexural mode (ZA) according to Eq.(4.4) to be discussed later in details. We can assign most of the observed phonons as flexural phonons, more specifically perpendicular acoustic (ZA) phonon modes. No data points were detected for the longitudinal acoustic (LA) or transverse acoustic (TA) modes. The latter would be anyway forbidden for planar scattering in the $\overline{\Gamma M}$ direction [101]. However, the LA mode should be present, in fact, it has been clearly detected on the graphite(001) surface with HAS [178].

First-principles calculations of the Gr/Cu(111) surface phonons (using LDA-DFT) predict a lifting of 3.14 meV of the ZA mode at the surface Brillouin zone center ($\overline{\Gamma}$ point) [177]. However, our measurements show that his

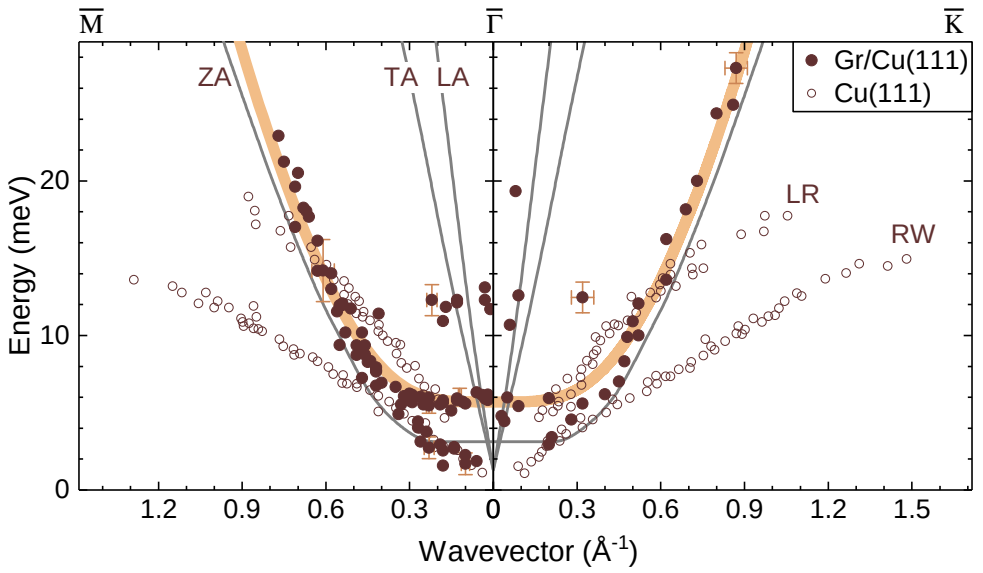

Figure 4.8: Experimentally derived surface phonons for Gr/Cu(111) (closed circles) measured along the $\overline{\Gamma M}$ and $\overline{\Gamma K}$ directions, Cu(111) phonons (open circles) measured by HAS from Ref. [176], DFT calculations for Gr/Cu(111) (dashed gray curves) from Ref. [177]. Thick curve is a fit according to Eq.(4.4).

value is $\omega_0 \sim 5.7$ meV, as clearly seen from the nondispersive part of ZA mode in Fig. 4.8, we assign this to the graphene copper interaction for the 0°R rotational domain because the same value was obtained using *super G* and Gr/Cu(111)/Al_2O_3 samples. A similar feature is seen at $\omega \sim 12$ meV, which can be assigned to an overtone of ω_0. Interestingly enough, the data points for the ZA mode follow a parabolic dispersion only at phonon wave vectors near the center of the Brillouin zone. A deviation from a parabolic law is observed for energies above 7 meV; a quasi-linear behavior is observed above this energy. The deviation from the quadratic dispersion of ZA branch, results in lower values of the phonon group velocity, and thus, a decrease in the relative contribution from ZA phonons to thermal conductivity [55].

The comparison with Cu(111) surface phonons in Fig. 4.8 reveals that the phonon mode below 5 meV and small values of the phonon wavevector is the Rayleigh wave (RW) of the Cu(111) surface. This is a counterintuitive result considering that HAS is a surface-only sensitive technique, however, recent advances in the interpretation of inelastic HAS revealed an interesting feature

where subsurface phonons can be detected. This is known as the *quantum sonar effect* where vibrational modes detectable by HAS can generated at several atomic layers beneath the surface; the depth of these layers is limited by the range of the electron-phonon interaction [100, 104, 179, 180, 181].

The dispersion curve of the flexural mode can be used to derive fundamental quantities of the samples like the graphene-Cu coupling strength (g) and the bending rigidity (κ) [182]. According to a model developed by Karssemeijer and Fasolino [183] for free-standing graphene the dispersion of the acoustic perpendicular (ZA) mode is given by

$$\omega_{ZA}^{free}(\Delta K) = \sqrt{\frac{\kappa}{\rho_{2D}}}\Delta K^2, \tag{4.3}$$

where $\rho = 7.6 \times 10^{-8}\,\mathrm{g/cm^2}$ is the two-dimensional mass density of graphene. A later model developed by Amorim and Guinea [75] includes the effect of coupling the graphene layer to a substrate which introduces a gap at a frequency ω_0 at the Γ point, and the dispersion relation is now given by

$$\omega_{ZA}^{coupled}(\Delta K) = \sqrt{\frac{\kappa}{\rho_{2D}}\Delta K^4 + {\omega_0}^2}, \tag{4.4}$$

where $\omega_0 = \sqrt{g/\rho_{2D}}$ and g is the coupling strength between graphene and substrate. Therefore, from a fit to the experimental data using Eq.(4.4) it is possible to determine both g and κ. We obtain $g = (5.7 \pm 0.4) \times 10^{19}\,\mathrm{N/m^3}$ for the graphene-Cu interaction. This derived value is 2–3 times smaller than that for graphene/SiO_2 interfaces [184]. We also obtain $\kappa = (1.30 \pm 0.15)\,\mathrm{eV}$, consistent with DFT calculations that predict κ = 1.20–1.61 eV [182].

The previous chapter included discussion of the background in angular diffraction spectra and how it can be resolved as the diffuse elastic peak in TOF spectra. The origin of the diffuse elastic peak is attributed to the imperfections on the surface. Its intensity is proportional to the density of translational-symmetry-breaking defects like step edges, vacancies, and adsorbates [4]. Fig. 4.9 shows a comparison of TOF spectra of He scattering from both Gr/Cu(111)/Al_2O_3 and *super G* at $T_S = 120\,\mathrm{K}$ using the same beam energy $E_i = 43\,\mathrm{meV}$ and selected angles of incidence ($\Delta\theta_i$ =3.5° - 6.5°). There are two clear features in each of the spectra: the diffuse-elastic peak at 1.6 ms, and a single phonon creation event with a position near ~ 1.7 ms that changes with $\Delta\theta_i$. The lower intensity of the diffuse-elastic peak in *super G* compared

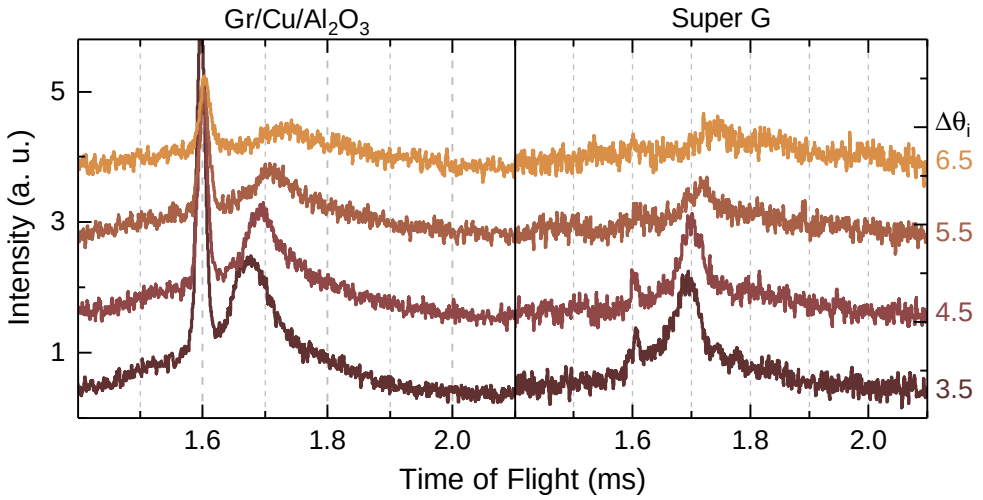

Figure 4.9: Comparison of TOF spectra from Gr/Cu(111)/Al_2O_3 (left) and *super G* (right) at the same experimental conditions (E_i = 43 meV and T_S = 120 K).

to Gr/Cu(111)/Al_2O_3 reflects the lower intensity of defects on the former surface. This result is consistent with the previous discussion on the presence of multiple rotational domains on the Gr/Cu(111)/Al_2O_3 surface and their absence on the *super G* surface in Section 3.1.2. To our knowledge, this is the first experimental work where the diffuse-elastic peak from TOF spectra has been used to compare the quality of a surface from different preparation techniques.

The Absence of LA mode

It is well known that the thermal conductivity in supported graphene decreases by an order of magnitude compared to that in free-standing graphene [175]. It has been suggested that this reduction is caused by leaking of ZA phonons across the graphene-support interface. However, the data shown in the previous section proves that ZA dispersion for Gr/Cu(111) is very similar to the one expected for free-standing graphene. The complete absence of data points from the LA mode suggests that this mode is also involved in heat conduction in graphene.

The kinematic parameters used when collecting a TOF spectrum are used in deriving scan curves that relate energy exchange to momentum exchange

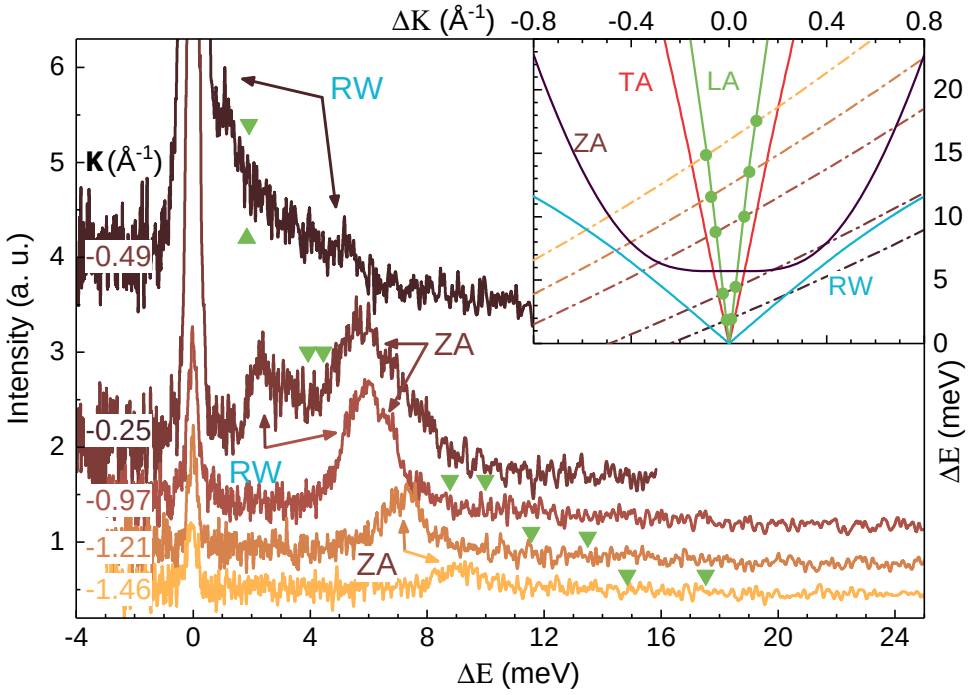

Figure 4.10: TOF spectra from Gr/Cu(111) indicating names of different phonon modes. Green triangles indicates the calculated positions of LA mode in TOF spectra obtained from the crossing of the corresponding scan curve with the LA dispersion curve as shown in the inset. Scan curves are plotted in the same color as their corresponding TOF spectra.

according to Eq.(1.11) are explained in more details in Section 1.3.3. We can estimate the expected position of single-phonon creation or annihilation event on a TOF spectrum when its corresponding scan curve is plotted on top the phonon dispersion curves; the crossing of the scan curve with a dispersion curve corresponds to a peak in the TOF spectrum.

The inset in Fig. 4.10 shows examples of this process. The dispersion curve of the ZA mode of Gr/Cu(111) is a fit of the experimental data according to Eq.(4.4) as in Fig. 4.8. TA and LA modes are theoretical calculations for free standing graphene [46]. The RW mode of the substrate is also plotted since it was detected in the experiment as well. Selected scan curves corresponding to the TOF spectra on the main panel are also plotted and their crossings with the LA mode are indicated by green circles. TOF spectra in Fig. 4.10 were

collected at $E_i = 17\,\text{meV}$ and angles $\Delta\theta_i = -2$ to $-12°$. The momentum exchange of elastically scattered beam parallel to the surface **K** is indicated next to each TOF spectrum in Å^{-1}.

TOF spectra and their corresponding scan curves are plotted in the same colors. The uppermost TOF spectrum in the right panel was measured at $\Delta\theta_i = -2°$, it corresponds to the lowest scan curve in the left panel which crosses the horizontal axis ($\Delta E = 0$) at $\Delta K = -0.25\,\text{Å}^{-1}$. This scan curve crosses RW curve in two different places, both are annihilation events where ΔE of the scattered helium atoms is > 0, however, one is a forward scattering event and the other is a backward scattering event. These two events appear as peaks at the expected ΔE position in the TOF spectrum as indicated by arrows. The second scan curve ($\Delta\theta_i = -2°$ and $\mathbf{K} = -0.49\,\text{Å}^{-1}$) crosses the RW mode in one position and the ZA mode in two close positions. This results in one RW peak and one wide ZA peak in the TOF spectrum. The third TOF spectrum $\mathbf{K} = -0.97\,\text{Å}^{-1}$ shows the peak that results from the crossing of the RW and ZA mode, and the last two spectra show peaks corresponding the ZA mode only.

The expected positions of the single LA phonon events are indicated by green triangles pointing to the corresponding TOF spectrum. Clearly no peaks were detected at any of these positions. Although this mode was measured on graphite(001) surface using HAS in Toennies group [178]. It is worth mentioning that Aksamija and Knezevic [185] predicted that for free-standing graphene nanoribbons (5 µm), thermal conductivity reaches its maximum at 130 K with a maximum contribution of in-plane modes (LA and TA). Their calculations show a maximum of the ZA mode below this temperature (~ 70 K), whereas our measurements reveal that ZA mode is the most dominant feature in TOF spectra at 120 K. This can indicate that either the LA mode has a very low partial density of states at this temperature or that it was affected by the presence of the substrate. Using higher surface temperatures resulted in the dominance of the multiphonon peak.

A. Cocemasov et al. [55] showed that ZA phonons dominate the specific heat in free standing graphene for $T \leq 200K$ and their contribution becomes comparable to that of LA and TA phonons in the temperature range $200K \leq T \leq 500K$. However, this does not imply that ZA phonons make the dominant contribution to the thermal conductivity which depends on the phonon mean free path as well [55]. On the other hand, L. Chen and S. Kumar [186]

found that the LA mode dominates the thermal conductivity of both isolated and supported graphene on Cu substrate and that the life time of ZA modes decreases by an order of magnitude due to the interactions with Cu substrate and ZA mode decreasing the thermal conductivity of Gr/Cu(111) by 44%. The ZA contribution to thermal conductivity decreases due to Umklapp scattering from other in-plane modes [186].

Since we have not detected any sign of LA at this temperature we believe that ZA mode is still the dominant thermal energy carrier in Gr/Cu(111). Our finding falls in-line with the theoretical predictions that ZA mode is the most dominant at this sample temperature. We have performed these measurements two years before the publication of the reviews that highlighted the controversy about the relative contribution of phonon modes in the thermal conductivity of graphene. It might be of interest in the future to perform a study on the effect of increasing the sample temperature on the observed intensities in the TOF spectra.

4.3 Surface Phonons of a Graphene-Passivated Metal: Gr/Ni(111)

Unlike Gr/Cu(111), the strong interaction between Gr and Ni(111) causes a strong softening of the graphene phonons. This softening can be decreased by intercalation with certain metals that interact weakly with Gr. These effects were measured by Oshima and Rieder groups using HREELS in the 1990s [69, 77, 81, 187, 188]. However, HREELS measurements could not access the low energy acoustic modes of Gr/Ni(111); HAS on the other hand, is very suitable for this purpose. The strong Gr-Ni interaction results in a strong hybridization of the Gr π-bands with the d-bands of nickel which creates a 4 eV gap in the electronic structure of Gr at $\overline{\mathrm{K}}$. This gap suppresses the electron-phonon coupling and eliminates the Kohn anomalies. Therefore, Gr/Ni(111) phonons are no longer Raman active [36, 49].

Fig. 4.11 shows the dispersion of the surface phonons of Gr/Ni(111) (full circles) compared to the surface phonons of Ni(111) measured along the $\overline{\Gamma\mathrm{M}}$ high symmetry direction. Two scan curves are also plotted in solid and dashed lines, they correspond to (E_i = 66.7 meV, $\Delta\theta_i$ = 3°) and (E_i = 34 meV, $\Delta\theta_i$ = 6°), respectively. Corresponding TOF spectra are shown in panels (a) and (d) in Fig. 4.12 which were measured on Gr/Ni(111) and Ni(111),

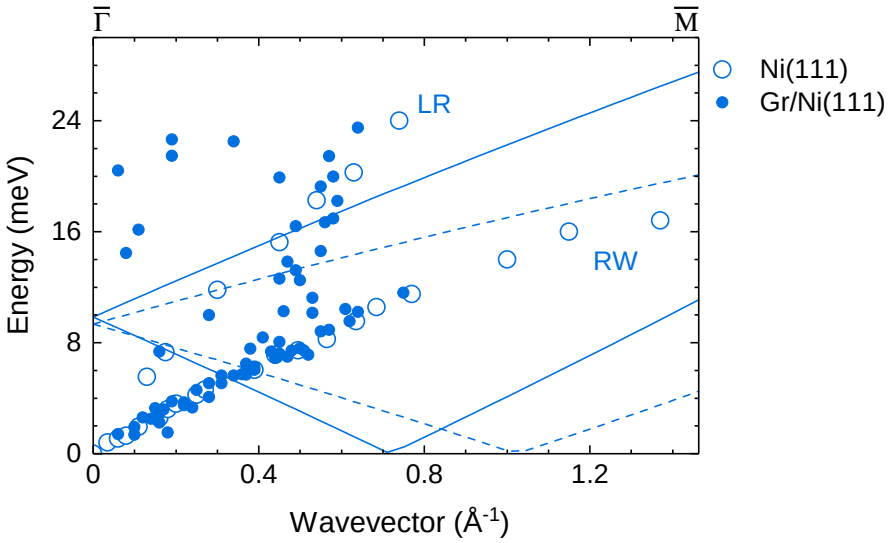

Figure 4.11: Surface phonons of Gr/Ni(111) (full circles) and Ni(111) (empty circles) measured along the $\overline{\Gamma M}$ high symmetry direction. Solid (dashed) line is a scan curve corresponding to TOF spectrum from Gr/Ni(111) (Ni(111)) plotted in Fig. 4.12.a(d).

respectively. In both surfaces the intensity of the RW peaks in the TOF spectra drops very quickly for wavevectors larger than $0.8\,\text{Å}^{-1}$ due to momentum cutoff. In fact, the few peaks above this value were measured in the vicinity of the specular position at $\Delta\theta_i < \pm 1°$.

Basically, the lower-energy acoustic surface phonon of Gr/Ni(111) follows exactly the RW dispersion of Ni(111) below $0.4\,\text{Å}^{-1}$, this is almost one third of the surface Brillouin zone. It splits afterwards into two modes, one continues following the RW mode and the other is more likely to be the ZA mode. Later in this section we discuss this with further details by comparison to previous measurements and calculations.

Representative TOF spectra converted to energy transfer scale taken at different incident conditions along the $\overline{\Gamma M}$ and $\overline{\Gamma K}$ directions for Gr/Ni(111) and bare Ni(111) are shown in Fig. 4.12. Scan curves using Eq.(1.11) are shown in black lines in each panel of this figure. The vertical axes show the value of momentum transfer of the scan curves; the intensities of the TOF spectra are not shown since their absolute values are not of importance for this discussion. Each spectrum was fitted with multiple Gaussian peaks. The diffuse elastic peak (blue shaded) was taken as the zero in the energy transfer scale.

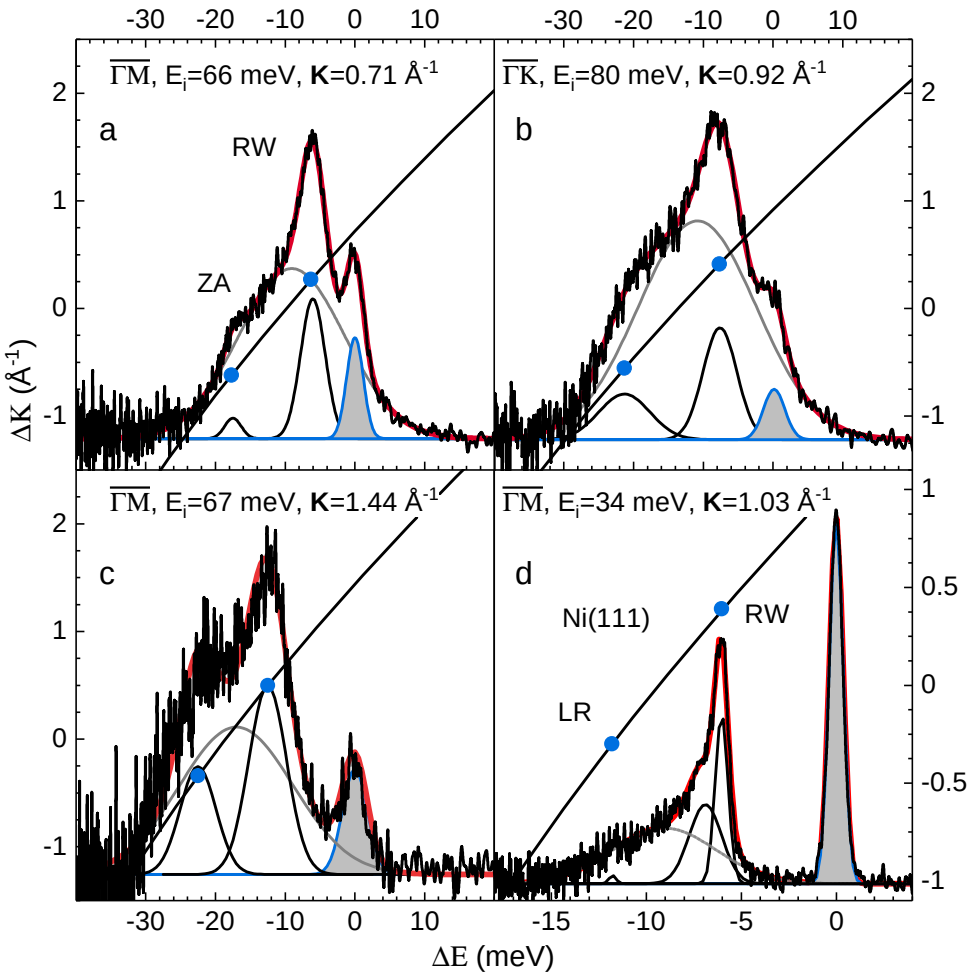

Figure 4.12: Selected TOF spectra in energy exchange scale for Gr/Ni(111) (a, b and c) and Ni(111) (d); the intensity scales of the TOF spectra are not shown. TOF spectra were fitted by multiple Gaussian peaks: diffuse elastic (blue, filled), broad multi–phonon peak (gray) and phonons. Solid black lines are scan curves; the corresponding momentum transfer ΔK are indicated on the vertical scales. The blue circles are data points extracted from these TOF spectra.

Multiphonon peaks (gray) appear as broad features that dominate the energy exchange between He-atoms and the studied surfaces. Peaks corresponding to different phonon modes, discussed later in details, are labeled: Rayleigh wave (RW), longitudinal resonances (LR) and out–of–plane acoustic mode (ZA).

The dominant feature in clean Ni(111) TOF spectra (Fig. 4.12.d) corresponds to the RW; the LR mode has very low intensity in comparison. A third peak appears close to RW peak which belongs to the bulk band edge, a similar feature was also reported from a Pt(111) surface [189]. Gr/Ni(111) TOF spectra in Figs. 4.12.a-c show two clear peaks other than the multiphonon peak: the peak with the higher intensity belongs to a mode that matches the dispersion of the RW mode of the substrate, while the smaller one belongs to the ZA mode of the graphene layer.

The width of the diffuse elastic peak, which corresponds to the energy spread of the incident beam, increases from 1 to 4 meV when increasing the beam energy from 34 to 80 meV, so clearly a lower incident energy is the best choice for resolving phonon modes with small energies whereas a higher energy is required to avoid the energy cutoff [190]. The intensity of the diffuse elastic peak decreases for higher beam energies while the intensity of the multiphonon peak increases due to the Debye-Waller effect. Therefore, up to 6 hours of data accumulation were needed for many of these measurements.

In this work, we have measured the low-energy part of the dispersion curves of the acoustic phonon modes for Gr/Ni(111) in the $\overline{\Gamma M}$ and $\overline{\Gamma K}$ directions of the surface Brillouin zone and the phonon dispersion of bare Ni(111) along $\overline{\Gamma M}$. Figure 4.13 shows the measured data in blue circles for Gr/Ni(111) and blue dashed lines for Ni(111); LR and RW dispersion were determined experimentally along the $\overline{\Gamma M}$ direction and mirrored to the $\overline{\Gamma K}$ side for visual comparison. For completeness, the figure also includes the low-energy data measured by HREELS along $\overline{\Gamma M}$ [69] and $\overline{\Gamma K}$ [187] (red circles) as well as results reported by *ab initio* calculations (dashed lines) [49]. The thick cyan curve is a fit of the flexural mode (ZA) according to Eq.(4.4).

The most pronounced feature in the measured phonon dispersion is the presence of the same RW of Ni(111) up to half the surface Brillouin zone in the $\overline{\Gamma M}$ direction, where it undergoes a hybridization with the LR mode, while no hybridization between LR and RW modes was observed for the bare Ni(111) surface. Also, a few data points of the LR mode have also been detected in the Gr/Ni(111) measurements. Since the He-phonon interaction is directly related to the electron-phonon coupling strength [100] and due to the strong C-Ni bonding, it is not surprising to detect the RW mode of the metallic substrate as has been the case for Gr/Ru(0001) [71]. Unlike the latter, no data points of RW of Gr/Ni(111) could be measured in the second half of the surface Brillouin zone due to the momentum cutoff for out-of-plane vibrations at large wave

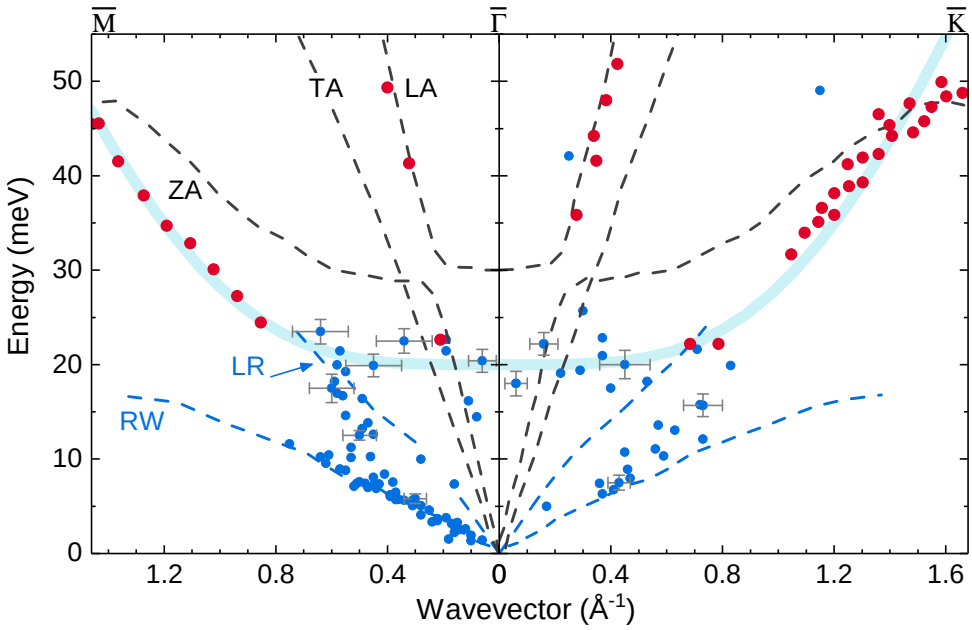

Figure 4.13: Surface phonon dispersion of Gr/Ni(111) along the $\overline{\Gamma M}$ and $\overline{\Gamma K}$ directions. Black circles are current low–energy data for Gr/Ni(111). Red circles: HREELS data from [69, 187]. Dashed gray lines are *ab initio* calculations of the Gr/Ni(111) modes [49]. Blue circles are measured data of Ni(111) surface phonon dispersion in $\overline{\Gamma M}$, Blue dashed lines are Ni(111) data mirrored from $\overline{\Gamma M}$ for visual comparison.

vectors, and thus no information on the mass loading effect could be obtained from the phonon dispersion.

Even more surprising is the different behavior of RW along the $\overline{\Gamma K}$ direction, where the data points appear at slightly higher energies. We note that the sagittal plane is not a mirror symmetry plane for the atomic displacements of the Shear Horizontal (SH) mode of Ni(111) in the $\overline{\Gamma K}$ direction, and thus the coupling to the impinging He-atoms' momentum to this mode is not forbidden by symmetry as is the case in the $\overline{\Gamma M}$ direction.

Only two data points corresponding to the LA mode have been resolved along $\overline{\Gamma M}$, while in the $\overline{\Gamma K}$ direction the large scattering of the data points at ca. 20 meV near $\overline{\Gamma}$ could be a result of the avoided crossing of the LA and ZA modes. Well-resolved peaks were not obtained because the elastic scattering is dominated by the multi-phonon scattering. The few resolved data points

are in good agreement with the dispersion curves measured by HREELS and calculated for LA mode of Gr/Ni(111).

Fitting our data, with consideration of HREELS data, using Eq.(4.4) gives $g = (7.2 \pm 7.0) \times 10^{20}\,\mathrm{N/m^3}$ and $\kappa = (0.43 \pm 0.07)\,\mathrm{eV}$. This gives an energy of $\omega_0 \sim 20\,\mathrm{meV}$ for the ZA mode at the $\overline{\Gamma}$ point. When compared with the value obtained for Gr/Cu(111), it is clear that the Gr-Ni coupling is much stronger, and that the graphene bending rigidity is reduced as a consequence of being forced to follow the surface vibrations of the Ni atoms.

It is worth pointing out that the DFT calculations reported in Ref. [49] for Gr/Ni(111) provide a good description of the optical phonon branches, including the softening of the ZO mode and the suppression of the Kohn anomaly observed by HREELS [69, 187] along $\overline{\Gamma\mathrm{M}}$. Actually, from the overestimation of the ZA/ZO gap at $\overline{\Gamma}$ and $\overline{\mathrm{K}}$ the authors of Ref. [49] concluded that their LDA calculations may be overestimating the adsorption strength of graphene on the Ni substrate, while the GGA calculations underestimated this value. Our current results seem to confirm this view. Although, the GGA calculations gave a reasonable value of ω_0.

The strong coupling strength between Gr and Ni(111) will enhance the thermal conductivity, because of the coupling of the ZA mode to the substrate RW results in a hybridized mode with higher group velocity than the original ZA mode in graphene [54].

Finally, the fact that the lowest observed branch on Gr/Ni(111) is actually the substrate RW accounts for the observed high specular reflectivity (ca. 20 %) to He atoms, and confirms that systems with a strong C-substrate interaction are the best candidates to be used as focusing mirrors in scanning He atom microscopy.

4.4 Effect of Moiré Structure on Phonon Dispersions: Gr/Ir(111)

Recent measurements of the phonon dispersion curves for Gr/Ir(111) using HREELS [74, 191] showed very small deviations from those of free standing graphene with two main differences: The Kohn anomaly at $\overline{\mathrm{K}}$ is weaker due to a decrease of the electron-phonon coupling (as a result of screening of graphene electron correlations by the metal substrate); and the moiré superstructure induces replicas of graphene phonon modes.

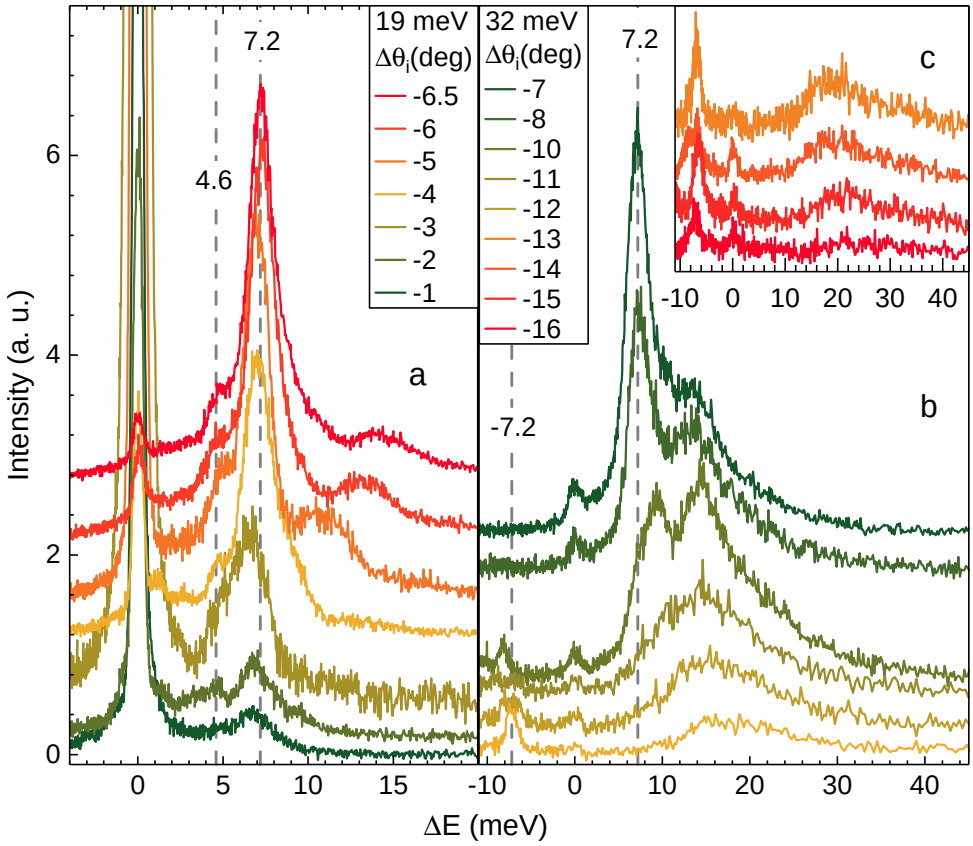

Figure 4.14: TOF series of He scattering from Gr/Ir(111) at different $\Delta\theta_i$ relative so the specular position, indicated in the legend, with beam energies 19 meV (a) and 32 meV (b and c). Gray dashed lines indicate features at 4.6 meV and ±7.2 meV.

The similarity of surface phonon modes of Gr/Ir(111) to those of free standing graphene is a result of the weak chemisorption of the 0°R Gr domain on Ir(111) [154]. Therefore, we expect to measure a ZA mode similar to that of Gr/Cu(111). However, the presence of a moiré superstructure might result in extra modes similar to what has been observed for Gr/Ru(0001) [71].

First we start by presenting TOF measurements on Gr/Ir(111) as they showed multiple features that were not observed in Gr/Cu(111) or Gr/Ni(111) measurements. Fig. 4.14 shows a series of TOF spectra measured using two beam energies and various angles of incidence along the $\overline{\Gamma M}$ direction of the

surface Brillouin zone of Gr. Spectra on panel (a) were measured using 19 meV He beam, we can identify clearly two nondispersing modes one with a small intensity at 4.6 meV and a more dominant one at 7.2 meV, we also observe a dispersing feature that can be clearly resolved for $|\Delta\theta_i| \geq 5°$. The feature at 0 meV is the diffuse elastic peak.

The spectra on panels (b and c) were measured using a higher beam energy (32 meV), the 7.2 meV peak is the most dominant feature, it also appears at −7.2 meV for angles farther that −10° from the specular position (equivalent to $\theta_i \geq 62.7°$). Panel (c) is a continuation of the TOF series in (b) with a close-up of the vertical axis, it shows how the intensity of the −7.2 meV feature becomes larger than that of the diffuse elastic peak at an angular position far from the specular position. Note that negative $\Delta\theta_i$ values mean that the incident angle is larger than the specular and thus, corresponds to larger values of $\mathbf{K}_i$ relative to the specular position.

The intensity of the diffuse elastic peak decreases with increasing $|\Delta\theta_i|$. However, a fit of the intensities of this peak showed that it is proportional to $1/\Delta K$ and thus, the decrease of intensity is slower than what would be expected from only point or only line defects. The intensity of the diffuse elastic peak in Gr/Ir(111) TOF spectra is in general much smaller than that of Gr/Ru(0001) [71]. This is a counterintuitive observation since Gr/Ru(0001) usually grows in very good quality compared to Gr/Ir(111). Due to the weak Gr-Ir interaction, the graphene layer which requires a high preparation temperature, suffers wrinkling upon cooling down. These wrinkles are expected to increase the intensity of the diffuse elastic peak. This observation can indicate an effect of the moiré corrugation on the diffuse elastic peak.

Our measurements show that the 4.6 meV feature is well resolved for low beam energies (< 20 meV) whereas it disappears completely when using a slightly higher energy (> 30 meV) (see Fig. 4.14). The 4.6 meV feature was not detected using a 32 meV beam energy even when using the same angles as in panel (a), despite of the low energy spread of the incident beam (2%). The 7.2 meV mode in panel (b) of Fig. 4.14 starts dispersing at $\Delta\theta_i = -10°$. The spectra in this panel also show another nondispersing feature at ∼ 14 meV. The intensity of this mode appears to dominate to spectra for $|\Delta\theta_i| \geq 10°$. These two modes overlap and become hard to resolve with increasing $|\Delta\theta_i|$, the derived phonon dispersion from this overlapping appears as an anomalous mode.

Figure 4.15 shows the experimentally determined vibrational modes of

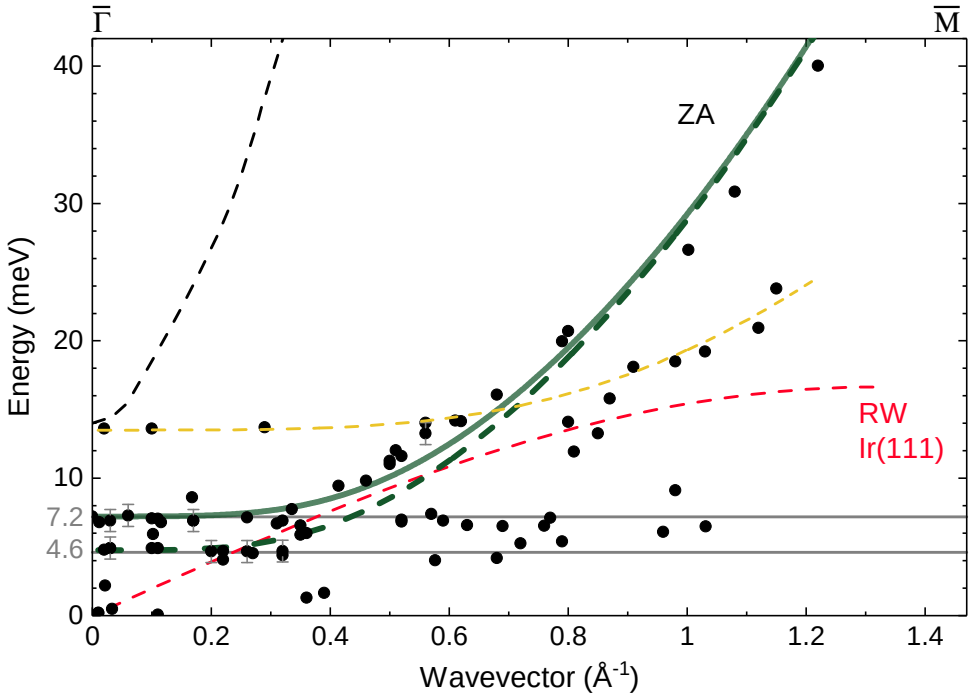

Figure 4.15: Vibrational modes of Gr/Ir(111) measured by HAS (black circles) compared with the RW of Ir(111) measured by HAS (dashed red line), also LA mode of Gr/Ir(111) is plotted (dashed black lines) [191]. Solid and dashed green lines are different fits of the ZA mode using Eq.(4.4). See text for the dashed yellow curve.

Gr/Ir(111) measured by HAS in black circles. The horizontal lines at 4.6 and 7.2 meV indicate well resolved features in the TOF spectra which can be seen in panel (a) in Fig. 4.14. We have also measured the RW of clean Ir(111), it is plotted in a red dashed line on the same graph for comparison.

The solid and dashed green curves are fits of two different flexural modes of Gr/Ir(111) using Eq.(4.4). The two modes have different energies at the surface Brillouin zone center $\overline{\Gamma}$, $\omega_0 = (7.2 \pm 0.5)$ meV for the solid curve and $\omega_0 = (4.6 \pm 0.7)$ meV for the dashed curve. From this fit we could obtain a bending rigidity and coupling strength for Gr/Ir(111). The solid curve yields $\kappa = (0.80 \pm 0.07)$ eV and $g = (10.3 \pm 1.5) \times 10^{19}$ N/m^3 and the dashed curve yields $\kappa = (0.86 \pm 0.05)$ eV and $g = (3.6 \pm 1.0) \times 10^{19}$ N/m^3. Note that the value of the coupling strength for Gr/Cu(111) ($(5.7 \pm 0.4) \times 10^{19}$ N/m^3) falls between the two values obtained for Gr/Ir(111).

The observation of two flexural modes can be attributed to the presence of two rotational domains 0°R and 30°R. ARPES measurements showed that the 30°R domains are physisorbed while 0°R are chemisorbed on the Ir(111) substrate [154], and thus, it makes sense that two coupling strengths from two different rotational domains can be measured. However, we have used LEED to verify the presence of only the 0°R domain before the measurement which raises doubts about this conclusion.

The anomalous mode, plotted in a dashed yellow line in Fig. 4.15, with $\omega = 14$ meV at $\overline{\Gamma}$ results from the aforementioned nondispersing feature in Fig. 4.14.b which overlaps with the ZA mode. The energy of this mode appears to be an overtone of the 7.2 meV mode. Such an overtone has also been observed for Gr/Cu(111) (see Fig. 4.8), although with much lower intensity. The dispersing part of this mode, along with the nondispersing data points from the two ZA mode (with wavevector $> 0.5\,\text{Å}^{-1}$) appear to be a result of Umklapp scattering process. In this process, phonons with wavevectors larger than that of the reciprocal lattice vector of the moiré superstructure can scatter back to a different moiré Brillouin zone which reduces their wavevector. It is worth mentioning that Endlich et al. [191] reported the observation of what they called *replicas* of the ZA mode induced by the moiré superstructure in their HREELS measurements of Gr/Ir(111) phonon dispersion curves.

An interesting effect was observed when a TOF spectrum was collected at the position of a moiré diffraction peak using a high beam energy. Since diffraction peaks are elastic in nature, the dominant feature in the TOF spectra at these angular positions is expected to be the elastic peak where $\Delta E = 0$. However, our measurements showed a different result. Panel (a) in Fig. 4.16 shows a series of TOF spectra taken with He beam of energy $E_i = 66$ meV and different $\Delta\theta_i$ relative to the specular position. Another TOF spectrum taken at the specular position (not shown) was used to determine E_i and mark the elastic peak position. Panel (b) shows an angular diffraction spectrum with the same beam energy, the vertical lines indicate the angular position at which the TOF spectrum of the same color was collected. The red-to-orange TOF spectra show the dispersion of the ZA mode, while the green spectra which coincide with the first and second order moiré diffraction peaks show a significant increase of the 7.2 meV peak.

Panel (c) in Fig. 4.16 shows TOF spectra measured with an 18 meV He beam and panel (b) shows an angular diffraction spectrum with the same beam energy. As expected, the intensity of the diffuse elastic peak increases

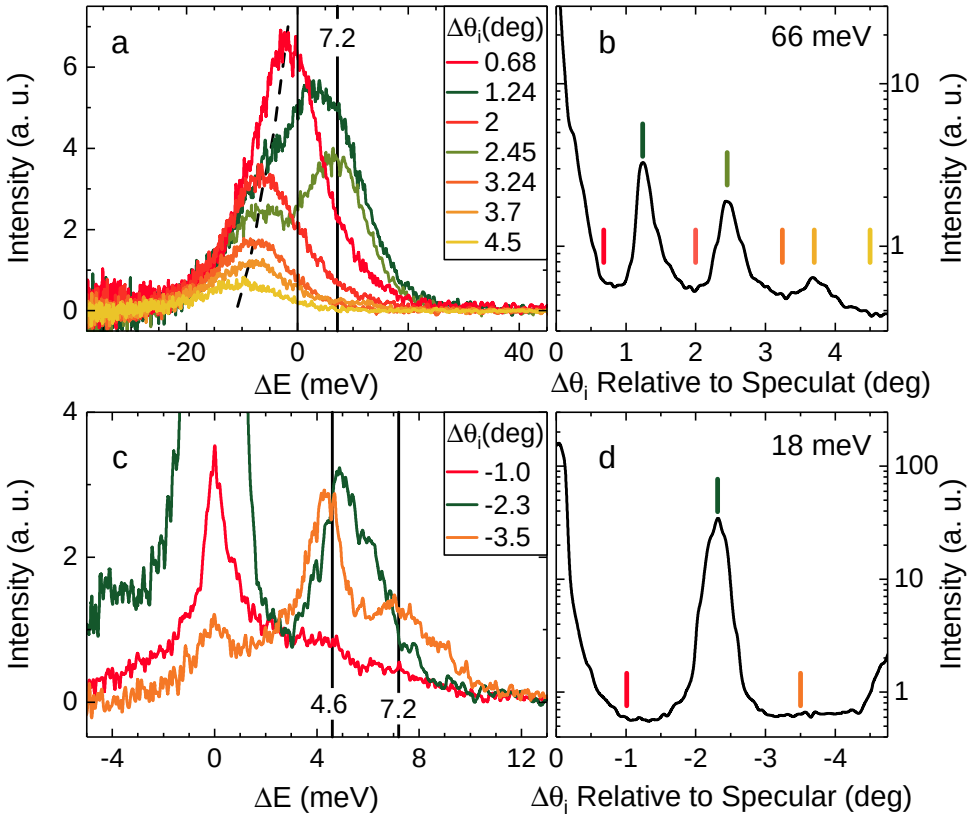

Figure 4.16: (a and c) TOF spectra at angles indicated in the legends using beam energies E_i = 66 and 18 meV, respectively. (b and d) Angular diffraction from Gr/Ir(111) with the same E_i in panels to their left, colored lines indicate angular position TOF spectra of the same color.

significantly when conducting a TOF measurement in the angular position of a diffraction peak. Note that the intensity of the 4.6 meV mode is significantly larger than that in Fig. 4.14.a. Although, the TOF spectra in figures 4.14 and 4.16 show that the detection of the 4.6 meV mode depends on the incident beam energy, it is not clear how this small change in beam energy can cause such an increase in the mode intensity. Theoretical calculations are needed for further understanding of this data.

Whereas, interpreting the presence of two ZA modes as a result of rotational domains is appealing, other observations like the low intensity of the diffuse

elastic peak and our LEED measurements weaken this assumption. Also the observation of the high intensity of the 7.2 meV mode at the angular positions of moiré diffraction peaks indicates that the moiré superstructure might play a role in the presence of two ZA modes. Since the moiré structure shows a large corrugation of $\sim$ 0.3 Å and the mean graphene-Ir(111) separation is $\sim$ 3.4 Å [192], it is possible that the regions farthest from the substrate have slightly different lattice dynamics that the regions closest to the substrate. In fact, DFT calculations [192] showed that the binding of the 0°R is not pure but is rather chemically modulated, where the carbon atoms in the moiré regions closer to the substrate form a weak covalent bond with Ir atoms. It is worth mentioning that Wu et al. [78] reported HREELS measurements for Gr/Ru(0001) where the ZA mode approached $\sim$ 27 meV at the $\overline{\Gamma}$ point, whereas Maccariello et al. [71] used a double linear chain model to fit HAS data for Gr/Ru(0001) and obtained a value of $\sim$ 16 meV for the ZA mode at the $\overline{\Gamma}$ point. This discrepancy requires a careful analysis, however, it falls in-line with our argument of the distinguishable moiré regions in phonon dispersion curves. Thus, there are actually two identifiable regions inside the moiré cell and the lattice dynamics are slightly different between them. We could identify the 4.6 meV mode as the one from the heights and the 7.2 meV mode as the one from the valleys of the moiré corrugation.

On the moiré corrugation of Gr/Ru(0001)

We have discussed earlier in Section 3.3.2 the corrugation of the moiré superstructure in Gr/Ir(111) and Gr/Ru(0001) and showed how HAS measurements indicated a much higher corrugation for the former. Clearly, this result contradicts the observations from other surface analysis techniques. However, in this chapter we have discussed how the Debye-Waller measurements revealed that HAS intensities are sensitive to the Gr-substrate bond strength, we have also found that phonon measurements indicate that HAS is sensitive to very small variations of the bond strength within the moiré unit cell as concluded from the phonon dispersions of Gr/Ir(111).

Now, consider the case of Gr/Ru(0001); the lowest regions of the moiré superstructure are separated from the substrate by 2.1 Å and the highest regions by 3.6 Å [61]. It is clear from the above observations that helium atoms impinging on these two regions are sensing two different surface masses. The lowest regions are almost 2.5 times as massive as the heights. As a result,

the two regions will give two different Debye-Waller factors. This should be considered when normalizing the intensities of the diffraction peaks using Debye-Waller factor as required for theoretical calculations. The measured intensity of specular HAS can be a result of reflection from only the lowest regions with a high effective mass while the high regions will have a negligible contribution. On the other hand, the intensity of the moiré peaks results from the interaction of He atoms with the two regions within the moiré unit cell where the contribution from the high regions is not negligible. Therefore, the intensities of the moiré diffraction peaks cannot be normalized to the intensity of the specular peak as was done for HAS measurements from Gr/Ru(0001) [157].

In fact, classical scattering of high-energy heavy-noble-gas atoms from room temperature Gr/Ru(0001) showed the same effect. Shichibe et al. [167] performed two-mass simulations using the classical smooth surface model and found that their scattering measurements can be explained only by assuming two different masses of the surface: one was equivalent to the mass they used for HOPG and the other one is heavier by including a contribution from the substrate.

This observation is interesting as it shows how HAS provides spatial resolution below 20 nm for spectroscopic measurements.

Chapter 5

Suppression of Quantum Coherence in Ne Atom Scattering

Helium is the preferred projectile gas in surface analysis by atom scattering due to its low mass and thus relatively large wavelength. The use of heavy-noble-gas atoms is disfavored in spectroscopy measurements, especially on hot surfaces, due to increasing thermal attenuation of the scattered beam where incoherent dynamics play an increasing role in the scattering process compared with the quantum part [193]. However, neon has been shown in many cases to give richer information about the surface [83, 85]. DFT calculation of rare-gas scattering from Ru(0001) [86] showed that anticorrugation effects are not present in Ne diffraction, contrary to He and Ar. Therefore, it is expected that a better contrast can be obtained using Ne in the neutral atom microscope.

Quantum effects can persist in atom-surface scattering even at high translational energies in spite of an expected transition from the quantum to the classical regime due to a small de Broglie wavelength, where energy-loss processes through purely mechanical exchange have been predicted to have an important effect on the distribution of the scattered lobe of projectile atoms [194]. For example, grazing-angle atom scattering with keV energies has produced quantum diffraction patterns, which is possible because only a small amount of the projectile's energy is dissipated to the crystal lattice under channeling conditions, even at high surface temperatures [195, 196, 197]. Even more intriguing is the restoration of quantum coherence in Ne scattering from $c(2\times2)$Li/Cu(100), where the low-energy out-of-plane phonons are suppressed, since high frequency phonons are not easily excited in a low energy collision

(which is the case for Ne scattering) phonon exchange is rendered ineffective. This results in the quenching of the argument of the Debye-Waller factor ($2W(T_S)$), which has been shown to be related to the phonon density of states (spectral density) [198, 199, 200].

While grazing-angle scattering measurements are an interesting example of the persistence of quantum coherence, despite the high projectile energies employed, we show here how the coherence can be almost completely lost for low beam energies due to a small increase in the surface temperature. We show angle-resolved and energy–resolved scattering measurements of Ne atoms with translational energy of 66 meV from a Ni(111) surface at temperatures up to 420 K and we compare our data to the earlier Ne scattering work of Feuerbacher and Willis [201] from this same surface. Although the Debye-Waller factor can be relatively large for this system, as evidenced by the appearance of a well-defined quantum specular diffraction peak at lower temperatures, increasing the temperature from 300 to 420 K results in losing all single-phonon features in the TOF data. We also show that a classical model, described in Section 1.3.3, provides very good description of the measured data at these slightly higher temperatures despite the presence of a small quantum specular reflection from the surface.

The investigation of the quantum-to-classical boundary is certainly an important issue, and here we discuss the possibility of using atom-surface scattering experiments to explore this subject. A second motivation for understanding inelastic losses in atom-surface scattering is the need to improve the reflectivity of mirrors for potential use in scanning matter-wave microscopy [15, 19, 21, 76]. Yet another need for understanding the nature of classical features is that in some circumstances they can appear as peaks in the energy-resolved spectra that mimic the appearances of single-phonon quantum excitations; for example, a classical feature can be mistaken for an anomalous phonon or plasmon dispersion when its energy is mistakenly plotted as a function of parallel momentum transfer [202].

5.1 Neon Diffraction from Clean Metals

Figure 5.1 (left panel) shows angular distributions of He and Ne atoms scattered from a clean Ni(111) surface, taken with fixed θ_{SD} and plotted as a function of $\Delta\theta_i$ relative to the specular position. The beam energy in all these

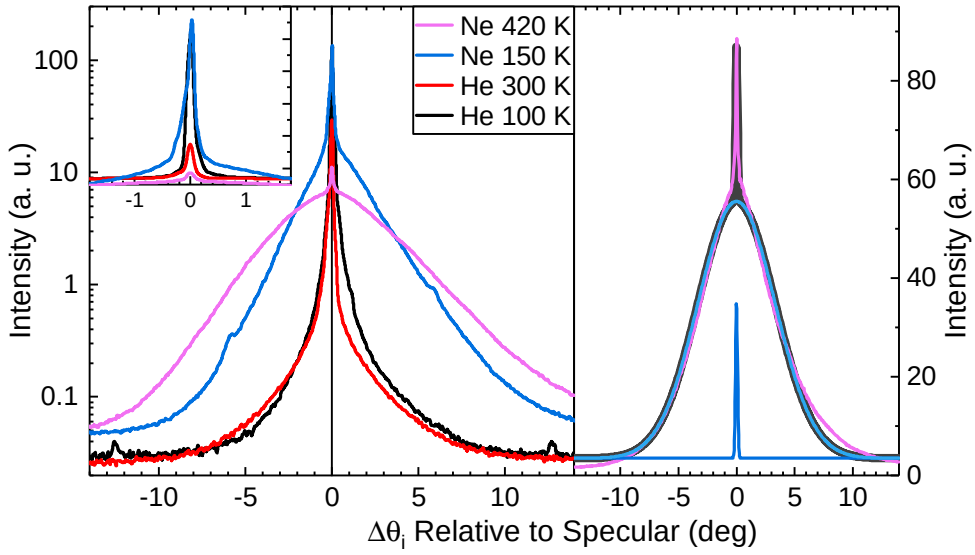

Figure 5.1: Left: Angular distributions of He and Ne scattered from Ni(111) at different surface temperatures and plotted on a logarithmic scale. The incident energy is 66 meV. The vertical line at 0° is for visual guidance. The inset is a close-up of the vicinity of the specular peak where the intensity is plotted in a linear scale. Right: Two Gaussian peak fit of the magenta diffraction spectrum from the left panel.

spectra is 66 meV, and the incident direction is along the high-symmetry direction $\overline{\Gamma M}$. The black spectrum exhibits He-diffraction peaks from a cold Ni(111) surface (100 K); the position of the peaks corresponds to a periodicity of (2.48 ± 0.02) Å, in agreement with the nearest-neighbor distance on the Ni(111) surface. Increasing the surface temperature to 300 K (red spectrum) lowers the intensities of the diffraction and specular peaks and gives rise to a broad background peak resulting from inelastic scattering. This background is slightly shifted to the left (subspecular) in comparison with the spectrum measured at 100 K.

The inelastic background is more prominent in the angular distribution spectra recorded for Ne scattering. Diffraction peaks are visible in the spectrum measured from a cold surface (blue) at $\Delta\theta_i = \pm(5.9 \pm 0.6)°$ from the specular position. When the surface temperature is increased, the intensity of both the specular and diffraction peaks is strongly reduced (magenta spectrum). This behavior is similar to the one observed for He scattering, however, there is a noticeable difference; in comparison with the case of He scattering the

Table 5.1: Parameters used in fitting the angular distribution spectra in Fig. 5.1 by two Gaussian peaks. A is the area under the inelastic peak normalized to the elastic peak for each spectrum. C is the shift in degrees of the center of the inelastic peak relative to the elastic peak. FWHM and FWHM_e are the widths in degrees of the inelastic and elastic peaks, respectively. Beam energy is 66 meV, and T_S is the surface temperature.

Gas	T_S (K)	A	C	FWHM	FWHM_e
He	100	0.4	0.04	0.76	0.13
	300	0.9	-0.10	0.53	0.14
Ne	150	5.3	0.23	4.38	0.21
	420	61.4	0.00	7.80	0.21

asymmetry in the inelastic background is observed even for the cold surface in the case of Ne where it is shifted to the right (supraspecular). We have chosen the temperature 420 K for our measurements because the Ni(111) surface gets contaminated quickly with adsorbates from the residual gases in the scattering chamber (mainly H_2) below this value. This contamination is very easily detected by HAS due to the large cross section of He scattering from single defects on the surface [5].

Table 5.1 summarizes the results of performing a two Gaussian peak fit to all the spectra shown in Fig. 5.1 (left panel). The intensity (area under the peak) of the inelastic peak relative to that of the elastic peak is shown by A. Whereas this value is smaller than 1 in the case of He scattering, it increases up to 61 for Ne scattering, indicating that inelastic scattering becomes the most important feature for this system. Actually, the background in the He spectra follows mostly a $1/\Delta K^2$ form, where ΔK is the momentum exchange parallel to the surface, rather than a Gaussian distribution. As discussed in more details in Section 3.2.2, this is an effect of surface defects, which also appears in the Ne angular distributions as a fit residual but with less significance. Therefore, the intensities for He peaks in Table 5.1 serve only for a qualitative comparison.

C in Table 5.1 gives the angular shift (in degrees) of the center of the inelastic peak relative to the elastic one. We have shown a similar comparison in Section 3.2.2, where the inelastic peak shifts by changing the surface temperature or the beam energy for He scattering from Gr/Ni(111). This explains

why the angular distributions of the scattering of heavy Ne from a hot surface and of light He from a cold surface are symmetric, while the inelastic peak in the case of Ne scattering from a cold surface is supra-specular and that of He scattering from a hot surface is subspecular.

The widths of the inelastic peaks (FWHM) and the elastic peaks ($FWHM_e$) are shown in the last two columns in Table 5.1. While the elastic peak maintains its width for different surface temperatures, as expected from the Debye-Waller model [5], the width of the inelastic peak increases significantly. The broadening of the inelastic peak with increasing temperatures agrees with the predictions of the SSM model of Eq.(1.14) and with the calculations done with a classical theory by Pollak and Miret-Artés [203] for the scattering of Ar from the Ag(111) surface.

The parameters of the calculation using the SSM model were fitted by weighted least-squares, giving lower weight to data points close to $\Delta E = 0$ since they show a substantial quantum component. The surface effective mass was $M = 164.1$ amu, equivalent to the mass of 2.8 Ni atoms. The phonon average velocity was $v_R = 2606.5\,\mathrm{m\,s^{-1}}$. These values are consistent with those used previously for heavy-rare-gas scattering from clean-metal-surfaces [110, 165].

Debye-Waller factor The validity of the theoretical smooth surface model (SSM) for classical scattering [98], discussed in Sec. 1.3.3, requires that the Debye-Waller exponent $2W(T_S)$ in Eq.(1.13) is much larger than 1. However, it is not easy to obtain the value of $2W(T_S)$ directly by measuring the thermal attenuation behavior of Ne scattering from Ni(111) mainly due to two factors: (1) the surface gets contaminated quickly at low temperatures, affecting the specular peak intensity, and (2) the inelastic background overcomes the specular peak quickly with increasing surface temperatures. Therefore, we have performed a comparative extrapolation by comparing the values of the mass-normalized factor for He and Ne scattering from Gr/Ni(111), shown earlier in Fig. 4.6. Since this is an inert surface, it remains clean at low temperatures. In addition, the effective surface mass M in Gr/Ni(111) is sufficiently high and expected to be similar to that of clean Ni(111) due to the strong Gr-Ni bond [70, 204]. These properties allow for the measurement of the Debye-Waller factor for Ne scattering from Gr/Ni(111), and the resulting values of $2W(T_S)$ are expected to be similar for Ne scattering from clean Ni(111) since these surfaces show similar low–energy phonon dispersions which are largely responsible for

the inelastic scattering [70, 200].

One of the main underlying reasons for the analysis of the Debye-Waller factors in this work is to show that $2W(T)$ for Ne scattering from clean Ni(111) in the temperature range of these experiments is large enough for the classical SSM of Eq.(1.14) to be valid. From the data shown in Fig. 4.6 and Table 4.1 the value of $2W(T_S)$ for Ne scattering from the Gr/Ni(111) surface can be extrapolated to give $2W(420) \approx 10$, implying that the classical theory is valid for that system. If we make the reasonable assumption, as was directly measured for He scattering, that also for Ne and clean Ni(111) the $2W(420)$ is only slightly smaller than for the Gr-covered surface, and thus by such comparison, we get $2W(420) \approx 7$, a value significantly larger than unity, and therefore, the classical theory can be applied. It is of interest to note that even if $m^{1/2}$ scaling were to be assumed, the value of $2W(420)$ would be about 3 or larger. A value in this range is still large enough for the classical SSM theory to be valid.

5.2 Energy Resolved Classical Ne Scattering

TOF spectra measured by scattering of a 66 meV Ne beam from a Ni(111) surface at 420 K for different incident angles are presented in Fig. 5.2. The data are shown in both flight–time and energy–exchange domains after normalizing their intensities by dividing by the maximum for each spectrum. The value (in degrees) of the incident angle $\Delta\theta_i$ relative to the specular position is shown next to each spectrum in the left panel. In the right panel, the component of the beam wavevector parallel to the surface is indicated for each spectrum (in Å^{-1}). The blue spectrum corresponds to the specular condition (i.e. $\theta_i = \theta_f = 52.7°$).

The absence of single-phonon features is noted, in contrast to the data reported by Feuerbacher and Willis [201]. It is worth mentioning that the data presented in Ref. [201] were recorded with the Ni(111) surface at 300 K, whereas in the current study the TOF data have been measured with the Ni(111) surface at 420 K. Another important difference with respect to the work in Ref. [201] is the novel observation here of multiphonon dispersion features, as discussed in more detail below.

The energy-resolved spectra of Fig. 5.2 are explained rather well by the SSM theory of Eq.(1.14). Fig. 5.3 shows individual spectra taken at incident angles of $\Delta\theta_i = \pm 4°$ and $\pm 8°$ relative to the specular position, with the data plotted as points and the calculations as solid curves. The positions and shape

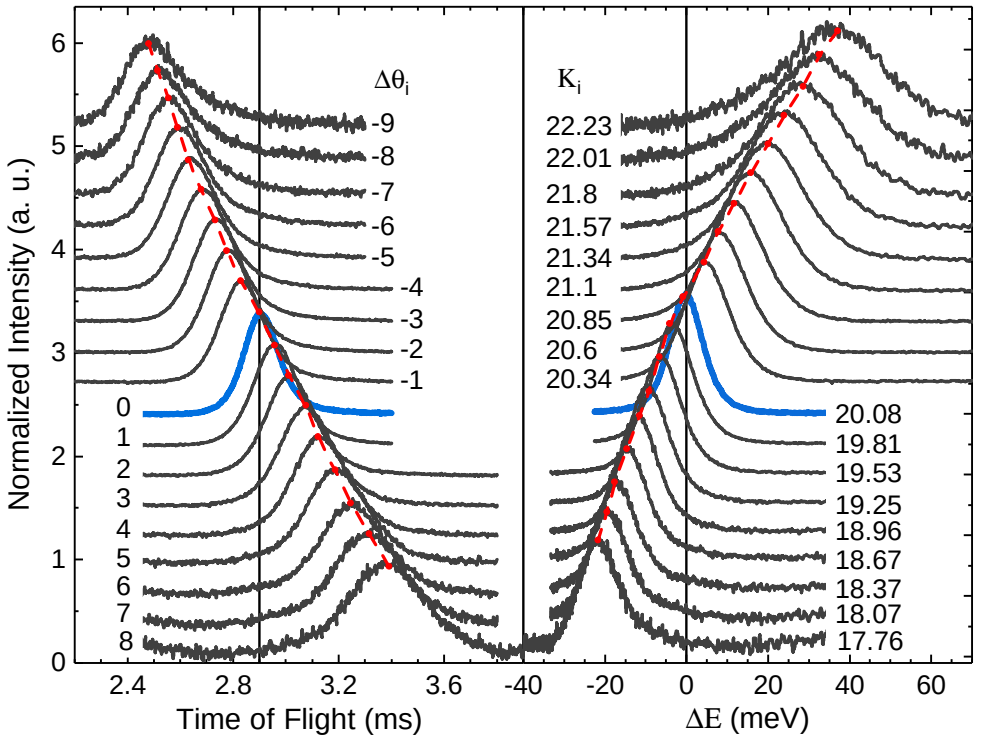

Figure 5.2: Time-of-flight spectra of Ne scattered from Ni(111) (left) and their conversion to energy–exchange domain (right). The incident energy is $E_i = 66$ meV, and the surface temperature $T_S = 420$ K. Blue spectra correspond to specular condition $\theta_i = \theta_f$. The vertical lines indicate the center of the elastically scattered peak at $t = 2.9$ ms and $\Delta E = 0$ meV. Red dashed lines are visual guides following the maxima of the spectra. Angles of incidence relative to the specular position $\Delta\theta_i$ (degrees) and the $\mathbf{K}_i(\text{Å}^{-1})$ are indicated next to each spectrum.

of the calculated peaks match those of the measurements over a large range of the most probable energy transfer -20 meV$\Delta E < +40$ meV.

Figure 5.4 shows a comparison of widths (FWHM) and relative intensities between the experimentally measured (black) and theoretically calculated (red) TOF spectra using the smooth surface model. The widths (left panel) and intensities (right panel) are presented as a function of the angle of incidence $\Delta\theta_i$ measured relative to specular position and the corresponding values of $\mathbf{K}_i$ the component of incident wavevector parallel to the surface are indicated on the top axis.

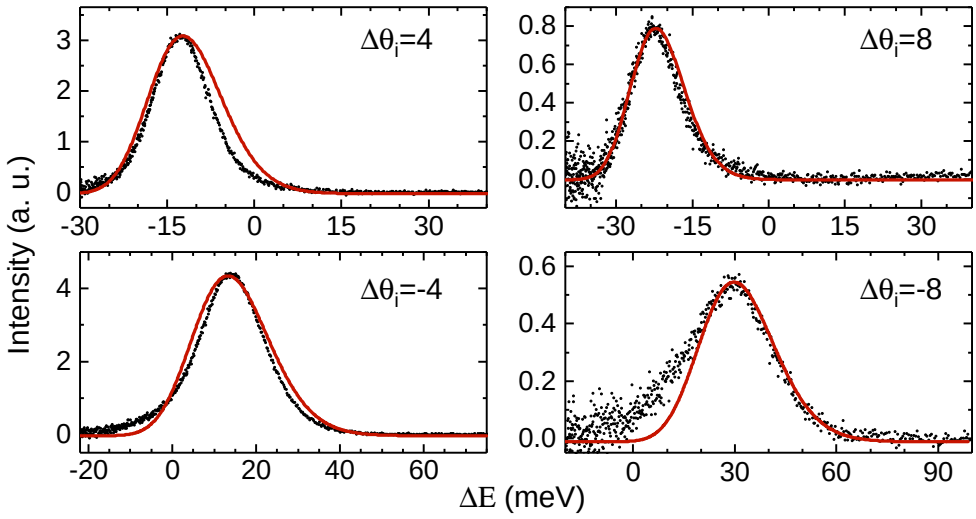

Figure 5.3: Energy-resolved spectra taken at $\Delta\theta_i = \pm 4°$ and $\pm 8°$ from Fig. 5.2 compared with scaled-to-maximum theoretical calculations. The experimental data are shown as black points, and the calculations from the theory of Eq.(1.14) are the red solid curves.

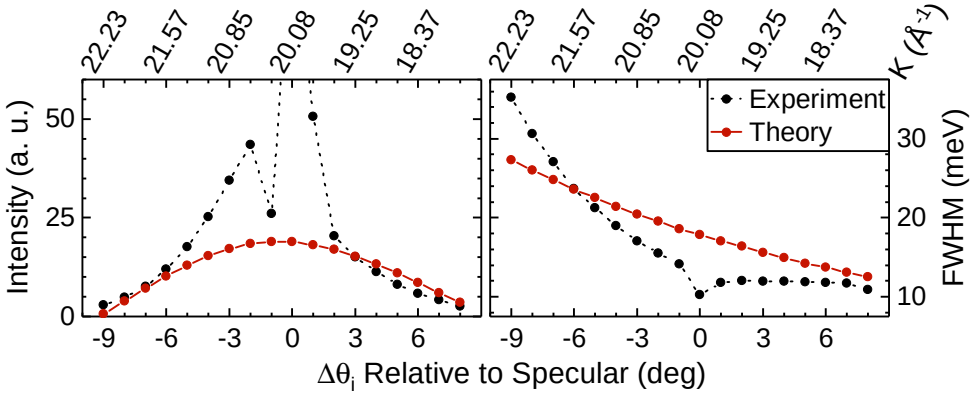

Figure 5.4: Comparison of the width (left panel) and intensity (right panel) of the time-of-flight spectra between experiment (black circles with dashed lines) and theory (red circles with solid lines). Experimental data were taken from spectra in the energy-exchange domain (right panel in Fig. 5.2). Indicated values on the horizontal axes are $\Delta\theta_i$ relative to the specular position (bottom axis) and the corresponding value of the component of k_i parallel to the surface (top axis).

The calculated FWHM values increase monotonically with increasing values of $\mathbf{K}_i$. In the experimental points, the only outlier is the peak width at the specular condition, but this is because the intensity at this point is dominated by the elastic specular diffraction peak and its broadness due to the angular spread of the incident beam. As can be seen from the angular distributions presented in Fig. 5.1 an important component of the intensity of scattered Ne atoms at this angle is due to coherent elastic scattering, which explains the presence of a sharper TOF peak. Excluding the TOF spectrum taken at the specular condition, the theoretical model qualitatively reproduces the experimental data to a reasonable degree.

The right panel of Fig. 5.4 shows the intensities of the TOF spectra as a function of incident angle $\Delta\theta_i$, measured relative to the specular position. The data points for θ_i near the specular position appear artificially large, again because of the influence of the elastic intensity in the region near the specular position. The data point at $\Delta\theta_i = -1^\circ$ is apparently spurious. The calculations of the classical smooth surface model predict the same general trends as observed in the experiment; that is, the intensities are largest at incident angles near the specular position, and then these intensities diminish as the incident angle deviates from the specular region.

Figure 5.5 shows the dispersions of the surface phonon modes of Ni(111), namely, the Rayleigh wave (RW) and the longitudinal resonances (LR) measured by helium scattering (blue circles). The two modes are well resolved and match the calculated surface phonon modes of Ni(111) shown by dashed gray lines [205]. The He TOF measurements were conducted over a range of different surface temperatures from 100 to 460 K. Several scan curves for Ne are also shown in red dotted lines, they are labeled by their corresponding incident angles $\Delta\theta_i$.

The peak positions of the energy-resolved inelastic spectra of Fig. 5.2 are shown in Fig. 5.5 as red dots, where they give the appearance of a dispersive phonon mode of large energy as a function of ΔK. However, this is clearly a false, or anomalous, mode because it is a multiphonon feature and cannot be assigned a specific value of ΔK according to the single-phonon scan curve. The way these points were assigned was that for each inelastic spectrum of Fig. 5.2 its most probable energy (the peak position energy) was assigned a value of ΔK according to where that peak energy fell on the scan curve for the corresponding incident angle $\Delta\theta_i$, i.e., essentially the same way such a ΔK assignment is made for a peak due to a true single–phonon excitation.

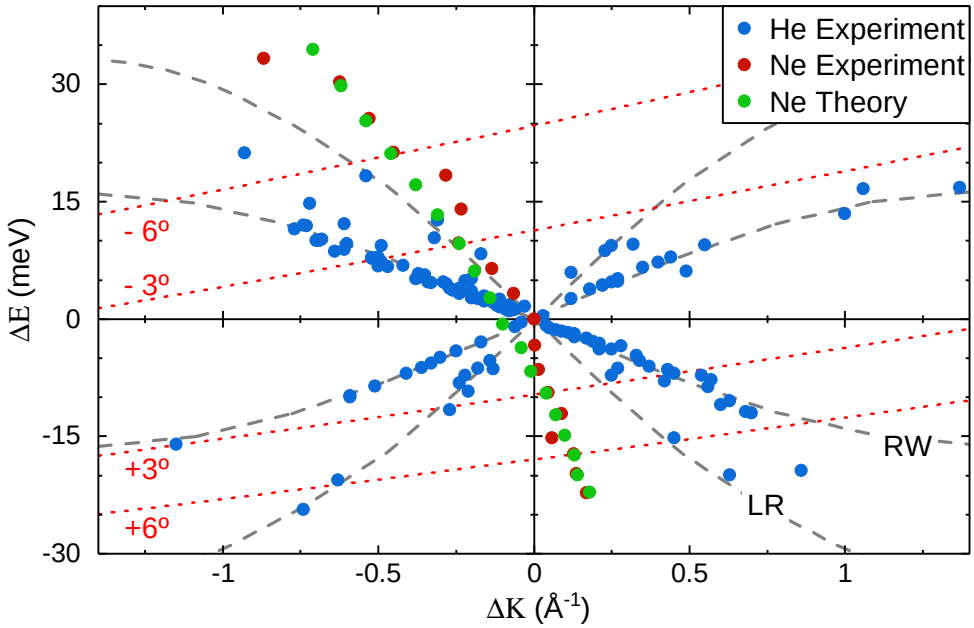

Figure 5.5: Blue circles are measured phonon dispersion curves using He scattering from a Ni(111) surface. Dashed gray lines are calculations of the Rayleigh wave (RW) and longitudinal resonance (LR) modes [205]. Red circles are the measured anomalous dispersion curve (actually a multiple phonon feature) by Ne scattering obtained from Fig. 5.2. Green circles are calculations performed with the SSM model. Red dotted lines are example scan curves for Ne scattering at selected $\Delta\theta_i$ as indicated on each curve.

Therefore, since the inelastic features of Fig. 5.2 are classical and multiphonon in nature, the application of the single-phonon scan curve is inappropriate.

In addition to the fact that this anomalous mode persists at a temperature and incident energy sufficiently large that no other single-phonon peaks appear, there are additional indications that it is not a single-phonon excitation. For example, its “apparent" phonon dispersion lies at energies much larger than any surface mode expected for the Ni(111) crystal face. Another indication is that the anomalous mode appears for positive ΔE only in the fourth quadrant of Fig. 5.5 and for negative ΔE only in the second quadrant, whereas data points for the known RW and LR phonon modes appear in all quadrants of Fig. 5.5. The appearance of the anomalous mode only in the fourth and second quadrants of Fig. 5.5 is predicted by the classical calculations of the SSM theory.

5.3 Ne Scattering from Graphene/Metal Surfaces

Since a passivated surface is of more importance for the focusing mirror, we compare here the scattering of Ne from Ni(111) to that from Gr/Ni(111). We present also diffraction measurements of He and Ne from the Gr/Ir(111) surface. According to Debye-Waller model the multi-phonon background will increase and elastic features will decrease depending on the surface effective mass and Debye temperature. Because Ne travels at lower speeds than those of He (795 and 1780 m/s with $E_i = 66$ meV, respectively) it will have more time to interact with surface phonons, increasing the probability of multiphonon scattering.

Gr/Ni(111)

Figure 5.6 shows a comparison between the angular diffraction spectra of Ne scattered from Gr/Ni(111) and Ni(111) using three different beam energies, both surfaces were at low temperatures during the measurements. Intensity values of scattered Ne from Gr/Ni(111) are shown on the left vertical axis and those from Ni(111) on the right one.

The width of the diffraction peaks is an indicator of the quality of the beam and the studied surface, in addition to an intrinsic instrumental width as was discussed earlier in Section 2.2. Widths and normalized intensities of several diffraction peaks of Ne scattering from Gr/Ni(111) are shown in Table 5.2. Using Eq.(2.10) and assuming the broadening due to surface quality to be negligible in comparison with other broadening factors we can separate the instrumental broadening from the broadening due to beam quality. Finally using Eq.(2.6) we can obtain an average energy spread of 3% in the incident Ne beam (for $E_i = 43.1$ meV), whereas TOF measurements gave an energy spread $\Delta E/E_i = 10\%$.

The relatively high corrugation of Gr/Ni(111) compared to Ni(111) results in the high intensity of the diffraction peak, second order peaks also appear, and even a trace of the third order diffraction peak can be seen for 43 meV. Peak intensities relative to the specular peak are shown in Table 5.2.

The intensity of the specular peak in Gr/Ni(111) is almost 10% of that in Ni(111) whereas the inelastic background is higher and broader. The value of out-of-plane Debye temperature of Ni(111) is 230 K [168] and 1287 K for graphene [55]. And since it appears squared in the argument of Debye-Waller

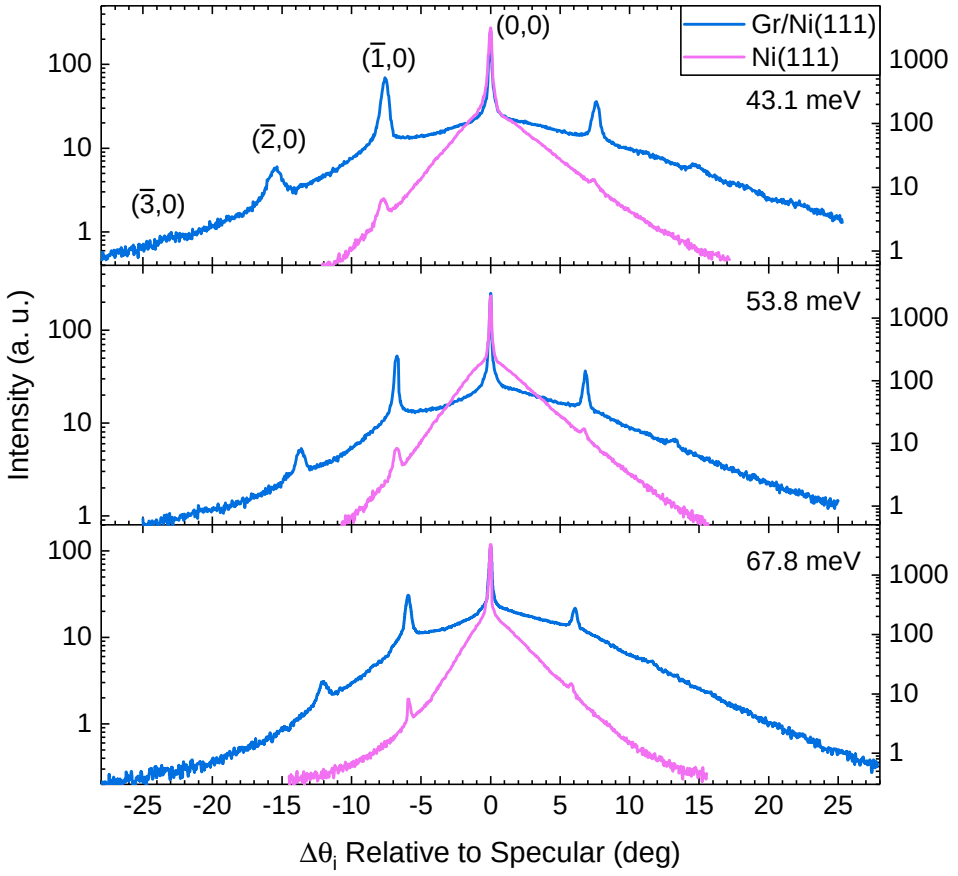

Figure 5.6: Angular diffraction of Ne scattering from Ni(111) and Gr/Ni(111) using different beam energies indicated on each panel. Surface temperature was 170 K for Ni(111) and 115 K for Gr/Ni(111).

factor, a change in Debye temperature would have a much higher effect on the reflectivity than a change in the surface atomic mass. We should expected an increase of 5 orders of magnitude in Ne reflectivity from Gr/Ni(111) compared to that of Ni(111) at low surface temperatures as a result of increased Debye temperature. Since diffraction measurements exhibit a decrease of one order of magnitude, the only interpretation can be that these two surfaces have similar Debye temperatures and the difference of reflectivity between them can be explained by the change in the interaction potential. In fact, if we assume the surface effective mass as discussed earlier in Section 4.1 (i.e. $M_{eff}(Gr/Ni) =$

Table 5.2: Widths and normalized intensities of diffraction peaks in Ne scattering from Gr/Ni(111) spectra using different beam energies.

E_i (meV)	FWHM (deg)			I/I_{00} (%)	
	(0,0)	$(\bar{1},0)$	$(\bar{2},0)$	$(\bar{1},0)$	$(\bar{2},0)$
43.1	0.22	0.62	1.2	72	8
53.8	0.18	0.38	0.76	39	4
67.8	0.23	0.56	0.86	53	5

$M(Ni) + 6M(C)$) and the same Debye temperature for both Gr/Ni(111) and Ni(111) surfaces we can use Eq.(1.13) to obtain a rough estimate of the value of the depth of the Ne-Gr/Ni(111) interaction potential $D =\sim 45$ meV.

Gr/Ir(111)

Debye-Waller model predicts an 80% decrease of the specular peak intensity when the projectile gas is Ne instead of He, because the value of the exponent of the Debye-Waller factor becomes 5 times larger. Our measurements on Gr/Ir(111), however, indicate a much larger decrease. Figure 5.7 shows angular distributions of scattered He (black) and Ne (red) from Gr/Ir(111) surface at the same surface temperature and beam energy; the only difference is the projectile mass. While He scattering gives many intense and sharp diffraction peaks, Ne scattering gives a wide background with no elastic features. The only difference between the two spectra involved a change in the projectile mass. This does not explain the dramatic change in reflectivity according to the conventional Debye-Waller model, which worked well for surfaces of single crystals.

We note that we could not find any publications on Ne scattering from graphitic surfaces. However, A. Levi and H. Suhl [206] mentioned unpublished measurements by P. Cantini of Ne scattering from graphite(0001) surface where no diffraction peaks were detected. This observation was explained as a result of the large well depth of the Ne-graphite interaction potential. Ne travels at low speeds (relative to the lattice atomic vibrations) and high energies (relative to the lattice phonons), furthermore, carbon is light compared with Ne. This results in what can be pictured as a heavy atom impinging on a soft lattice

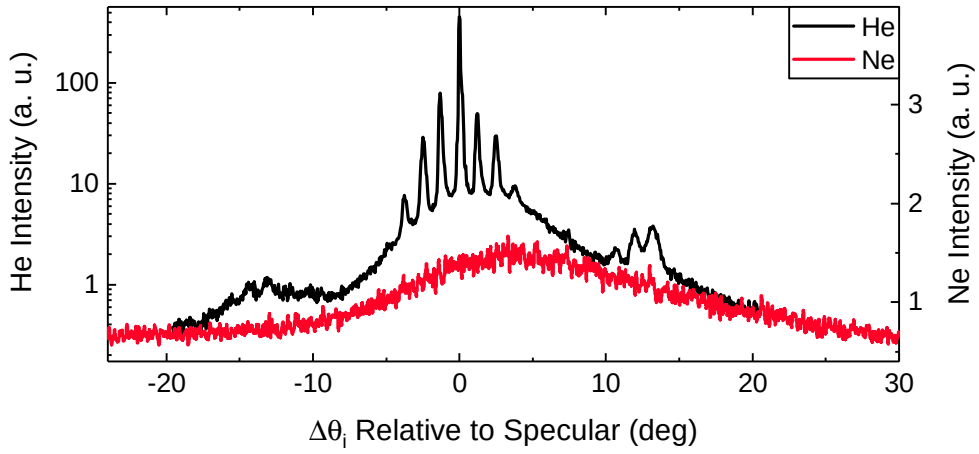

Figure 5.7: Angular scattering spectra of He (black) and Ne (red) from Gr/Ir(111) surface. $E_i = 66\,\text{meV}$ and $T_S =\sim 120\,\text{K}$

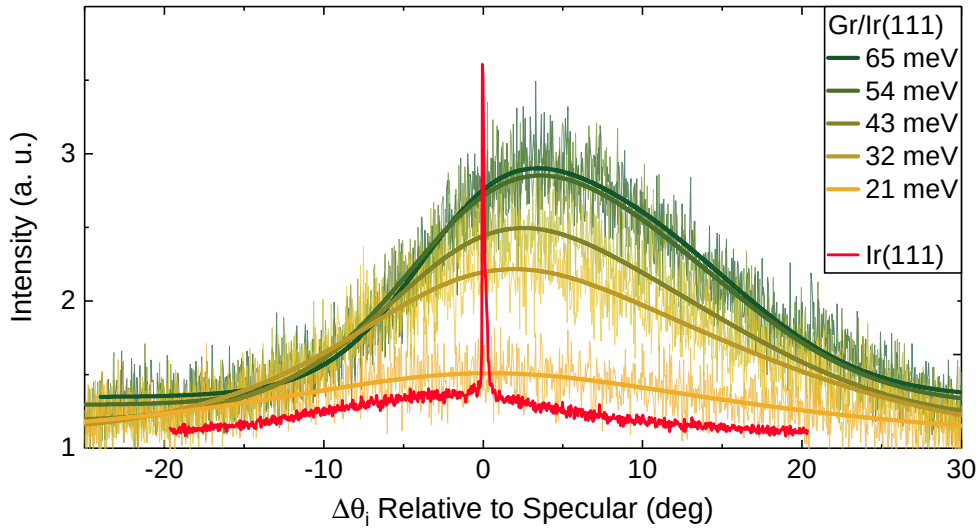

Figure 5.8: Angular scattering spectra of Ne from Gr/Ir(111) (green to orange) with $T_S =\sim 120\,\text{K}$ and different beam energies, and from Ir(111) (red) with $E_i = 21\,\text{meV}$ and $T_S = 650\,\text{K}$.

where the surface has enough time to adjust to the position of the slowly moving projectile [206], this picture is similar to a football hitting the goal net. The Debye-Waller model assumes a weak and fast scattering, it was originally

developed for photon and electron scattering then later adapted for He atom scattering from surfaces. Ne scattering from Gr/Ir(111) is a large deviation from this assumption.

Fig. 5.8 shows scattering spectra of Ne from Gr/Ir(111) at surface temperature $T_S = 120\,\mathrm{K}$ and different beam energies 65 to 21 meV. For comparison, a Ne scattering spectrum from Ir(111) using 21 meV and $T_S = 650\,\mathrm{K}$ is also plotted (red line). Our measurement agrees with the interpretation of Levi and Suhl where we observe a reduction of the scattered intensity of Ne from Gr/Ir(111) with decreasing beam energies, which can be attributed to trapping by the Ne-surface potential. On the other hand, the diffraction spectrum of Ne from Ir(111) produces a sharp specular diffraction peak.

Comparing Ne scattering from Gr/Ni(111) and Gr/Ir(111) indicates that the interpretation of Levi and Suhl provides only half the picture. Our measurements clearly show that the effective mass of the surface atoms is more important than the surface potential, since the Ne-surface potential is expected to be similar for the two graphene terminated surfaces whereas the effective mass (which is affected by the Gr-substrate interaction strength) is the main difference between them. The measurements presented here along with the ones presented in Section 4.1 indicate that understanding the diffraction intensities in noble gas scattering from surfaces of layered materials requires a more complicated model, where phonon dispersions and density of states along with the interlayer interactions are included.

Discussion

In this chapter we have made a comparative analysis of He and Ne scattering from a clean Ni(111) surface and graphene covered surfaces. Using the heavier-rare-gas projectile Ne provides an interesting system with which to examine the decoherence transition from quantum-mechanical coherence to classical incoherent scattering, and this is studied mainly as a function of increasing surface temperature and also by increasing the incident translational energy. The mechanism causing the quantum decoherence is the excitation of multiple quanta of vibrational modes. At lower temperatures and smaller projectile mass, where the Debye-Waller factor is not significantly smaller than unity, the Ne scattering spectrum exhibits clear quantum-mechanical features, e.g., specular and other nonzero reciprocal lattice vector diffraction peaks as well as single-quantum phonon excitation peaks for the known surface-localized RW

and LR modes of the Ni(111) face. As either the temperature or projectile mass is increased the Debye-Waller factor becomes smaller to the point where all sharp quantum excitation features are suppressed, and only a classical multiphonon peak feature survives. Remnants of this classical, multiphonon feature persist even at the lower temperatures and energies where clear quantum features are observed, and we showed that if this classical feature is misinterpreted as a single-phonon peak, it can appear as an anomalous dispersive mode in a graph of surface phonon dispersion curves.

This anomalous dispersion mode is of interest in part because there is a long history of classical multiphonon features being potentially misinterpreted as single-phonon excitation in atom-surface energy-resolved spectra [202]. This anomalous feature in the energy-resolved spectra appears as a broad peak in the intensity but not broader than is routinely observed for some known single-phonon peaks, such as those due to the LR mode on close-packed metal surfaces. Thus, we performed a careful analysis of this feature in order to exclude its identification as a single-phonon peak. Although the anomalous peak persists and is apparent in the Ne/Ni(111) energy-resolved scattering spectra at lower temperatures and energies where true quantum peaks appear, as shown in Fig. 5.2, it is the sole peak that remains at $T = 420\,\mathrm{K}$ and $E_i = 66\,\mathrm{meV}$ because the Debye-Waller factor is so small that all quantum features are suppressed. Additionally, the anomalous dispersion mode appears at energy and parallel momentum combinations for which no surface-localized phonon modes are expected to appear on Ni(111); that is, for a given parallel momentum (falsely) obtained by assigning its energy a position on the single-phonon scan curve, its apparent energy is much too large to be a believable mode of Ni(111). Further evidence of the multiphonon nature of the anomalous mode comes from comparison with the classical SSM theory (in Section 1.3.3). The behavior of the intensities and FWHMs of the anomalous mode as a function of incident angle θ_i are qualitatively explained. The SSM calculations explain quantitatively the shape of the false anomalous dispersion curve when plotted in a phonon energy vs. parallel wave vector graph. In particular, the SSM calculations explain why the anomalous mode appears only in the second and fourth quadrants of the graph in Fig. 5.5; that is, the multiphonon feature appears to have positive parallel momentum when Ne loses energy (net phonon creation) and negative parallel momentum when Ne gains energy (net phonon annihilation). Thus this anomalous inelastic feature can be clearly identified as multiphonon, and hence classical and incoherent in nature.

There are other reasons why Ne can be a particularly interesting probe for surface scattering experiments. Because the outer electrons of Ne are less tightly bound than those of He, despite being in a closed-shell configuration, they can make virtual exchange excursions into the empty *D*-shell states of transition metals such as Ni as the Ne atom approaches close to the surface. This mechanism of interaction, which is much less active for He projectiles, gives rise to anticorrugation effects [83, 84, 86]; that is, the Ne interaction potential can have significantly different corrugation than that encountered by He.

The Ne/Ni(111) system has been investigated previously by Feuerbacher and Willis [201] using similar incident Ne energies and an ambient (300 K) temperature Ni(111) target, and they observed what appeared to be single quantum excitation of phonon modes. Our investigation indicates that at temperatures lower than about 420 K the Ni(111) surface rapidly becomes contaminated, most likely due to a small partial pressure of hydrogen in the vacuum chamber. Consequently, we would conclude that the earlier work of Feuerbacher and Willis did not exhibit Ne scattering from clean Ni(111), but rather, the surface was covered by adsorbates, and the apparent coherence in their work was more likely a result of limiting Ne access to in-plane phonons by partial coverage of the surface, presumably with hydrogen.

In conclusion, we have demonstrated, for the system of Ne atom scattering from Ni(111), the transition from the regime of quantum mechanics, distinguished by sharp diffraction and single phonon peaks in the scattering spectra, to the classical regime, which exhibits only a single peak feature in both the angular-resolved and energy-resolved spectra. This transition is exhibited by varying either the surface temperature or the incident translational energy over relatively small and easily accessible ranges. Thus, the Ne/Ni(111) system presents an interesting example of the transition from a quantum coherent state, through decoherence, and onward to the classical incoherent state, and the mechanism of the observed decoherence is the excitation of multiple quanta of phonon modes.

Finally, we have presented a comparison of Ne scattering from Gr/Ni(111) and Gr/Ir(111). Our measurements show that Ne-surface interaction is very sensitive to the effective mass of the surface atoms. The diffraction spectra from Gr/Ni(111) are similar to those of Ni(111) due to the strong Gr-Ni interaction, while the Gr/Ir(111) surface results in classical scattering due to the low mass of the surface atoms in comparison with the Ne mass. When the surface

effective mass is low enough the effect of the Ne-surface potential appears to have an additional effect of the scattering where trapping of Ne in the attractive potential well is observed for low beam energies. The effective mass of the surface atoms is affected by the strength of intralayer and interlayer bonds.

Chapter 6

Conclusions and Remarks

This work presented systematic experimental measurements of HAS from Gr/Cu(111), Gr/Ni(111) and Gr/Ir(111). Diffraction measurements included the determination of the lattice structure and thermal expansion of all these surfaces. The study included the optimization of the preparation of Gr/Cu(111)/Al_2O_3 surface in collaboration with another research group to obtain a suitable sample for HAS measurements. Angle and energy resolved measurements were used to compare two preparation methods of Gr/Cu(111). As far as we know, this work presented the first experimental measurements were the diffuse elastic peak in TOF measurements was used for quality control. As part of the preparation process of Ni(111) surface an oxide layer p(2×2)O/Ni(111) was grown, which was found to be expanded by 14% over the Ni(111) surface.

During the work of this thesis, a LabVIEW software for the measurement control and data acquisition setup was developed, in addition to a data analysis software where diffraction and TOF measurements can be easily analyzed. One of the scattering machines used in this study (ERASMO) was modified to allow for using molecular beams other than He. This work also included the design and fabrication of several parts shown in the Appendix.

Gr/Ni(111) was found to give a very high He reflectivity (20%) and very low density of defects where the FWHM of the measured specular peak was smaller than the instrumental resolution of HAS apparatus. Creating surface defects on Gr/Ni(111) surface resulted in a 1% expansion of the surface when the defect concentration was $\sim$ 1% of a monolayer. This expansion is sufficient to accommodate the graphene lattice to that of the Ni(111).

Diffraction measurements of He scattering were used to obtain structural in-

formation of the studied surfaces. Diffraction from Gr/Ni(111) and Gr/Ir(111) revealed a 3-fold surface symmetry instead of the 6-fold symmetry expected for hexagonal surfaces. This result indicates that the asymmetries in diffraction spectra should not be dismissed as simply a result of bad adjustment of the azimuthal orientation.

Thermal expansion measurements were used as a tool for probing the graphene-substrate interaction. Gr/Cu(111) lattice was shown to remain constant in the temperature range from 110 to 510 K even when the substrate expands, this is an indication of the weak Gr-Cu coupling. Gr/Ni(111) lattice expands in a similar way to that of Ni(111): Gr grows epitaxially on Ni(111) creating a (1×1) structure where Gr is strongly coupled to the substrate. Gr/Ir(111) expansion revealed an accumulated stress in the graphene layer which can be released upon expansion. The stress release is not gradual; it results in abrupt changes in the surface atomic structure. This behavior is related to the moiré superstructure.

Low-energy acoustic surface phonons were determined for all three surfaces investigated in this work. The hybridization of ZA mode of Gr with the RW of Ni(111) indicates the strong Gr-Ni(111) interaction. ZA modes of Gr/Cu(111) and Gr/Ir(111) are similar in the sense that no hybridization with substrate modes was detected. However, the complicated surface structure of Gr/Ir(111) resulted in complicated phonon dispersions of this surface. Our measurements resulted in resolving two ZA modes for Gr/Ir(111) with $\omega_0 = 7.2$ and 4.5 meV at $\overline{\Gamma}$. These phonon modes are attributed to the different high and valley regions on the moiré corrugation of Gr/Ir(111) as indicated by observations from TOF and diffraction measurements. We could not detect the LA mode in any of our measurements, this is a useful result in itself for researchers investigating the contributions of different phonon modes to the thermal conductivity of graphene-metal interfaces. Our finding falls in-line with the theoretical predictions that ZA mode the most dominant in the thermal properties of Gr/Cu(111) at temperatures in the vicinity of 120 K.

This work presents a systematic analysis of the graphene's bending rigidity and its coupling strength with different substrates, based on the first high-resolution experimental determination of the low-energy part of the flexural mode of graphene. Comparing the results of this work to earlier neutron scattering measurements on graphite [44] indicates that better measurements on graphite are required as it does not make sense that its ZA mode appears similar to that of Gr/Ni(111) rather than to Gr/Cu(111), especially when considering

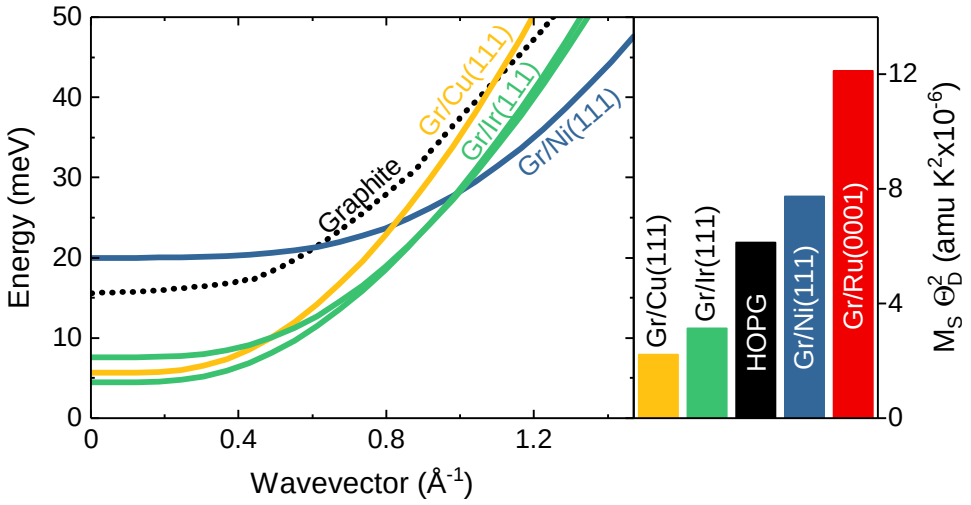

Figure 6.1: Left: Comparison of ZA mode of several Gr/metals surfaces and graphite, colors correspond to right panel. Black dotted line was measured graphite using neutron scattering [44]. Right: Comparison of surface parameters of Debye-Waller factor of the same surfaces. HOPG data from [166] and Gr/Ru(0001) from [23].

the interlayer bonds and distances. These results are summarized in Fig. 6.1 and Table 6.1.

The results for Gr/Ir(111) are a good example of the added complexity of a system that includes two periodicities within the moiré unit cell. This poses several difficulties in interpreting the data using the established theories that were previously derived for surfaces with only one periodicity. This includes the correlation of surface corrugation with diffraction intensities, the angular position of diffraction peaks with increasing out-of-plane angle, the assignments of SAR resonances, and the interpretation of low-energy phonon modes. The results for Gr/Ir(111) have been compared to earlier results from Gr/Ru(0001). This resulted in a reasonable explanation of the underestimation of the moiré corrugation of Gr/Ru(0001) in earlier HAS measurements [157]. This comparison also explains the presence of two ZA modes for Gr/Ir(111) surface and highlights a discrepancy between HREELS [78] and HAS [71] measurements for the ZA mode of Gr/Ru(0001). There are two identifiable regions within the moiré unit cell and the lattice dynamics are slightly different between them. This small difference could be identified by HAS. The 4.6 meV mode is the one from the heights and the 7.2 meV mode is the one from the

Table 6.1: Surface properties from Debye-Waller factor; M_S is effective atomic mass of the surface and Θ_D is its Debye temperature, $E_{ZA}(\overline{\Gamma})$ is the energy of ZA mode at $\overline{\Gamma}$, κ is the graphene's bending rigidity and g is the Gr-substrate coupling strength.

Surface	$M_S\Theta_D^2 \times 10^{-6}$ (amu K^2)	$E_{ZA}(\overline{\Gamma})$ (meV)	κ (eV)	$g \times 10^{19}$ (N m^{-3})
Gr/Ni(111)	7.7	20	0.43	71.5
Gr/Ir(111)	3.1	7.2	0.80	10.3
		4.6	0.86	3.6
Gr/Cu(111)	2.2	5.7	1.30	5.7

valleys of the moiré corrugation.

This work included a systematic study of the quantum to classical transition in atom-surface scattering using Ne scattering from Ni(111). Angular diffraction and TOF measurements were conducted using ERASMO setup, which required several modifications to the experimental apparatus. We have used a straightforward classical model that provided a quantitative explanation of the experimental results. This study showed that what is clearly multi-phonon features can by mistakenly interpreted as anomalous single phonon mode. Comparing our results to earlier Ne scattering measurements from Ni(111) indicates that our measurements lie on the onset of quantum decoherence, especially thanks to the relatively low effective mass of Ni atoms. Theoretical calculations using the smooth surface model were conducted by myself, with help from Prof. J. R. Manson.

Ne scattering has also been used to test Debye-Waller model. We verified an m dependence of the Debye-Waller factor for Gr/Ni(111) instead of a theoretically-predicted $\sqrt{m}$ dependence. We compared the reflectivity and the Debye-Waller factor for Gr/Ni(111) and Ni(111) using He and Ne scattering. The relative reflectivity from Gr/Ni(111) compared to Ni(111) is 50% using He and 10% using Ne. This indicates the importance of the atom-surface interaction potential in the Debye-Waller attenuation. Moreover, this result is inconsistent with the prediction from the Debye-Waller model when using the surface atomic masses of carbon and nickel and the Debye temperatures of graphene and Ni(111). This shows that the Debye-Waller model does not hold

for layered materials. Our measurements of Ne scattering from Gr/Ir(111) show that the "soft lattice model" is a valid description of the experimental finding, we have also verified the trapping effect due to the large Ne-Gr interaction potential depth.

Debye-Waller measurements along with angular diffraction of Ne from the studied surfaces showed sufficient evidence that the conventional Debye-Waller model cannot be used for describing gas scattering from layered materials, since the effective atomic mass of the surface appears multiplied to the ambiguous surface Debye temperature in the Debye-Waller factor exponent. This results in an erroneous derivation of the Debye temperature of the surface. However, the slope of the Debye-Waller attenuation measurements is a useful method for obtaining qualitative yet valuable information on the interlayer coupling strength.

Conclusiones

En esta tesis se realizó un estudio sistemático de la estructura y dinámica de grafeno crecido en Cu(111), Ir(111) y Ni(111) mediante la Dispersión Atómica de Helio (HAS, Helium Atom Scattering). Las medidas de difracción incluyeron la determinación de la estructura atómica de la red y la expansión térmica de las superficies mencionadas. El estudio incluyó la optimización del método de preparación de la superficie de Gr/Cu(111)/Al_2O_3 en colaboración con otro grupo de investigación de modo que sean aptas para realizar medidas con HAS.

Se usaron medidas de difracción y tiempo de vuelo para comparar dos métodos de preparación de Gr/Cu(111). Hasta donde sabemos, este trabajo presenta las primeras medidas experimentales donde se usó el pico elástico difuso en las medidas de TOF para el control de calidad de superficies. Como parte del proceso de preparación de la superficie de Ni(111), se hizo crecer una capa de óxido p(2×2)O/Ni(111), y se encontró que esta capa está expandida un 14% más que la superficie de Ni(111).

Una parte del trabajo de esta tesis consistió en el desarrollo de software de LabVIEW para el control de medición y la adquisición de datos, además de un nuevo software de análisis de datos con el que las medidas de difracción y TOF pueden ser fácilmente analizadas. Una de las máquinas de dispersión utilizadas en este estudio (ERASMO) se modificó para poder utilizar haces moleculares diferentes de He. Este trabajo también incluyó el diseño y la fabricación de varias piezas y montajes presentados en el Apéndice.

En Gr/Ni(111) se midió una reflectividad muy alta (20%) y una densidad muy baja de defectos en la superficie, donde el FWHM del pico especular medido es menor que la resolución instrumental del aparato HAS. La creación de defectos superficiales en la superficie de Gr/Ni(111) dio como resultado una expansión del 1% de la superficie, cuando la concentración de defectos es $\sim$ 1% de una monocapa. Esta expansión es suficiente para acomodar la red de

grafeno a la del Ni(111).

Las medidas de difracción de He se utilizaron para realizar una caracterización estructural de las superficies estudiadas. Las medidas de difracción en Gr/Ni(111) y Gr/Ir(111) revelaron una simetría de 120° de la superficie, en lugar de 60°, que es la esperada para superficies hexagonales. Este resultado indica que las asimetrías en los espectros de difracción no deben ser simplemente descartadas como un resultado de un mal ajuste de la orientación azimutal.

Las medidas de expansión térmica se utilizaron como una herramienta para probar la interacción grafeno-sustrato. La constante de red de Gr/Cu(111) no cambia en el rango de temperaturas desde 110 a 510 K incluso cuando el sustrato se expande, esto es una indicación del acoplamiento débil de Gr-Cu. La red de Gr/Ni(111) se expande de manera similar a la de Ni(111): el Gr crece epitaxialmente sobre Ni(111) creando una estructura (1×1) donde el Gr está fuertemente acoplado al sustrato. La expansión Gr/Ir(111) reveló una tensión acumulada en la capa de grafeno que se puede liberar tras la expansión. La liberación de estrés no es gradual, sino que se da mediante cambios abruptos en la estructura atómica de la superficie. Este comportamiento se relaciona con la superestructura moiré.

Se ha estudiado por primera vez el modo de fonones ZA ("flexural mode") del grafeno en varias superficies a muy bajas energías (debajo de 10 meV). La hibridación del modo ZA de Gr con el RW de Ni(111) indica una fuerte interacción Gr-Ni(111). Los modos ZA de Gr/Cu(111) y Gr/Ir(111) son similares en el sentido de que no se detectó hibridación con los modos del sustrato. Sin embargo, la compleja estructura de la superficie de Gr/Ir(111) resulta en curvas de dispersión de fonones más complicadas. Nuestras medidas muestran la presencia de dos modos flexurales en Gr/Ir(111) con $\omega_0 = 7.2$ y 4.5 meV en $\overline{\Gamma}$. Estos modos de fonones se atribuyen a las diferentes regiones altas y bajas en la corrugación de la estructura de moiré en Gr/Ir(111), como indican las observaciones en las medidas de TOF y difracción. No hemos podido detectar el modo LA en ninguna de nuestras medidas, lo que representa un resultado muy útil para quienes investigan la contribución de los diferentes modos de fonones en la conductividad térmica en la interfaz grafeno-metal. Nuestro resultado está en línea con las predicciones teóricas que indican que el modo ZA es el que domina las propiedades térmicas de Gr/Cu(111) a temperaturas cercanas a 120 K.

Este trabajo presenta un análisis sistemático de la ligadura grafeno-metal,

como la llamada “bending rigidity” para estos sistemas. Este análisis se efectuó usando las medidas experimentales de alta resolución a baja energía del modo “flexural” del grafeno. La comparación de los resultados de este trabajo con medidas anteriores con dispersión de neutrones en grafito [44] indica que se requieren mejores medidas en grafito, ya que no tiene sentido que su modo ZA aparezca similar al de Gr/Ni(111) en lugar de Gr/Cu(111), especialmente cuando se consideran los enlaces y distancias entre capas. Estos resultados se resumen en la Fig. 6.1 y la tabla 6.1.

Los resultados para Gr/Ir(111) son un buen ejemplo de la complejidad añadida de un sistema que incluye dos periodicidades dentro de la celda unidad de moiré. Esto plantea varias dificultades en la interpretación de los datos utilizando las teorías establecidas que se derivaron previamente para las superficies con una sola periodicidad. Esto incluye la correlación de la corrugación con las intensidades de difracción, la posición angular de los picos de difracción con el aumento del ángulo fuera del plano, la asignación de las resonancias SAR y la interpretación de los modos de fonones de baja energía. Los resultados para Gr/Ir(111) se han comparado con resultados anteriores para Gr/Ru(0001). Esto dio lugar a una explicación razonable de la subestimación de la corrugación de moiré en Gr/Ru(0001), derivada de las medidas de HAS [157]. Esta comparación también explica la presencia de dos modos ZA en la superficie de Gr/Ir(111) y destaca una discrepancia entre las medidas de HREELS [78] y HAS [71] del modo ZA en Gr/Ru(0001). Hay dos regiones identificables dentro de la celda unitaria de moiré y la dinámica de la red es ligeramente diferente entre ellas. Esta pequeña diferencia podría ser detectada por HAS. El modo de 4.6 meV correspondería a las regiones altas y el modo de 7.2 meV a las regiones más bajas en la corrugación de la celda de moiré.

Este trabajo incluyó un estudio sistemático de la transición cuántica-a-clásica en la dispersión átomo-superficie utilizando la dispersión de Ne en Ni(111). Las medidas de difracción angular y TOF se realizaron utilizando el sistema ERASMO después de realizar varias modificaciones en el aparato experimental. Hemos utilizado un modelo clásico que proporciona una explicación cuantitativa de los resultados experimentales. Este estudio demostró que las características de fonones múltiples pueden ser interpretadas erróneamente como un modo anómalo de fonones. La comparación de nuestros resultados con medidas anteriores de dispersión de Ne en Ni(111) [201] indica que nuestras medidas se encuentran en el inicio de la decoherencia cuántica, especialmente gracias a la masa efectiva relativamente baja de los átomos de

Ni. Los cálculos teóricos utilizando el modelo "smooth surface model" fueron realizados por mí con la ayuda del Prof. J. R. Manson.

La dispersión de Ne se ha utilizado también para probar el modelo de Debye-Waller. Hemos verificado una dependencia en función de m del factor Debye-Waller para Gr/Ni(111), en lugar de una dependencia con $\sqrt{m}$ como ha sido predicho teóricamente. Se comparó la reflectividad y el factor de Debye-Waller para Gr/Ni(111) y Ni(111) utilizando la dispersión de He y Ne. La reflectividad relativa de Gr/Ni(111) en comparación con Ni(111) es 50% usando He y 10% usando Ne. Esto indica la importancia del potencial de interacción átomo-superficie en la atenuación de Debye-Waller. Además, este resultado es inconsistente con la predicción del modelo de Debye-Waller cuando se usan las masas atómicas de las superficies de carbono y de níquel con las temperaturas de Debye del grafeno y de Ni(111). Esto demuestra que el modelo convencional de Debye-Waller no es adecuado para describir la dispersión de átomos de gases nobles en superficies de materiales laminados. Nuestras medidas de dispersión de Ne en Gr/Ir(111) muestran que el "modelo de red blanda" es una descripción válida de los resultado experimentales, también hemos verificado el efecto de "atrapamiento" debido a la profundidad del pozo del potencial de interacción Ne-Gr.

Las medidas de Debye-Waller junto con la difracción angular de Ne en las superficies estudiadas mostraron evidencia suficiente de que el modelo convencional de Debye-Waller no es adecuado para describir la dispersión de gases de materiales laminados, ya que la masa atómica efectiva de la superficie aparece multiplicada por la ambigua temperatura de Debye de la superficie en el exponente del factor Debye-Waller. Esto da lugar a una derivación errónea de la temperatura de Debye de la superficie. Sin embargo, la pendiente de las medidas de la atenuación Debye-Waller es un método útil para obtener información cualitativa y valiosa sobre la fuerza de acoplamiento entre las primeras capas de la superficie.

Appendix

Copper evaporator

A homemade copper evaporator was mounted in ERASMO before the work of this study. The old evaporator was bulky and collapsed under its own weight. A new design was made. The flange was recycled from an old Bayard–Alpert ionization gauge with a light tube welded to the flange. The total length of the evaporator is 56 cm. The crucible is insulated from ground and can be heated by electron bombardment using one of two tungsten filaments located next to it. A K-type thermocouple is spot-welded to the crucible which is connected via a high-voltage isolation circuit to the PC. Figure 6.2 shows a photograph of this evaporator.

Figure 6.2: Light-weight evaporator installed in ERASMO

Piezoelectric module A piezoelectric table with a mounted 20 µm slit has been installed in the first chamber of the TOF arm, the purpose of this table is to measure the spot size of the reflected beam once it was reduced to below 100 nm. The table can be controlled from the PC via the LabVIEW software. Fig. 6.3 shows an example measurement using the piezo module. A profile of the peak is reconstructed using multiple scans with the piezo table each after rotating the sample 0.04°.

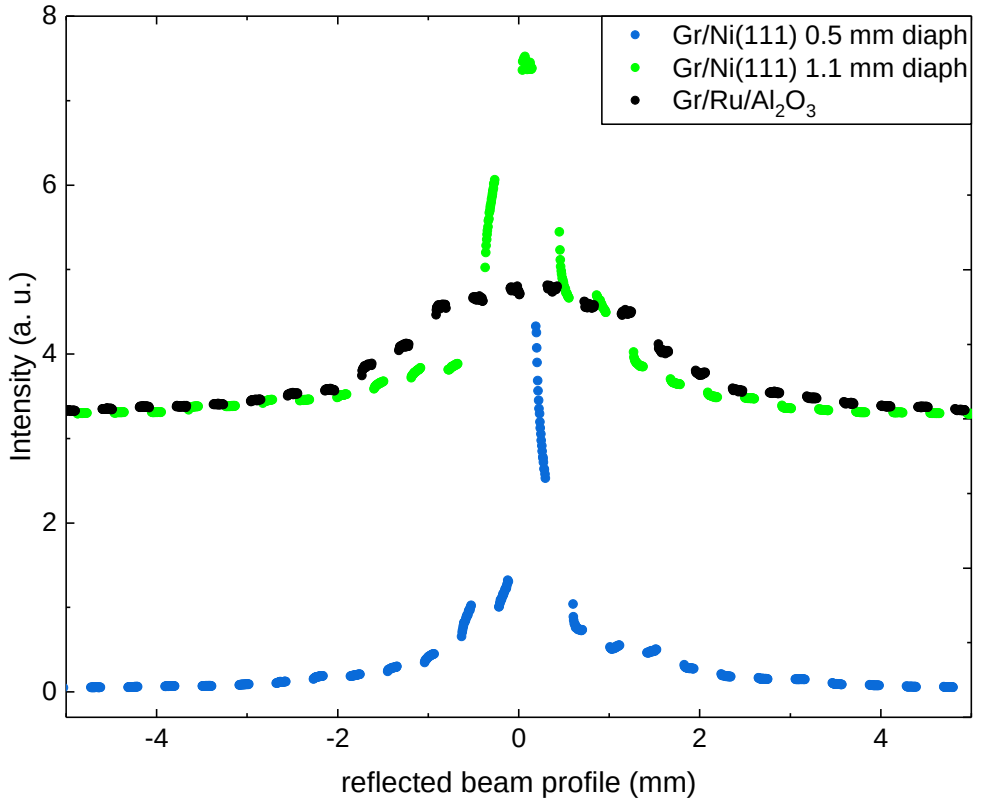

Figure 6.3: Angular distribution modulated by a movable slit on a piezo table of He scattering from different samples.

Mirror bending manipulators

Figure 6.4 shows a scheme of the electrostatic plate-bending holder to be used in TEAMS. It can be mounted using the Load-lock chamber. The sample in this holder can be mounted between the first two disks (from the left), a margin of 0.5 mm allows for bending with less resistance. Three ceramics isolate the sample from the third disk which is to be connected high voltage. The sample is grounded in this setup.

Fig. 6.5 shows a mechanical bending mechanism, here the azimuth controller is disconnected and the azimuthal degree of freedom is locked in place. The azimuthal motion controller is then connected to a rotary wedge which can slide below a motion transformer which is a rectangular piece that can rotate

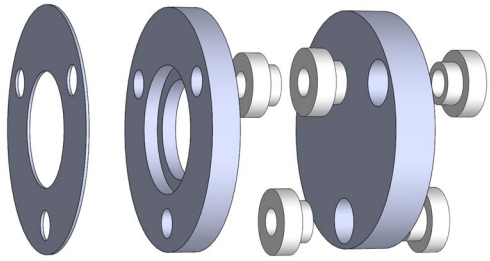

Figure 6.4: Scheme of electrostatic thin mirror bender.

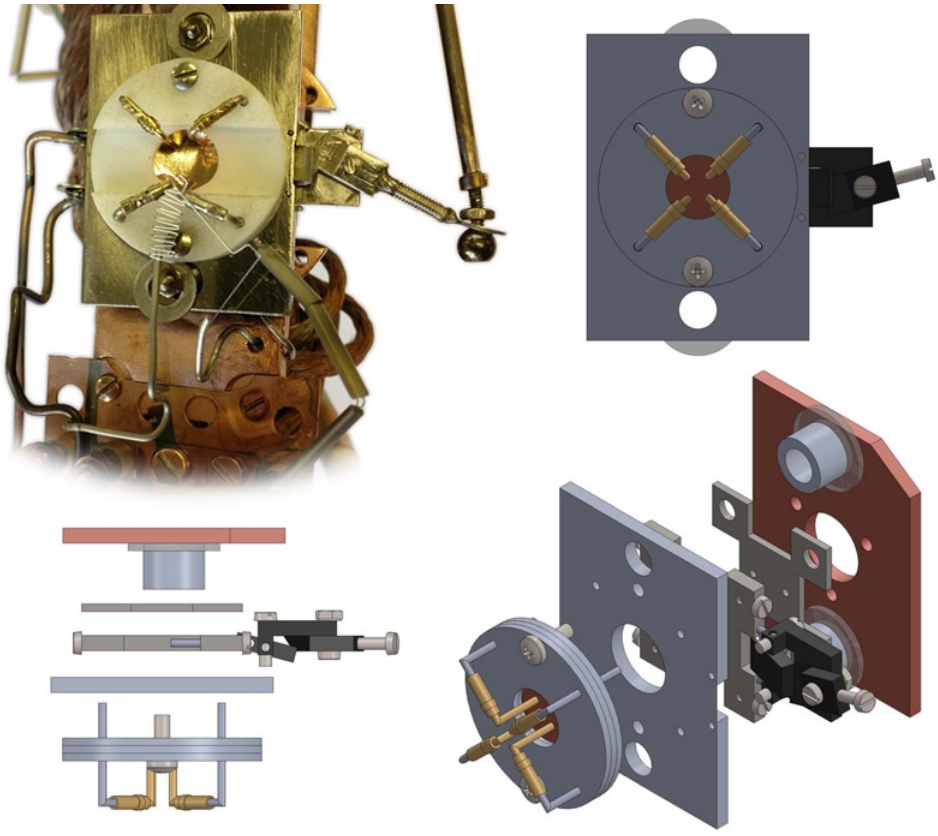

Figure 6.5: Thin mirror mechanical bender to be used in ERASMO

around a shaft perpendicular to the wedge's shaft. The result is converting the

vertical linear motion of the azimuth manipulator to a horizontal motion. The sample is sandwiched between a thick Teflon disc and one stainless steel disc. Four finger pass through the Teflon disc to be screwed on the motion transformer. The Teflon disc serves as a controller of the uniformity of the motion of the fingers which are gloved with gold-plated pins. Gold is the material that has the weakest interaction with graphene. Moving the azimuth manipulator permits the fingers to push against the surface of the sample. Several modifications had to be done after the initial design which is shown in the scheme in Fig. 6.5 and the final product is shown in the photograph. The parts have been assembled and tested in air, sufficient force can be applied with this design to curve a *super G* sample.

Adapter for large sample for TEAMS Using curved surfaces for a focusing mirror reduces the technical problems that can arise in mechanically or electrostatically bending a thin film. However, commercially available lenses are too large for the current design of the Load-Lock chamber which allows for a fast change of the sample without breaking the vacuum in the main chamber. Thus, an adapter was needed especially since more than 50 samples were used in TEAMS during the last few years. The design is shown in Fig. 6.6. The measurements conducted using this adapter are included the PhD. thesis of Gloria Anomene (in preparation).

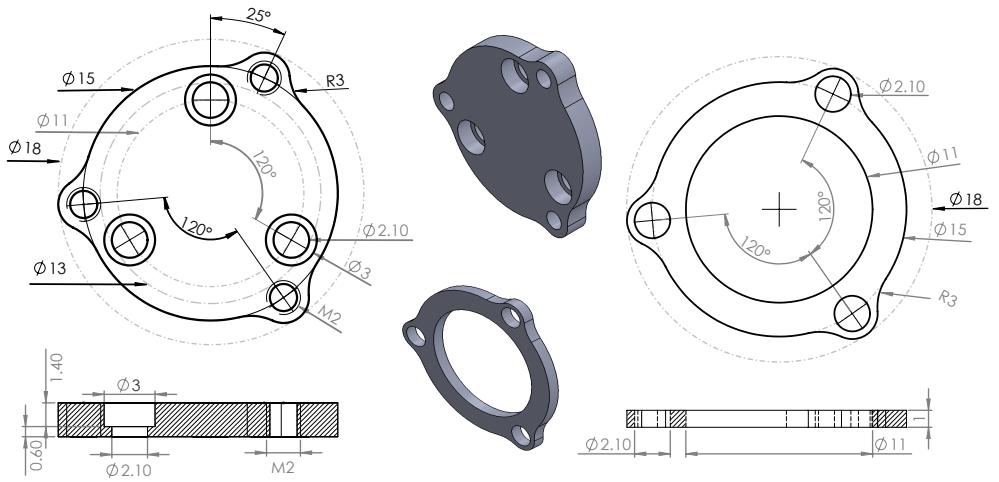

Figure 6.6: Adapter for larger samples used in TEAMS.

Publications related to this work

- A. Al Taleb, H. K. Yu, G. Anemone, D. Farías, and A. M. Wodtke (2015) **Helium diffraction and acoustic phonons of graphene grown on copper foil**. *Carbon*, **95**:731 DOI:10.1016/j.carbon.2015.08.110
- A. Al Taleb, G. Anemone, D. Farías, and R. Miranda (2016) **Acoustic surface phonons of graphene on Ni(111)**. *Carbon* **99**:416 DOI:10.1016/j.carbon.2015.12.043
- A. Al Taleb and D. Farías. (2016) **Phonon dynamics of graphene on metals**. Journal of Physics: Condensed Matter **28**(10):103005 DOI: 10.1088/0953-8984/28/10/103005
- A. Al Taleb, G. Anemone, W. W. Hayes, J. R. Manson, and D. Farías (2017) **Multiphonon excitation and quantum decoherence in neon scattering from solid surfaces**. *Physical Review B* **95**(7):75414 DOI:10.1103/PhysRevB.95.075414

Other publications

- G. Anemone, E. Climent-Pascual, H. K. Yu, A. Al Taleb, F Jiménez-Villacorta, C. Prieto, A. M. Wodtke, A. De Andrés, and D. Farías (2016) **Quality of graphene on sapphire: long-range order from helium diffraction versus lattice defects from Raman spectroscopy**. *RSC Advances* **6**(25):21235 DOI:10.1039/C5RA27452D
- D. Maccariello, A. Al Taleb, F. Calleja, A. L. Vázquez de Parga, P. Perna, J. Camarero, E. Gnecco, D. Farías, and R. Miranda (2016) **Observation of localized vibrational modes of graphene nanodomes by inelastic atom scattering**. *Nano Letters* **16**(1):2 DOI:10.1021/acs.nanolett.5b02887
- D. Maccariello, D. Campi, A. Al Taleb, G. Benedek, D. Farías, M. Bernasconi, and R. Miranda (2015) **Low-energy excitations of graphene on Ru(0001)**. *Carbon* **93**:1 DOI:10.1016/j.carbon.2015.05.028
- D. Farías, M. Minniti, A. Al Taleb, and R. Miranda (2013) **Initial sticking coefficient of H_2 on the Pd-Cu(111) surface alloy at very low coverages**. *Zeitschrift Für Physikalische Chemie* **227**(9-11):1491 DOI:10.1524/zpch.2013.0392
- K. Haddad, M. Kattan, and A. Al Taleb (2011) **Measurement of 60 Co high gamma dose using gamma activation of 115 In and 111 Cd foils**. *Applied Radiation and Isotopes* **69**(1):180 DOI:j.apradiso.2010.07.017

Bibliography

[1] M. P. Oxley, A. R. Lupini and S. J. Pennycook. Ultra-high resolution electron microscopy. *Reports Prog. Phys.* **80**(2):026101 (2017). http://dx.doi.org/10.1088/1361-6633/80/2/026101.

[2] G. Hlawacek, V. Veligura, R. van Gastel and B. Poelsema. Helium ion microscopy. *J. Vac. Sci. Technol. B Microelectron. Nanom. Struct.* **32**(2):020801 (2014). http://dx.doi.org/10.1116/1.4863676.

[3] J. P. Toennies. Experimental Determination of Surface Phonons by Helium Atom and Electron Energy Loss Spectroscopy. W. Kress and F. W. de Wette (eds.), *Surface Phonons*, chap. 5, 111–166 (Springer-Verlag, Berlin, 1991).

[4] E. Hulpke (ed.). *Helium Atom Scattering from Surfaces*. Springer Series in Surface Sciences (Springer Berlin Heidelberg, Berlin, Heidelberg, 1992). ISBN 978-3-642-08115-6. http://dx.doi.org/10.1007/978-3-662-02774-5.

[5] D. Farías and K. H. Rieder. Atomic beam diffraction from solid surfaces. *Rep. Prog. Phys.* **61**(12):1575 (1998). http://dx.doi.org/10.1088/0034-4885/61/12/001.

[6] G. Bracco and B. Holst. *Surface Science Techniques*, *Springer Series in Surface Sciences*, vol. 51 (Springer-Verlag Berlin Heidelberg, Berlin, Heidelberg, 2013). ISBN 978-3-642-34242-4. http://dx.doi.org/10.1007/978-3-642-34243-1.

[7] D. A. Maclaren, B. Holst, D. J. Riley and W. Allison. Focusing elements and design considerations for a scanning helium microscope (SHeM). *Surf. Rev. Lett.* **10**(2-3):249 (2003). http://dx.doi.org/10.1142/S0218625X03005062.

[8] C. B. Lucas. *Atomic and Molecular Beams: Production and Collimation* (CRC Press, 2013). ISBN 978-1-4665-6106-9.

[9] I. Estermann and O. Stern. Beugung von Molekularstrahlen. *Zeitschrift für Physik* **61**(1):95 (1930). http://dx.doi.org/10.1007/BF01340293.

[10] A. Kantrowitz and J. Grey. A high intensity source for the molecular beam. Part

I. Theoretical. *Rev. Sci. Instrum.* **22**(5):328 (1951). http://dx.doi.org/10.1063/1.1745921.

[11] G. B. Kistiakowsky and W. P. Slichter. A High Intensity Source for the Molecular Beam. Part II. Experimental. *Rev. Sci. Instrum.* **22**(5):333 (1951). http://dx.doi.org/10.1063/1.1745922.

[12] D. Keith, M. Schattenburg, H. Smith and D. Pritchard. Diffraction of Atoms by a Transmission Grating. *Phys. Rev. Lett.* **61**(14):1580 (1988). http://dx.doi.org/10.1103/PhysRevLett.61.1580.

[13] J. J. Berkhout, O. J. Luiten, I. D. Setija, T. W. Hijmans, T. Mizusaki and J. T. M. Walraven. Quantum reflection: Focusing of hydrogen atoms with a concave mirror. *Phys. Rev. Lett.* **63**(16):1689 (1989). http://dx.doi.org/10.1103/PhysRevLett.63.1689.

[14] O. Carnal, M. Sigel, T. Sleator, H. Takuma and J. Mlynek. Imaging and focusing of atoms by a fresnel zone plate. *Phys. Rev. Lett.* **67**(23):3231 (1991). http://dx.doi.org/10.1103/PhysRevLett.67.3231.

[15] B. Holst and W. Allison. An atom-focusing mirror. *Nature* **390**(6657):244 (1997). http://dx.doi.org/10.1038/36769.

[16] J. Braun, P. K. Day, J. P. Toennies, G. Witte and E. Neher. Micrometer-sized nozzles and skimmers for the production of supersonic He atom beams. *Rev. Sci. Instrum.* **68**(8):3001 (1997). http://dx.doi.org/10.1063/1.1148233.

[17] R. B. Doak, R. Grisenti, S. Rehbein, G. Schmahl, J. P. Toennies and C. Wöll. Towards Realization of an Atomic de Broglie Microscope: Helium Atom Focusing Using Fresnel Zone Plates. *Phys. Rev. Lett.* **83**(21):4229 (1999). http://dx.doi.org/10.1103/PhysRevLett.83.4229.

[18] M. Koch, S. Rehbein, G. Schmahl, T. Reisinger, G. Bracco, W. E. Ernst and B. Holst. Imaging with neutral atoms—a new matter-wave microscope. *J. Microsc.* **229**(1):1 (2008). http://dx.doi.org/10.1111/j.1365-2818.2007.01874.x.

[19] D. Barredo, F. Calleja, P. Nieto, J. Hinarejos, G. Laurent, A. l. Vázquez de Parga, D. Farías and R. Miranda. A Quantum-Stabilized Mirror for Atoms. *Adv. Mater.* **20**(18):3492 (2008). http://dx.doi.org/10.1002/adma.200800866.

[20] H. C. Schewe, B. S. Zhao, G. Meijer and W. Schöllkopf. Focusing a helium atom beam using a quantum-reflection mirror. *New J. Phys.* **11**(11):113030 (2009). http://dx.doi.org/10.1088/1367-2630/11/11/113030.

[21] K. Fladischer, H. Reingruber, T. Reisinger, V. Mayrhofer, W.-E. Ernst, A. Ross, D. MacLaren, W. Allison, D. Litwin, J. Galas, S. Sitarek, P. Nieto, D. Barredo, D. Farías, R. Miranda, B. Surma, A. Miros, B. Piatkowski, E. Søndergård and B. Holst. An ellipsoidal mirror for focusing neutral atomic and molecular

beams. *New J. Phys.* **12**(3):033018 (2010). http://dx.doi.org/10.1088/1367-2630/12/3/033018.

[22] E. Sutter, P. M. Albrecht, F. E. Camino and P. Sutter. Monolayer graphene as ultimate chemical passivation layer for arbitrarily shaped metal surfaces. *Carbon* **48**(15):4414 (2010). http://dx.doi.org/10.1016/j.carbon.2010.07.058.

[23] A. Politano, B. Borca, M. Minniti, J. Hinarejos, A. l. Vázquez de Parga, D. Farías and R. Miranda. Helium reflectivity and Debye temperature of graphene grown epitaxially on Ru(0001). *Phys. Rev. B* **84**(3):23 (2011). http://dx.doi.org/10.1103/PhysRevB.84.035450.

[24] P. J. Witham and E. J. Sánchez. A simple approach to neutral atom microscopy. *Rev. Sci. Instrum.* **82**(10):103705 (2011). http://dx.doi.org/10.1063/1.3650719.

[25] S. D. Eder, T. Reisinger, M. M. Greve, G. Bracco and B. Holst. Focusing of a neutral helium beam below one micron. *New J. Phys.* **14**(7):073014 (2012). http://dx.doi.org/10.1088/1367-2630/14/7/073014.

[26] P. J. Witham and E. J. Sánchez. Increased resolution in neutral atom microscopy. *J. Microsc.* **248**(3):223 (2012). http://dx.doi.org/10.1111/j.1365-2818.2012.03665.x.

[27] M. Barr, K. M. O'Donnell, A. Fahy, W. Allison and P. C. Dastoor. A desktop supersonic free-jet beam source for a scanning helium microscope (SHeM). *Meas. Sci. Technol.* **23**(10):105901 (2012). http://dx.doi.org/10.1088/0957-0233/23/10/105901.

[28] M. Barr, A. Fahy, J. Martens, A. P. Jardine, D. J. Ward, J. Ellis, W. Allison and P. C. Dastoor. Unlocking new contrast in a scanning helium microscope. *Nat. Commun.* **7**:10189 (2016). http://dx.doi.org/10.1038/ncomms10189.

[29] B. S. Zhao, H. C. Schewe, G. Meijer and W. Schöllkopf. Coherent Reflection of He Atom Beams from Rough Surfaces at Grazing Incidence. *Phys. Rev. Lett.* **105**(13):133203 (2010). http://dx.doi.org/10.1103/PhysRevLett.105.133203.

[30] R. N. Zare. Otto Stern and the double bank shot. *Zeitschrift für Phys. D* **10**(2-3):377 (1988). http://dx.doi.org/10.1007/BF01384873.

[31] S. D. Eder, X. Guo, T. Kaltenbacher, M. M. Greve, M. Kalläne, L. Kipp and B. Holst. Focusing of a neutral helium beam with a photon-sieve structure. *Phys. Rev. A* **91**(4):043608 (2015). http://dx.doi.org/10.1103/PhysRevA.91.043608.

[32] C. Brand, M. Sclafani, C. Knobloch, Y. Lilach, T. Juffmann, J. Kotakoski, C. Mangler, A. Winter, A. Turchanin, J. Meyer, O. Cheshnovsky and M. Arndt.

An atomically thin matter-wave beamsplitter. *Nat. Nanotechnol.* **10**(10):845 (2015). http://dx.doi.org/10.1038/nnano.2015.179.

[33] T. Kaltenbacher. Optimization of a constrained linear monochromator design for neutral atom beams. *Ultramicroscopy* **163**:62 (2016). http://dx.doi.org/10.1016/j.ultramic.2016.02.003.

[34] A. H. Castro Neto, N. M. R. Peres, K. S. Novoselov and A. K. Geim. The electronic properties of graphene. *Rev. Mod. Phys.* **81**(1):109 (2009). http://dx.doi.org/10.1103/RevModPhys.81.109.

[35] M. Mohr, J. Maultzsch, E. Dobardžić, S. Reich, I. Milošević, M. Damnjanović, a. Bosak, M. Krisch and C. Thomsen. Phonon dispersion of graphite by inelastic X-ray scattering. *Phys. Rev. B* **76**(3):035439 (2007). http://dx.doi.org/10.1103/PhysRevB.76.035439.

[36] L. M. Malard, M. A. Pimenta, G. Dresselhaus and M. S. Dresselhaus. Raman spectroscopy in graphene. *Phys. Rep.* **473**(5-6):51 (2009). http://dx.doi.org/10.1016/j.physrep.2009.02.003.

[37] M. S. Dresselhaus, A. Jorio and R. Saito. Characterizing Graphene, Graphite, and Carbon Nanotubes by Raman Spectroscopy. *Annu. Rev. Condens. Matter Phys.* **1**(1):89 (2010). http://dx.doi.org/10.1146/annurev-conmatphys-070909-103919.

[38] H. Yanagisawa, T. Tanaka, Y. Ishida, M. Matsue, E. Rokuta, S. Otani and C. Oshima. Analysis of phonons in graphene sheets by means of HREELS measurement andab initio calculation. *Surf. Interface Anal.* **37**(2):133 (2005). http://dx.doi.org/10.1002/sia.1948.

[39] K. Michel and B. Verberck. Theory of the evolution of phonon spectra and elastic constants from graphene to graphite. *Phys. Rev. B* **78**(8):085424 (2008). http://dx.doi.org/10.1103/PhysRevB.78.085424.

[40] J. Wintterlin and M. L. Bocquet. Graphene on metal surfaces. *Surf. Sci.* **603**(10-12):1841 (2009). http://dx.doi.org/10.1016/j.susc.2008.08.037.

[41] G. Giovannetti, P. A. Khomyakov, G. Brocks, V. M. Karpan, J. Van Den Brink and P. J. Kelly. Doping graphene with metal contacts. *Phys. Rev. Lett.* **101**(2):4 (2008). http://dx.doi.org/10.1103/PhysRevLett.101.026803.

[42] C. Oshima, T. Aizawa, R. Souda, Y. Ishizawa and Y. Sumiyoshi. Surface phonon dispersion curves of graphite(0001) over the entire energy region. *Solid State Commun.* **65**(12):1601 (1988). http://dx.doi.org/10.1016/0038-1098(88)90660-6.

[43] S. Siebentritt, R. Pues, K. H. Rieder and A. M. Shikin. Surface phonon dispersion in graphite and in a lanthanum graphite intercalation compound. *Phys.*

Rev. B **55**(12):7927 (1997). http://journals.aps.org/prb/abstract/10.1103/PhysRevB.55.7927.

[44] R. Nicklow, N. Wakabayashi and H. G. Smith. Lattice Dynamics of Pyrolytic Graphite. *Phys. Rev. B* **5**(12):4951 (1972). http://dx.doi.org/10.1103/PhysRevB.5.4951.

[45] J. Maultzsch, S. Reich, C. Thomsen, H. Requardt and P. Ordejón. Phonon Dispersion in Graphite. *Phys. Rev. Lett.* **92**(7):075501 (2004). http://dx.doi.org/10.1103/PhysRevLett.92.075501.

[46] J.-A. Yan, W. Y. Ruan and M. Y. Chou. Phonon dispersions and vibrational properties of monolayer, bilayer, and trilayer graphene: Density-functional perturbation theory. *Phys. Rev. B* **77**:125401 (2008). http://dx.doi.org/10.1103/PhysRevB.77.125401.

[47] L. Wirtz and A. Rubio. The phonon dispersion of graphite revisited. *Solid State Commun.* **131**(3-4):141 (2004). http://dx.doi.org/10.1016/j.ssc.2004.04.042.

[48] V. Meunier, A. G. Souza Filho, E. B. Barros and M. S. Dresselhaus. Physical properties of low-dimensional sp^2-based carbon nanostructures. *Rev. Mod. Phys.* **88**(2):025005 (2016). http://dx.doi.org/10.1103/RevModPhys.88.025005.

[49] A. Allard and L. Wirtz. Graphene on metallic substrates: suppression of the Kohn Anomalies in the phonon dispersion. *Nano Lett.* **10**(11):4335 (2010). http://dx.doi.org/10.1021/nl101657v.

[50] A. Politano, G. Chiarello, G. Benedek, E. V. Ch. and P. M. Echenique. Vibrational spectroscopy and theory of alkali metal adsorption and co-adsorption on single-crystal surfaces. *Surf. Sci. Rep.* **68**(3-4):305 (2013). http://dx.doi.org/10.1016/j.surfrep.2013.07.001.

[51] W. Kohn. Image of the Fermi surface in the vibration spectrum of a metal. *Phys. Rev. Lett.* **2**(9):393 (1959). http://dx.doi.org/10.1103/PhysRevLett.2.393.

[52] J. Kröger. Electron–phonon coupling at metal surfaces. *Reports Prog. Phys.* **69**(4):899 (2006). http://dx.doi.org/10.1088/0034-4885/69/4/R02.

[53] S. Piscanec, M. Lazzeri, F. Mauri, a. Ferrari and J. Robertson. Kohn Anomalies and Electron-Phonon Interactions in Graphite. *Phys. Rev. Lett.* **93**(18):185503 (2004). http://dx.doi.org/10.1103/PhysRevLett.93.185503.

[54] J.-W. Jiang, B.-S. Wang, J.-S. Wang and H. S. Park. A review on the flexural mode of graphene: lattice dynamics, thermal conduction, thermal expansion, elasticity and nanomechanical resonance. *J. Phys. Condens. Mat-*

ter **27**(8):083001 (2015). http://dx.doi.org/10.1088/0953-8984/27/8/083001.

[55] A. I. Cocemasov, D. L. Nika and A. A. Balandin. Engineering of the thermodynamic properties of bilayer graphene by atomic plane rotations: the role of the out-of-plane phonons. *Nanoscale* **7**(30):12851 (2015). http://dx.doi.org/10.1039/C5NR03579A.

[56] X. Xu, J. Chen and B. Li. Phonon thermal conduction in novel 2D materials. *J. Phys. Condens. Matter* **28**(48):483001 (2016). http://dx.doi.org/10.1088/0953-8984/28/48/483001.

[57] D. L. Nika and A. A. Balandin. Phonons and thermal transport in graphene and graphene-based materials. *Reports Prog. Phys.* **80**(3):036502 (2017). http://dx.doi.org/10.1088/1361-6633/80/3/036502.

[58] S. Chen, Q. Wu, C. Mishra, J. Kang, H. Zhang, K. Cho, W. Cai, A. A. Balandin and R. S. Ruoff. Thermal conductivity of isotopically modified graphene. *Nat. Mater.* **11**(3):203 (2012). http://dx.doi.org/10.1038/nmat3207.

[59] Z. Xu. Heat transport in low-dimensional materials: A review and perspective. *Theor. Appl. Mech. Lett.* **6**:113 (2016). http://dx.doi.org/10.1016/j.taml.2016.04.002.

[60] C. Lee, X. Wei, J. W. Kysar and J. Hone. Measurement of the Elastic Properties and Intrinsic Strength of Monolayer Graphene. *Science* **321**(5887):385 (2008). http://dx.doi.org/10.1126/science.1157996.

[61] M. Batzill. The surface science of graphene: Metal interfaces, CVD synthesis, nanoribbons, chemical modifications, and defects. *Surf. Sci. Rep.* **67**(3-4):83 (2012). http://dx.doi.org/10.1016/j.surfrep.2011.12.001.

[62] J. M. MacLeod and F. Rosei. Molecular Self-Assembly on Graphene. *Small* **10**(6):1038 (2014). http://dx.doi.org/10.1002/smll.201301982.

[63] A. Dahal and M. Batzill. Graphene-nickel interfaces: a review. *Nanoscale* **6**(5):2548 (2014). http://dx.doi.org/10.1039/c3nr05279f.

[64] C. M. Sung and M. F. Tai. Reactivities of Transition Metals with Carbon: Implications to the Mechanism of Diamond Synthesis Under High Pressure. *Int. J. Refract. Met. Hard Mater.* **15**(4):237 (1997). http://dx.doi.org/10.1016/S0263-4368(97)00003-6.

[65] T. Aizawa, R. Souda, S. Otani, Y. Ishizawa and C. Oshima. Anomalous bond of monolayer graphite on transition-metal carbide surfaces. *Phys. Rev. Lett.* **64**(7):768 (1990). http://dx.doi.org/10.1103/PhysRevLett.64.768.

[66] T. Aizawa, R. Souda, S. Otani, Y. Ishizawa and C. Oshima. Bond softening in monolayer graphite formed on transition-metal carbide surfaces. *Phys. Rev.*

B **42**(18):11469 (1990). http://prb.aps.org/abstract/PRB/v42/i18/p11469_1.

[67] Y. Hwang, T. Aizawa, W. Hayami, S. Otani, Y. Ishizawa and S. Park. Surface phonon and electronic structure of a graphite monolayer formed on ZrC(111) and (001) surfaces. *Surf. Sci.* **271**(1-2):299 (1992). http://dx.doi.org/10.1016/0039-6028(92)90886-B.

[68] T. Aizawa, Y. Hwang, W. Hayami, R. Souda, S. Otani and Y. Ishizawa. Phonon dispersion of monolayer graphite on Pt(111) and NbC surfaces: bond softening and interface structures. *Surf. Sci.* **260**(1-3):311 (1992). http://dx.doi.org/10.1016/0039-6028(92)90046-9.

[69] T. Aizawa, R. Souda, Y. Ishizawa, H. Hirano, T. Yamada, K. Tanaka and C. Oshima. Phonon dispersion in monolayer graphite formed on Ni(111) and Ni(001). *Surf. Sci.* **237**(1-3):194 (1990). http://dx.doi.org/10.1016/0039-6028(90)90531-C.

[70] A. Al Taleb, G. Anemone, D. Farías and R. Miranda. Acoustic surface phonons of graphene on Ni(111). *Carbon* **99**:416 (2016). http://dx.doi.org/10.1016/j.carbon.2015.12.043.

[71] D. Maccariello, D. Campi, A. Al Taleb, G. Benedek, D. Farías, M. Bernasconi and R. Miranda. Low-energy excitations of graphene on Ru(0001). *Carbon* **93**:1 (2015). http://dx.doi.org/10.1016/j.carbon.2015.05.028.

[72] A. Politano, A. R. Marino and G. Chiarello. Phonon dispersion of quasi-freestanding graphene on Pt(111). *J. Phys. Condens. Matter* **24**(10):104025 (2012). http://dx.doi.org/10.1088/0953-8984/24/10/104025.

[73] A. Al Taleb, H. K. Yu, G. Anemone, D. Farías and A. M. Wodtke. Helium diffraction and acoustic phonons of graphene grown on copper foil. *Carbon* **95**:731 (2015). http://dx.doi.org/10.1016/j.carbon.2015.08.110.

[74] M. Endlich, A. Molina-Sánchez, L. Wirtz and J. Kröger. Screening of electron-phonon coupling in graphene on Ir(111). *Phys. Rev. B* **88**(20):205403 (2013). http://dx.doi.org/10.1103/PhysRevB.88.205403.

[75] B. Amorim and F. Guinea. Flexural mode of graphene on a substrate. *Phys. Rev. B* **88**(11):115418 (2013). http://dx.doi.org/10.1103/PhysRevB.88.115418.

[76] P. Sutter, M. Minniti, P. Albrecht, D. Farías, R. Miranda and E. Sutter. A high-reflectivity, ambient-stable graphene mirror for neutral atomic and molecular beams. *App. Phys. Lett.* **99**(21):211907 (2011). http://dx.doi.org/10.1063/1.3663866.

[77] A. M. Shikin, D. Farías and K. H. Rieder. Phonon stiffening induced by copper

intercalation in monolayer graphite on Ni(111). *Europhys. Lett.* **44**(1):44 (1998). http://iopscience.iop.org/0295-5075/44/1/044.

[78] M.-C. Wu, Q. Xu and D. W. Goodman. Investigations of Graphitic Overlayers Formed from Methane Decomposition on Ru(0001) and Ru(11$\bar{2}$0) Catalysts with Scanning Tunneling Microscopy and High-Resolution Electron Energy Loss Spectroscopy. *J. Phys. Chem.* **98**(19):5104 (1994). http://dx.doi.org/10.1021/j100070a027.

[79] C. Oshima and A. Nagashima. Ultra-thin epitaxial films of graphite and hexagonal boron nitride on solid surfaces. *J. Phys. Condens. Matter* **9**(1):1 (1997). http://dx.doi.org/10.1088/0953-8984/9/1/004.

[80] A. Nagashima, N. Tejima and C. Oshima. Electronic states of the pristine and alkali-metal-intercalated monolayer graphite/Ni(111) systems. *Phys. Rev. B* **50**:17487 (1994). http://dx.doi.org/10.1103/PhysRevB.50.17487.

[81] D. Farías, A. M. Shikin, K. H. Rieder and Y. S. Dedkov. Synthesis of a weakly bonded graphite monolayer on Ni(111) by intercalation of silver. *J. Phys. Condens. Matter* **11**(43):8453 (1999). http://dx.doi.org/10.1088/0953-8984/11/43/308.

[82] A. M. Shikin, V. K. Adamchuk and K.-H. Rieder. Formation of quasi-free graphene on the Ni(111) surface with intercalated Cu, Ag, and Au layers. *Phys. Solid State* **51**(11):2390 (2009). http://dx.doi.org/10.1134/S1063783409110316.

[83] K. H. Rieder and W. Stocker. Observation of Pronounced Neon Diffraction from Low-Index Metal Surfaces. *Phys. Rev. Lett.* **52**(5):352 (1984). http://dx.doi.org/10.1103/PhysRevLett.52.352.

[84] M. Petersen, S. Wilke, P. Ruggerone, B. Kohler and M. Scheffler. Scattering of Rare-Gas Atoms at a Metal Surface: Evidence of Anticorrugation of the Helium-Atom Potential Energy Surface and the Surface Electron Density. *Phys. Rev. Lett.* **76**(6):995 (1996). http://dx.doi.org/10.1103/PhysRevLett.76.995.

[85] D. Farías, M. Patting and K. H. Rieder. A helium atom scattering study of the H/NiAl(110) adsorption system. *J. Chem. Phys.* **117**(4):1797 (2002). http://dx.doi.org/10.1063/1.1486216.

[86] M. Minniti, C. Díaz, J. L. Fernández Cuñado, A. Politano, D. Maccariello, F. Martín, D. Farías and R. Miranda. Helium, neon and argon diffraction from Ru(0001). *J. Phys. Condens. Matter* **24**(35):354002 (2012). http://dx.doi.org/10.1088/0953-8984/24/35/354002.

[87] A. Sanz and S. Miret-Artés. Selective adsorption resonances: Quantum and

stochastic approaches. *Phys. Rep.* **451**(2-4):37 (2007). http://dx.doi.org/10.1016/j.physrep.2007.08.001.

[88] F. Hofmann, J. Toennies and J. R. Manson. A comprehensive experimental study of the dynamical interaction of He atoms with Cu(001) surface phonons. *J. Chem. Phys.* **101**(11):10155 (1994). http://dx.doi.org/10.1063/1.468005.

[89] B. Poelsema and G. Comsa. *Scattering of Thermal Energy Atoms*, vol. 115 (Springer-Verlag, Berlin Heidelberg, 1989). http://dx.doi.org/10.1007/BFb0045229.

[90] T. Engel and K. H. Rieder. *Structural Studies of Surfaces with Atomic and Molecular Beam Diffraction*, *Springer Tracts in Modern Physics*, vol. 91 (Springer, Berlin Heidelberg, 1982). ISBN 3-540-10964-1. http://dx.doi.org/10.1007/BFb0041340.

[91] L. Mattera, R. Musenich, C. Salvo and S. Terreni. Hydrogen diffraction from the (110) surface of silver. *Faraday Discuss. Chem. Soc.* **80**(1 10):115 (1985). http://dx.doi.org/10.1039/dc9858000115.

[92] H. Ibach. *Physics of Surfaces and Interfaces*. 1st edn. (Springer-Verlag, Berlin Heidelberg, 2006). ISBN 978-3-540-34710-1.

[93] G. Benedek, F. Hofmann, P. Ruggerone, G. Onida and L. Miglio. Surface phonons in layered crystals: theoretical aspects. *Surf. Sci. Rep.* **20**(1):1 (1994). http://dx.doi.org/10.1016/0167-5729(94)90002-7.

[94] G. Brusdeylins, R. B. Doak and J. P. Toennies. Observation of selective desorption of one-phonon inelastically scattered He atoms from a LiF crystal surface. *J. Chem. Phys.* **75**(4):1784 (1981). http://dx.doi.org/10.1063/1.442257.

[95] R. Doak and J. P. Toennies. Inelastic molecular beam scattering from solid surfaces. *Surf. Sci.* **117**(1-3):1 (1982). http://dx.doi.org/10.1016/0039-6028(82)90479-4.

[96] D. M. Smilgies and J. P. Toennies. Resolution and intensity considerations of an ideal He atom time-of-flight spectrometer for measurements of surface phonon dispersion curves. *Rev. Sci. Instrum.* **59**(10):2185 (1988). http://dx.doi.org/10.1063/1.1139984.

[97] G. Benedek, P. M. Echenique, J. P. Toennies and F. Traeger. Atoms riding Rayleigh waves. *J. Phys. Condens. Matter* **22**:359801 (2010). http://dx.doi.org/10.1088/0953-8984/22/35/359801.

[98] W. W. Hayes and J. R. Manson. Classical and semiclassical theories of atom scattering from corrugated surfaces. *Phys. Rev. B* **89**(4):045406 (2014). http://dx.doi.org/10.1103/PhysRevB.89.045406.

[99] P. Senet, J. Toennies and G. Benedek. Theory of the He-phonon forces at a metal surface. *Europhys. Lett.* **57**(3):430 (2002). http://iopscience.iop.org/0295-5075/57/3/430.

[100] G. Benedek, M. Bernasconi, K.-P. Bohnen, D. Campi, E. V. Chulkov, P. M. Echenique, R. Heid, I. Y. Sklyadneva and J. P. Toennies. Unveiling mode-selected electron–phonon interactions in metal films by helium atom scattering. *Phys. Chem. Chem. Phys.* **16**(16):7159 (2014). http://dx.doi.org/10.1039/c3cp54834a.

[101] F. de Juan, A. Politano, G. Chiarello and H. a. Fertig. Symmetries and selection rules in the measurement of the phonon spectrum of graphene and related materials. *Carbon* **85**:225 (2015). http://dx.doi.org/10.1016/j.carbon.2014.12.105.

[102] J. L. Erskine, E. J. Jeong, J. Yater, Y. Chen and S. Y. Tong. Detection of odd symmetry shear modes at metal surfaces by inelastic electron scattering: Experiment and theory. *J. Vac. Sci. Technol. A Vacuum, Surfaces, Film.* **8**(3):2649 (1990). http://dx.doi.org/10.1116/1.576687.

[103] D. L. Nika, E. P. Pokatilov, A. S. Askerov and A. A. Balandin. Phonon thermal conduction in graphene: Role of Umklapp and edge roughness scattering. *Phys. Rev. B* **79**(15):155413 (2009). http://dx.doi.org/10.1103/PhysRevB.79.155413.

[104] J. R. Manson, G. Benedek and S. Miret-Artés. Electron–Phonon Coupling Strength at Metal Surfaces Directly Determined from the Helium Atom Scattering Debye–Waller Factor. *J. Phys. Chem. Lett.* 1016 (2016). http://dx.doi.org/10.1021/acs.jpclett.6b00139.

[105] R. Brako and D. M. Newns. Differential Cross Section for Atoms Inelastically Scattered from Surfaces. *Phys. Rev. Lett.* **48**(26):1859 (1982). http://dx.doi.org/10.1103/PhysRevLett.48.1859.

[106] R. Brako and D. Newns. Energy and angular distribution of atoms scattered from surfaces. *Surf. Sci.* **117**(1-3):42 (1982). http://dx.doi.org/10.1016/0039-6028(82)90483-6.

[107] J. R. Manson. Inelastic scattering from surfaces. *Phys. Rev. B* **43**(9):6924 (1991). http://dx.doi.org/10.1103/PhysRevB.43.6924.

[108] W. W. Hayes and J. R. Manson. Rare gas collisions with molten metal surfaces. *J. Chem. Phys.* **127**(16):164714 (2007). http://dx.doi.org/10.1063/1.2786073.

[109] W. W. Hayes and J. R. Manson. Argon scattering from Ru(0001): Calculations and comparison with experiment. *Phys. Rev. B* **75**(11):113408 (2007). http://dx.doi.org/10.1103/PhysRevB.75.113408.

[110] W. W. Hayes and J. R. Manson. Determination of the Surface Corrugation Amplitude from Classical Atom Scattering. *Phys. Rev. Lett.* **109**(6):063203 (2012). http://dx.doi.org/10.1103/PhysRevLett.109.063203.

[111] D. R. Miller. *Atomic and Molecular Beam Methods*, vol. 1 (Oxford university press, New York, Oxford, 1988). ISBN 978-0195042801.

[112] H. Pauly. *Atom, Molecule, and Cluster Beams I*, *Springer Series on Atomic, Optical, and Plasma Physics*, vol. 28 (Springer Berlin Heidelberg, Berlin, Heidelberg, 2000). ISBN 978-3-642-08623-6. http://dx.doi.org/10.1007/978-3-662-04213-7.

[113] P. Nieto, D. Barredo, D. Farías and R. Miranda. In-Plane and Out-of-Plane Diffraction of H_2 from Ru(001). *J. Phys. Chem. A* **115**(25):7283 (2011). http://dx.doi.org/10.1021/jp200502v.

[114] D. Barredo. *Dinámica de interacción de haces de He, H_2 y D_2 de energía térmica con superficies*. Ph.D. thesis, Universidad Autónoma de Madrid (2009).

[115] P. Nieto. *An Experimental Study of H_2 Diffraction from Metal Surfaces*. Ph.D. thesis, Universidad Autónoma de Madrid (2009).

[116] G. Comsa. Coherence length and/or transfer width? *Surf. Sci.* **81**(1):57 (1979). http://dx.doi.org/10.1016/0039-6028(79)90505-3.

[117] J. Lapujoulade, Y. Lejay and G. Armand. The thermal attenuation of coherent elastic scattering of noble gas from metal surfaces. *Surf. Sci.* **95**(1):107 (1980). http://dx.doi.org/10.1016/0039-6028(80)90131-4.

[118] G. Brusdeylins, R. B. Doak and J. P. Toennies. High-resolution helium time-of-flight studies of Rayleigh surface-phonon dispersion curves of LiF, NaF, and KCl. *Phys. Rev. B* **27**(6):3662 (1983). http://dx.doi.org/10.1103/PhysRevB.27.3662.

[119] D. Maccariello. *Structure and dynamics at graphene interfaces: from metal substrates to adsorbed molecules*. Ph.D. thesis, Universidad Autónoma de Madrid (2014).

[120] X. Li, W. Cai, J. An, S. Kim, J. Nah, D. Yang, R. Piner, A. Velamakanni, I. Jung, E. Tutuc, S. K. Banerjee, L. Colombo and R. S. Ruoff. Large-Area Synthesis of High-Quality and Uniform Graphene Films on Copper Foils. *Science* **324**(5932):1312 (2009). http://dx.doi.org/10.1126/science.1171245.

[121] R. Muñoz and C. Gómez-Aleixandre. Review of CVD Synthesis of Graphene. *Chem. Vap. Depos.* **19**(10-11-12):297 (2013). http://dx.doi.org/10.1002/cvde.201300051.

[122] X. Li, L. Colombo and R. S. Ruoff. Synthesis of Graphene Films on Copper

Foils by Chemical Vapor Deposition. *Adv. Mater.* **28**(29):6247 (2016). http://dx.doi.org/10.1002/adma.201504760.

[123] H. K. Yu, K. Balasubramanian, K. Kim, J.-L. Lee, M. Maiti, C. Ropers, J. Krieg, K. Kern and A. M. Wodtke. Chemical vapor deposition of graphene on a "peeled-off" epitaxial cu(111) foil: a simple approach to improved properties. *ACS Nano* **8**(8):8636 (2014). http://dx.doi.org/10.1021/nn503476j.

[124] S. Ogawa, T. Yamada, S. Ishidzuka, A. Yoshigoe, M. Hasegawa, Y. Teraoka and Y. Takakuwa. Graphene Growth and Carbon Diffusion Process during Vacuum Heating on Cu(111)/Al_2O_3 Substrates. *Jpn. J. Appl. Phys.* **52**(11R):110122 (2013). http://dx.doi.org/10.7567/JJAP.52.110122.

[125] J. B. Nelson and D. P. Riley. The thermal expansion of graphite from 15 °C to 800 °C: part I. Experimental. *Proc. Phys. Soc.* **57**(6):477 (1945). http://dx.doi.org/10.1088/0959-5309/57/6/303.

[126] J. M. Cowley and J. A. Ibers. The structures of some ferric chloride-graphite compounds. *Acta Crystallogr.* **9**(5):421 (1956). http://dx.doi.org/10.1107/S0365110X56001200.

[127] D. Akinwande, C. J. Brennan, J. S. Bunch, P. Egberts, J. R. Felts, H. Gao, R. Huang, J.-S. Kim, T. Li, Y. Li, K. M. Liechti, N. Lu, H. S. Park, E. J. Reed, P. Wang, B. I. Yakobson, T. Zhang, Y.-W. Zhang, Y. Zhou and Y. Zhu. A Review on Mechanics and Mechanical Properties of 2D Materials – Graphene and Beyond. *arXiv* **1611**:01555 (2017). https://arxiv.org/abs/1611.01555.

[128] K. Chae, H. Lu and T. Gustafsson. Medium-energy ion-scattering study of the temperature dependence of the structure of Cu(111). *Phys. Rev. B* **54**(19):14082 (1996). http://dx.doi.org/10.1103/PhysRevB.54.14082.

[129] N. Mounet and N. Marzari. First-principles determination of the structural, vibrational and thermodynamic properties of diamond, graphite, and derivatives. *Phys. Rev. B* **71**:205214 (2005). http://dx.doi.org/10.1103/PhysRevB.71.205214.

[130] L. L. Patera, C. Africh, R. S. Weatherup, R. Blume, S. Bhardwaj, C. Castellarin-Cudia, A. Knop-Gericke, R. Schloegl, G. Comelli, S. Hofmann and C. Cepek. In situ observations of the atomistic mechanisms of ni catalyzed low temperature graphene growth. *ACS Nano* **7**(9):7901 (2013). http://dx.doi.org/10.1021/nn402927q.

[131] A. Tamtögl, E. Bahn, J. Zhu, P. Fouquet, J. Ellis and W. Allison. Graphene on Ni(111): Electronic Corrugation and Dynamics from Helium Atom Scattering. *J. Phys. Chem. C* **119**(46):25983 (2015). http://dx.doi.org/10.1021/acs.jpcc.5b08284.

[132] M. I. Trioni, G. Fratesi, S. Achilli and G. P. Brivio. Dynamics of electron distributions probed by helium scattering. *J. Phys. Condens. Matter* **21**(26):264003 (2009). http://dx.doi.org/10.1088/0953-8984/21/26/264003.

[133] J. R. Manson. Multiphonon atom-surface scattering. *Comput. Phys. Commun.* **80**(1-3):145 (1994). http://dx.doi.org/10.1016/0010-4655(94)90101-5.

[134] T. Narusawa, W. M. Gibson and E. Törnqvist. Relaxation of Ni(111) Surface by Oxygen Adsorption. *Phys. Rev. Lett.* **47**(6):417 (1981). http://prl.aps.org/abstract/PRL/v47/i6/p417{_}1.

[135] M. Pedio, L. Becker, B. Hillert, S. De Addato and J. Haase. Oxygen on Ni(111): A multiple-scattering analysis of the near-edge X-ray-absorption fine structure. *Phys. Rev. B* **41**(11):7462 (1990). http://dx.doi.org/10.1103/PhysRevB.41.7462.

[136] E. Schmidtke, C. Schwennicke and H. Pfnür. The O/Ni(111)-p(2×2) structure: adsorbate induced relaxations. *Surf. Sci.* **312**(3):301 (1994). http://dx.doi.org/10.1016/0039-6028(94)90723-4.

[137] D. T. Vu Grimsby, Y. K. Wu and K. A. R. Mitchell. A LEED analysis for the Ni(111)-((2×2))-O surface structure: Evidence for oxygen-induced relaxations of both vertical and lateral types in the close packed surface layer of nickel. *Surf. Sci.* **232**(1-2):51 (1990). http://dx.doi.org/10.1016/0039-6028(90)90586-W.

[138] Y. Gamo, A. Nagashima, M. Wakabayashi, M. Terai and C. Oshima. Atomic structure of monolayer graphite formed on Ni(111). *Surf. Sci.* **374**(1-3):61 (1997). http://dx.doi.org/10.1016/S0039-6028(96)00785-6.

[139] S. M. Kozlov, F. Viñes and A. Görling. Bonding mechanisms of graphene on metal surfaces. *J. Phys. Chem. C* **116**(13):7360 (2012). http://dx.doi.org/10.1021/jp210667f.

[140] V. I. Artyukhov, Y. Hao, R. S. Ruoff and B. I. Yakobson. Breaking of Symmetry in Graphene Growth on Metal Substrates. *Phys. Rev. Lett.* **114**(11):115502 (2015). http://dx.doi.org/10.1103/PhysRevLett.114.115502.

[141] T. G. Kollie. Measurement of the thermal-expansion coefficient of nickel from 300 to 1000 K and determination of the power-law constants near the Curie temperature. *Phys. Rev. B* **16**(11):4872 (1977). http://dx.doi.org/10.1103/PhysRevB.16.4872.

[142] J. Gao, J. Zhao and F. Ding. Transition metal surface passivation induced graphene edge reconstruction. *J. Am. Chem. Soc.* **134**(14):6204 (2012). http://dx.doi.org/10.1021/ja2104119.

[143] B. Dlubak, M. B. Martin, R. S. Weatherup, H. Yang, C. Deranlot, R. Blume, R. Schloegl, A. Fert, A. Anane, S. Hofmann, P. Seneor and J. Robertson. Graphene-passivated nickel as an oxidation-resistant electrode for spintronics. *ACS Nano* **6**(12):10930 (2012). http://dx.doi.org/10.1021/nn304424x.

[144] M. B. Martin, B. Dlubak, R. S. Weatherup, M. Piquemal-Banci, H. Yang, R. Blume, R. Schloegl, S. Collin, F. Petroff, S. Hofmann, J. Robertson, A. Anane, A. Fert and P. Seneor. Protecting nickel with graphene spin-filtering membranes: A single layer is enough. *Appl. Phys. Lett.* **107**(1):6 (2015). http://dx.doi.org/10.1063/1.4923401.

[145] A. Politano, A. R. Marino, V. Formoso and G. Chiarello. Hydrogen bonding at the water/quasi-freestanding graphene interface. *Carbon N. Y.* **49**(15):5180 (2011). http://dx.doi.org/10.1016/j.carbon.2011.07.034.

[146] A. Politano, M. Cattelan, D. Boukhvalov, D. Campi, A. Cupolillo, S. Agnoli, N. G. Apostol, P. Lacovig, S. Lizzit, D. Farías, G. Chiarello, G. Granozzi and R. Larciprete. Unveiling the Mechanisms Leading to H_2 Production Promoted by Water Decomposition on Epitaxial Graphene at Room Temperature. *ACS Nano* **10**(4):4543 (2016). http://dx.doi.org/10.1021/acsnano.6b00554.

[147] G. López-Polín, C. Gómez-Navarro, V. Parente, F. Guinea, M. I. Katsnelson, F. Pérez-Murano and J. Gómez-Herrero. Increasing the elastic modulus of graphene by controlled defect creation. *Nat. Phys.* **11**(1):26 (2014). http://dx.doi.org/10.1038/nphys3183.

[148] J. N. Grima, S. Winczewski, L. Mizzi, M. C. Grech, R. Cauchi, R. Gatt, D. Attard, K. W. Wojciechowski and J. Rybicki. Tailoring graphene to achieve negative poisson's ratio properties. *Adv. Mater.* **27**(8):1455 (2015). http://dx.doi.org/10.1002/adma.201404106.

[149] M. M. Ugeda, D. Fernández-Torre, I. Brihuega, P. Pou, a. J. Martínez-Galera, R. Pérez and J. M. Gómez-Rodríguez. Point Defects on Graphene on Metals. *Phys. Rev. Lett.* **107**(11):116803 (2011). http://dx.doi.org/10.1103/PhysRevLett.107.116803.

[150] Z. Song and Z. Xu. Geometrical effect 'stiffens' graphene membrane at finite vacancy concentrations. *Extrem. Mech. Lett.* **6**:82 (2016). http://dx.doi.org/10.1016/j.eml.2015.12.010.

[151] J. Coraux, A. T. N'Diaye, C. Busse and T. Michely. Structural coherency of graphene on Ir(111). *Nano Lett.* **8**(2):565 (2008). http://dx.doi.org/10.1021/nl0728874.

[152] A. T. N'Diaye, J. Coraux, T. Plasa, C. Busse and T. Michely. Structure of

epitaxial graphene on Ir(111). *New J. Phys.* **10**(4):043033 (2008). http://dx.doi.org/10.1088/1367-2630/10/4/043033.

[153] I. Pletikosić, M. Kralj, P. Pervan, R. Brako, J. Coraux, A. T. N'Diaye, C. Busse and T. Michely. Dirac Cones and Minigaps for Graphene on Ir(111). *Phys. Rev. Lett.* **102**(5):056808 (2009). http://dx.doi.org/10.1103/PhysRevLett.102.056808.

[154] E. Starodub, A. Bostwick, L. Moreschini, S. Nie, F. Gabaly, K. F. McCarty and E. Rotenberg. In-plane orientation effects on the electronic structure, stability, and Raman scattering of monolayer graphene on Ir(111). *Phys. Rev. B* **83**(12):125428 (2011). http://dx.doi.org/10.1103/PhysRevB.83.125428.

[155] W. H. Chung, D. S. Tsai, L. J. Fan, Y. W. Yang and Y. S. Huang. Surface oxides of Ir(111) prepared by gas-phase oxygen atoms. *Surf. Sci.* **606**(23-24):1965 (2012). http://dx.doi.org/10.1016/j.susc.2012.08.020.

[156] A. T. N'Diaye, R. van Gastel, A. J. Martínez-Galera, J. Coraux, H. Hattab, D. Wall, F. J. Meyer zu Heringdorf, M. Horn-von Hoegen, J. M. Gómez-Rodríguez, B. Poelsema, C. Busse and T. Michely. In situ observation of stress relaxation in epitaxial graphene. *New J. Phys.* **11**(11):113056 (2009). http://dx.doi.org/10.1088/1367-2630/11/11/113056.

[157] B. Borca, S. Barja, M. Garnica, M. Minniti, A. Politano, J. M. Rodriguez-García, J. J. Hinarejos, D. Farías, A. L. Vázquez de Parga and R. Miranda. Electronic and geometric corrugation of periodically rippled, self-nanostructured graphene epitaxially grown on Ru(0001). *New J. Phys.* **12**(9):093018 (2010). http://dx.doi.org/10.1088/1367-2630/12/9/093018.

[158] H. P. Singh. Determination of thermal expansion of germanium, rhodium and iridium by X-rays. *Acta Cryst. A* **24**(4):469 (1968). https://doi.org/10.1107/S056773946800094X.

[159] M. Pozzo, D. Alfè, P. Lacovig, P. Hofmann, S. Lizzit and A. Baraldi. Thermal Expansion of Supported and Freestanding Graphene: Lattice Constant versus Interatomic Distance. *Phys. Rev. Lett.* **106**(13):135501 (2011). http://dx.doi.org/10.1103/PhysRevLett.106.135501.

[160] H. Hattab, A. T. N'Diaye, D. Wall, C. Klein, G. Jnawali, J. Coraux, C. Busse, R. van Gastel, B. Poelsema, T. Michely, F. J. Meyer zu Heringdorf and M. Horn-von Hoegen. Interplay of wrinkles, strain, and lattice parameter in graphene on iridium. *Nano Lett.* **12**(2):678 (2012). http://dx.doi.org/10.1021/nl203530t.

[161] D. Maccariello, A. Al Taleb, F. Calleja, A. L. Vázquez de Parga, P. Perna, J. Camarero, E. Gnecco, D. Farías and R. Miranda. Observation of Lo-

calized Vibrational Modes of Graphene Nanodomes by Inelastic Atom Scattering. *Nano Letters* **16**(1):2 (2016). http://dx.doi.org/10.1021/acs.nanolett.5b02887.

[162] S. Schumacher, D. F. Förster, M. Rösner, T. O. Wehling and T. Michely. Strain in Epitaxial Graphene Visualized by Intercalation. *Phys. Rev. Lett.* **110**(8):086111 (2013). http://dx.doi.org/10.1103/PhysRevLett.110.086111.

[163] G. Boato, P. Cantini, C. Guidi, R. Tatarek and G. P. Felcher. Bound-state resonances and interaction potential of helium scattered by graphite(0001). *Phys. Rev. B* **20**(10):3957 (1979). http://dx.doi.org/10.1103/PhysRevB.20.3957.

[164] E. Ghio, L. Mattera, C. Salvo, F. Tommasini and U. Valbusa. Vibrational spectrum of H and D on the (0001) graphite surface from scattering experiments. *J. Chem. Phys.* **73**(1):556 (1980). http://dx.doi.org/10.1063/1.439855.

[165] W. W. Hayes, H. Ambaye and J. R. Manson. Atomic and molecular collisions with surfaces: comparisons of Ar and N_2 scattering from Ru(0001). *J. Phys.: Condens. Matter* **19**:305007 (2007). http://dx.doi.org/10.1088/0953-8984/19/30/305007.

[166] J. P. Oh, T. Kondo, D. Hatake and J. Nakamura. Elastic and inelastic scattering components in the angular intensity distribution of He scattered from graphite. *Surf. Sci.* **603**(6):895 (2009). http://dx.doi.org/10.1016/j.susc.2009.02.007.

[167] H. Shichibe, Y. Satake, K. Watanabe, A. Kinjyo, A. Kunihara, Y. Yamada, M. Sasaki, W. W. Hayes and J. R. Manson. Probing interlayer interactions between graphene and metal substrates by supersonic rare-gas atom scattering. *Phys. Rev. B* **91**(15):155403 (2015). http://dx.doi.org/10.1103/PhysRevB.91.155403.

[168] D. P. Jackson. Approximate calculation of surface Debye temperatures. *Surf. Sci.* **43**(2):431 (1974). http://dx.doi.org/10.1016/0039-6028(74)90267-2.

[169] E. Ferrari, L. Galli, E. Miniussi, M. Morri, M. Panighel, M. Ricci, P. Lacovig, S. Lizzit and A. Baraldi. Layer-dependent Debye temperature and thermal expansion of Ru(0001) by means of high-energy resolution core-level photoelectron spectroscopy. *Phys. Rev. B* **82**(19):195420 (2010). http://dx.doi.org/10.1103/PhysRevB.82.195420.

[170] K. Burke and W. Kohn. Finite Debye-Waller factor for "classical" atom-surface scattering. *Phys. Rev. B* **43**:2477 (1991). http://dx.doi.org/10.1103/PhysRevB.43.2477.

[171] T. Andersson, F. Althoff, P. Linde, S. Andersson and K. Burke. Probing a cold

surface with slow heavy-atom scattering: Experimental results and theoretical calculations. *Phys. Rev. B* **65**:045409 (2002). http://dx.doi.org/10.1103/PhysRevB.65.045409.

[172] F. Althoff, T. Andersson and S. Andersson. Quantum Scattering of Heavy Particles from a 10 K Cu(111) Surface. *Phys. Rev. Lett.* **79**:4429 (1997). http://dx.doi.org/10.1103/PhysRevLett.79.4429.

[173] A. Šiber and B. Gumhalter. Comment on "Quantum Scattering of Heavy Particles from a 10 K Cu(111) Surface". *Phys. Rev. Lett.* **81**:1742 (1998). http://dx.doi.org/10.1103/PhysRevLett.81.1742.

[174] F. Althoff, T. Andersson and S. Andersson. Althoff, Andersson, and Andersson Reply:. *Phys. Rev. Lett.* **81**:1743 (1998). http://dx.doi.org/10.1103/PhysRevLett.81.1743.

[175] D. L. Nika and A. A. Balandin. Two-dimensional phonon transport in graphene. *J. Phys. Condens. Matter* **24**(23):233203 (2012). http://dx.doi.org/10.1088/0953-8984/24/23/233203.

[176] C. Kaden, P. Ruggerone, J. P. Toennies, G. Zhang and G. Benedek. Electronic pseudocharge model for the Cu(111) longitudinal-surface-phonon anomaly observed by helium-atom scattering. *Phys. Rev. B* **46**(20):13509 (1992). http://dx.doi.org/10.1103/PhysRevB.46.13509.

[177] L. Chen, Z. Huang and S. Kumar. Phonon transmission and thermal conductance across graphene/Cu interface. *Appl. Phys. Lett.* **103**(12):2011 (2013). http://dx.doi.org/10.1063/1.4821439.

[178] G. Benedek, G. Brusdeylins, C. Heimlich, J. P. Toennies and U. Valbusa. Surface phonons in graphite(001). *Surf. Sci.* **178**(1-3):545 (1986). http://dx.doi.org/10.1016/0039-6028(86)90331-6.

[179] I. Y. Sklyadneva, G. Benedek, E. V. Chulkov, P. M. Echenique, R. Heid, K. P. Bohnen and J. P. Toennies. Mode-Selected Electron-Phonon Coupling in Superconducting Pb Nanofilms Determined from He Atom Scattering. *Phys. Rev. Lett.* **107**(9):095502 (2011). http://dx.doi.org/10.1103/PhysRevLett.107.095502.

[180] V. Chis and G. Benedek. Phonon-induced surface charge density oscillations in quantum wells: a first-principles study of the (2×2)-K overlayer on Be(0001). *J. Phys. Chem. A* **115**(25):7242 (2011). http://dx.doi.org/10.1021/jp200373h.

[181] D. Campi, M. Bernasconi, G. Benedek and J. P. Toennies. Surface Dynamics of Xe(111): An Ambiguous Nobility. *J. Phys. Chem. C* **119**(26):14579 (2015). http://dx.doi.org/10.1021/jp511886f.

[182] Y. Wei, B. Wang, J. Wu, R. Yang and M. L. Dunn. Bending rigidity and Gaussian bending stiffness of single-layered graphene. *Nano Lett.* (2013). http://dx.doi.org/10.1021/nl303168w.

[183] L. J. Karssemeijer and A. Fasolino. Phonons of graphene and graphitic materials derived from the empirical potential LCBOPII. *Surf. Sci.* **605**(17-18):1611 (2011). http://dx.doi.org/10.1016/j.susc.2010.10.036.

[184] B. N. J. Persson and H. Ueba. Heat transfer between weakly coupled systems: Graphene on a-SiO_2. *Europhys. Lett.* **91**(5):56001 (2010). http://dx.doi.org/10.1209/0295-5075/91/56001.

[185] Z. Aksamija and I. Knezevic. Lattice thermal conductivity of graphene nanoribbons: Anisotropy and edge roughness scattering. *Appl. Phys. Lett.* **98**(14):141919 (2011). http://dx.doi.org/10.1063/1.3569721.

[186] L. Chen and S. Kumar. Thermal transport in graphene supported on copper. *J. Appl. Phys.* **112**(4):043502 (2012). http://dx.doi.org/10.1063/1.4740071.

[187] A. M. Shikin, D. Farías, V. K. Adamchuk and K.-H. Rieder. Surface phonon dispersion of a graphite monolayer adsorbed on Ni(111) and its modification caused by intercalation of Yb, La and Cu layers. *Surf. Sci.* **424**(1):155 (1999). http://dx.doi.org/10.1016/S0039-6028(99)00099-0.

[188] D. Farías, K. H. Rieder, A. M. Shikin, V. K. Adamchuk, T. Tanaka and C. Oshima. Modification of the surface phonon dispersion of a graphite monolayer adsorbed on Ni(111) caused by intercalation of Yb, Cu and Ag. *Surf. Sci.* **454-456**(1):437 (2000). http://dx.doi.org/10.1016/S0039-6028(00)00253-3.

[189] K. Kern, R. David, R. L. Palmer, G. Comsa and T. S. Rahman. Surface phonon dispersion of platinum (111). *Phys. Rev. B* **33**(6):4334 (1986). http://dx.doi.org/10.1103/PhysRevB.33.4334.

[190] G. Benedek, M. Bernasconi, V. Chis, E. Chulkov, P. M. Echenique, B. Hellsing and J. P. Toennies. Theory of surface phonons at metal surfaces: recent advances. *J. Phys.: Condens. Matter* **22**(8):084020 (2010). http://dx.doi.org/10.1088/0953-8984/22/8/084020.

[191] M. Endlich, H. P. C. Miranda, A. Molina-Sánchez, L. Wirtz and J. Kröger. Moiré-induced replica of graphene phonons on Ir(111). *Ann. Phys.* **526**(9-10):372 (2014). http://dx.doi.org/10.1002/andp.201400091.

[192] C. Busse, P. Lazić, R. Djemour, J. Coraux, T. Gerber, N. Atodiresei, V. Caciuc, R. Brako, A. T. N'Diaye, S. Blügel, J. Zegenhagen and T. Michely. Graphene on Ir(111): Physisorption with Chemical Modulation. *Phys. Rev. Lett.*

107(3):036101 (2011). http://dx.doi.org/10.1103/PhysRevLett.107.036101.

[193] A. W. Laskar, N. S., A. Mukherjee and S. Ghosh. Interplay of classical and quantum dynamics in a thermal ensemble of atoms. *New J. Phys.* **18**(5):053022 (2016). http://dx.doi.org/10.1088/1367-2630/18/5/053022.

[194] J. R. Manson and R. H. Ritchie. Energy loss in fast-particle surface scattering at grazing incidence. *Phys. Rev. B* **49**(7):4881 (1994). http://dx.doi.org/10.1103/PhysRevB.49.4881.

[195] F. Aigner, N. Simonović, B. Solleder, L. Wirtz and J. Burgdörfer. Suppression of Decoherence in Fast-Atom Diffraction at Surfaces. *Phys. Rev. Lett.* **101**(25):253201 (2008). http://dx.doi.org/10.1103/PhysRevLett.101.253201.

[196] A. Mertens and H. Winter. Energy Transfer from Fast Atomic Projectiles to a Crystal Lattice under Channeling Conditions. *Phys. Rev. Lett.* **85**(13):2825 (2000). http://dx.doi.org/10.1103/PhysRevLett.85.2825.

[197] J. Villette, A. G. Borisov, H. Khemliche, A. Momeni and P. Roncin. Subsurface-Channeling-Like Energy Loss Structure of the Skipping Motion on an Ionic Crystal. *Phys. Rev. Lett.* **85**:3137 (2000). http://dx.doi.org/10.1103/PhysRevLett.85.3137.

[198] D. A. MacLaren, C. Huang, A. C. Levi and W. Allison. Coverage-dependent quantum versus classical scattering of thermal neon atoms from Li/Cu(100). *J. Chem. Phys.* **129**(9):094706 (2008). http://dx.doi.org/10.1063/1.2976766.

[199] A. C. Levi, C. Huang, W. Allison and D. A. MacLaren. Quantum scattering of neon from a nanotextured surface. *J. Phys. Condens. Mat.* **21**(22):225009 (2009). http://dx.doi.org/10.1088/0953-8984/21/22/225009.

[200] A. C. Levi. Return to coherence via debye–waller factor quenching. *J. Phys. Condens. Mat.* **21**(40):405004 (2009). http://dx.doi.org/10.1088/0953-8984/21/40/405004.

[201] B. Feuerbacher and R. Willis. Momentum Transfer Cutoff in the Scattering of Neon Atoms from a Nickel (111) Surface. *Phys. Rev. Lett.* **47**(7):526 (1981). http://dx.doi.org/10.1103/PhysRevLett.47.526.

[202] V. Celli, D. Himes, P. Tran, J. P. Toennies, C. Wöll and G. Zhang. Multiphonon processes in atom-surface scattering. *Phys. Rev. Lett.* **66**(24):3160 (1991). http://dx.doi.org/10.1103/PhysRevLett.66.3160.

[203] E. Pollak and S. Miret-Artés. Classical theory for the in-plane scattering of atoms from corrugated surfaces: Application to the Ar–Ag(111) system.

J. Chem. Phys. **130**(19):194710 (2009). http://dx.doi.org/10.1063/1.3131182.

[204] A. Al Taleb and D. Farías. Phonon dynamics of graphene on metals. *J. Phys.: Condens. Matter* **28**(10):103005 (2016). http://dx.doi.org/10.1088/0953-8984/28/10/103005.

[205] D. Campi and G. Benedek. private communication.

[206] A. C. Levi and H. Suhl. Quantum theory of atom-surface scattering: Debye-Waller factor. *Surf. Sci.* **88**(1):221 (1979). http://dx.doi.org/10.1016/0039-6028(79)90577-6.